# Characterisation and Modelling of the Shear-Tension Coupling and Variability of Woven Engineering Fabrics

by

*Farag Abdussalm Ali Abdiwi*

*M.Sc*

Submitted in fulfilment of the requirements for the degree of Doctor of Philosophy

School of Engineering

University of Glasgow

March 2013

## ABSTRACT

Woven engineering fabrics generally serve as advanced composite preforms and are an important class of engineering material. This thesis focuses on improving the accuracy of Computer Aided Engineering (CAE) tools for simulating the deformation of such materials during the press-forming manufacture process. Specifically, this has involved better understanding: (i) the material behaviour during deformation and (ii) the extent and influence of material variability on forming behaviour. To this end, the use of a novel fabric shear test, the BBE test, capable of characterising the shear-tension coupling of engineering fabrics has been used for the first time in an extensive characterisation program, involving three different woven engineering fabrics. Results show a strong dependence of shear compliance on in-plane tension. Wrinkling behaviour during shear has also been characterised using two new analysis methods, a transmitted backlighting technique and a tracer line analysis technique. The onset of wrinkling is clearly shown to be an increasing function of the in-plane tension applied to the deforming fabric. Variability of fibre orientation, otherwise known as 'tow meander' can degrade the final mechanical properties of a textile composite part and can also influence measurements of the fabric's shear compliance. Accordingly, variability of tow orientation in a pre-consolidated textile composite and three engineering fabrics has been characterised using two different image processing methods: a simple manual method and a semi-automated method. The latter has been found to be a promising tool in terms of increasing accuracy and in reducing manual effort during the characterisation process. Modelling tow meander has also been conducted using a numerical code, Varifab$^{GA}$, that has been developed during the course of this work. The code has allowed the effects of tow meander on shear compliance to be investigated in numerical simulations using a technique of assigning an initial fibre orientation to each element in a Finite Element (FE) mesh before conducting shear test simulations. The experimentally measured shear-tension coupling has also been modelled by enhancing a pre-existing Non-Orthogonal Constitutive Model (NOCM). A comparison between model predictions and experimental results of the sensitivity of this shear-tension coupling has shown that the model provides good results. Finally, a novel geometrically complex 3D forming tool of a kart wheel has been designed and manufactured for use in experimental and numerical forming studies. The part provides a challenging modelling problem with which to demonstrate the use of the new computational tools developed during the course of this work.

## Definition of Symbols

| | |
|---|---|
| $\alpha$ | angle between the horizontal ($x$) axis and tether connecting transverse load to sample |
| $d_x$ | horizontal displacement of the side corner of Region A of BBE test sample when undergoing ideal kinematics |
| $d_y$ | vertical crosshead displacement |
| $d_x^*$ | measured horizontal displacement of the side corner of Region A of BBE test sample |
| $d_y^*$ | measured vertical displacement of the side corner of Region A of BBE test sample |
| $D$ | distance between the centre of the pulley and the side corner of Region A of BBE test sample when undergoing ideal kinematics |
| $D^*$ | measured distance between the centre of the pulley and the side corner of Region A of BBE test sample |
| $F_c$ | transverse force applied to BBE test sample |
| $F_f$ | friction force measured in the side pulleys during BBE test |
| $F_m$ | material force due to deformation of the sample during BBE test |
| $F_{mis}$ | misalignment force due to offset of sample from ideal alignment during BBE test |
| $F_r$ | reaction force measured due to transverse load during BBE test |
| $F_T$ | total force measured during BBE test |
| $L$ | vertical length of the UBE sample |
| $v_y$ | vertical velocity of crosshead during BBE test |
| $v_x$ | horizontal velocity of side corner of Region A of BBE test sample during ideal kinematics |
| $v_y^*$ | measured vertical velocity of upper corner of Region A of BBE test sample |
| $v_x^*$ | measured velocity of side corner of Region A of BBE test sample |
| $W$ | Width of the UBE sample. Also a convention is used when referring to the following quantities: |
| $C$ | length of vertical diagonal across Region C |
| $\overline{\Delta C}$ | average change in length of vertical diagonal across Region C |
| $L'$ | measured straight side length of Region A of UBE and BBE tests samples |
| $L''$ | measured curved side length of Region A of UBE and BBE tests samples |
| $\theta$ | shear angle in Region A |

| | |
|---|---|
| Namely, the first subscript for each symbol, *m* or *t*, indicates measured or theoretical (ideal) values, the second subscript, *p*, *u* or *b*, refers to PF, UBE and BBE tests data respectively, e.g. $C_{mu}$ indicates the measured value of the quantity *C* during UBE tests. | |
| | |
| $X$ | Arrays that are added to a matrix containing all the nodal coordinates of the expanding mesh in x axis (see Figure 3.3). |
| $Y$ | Arrays that are added to a matrix containing all the nodal coordinates of the expanding mesh in y axis (see Figure 3.3). |
| $n$ | The number of elements from the centre of the blank to the right, left, top or bottom edge of the mesh (e.g. in Figure 3.3, $n$=4). |
| $i$ | The node number when counting outwards from the centre of the blank towards the outer edge of the mesh along the vertical or horizontal mesh centrelines (e.g. $n$ = 3 for those nodes marked in red in Figure 3.3a). |
| $a_n$ | An array containing the half lengths of the horizontal diagonal element lengths (see Figure 3.5b). |
| $b_n$ | An array containing the half lengths of the vertical diagonal element lengths (see Figure 3.5b). |
| $\varepsilon_i$ | An array defined by Eq (3.5) which gradually decreases the stretch/contraction of the elements towards 0 when moving from the centre towards the left corner of the mesh. |
| $A$ | The peak amplitude of the perturbation. |
| $\omega_k t$ | Controls the periodicity of the perturbation. |
| $t$ | Parameter can lie between 0 and 5 and controls the wavelength of the perturbation and $\omega_k t$ is an array. |
| $X_k$ | The $x$ coordinates of nodes across the entire mesh. |
| $Y_k$ | The $y$ coordinates of nodes across the entire mesh. |
| $FT_{mu}$ | The fitness function of the mean of the angle across the sheet |
| $mu_m$ | The measured mean across a given specimen. |
| $mu_p$ | The predicted mean for a mesh of the same area. |
| $FT_{std}$ | The fitness function for the standard deviation of the mean inter-tow angle for a given sampling area |
| $std_m$ | The measured value of the standard deviation of the mean inter-tow angle for a given sampling area. |
| $std_p$ | The predicted value of the standard deviation of the mean inter-tow angle for a given sampling area. |

| | |
|---|---|
| $FC_{mu}$ | The criteria of the mean. |
| $FC_{std}$ | The criteria of the standard deviation. |
| $I$ | image intensity |
| $\nabla I$ | the first derivative vector of image intensity |
| $G_1$ | The shear modulus that related to the shear force increment $dF_s$ and shear angle increment $d\theta$ |
| $G_2$ | The shear modulus that related to the shear force $F_s$ and shear angle $\theta$ |
| $g_1^1, g_1^2$ | Components of unit covariant base vector, $g_1$ based on an orthogonal frame. $g^{11}$ diagonal component of metric tensor $= g^1.g^1$. |
| $g_2^1, g_2^2$ | Components of unit covariant base vector, $g_2$ based on an orthogonal frame. $g^{11}$ diagonal component of metric tensor $= g^1.g^1$. |
| $F_t(t)$ | the inertia forces at time *t* |
| $F_D(t)$ | the damping forces at time *t* |
| $F_E(t)$ | the elastic forces at time *t* |
| $R(t)$ | the externally applied load at time *t* |
| ${}^tF$ | the force corresponding to the internal element stresses at time *t* |
| $C'$ | damping coefficient |
| $M$ | mass |
| ${}^t\widehat{R}$ | the effective load vector |
| $U$ | Nodal displacement |
| $\dot{U}$ | Nodal velocity |
| $\ddot{U}$ | Nodal acceleration |
| K | stiffness matrix |
| $\Delta t$ | time increment |
| $L_{min}$ | element length |
| $c_d$ | the dilatational wave speed |
| $\rho$ | material density |
| $E$ | Young's modulus |
| $v$ | poisson's ratio |
| $A_1$ | cross sectional area per unit length of any typical yarn |

| | |
|---|---|
| $A_2$ | cross sectional area per unit length of the truss element |
| $E_1$ | the tensile stiffness of typical tow |
| $E_2$ | the stiffness of the truss element |
| $F_{Tpr}$ | the total predicted axial force |
| $F_{mpr}$ | the predicted material force |
| $F_{cpr}$ | numerically applied transverse force |
| $V_{ypr}$ | the predicted vertical velocity |
| $V_{xpr}$ | the predicted horizontal velocity |
| $F_s$ | the shear force |
| $\varepsilon_{warp}$ | the tensile strains along the warp fibre directions |
| $\varepsilon_{weft}$ | the tensile strains along the weft fibre directions |
| $\Psi$ | the average tensile strains along the warp and weft fibre directions |
| $\psi_p^i(\theta)$ | a polynomial curve fitted from each of the five BBE simulations, the coefficients of which are stored for later reference by the enhanced shear non-orthogonal constututive model |
| $R_p^i(\theta)$ | polynomial functions fitted to each ratio curve (the ratio curve is the input shear force versus shear angle curves are divided by the predicted shear force versus shear angle curves) |
| $\Delta\sigma_{ij}$ | the shear stress increment |
| $\Delta\theta$ | the shear strain increment |
| $\frac{d\sigma_{ij}}{d\theta}$ | the shear stress derivative |

# ACKNOWLEDGEMENTS

First and foremost, I would like to express my deepest thanks to Allah Almighty for giving me health and the ability to complete this work. I also would like to express my great appreciation and thanks to my supervisor Dr. Philip Harrison for his constant support and encouragement in making this work possible. Thanks also connected to Libyan government for helping fund this work and to all technicians who helped me with experimental tests in material lab and with manufacturing the forming tooling. I also would like to express very special thanks to my wife and children (Abdussalm, Mohammed, Raggad, Rahmma and Raffif), who have been patient and long-suffering. Thanks also to my parents for their moral and spiritual support.

# Table of Contents

# 1. Introduction

The importance of composite materials derives from their unique material properties such as high specific strength and stiffness. The strength to weight ratio and stiffness to weight ratio are much greater than those of steel and aluminium. As a result, many advantages of using composite material in several industrial sectors (aircraft, automotive, sport and recreation, civil infrastructure and microwave technology) have been noticed such as reduction in fuel consumption, long life span and lower maintenance costs, high energy absorption in impact events, and high corrosion and fatigue resistance. The high strength to weight ratio and corrosion resistance features of composite materials make them ideal for use in aircraft applications. The Boeing 787 makes greater use of composite materials in its airframe and primary structure than any previous Boeing commercial airplane. Undertaking the design process without preconceived ideas enabled Boeing engineers to specify the optimum material for specific applications throughout the airframe (see Figure 1.1) [1].

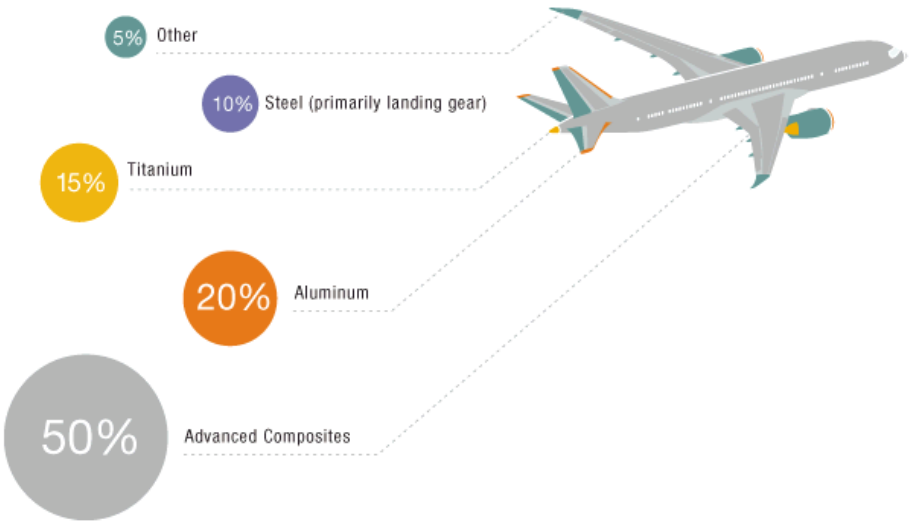


Figure 1.1. The percentage of the different materials used in the airframe of Boeing 78 [1]

In the automotive sector, Bentley Motors have conducted research that focussed on reducing the mass of the main structural components of a vehicle by 60% in order to achieve lower carbon emissions and lower fuel consumption [2]. Another example of composite material application is in making wind turbine blades. The challenge in this

industry is toward increasing the length of the blades. Blades of longer length have been successfully manufactured and some even exceed 80 metres [3].

Some of the main engineering challenges associated with composite material manufacturing are the high costs associated with labour intensive production and low productivity rates and also the anisotropic behaviour of advanced composites that can result in design and manufacture problems and therefore require the development of novel computational tools to guide manufacture processes. The challenge is how to overcome these limitations. Introducing computer integrated engineering into the design and manufacture process is an important step. In this chapter, an overview of composite materials and their preforms are presented with the aim of describing polymer composites in general and then focusing on woven engineering fabrics, the latter being the main topic of this thesis. The composition, processing, and typical applications of the materials are outlined. The aim is to provide the reader with an idea of the range of composite materials available and then to define the scope of this investigation. To do this the usual classification systems for composite materials are used.

## 1.1 Composite material

A composite is a combination of two or more materials on a macro or micro-scale [4]. Composite materials usually consist of both reinforcement and a matrix phase. The mechanical properties of engineering composites are usually enhanced when compared to those of the individual components (the reinforcement and the matrix). In fibre reinforced composites the reinforcement is produced from fibres. The mechanical properties of the reinforcement tend to be higher than those of the matrix. Thus, the stiffness and strength of fibre-reinforced composites is mainly due to the reinforcement. The usefulness of the matrix is in gluing and holding the fibres together in order to transfer the stress between fibres, and also in acting as a protective skin around the fibres by protecting them from environmental risks such as corrosion and abrasion. There are three main types of matrices: polymer, metal, and ceramic. The polymer matrix is used for applications that require temperature $\leq 250$ °C. Metal matrix is used for applications that require temperature from 200-800°C and it gives electrical conductivity, ductility, high strength, and high stiffness. For applications of much higher temperature, requiring high corrosion resistance, high

stiffness and high oxidation resistance, the matrices of choice are ceramics. However, in this work, attention is restricted to polymer composite.

## 1.2 Categorization of Composite Materials Based on Matrix Type

In general, matrices are the means of holding reinforcements together and transfering stresses to the reinforcements. Polymer composites can be categorized according to their matrix or the type of reinforcement. Categorizing polymer composites in terms of matrix type results in two broad categories known as thermoset and thermoplastic composites. The main types of thermosetting and thermoplastic polymers used in polymer composites are briefly introduced in the following section.

### 1.2.1 Thermosetting Polymers

There are a number of thermoset matrices as follows: phenol-formaldehyde resin, Duroplast, urea-formaldehyde, Melamine resin, polyimides and epoxy resin. Epoxy resin and curing agent (hardener) are the two components that form the epoxy thermoset matrix through a chemical reaction. In fibre and carbon reinforced polymer applications, epoxy is used as the matrix component. The chemical reaction of the epoxy is shown in Figure 1.2 [5].

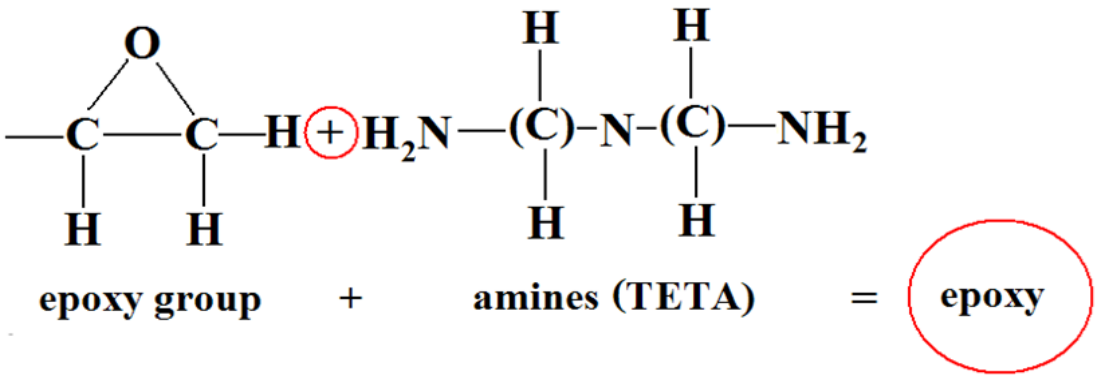


Figure 1.2. The chemical reaction of the Epoxy [5]

The main feature of thermosetting polymers is that the resin system requires a chemical cross-linking step in order to turn the liquid matrix into a solid polymer. Various thermosetting resin systems are available including polyester, phenolics, polyurethane,

silicone, polyimids and epoxy resin. The cheapest of these is polyester resin and the most expensive tends to be epoxy resin. Despite their higher cost epoxy resins systems are still widely employed due to their advantages in terms of both superior mechanical properties and their better resistance to alkaline conditions [6].

Thermosetting resin systems require the addition of a curing agent (hardener) to enable the cure process. The chemical curing time depends on the reaction rate which can be very slow (24-28 hours) at low temperature, 27°C, but can be accelerated using chemical additives or heating [7, 8]. A typical chemical reaction involved in the cure of an epoxy resin system is shown in figure 1.2 and demonstrates the formation of cross-links that produce the network of strong covalent interatomic bonds that are responsible for the excellent final mechanical properties typical of thermosetting resin systems. Common types of thermoset matrix are vulcanized rubberr, bakelite, a phenol-formaldehyde resin, Duroplast, urea-formaldehyde, Melamine resin, epoxy resin, polyimides and cyanate esters or polycyanurates. However, the most used matrix in glass and carbon reinforced composite is epoxy resin [5, 9]. The crosslink of epoxy is shown in Figure 1.2. At one end of the resin, an epoxide group is linked. It is formulated from two components which are epoxy resin (epichlorohydrin and bisphenol-A) and a hardener (tri-ethylene-tetra-mine (TETA)). The hardener groups react with the epoxide groups to form a covalent bond when the resin and hardener compounds are mixed [10].

Polyesters are polymers with repeating carboxylate groups in their backbone chain. Polyesters are a type of polymer which have carboxylate groups at both ends as shown in Figure 1.3.

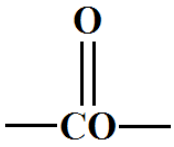


Figure 1.3. Repeating carboxylate group [10]

Figure 1.4 shows the typical esterification reactions that are used to synthesize the polyesters. Polyesters are fused by typical esterification reactions, which can be generalized by the reaction shown in Figure 1.2.

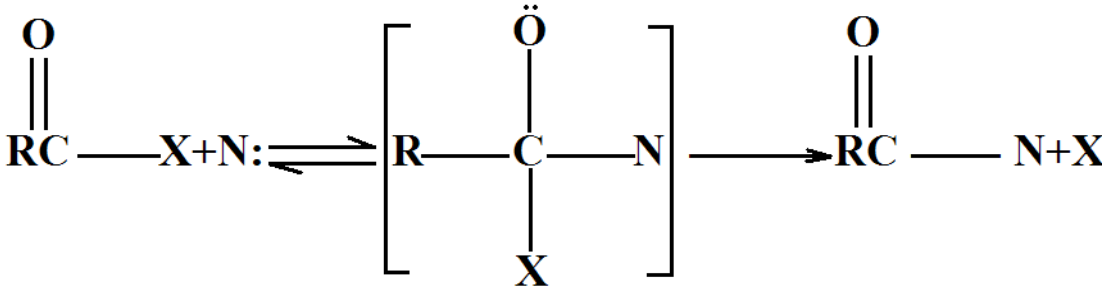

Figure 1.4. The esterification reactions of synthesizing the polyesters [10]

where N: is a nucleophilic reagent such as OR'. The rate of reaction is dependent on the structure of R, R', X, and N and on whether a catalyst is used [9].

Vinyl ester is a type of resin that is synthesized by typical esterification reactions. The esterification reactions are between two compounds: an epoxy resin and an unsaturated monocarboxylic acid. Vinyl ester has properties such as strength and thermal shock resistance midway between polyester and epoxy. The most broadly utilized vinyl ester product is the bisphenol-A epoxy based vinyl ester resin that is synthesized by the reaction of a bisphenol-A glycidylether with methacrylic acid as shown in Figure 1.5 [11].

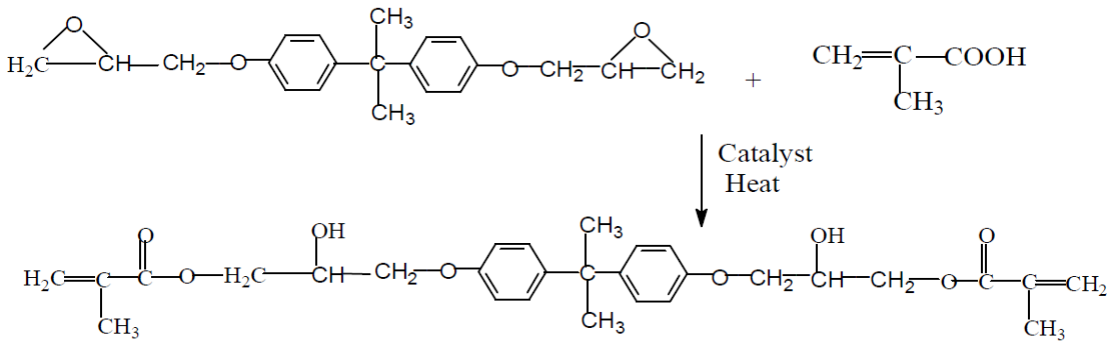


Figure 1.5. The esterification reactions of synthesizing the vinyl ester resin [11]

The advantages of thermosetting polymer resins are exemplified by excellent resistance to flame, heat, creep, solvents and excellent mechanical properties such as high stiffness and high impact resistance [12]. Their disadvantages include long processing time; polyesters

have a short shelf life as they crystallize over a long period of time. Thermoset resins can degrade at raised temperatures due to moisture absorption from the atmosphere, the so called ‘imide corrosion’ phenomenon, a potential problem with polymers that contain an imide end-group. Thermoset resins cannot be remelted after the resin gels, and in general thermoset matrices are more expensive than thermoplastic matrices.

### 1.2.2 Thermoplastic Polymers

Thermoplastic polymers have a fundamentally different molecular structure to thermosetting polymers. Unlike thermosetting polymers, which are highly cross-linked through covalent chemical bonds, thermoplastic polymers owe their mechanical properties to physical bonds. As an example, the molecular structure of nylon 6 $(C_6H_{11}NO)_n$ is shown in Figure 1.6; the high strength of nylon is due to strong interatomic van der Waal forces occurring between the main chains of the polymer molecules.

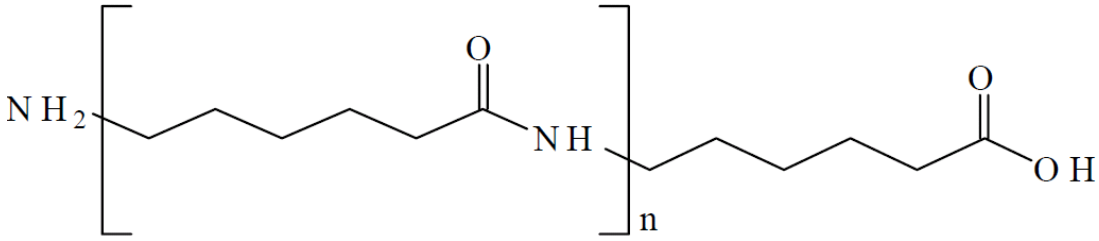


Figure 1.6. The molecular structure of nylon 6 [12]

The physical as opposed to chemical bonds between polymer chains in thermoplastic polymers result in a very different response to changes in temperature. The curing process of thermoset resin is based on cross-links which eventually produce a stiff solid (see Figure 1.7). However, thermoset matrices are inherently brittle due to the high cross-link densities which produce high-performance thermoset systems. During processing thermoplastics melt and flow as fully reacted polymers that are held together by secondary bonds but do not form cross-linking reactions. Moreover thermoplastics can be reprocessed by simply reheating to the melting temperature, and then reforming since they do not form irreversible cross-links during processing.

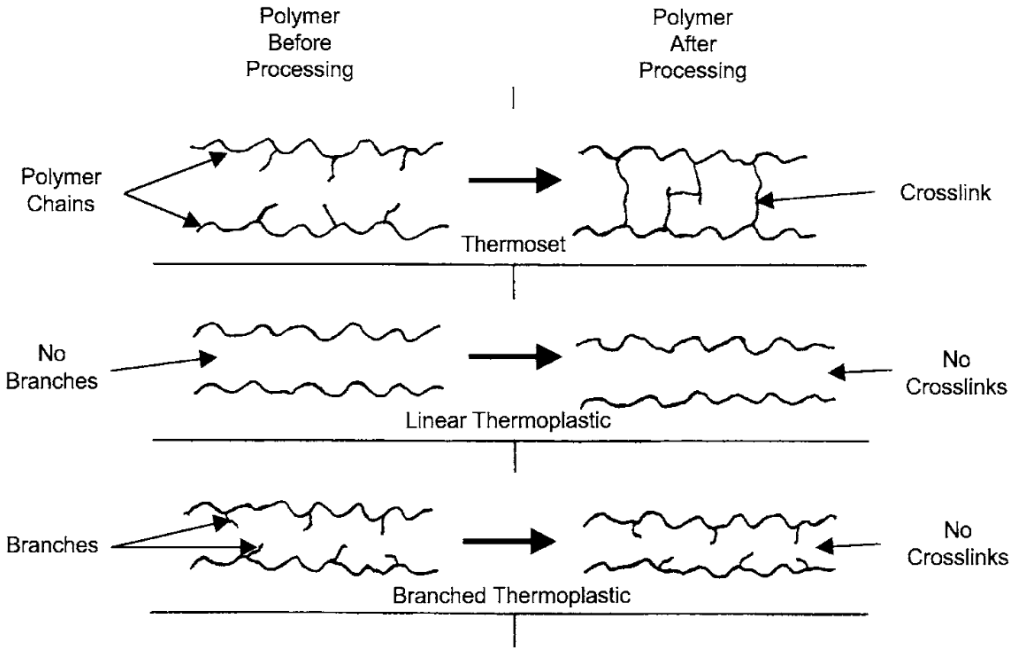


Figure 1.7. Thermoset and thermoplastic polymer structure before and after processing [10]

The three semi-crystalline thermoplastics polyetheretherketone (PEEK), polyphenylene sulfide (PPS) and polypropylene (PP) are the most used thermoplastic materials in composites, whereas the most important amorphous thermoplastic is polyetherimide (PEI) (see Figure 1.8).

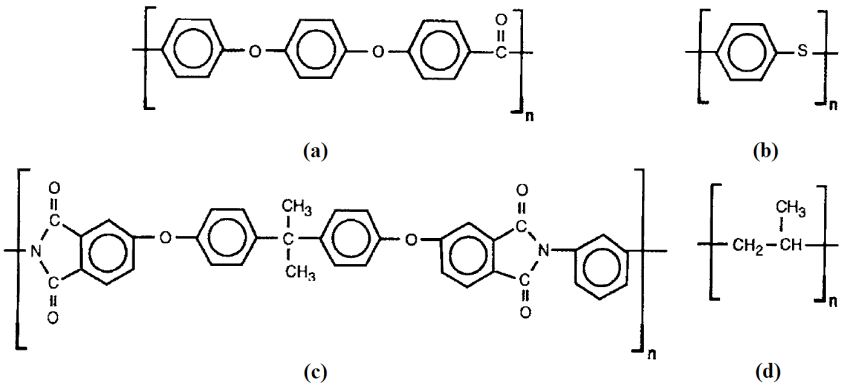


Figure 1.8. The molecular structure of (a) Polyetheretherketone (b) Polyphenylene sulphide (c) Polyetherimide and (d) Polypropylene [10]

PEEK polymers are produced as a result of the reaction of 4,4'-difluorobenzophenone $(FC_6H_4)_2CO$ with the disodium salt of hydroquinone $C_6H_4(OH)_2$, and the disodium salt of hydroquinone is produced by deprotonation with sodium carbonate $Na_2CO_3$ as shown in Figure 1.9.

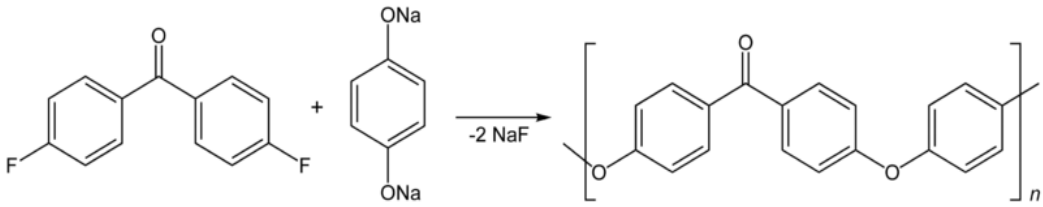


Figure 1.9. The reaction process of Polyetheretherketone PEEK polymers [10]

PPS is an organic polymer consisting of aromatic rings linked with sulfides as shown in Figure 1.8b. PP is made under specified heat and pressure by polymerizing propylene $C_3H_6$ in the presence of a catalyst [13].

## 1.3 Reinforcement

There are some terms that are used to describe the hierarchy or the structure of composite reinforcement such as fibre, yarn and tow. Fibre is a filament made from either natural or synthetic material and has high length-to-diameter ratio. Tow is a group of fibres with almost equal length. According to TORAYCA® [14] the typical number of fibres in a tow varies from 1000 to 48,000. A yarn is a bundle of filaments that are grouped by twisting. The reinforcement can be classified both in terms of the material and the dimensions of the reinforcement. The former type of classification is considered first before discussing composites in terms of the reinforcement dimensions (e.g. nano, particulate, short, long or continuous fibres). Glass, carbon and aramid are the most commonly used fibre reinforcements in composites. Less common are natural fibres (such as jute, flax, kenaf and hemp) due to their lower toughness and lower strength compared to glass, carbon and aramid fibres. There are also a number of other natural fibres that are used for specialist applications. Since synthetic fibres such as glass, carbon and aramid are materials that are based on the chemical compounds silica and oil, and these compounds are believed to waste energy and their prices are always rising, renewed attention on the use of natural fibres has been noted, since natural fibres are recyclable materials that minimize waste.

Fibre reinforcements in composite materials are mainly categorized into three types namely: particulate, short or discontinuous fibre and continuous fibre (see Figure 1.10). The particulate reinforcement is characterized by approximately equal dimension in all directions. A common example of particulate reinforcement is gravel in concrete. There are

two types of short fibres: chopped and grinded fibres. The length of these fibres is not always equal and can range from millimetres to centimetres, whereas the diameter of most fibres is a few microns. Chopped fibre and random mat are two examples of discontinuous reinforcements that are randomly orientated [15].

The difference between continuous and discontinuous reinforcements is their aspect ratio, i.e. length-to-diameter ratio; continuous reinforcements have longer (effectively infinite) aspect ratios compared to discontinuous reinforcements. Continuous fibre reinforcement is usually arranged into three types of structure namely: unidirectional, two directional (2D) and three directional (3D). If the third direction is through the thickness of the fabric structure this is known as a 3D fabric. Woven fabric, 2D braided, 2D knit and non-crimp fabrics all have essentially 2D architectures. While 3D woven and 3D knit have 3D architectures. Woven, knitted, braided and stitched fabrics are different types of 2D fabrics.

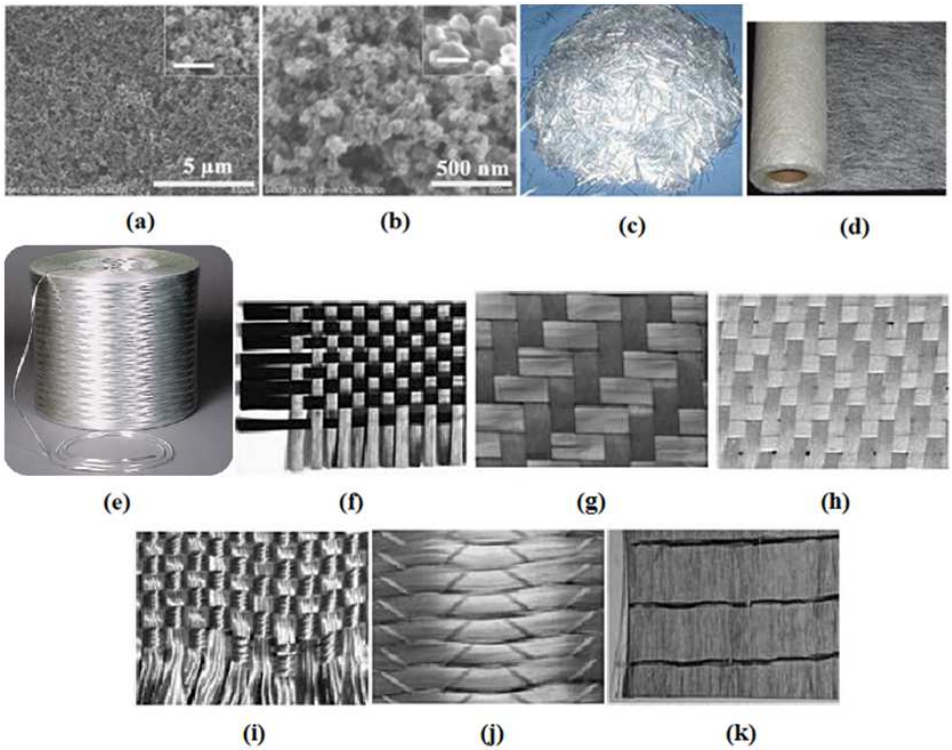


Figure 1.10. (a) continuous fibres (b) discontinuous fibres (c) discontinuous nano-fibre, nano-powder with different magnifications [16] (d) discontinuous short, chopped strand (e) continuous chopped strand mat (f) continuous one direction fibre and (g) continuous two direction plain fabric (h) continuous bi-directional twill fabric (i) continuous bi-directional satin fabric (j) continuous bi-directional basket fabric and (k) continuous bi-directional stitched fabric [4]

### 1.3.1 Woven Fabrics

Woven fabric is the most used type of two-directional reinforcement due to its excellent stability, draping and stability of the fabric compared to other weave styles [17]. The weaving process of woven fabric is performed by interlacing the yarns in the first principal material direction at 0° (warps) and the yarns in the second principal material direction at 90° (fillings or wefts) (see Figure 1.11). The interlacing of yarns provides the natural coherence of the fabric. The formability of the fabric i.e. the ability of the fabric to conform to a complex surface, is in large part determined by its weave style. A description of three types of woven fabrics is presented in the following sections.

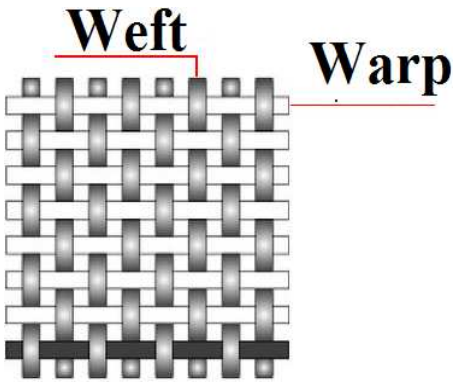


Figure 1.11. Sketch of the interlacing of warps and wefts [17]

**a) Plain Weave**

As shown in the Figure 1.12 the interlacements of the warps and wefts are in criss-cross pattern. They cross each other under and over alternately. The formability of this fabric is relatively low and its high degree of tow crimp is the main reason for low mechanical properties compared to other woven fabrics. However, it has a coherent structure and high porosity [18, 19].

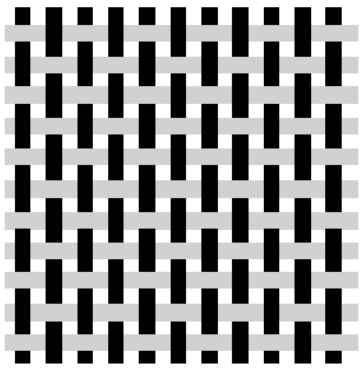

Figure 1.12. The graphical structure of plain weave fabric [18]

### b) Twill Weave

A twill weave is as shown in Figure 1.13. The interlacement of twill weave is produced by passing the warps under and over two or more wefts alternately i.e. as shown in Figure 1.13. The warp in the first row at the left crosses over two wefts in the first and second columns while the warp in the second row at the left crosses over the fourth and fifth columns. The formability and the mechanical properties of twill weave fabrics are higher than those of plain weave fabrics due to the lower degree of interlacing [18-20].

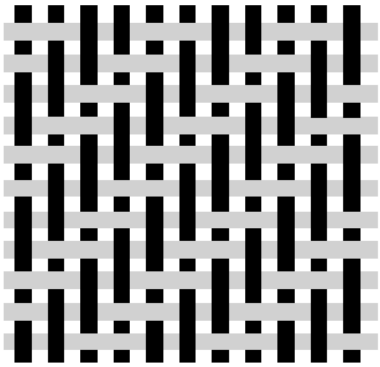

Figure 1.13. The graphical structure of twill weaves fabric [18]

### c) Satin Weave

A warp passes over a number of wefts and then under one weft (Figure 1.14 shows five harness whith four warps over and one warp under). The harnesses are four, five and eight, which means the warp is over four wefts and under one weft in case of five harnesses as shown in Figure 1.14. This weave style has good formability and final material properties when converted into a composite material, which can be attributed to the very low tow crimp resulting from the weaving pattern. However, the style's low stability and asymmetry needs to be considered. The asymmetry causes one face of the fabric to have fibre running predominantly in the warp direction while the other face has fibres running predominantly in the weft direction. Care must be taken in assembling multiple layers of these fabrics to ensure that stresses are not built into the component through this asymmetric effect [18-20].

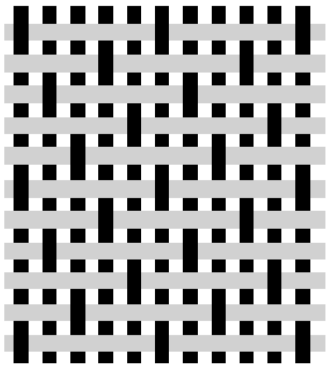

Figure 1.14. The graphical structure of satin weave fabric [18]

### 1.3.2 Advanced composites

Advanced composites are typically understood to include continuous fibre reinforcement with a high degree of fibre alignment embedded within a matrix material. In terms of structure, unidirectional reinforcements are considered the simplest while bi-directional reinforcements are considered advanced, including highly aligned fibres in one direction for the unidirectional reinforcements and two directions for the bidirectional. They can include both low and high length-to-diameter aspect ratio fibres. This thesis focuses on two main themes in relation to advanced composites. One is on understanding the variability of the fibre direction in biaxial advanced composites and the other is on understanding the mechanical couplings that occur in woven engineering fabrics during forming. It should be noted that while the work on variability can be generally applied to all 2-D biaxial composites, due to time constraints attention has been restricted to just woven fabrics architectures in this thesis.

### 1.3.3 Combining reinforcement and matrix phases for advanced composites

Prepreg is a result of combining reinforcements (yarns, fabric or strand mat) and matrix (thermoset or thermoplastic). This process is named an impregnation or prepreg with the reinforcements impregnated with the given matrix under high temperature and appropriate pressure. The most useful property of the thermoset prepreg is its potential to be stored for use later from weeks to months when stored under low temperature (its shelf life below -18°C is from 6-12 months). On the other hand, processing of the thermoplastic prepregs (commingled fabric) is quite different from processing of thermoset prepregs. Processing

of thermoplastic prepregs is based on heating the prepregs beyond the melting temperature of the thermoplastic polymer. The second process step is consolidating which takes place by cooling down with appropriate pressure. The shelf lives of the thermoplastic prepregs are unlimited when stored in an appropriate environment (low humidity at room temperature) [21].

## 1.4 Forming processes for 2-D textile composites

In general, forming of composite material depends on the type of composite. Different forming techniques are used for thermoset and thermoplastic material composites [22, 23]. Advanced composits can be formed as dry fabric performs and then impregnated by a resin infusion process or they can be obtained as prepregs and then formed.

### 1.4.1 Forming processes for thermoset polymer composites

Automating the forming of textile composites results in faster processing, increased productivity and part quality and a reduction in the labour cost. Forming processes of thermoset polymer composites can be characterised based on the process speed. These consist of low speed open mould processes such as hand-layup and spray-up and faster closed mould processes such as vacuum infusion of dry fabric, diaphragm forming, compression moulding of prepregs, and stamp-forming or thermoforming. Hand lay-up and spray-up have similar cycle stages, which include draping the reinforcement (mat strand, woven fabric, unidirectional cross plies or non-crimp fabric) on the open mould, applying resin usually by brush or spray, entrapped air is removed manually by squeezing the perform using squeegees or rollers, and finally the resin is cured. This depends on the resin curing time which can be accelerated by using higher temperatures. The vacuum infusion process cycle involves seven main successive stages including preparation and cleaning of the lower plate, loading the fabrics in place (reinforcements, peel ply and breather cloth respectively), placing spiral tubing in the appropriate place and sealing the resin infusion bag, forming the part by removing the air using a vacuum pump, infusing the resin, and finally, curing and then de-moulding the part (see Figure 1.15b) [23], [24]. The diaphragm forming process of thermoset composite is a higher class of vacuum infusion process, the only differences being that the reinforcements are placed between two diaphragm films and the air between the two films is removed before forming and finally curing in an autoclave oven.

In this thesis a closed mould process was used due to several advantages over open mould processes such as more comfortable and cleaner environment, higher production rate, higher part quality, less voids, better mechanical properties and consistency.

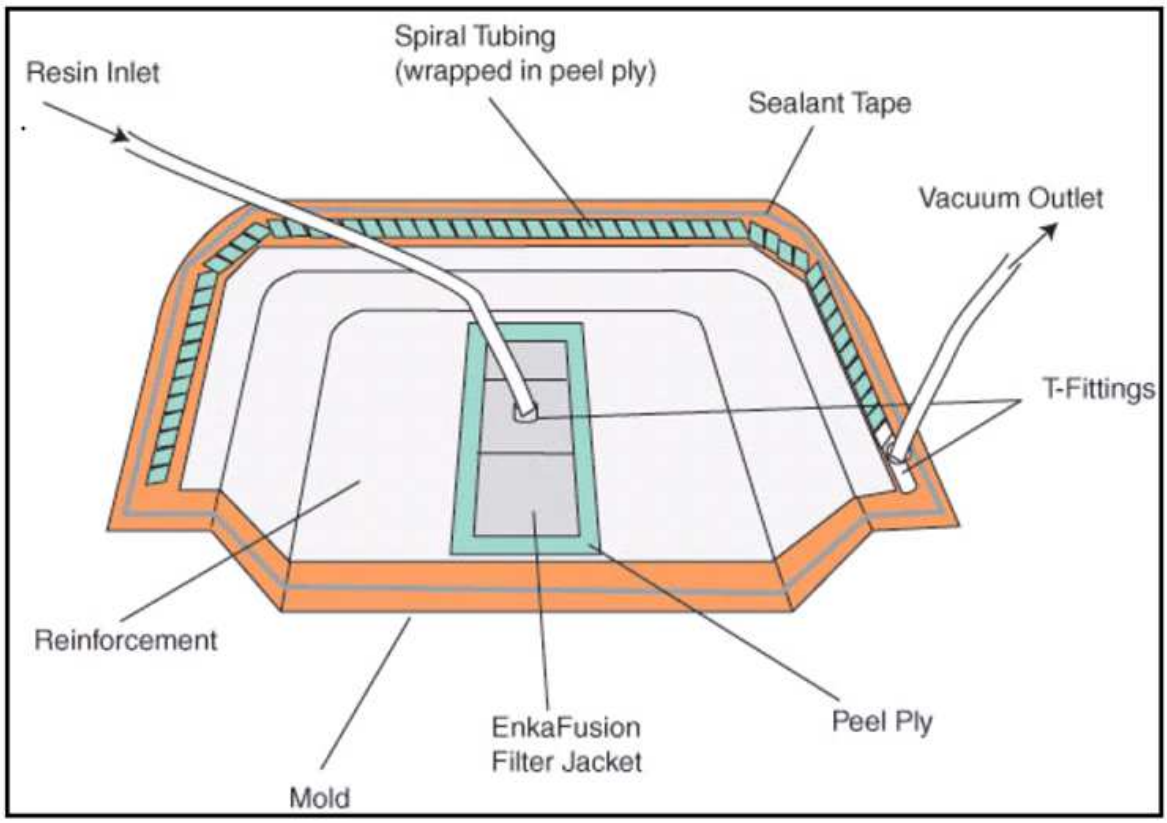


Figure 1.15. Sketch of resin infusion process set-up [25]

The compression moulding process usually consists of a rubber die and a matched punch or vice versa. A blank holder is also used for applying in-plane tension stresses to reduce or even eliminate wrinkling. The compression moulding process cycle is reduced to only two stages: forming the prepreg and the curing stage (see Figure 1.16).

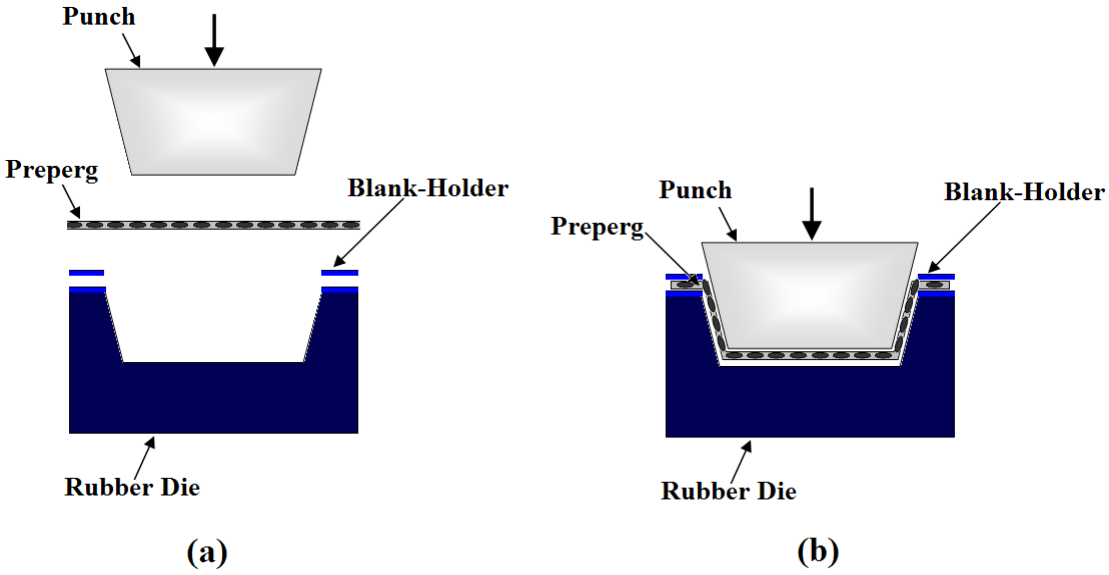


Figure 1.16. Compression moulding forming process [26]

The advantage of compression moulding over the vacuum infusion process is that the process of resin infusion is eliminated since the prepreg material has the resin already infused in the fabric, thanks to the prepreg process [26, 27]. However, the disadvantages of the compression moulding process include the high cost of the pre-impregnated fabric. The consolidation level of the horizontal surfaces in the formed part is also much higher than in the vertical and sloped surfaces as a result of the applied non-hydrostatic pressure.

### 1.4.2 Forming Processes of thermoplastic polymer composite

Since cost reduction is a major aim in industry today, materials such as thermoplastic film stacks, commingled yarns, commingled fabrics and powder-impregnated fibre bundles, which are incompletely impregnated, offer a way to more proficient manufacturing of thermoplastic composites. These materials are midway materials between engineering fabrics and composite parts. Incorporating the thermoplastic matrix into the yarns is an important step in processing and offers fabrication cost reduction in textile composite technology. The most common technique of producing yarns with thermoplastic matrix is commingling. Commingled yarns provide an excellent circulation of matrix and reinforcement before fabrication. The unconsolidated commingled fabric is formed by twining filaments of reinforcements and matrix to produce tows as a combination of the two materials, which is then woven into a commingled fabric. The most common technique was developed by St-Gobain Vetrotex [28] for their product called Twintex-

commingled glass/PP or PET. This technique is based on extruding filaments of polymers within filaments of glass. On the other hand, consolidated commingled yarns and sheets are available as sheets and tapes and are processed by fully consolidating a UD impregnated yarn or fabrics in polymer, by heating to the melting temperature, applying a pressure and then cooling [29]. In terms of processing speed, stamp forming of pre-consolidated or dry commingled fabric is considered as a fast process and is capable of a high production rate with small cycle time. A lower speed process is the vacuum bagging forming technique.

**a) Stamp forming techniques**

Textile thermoplastic composite can be formed using a stamp forming technique using a metal tool set (die, punch, and blank-holder). The forming stages of stamp forming of midway materials, e.g. dry commingled fabric or pre-consolidated commingled plate are as follows. The blank is heated to a temperature slightly higher than the melting temperature of the polymer matrix and then transferred to the stamping unit. Finally, the pre-heated material is formed and pressure is applied to guarantee good stacking and consolidation before cooling the temperature of the blank and the tools [29, 30]. In order to obtain a product free of wrinkling (due to out-of-plane buckling stresses) and rupturing (due to redundancy in plane tension stresses), a blank-holder actuator is usually used to introduce frictional traction force between the blank-holder plates and the blank.

The degree of consolidation depends on the geometry of the part i.e. depends on the surfaces angle and thickness e.g. high degree of consolidation likely to be obtained when the pressure of a punch is normal to the given surfaces whereas the degree of consolidation is expected to reduce gradually when the angle between the load and the given surface is decreased from 90° toward 0°. In order to overcome this problem a hydrostatic pressure on all surfaces, regardless to their position, is needed. A silicon rubber or polyurethane mould is often used in place of metal tooling (see Figure 1.17). However, this increases the cycle time as a result of the lower cooling rate due to the lower thermal conductivity. The short life span of the silicon rubber tool is another disadvantage of this technique.

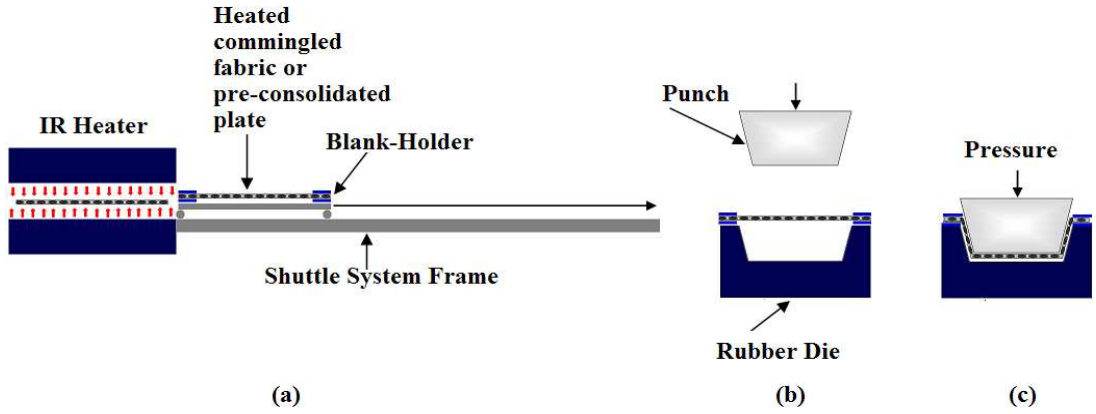


Figure 1.17. Schematic of the stamp forming process (a) heating and transferring the intermediate material (b) placing in the mould set (c) forming and cooling

### b) Vacuum Bagging Forming Process

In terms of forming speed, the cycle time of vacuum bagging forming is longer than that of the stamp forming process. Either pre-consolidated commingled plate or dry commingled fabric can be used in the vacuum bagging process. The basic vacuum bagging processing steps are as follows: cleaning the single mould surface, applying a high temperature resistance liquid or a film release agent on the surface, placing the material on the top of the area where the release agent is applied, placing a high temperature resistance release film (peel ply) on the top of the material (for easy release of the material from the mould after cooling down), placing a breather cloth on the top of the peel ply (for ensuring all air is vacuumed), and then covering and sealing the set with vacuum bagging film and sealing tape (see Figure 1.18). The heating stage can be done either by putting all the vacuum set in an oven or heating it in the single metal mould, with the temperature increased up to the melting temperature of the matrix. The final two stages are consolidation while maintaining vacuum, which depends on the size and thickness of the formed part, and then de-moulding [26].

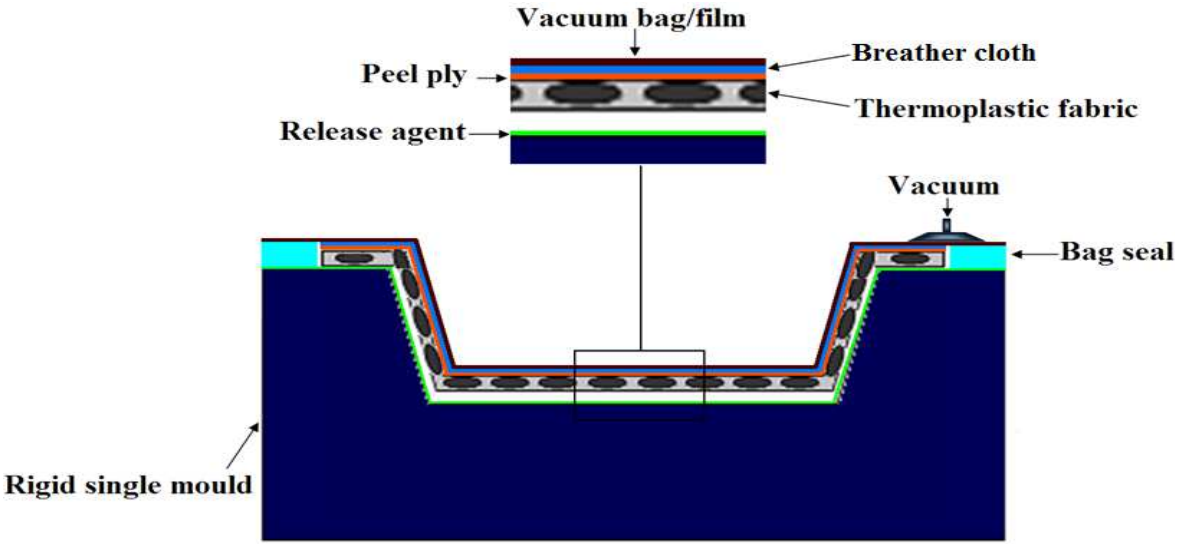


Figure 1.18. Vacuum bagging forming process setup

## 1.5 Deformation Mechanisms in Forming Textile Composite

During forming, a number of deformation mechanisms take place. They are in-plane shear, in-plane tension, blank/yarn bending and ply compaction. However, two main sources of stress generally occur within the forming sheet; one is due to strain along the fibre directions and the other due to in-plane shear. In the literature, extensive work has been carried out on the investigation of the in-plane shear and tensile stresses that occur during forming. However, in practice all the deformation mechanisms such as in-plane shear and in-plane tension occur concurrently. The connection between these two mechanisms has not been extensively investigated and this topic is a key factor in terms of developing appropriate constitutive models.

## 1.6 Textile Characterisation Tests

Modelling the draping or forming simulation of the engineering fabrics and heated textile composite required characterising the shear and tension mechanisms of the material. The material properties are required for modelling the forming simulation; therefore, a standard characterisation testing method is required. Existed testing methods such as the PF and the UBE tests have some drawbacks. In order to eliminate these, an extensive study on their causes and their possible remedies, or an alternative novel method, is required.

## 1.7 Inherent Variability of Woven Textile Composites

Product variability and discard rates of manufactured goods are closely related to the inherent variability of the materials from which they are made. Tow and fibres within actual advanced composites inevitably contain at least some degree of stochastic deviation from their ideal architecture. The development of accurate process design tools that can account for this type of variability is aimed at reducing the cost of the pre-manufacture assessment and the optimization of parts by minimising design iterations and prototyping. Variability in the architecture of advanced composites can be introduced at numerous stages in the manufacturing process such as during weaving or stitching of the fabrics, pre-impregnation of prepregs, pre-consolidation of co-mingled thermoplastic textile composites, or handling and cutting of fabrics off the fabric roll. Understanding the resulting inherent variability in the architecture is important as it can influence subsequent stages in the manufacturing process.

## 1.8 The objectives of this work

1. Measurement of the shear-tension coupling of engineering fabrics using a novel testing technique, the BBE test.

2. Investigating the wrinkling behaviour under arbitrary in-plane tension conditions using the biaxial technique.

3. Characterisation of the variability of inter-tow angles in a range of engineering fabrics and use of the measured global statistics to reproduce representative variability with realistic spatial correlations in meshes suitable for use in finite element forming simulations.

4. Extension of the Non-Orthogonal Constitutive Model to include a shear tension-coupling.

5. Investigation of the effect of variability and shear-tension coupling on the stamp forming process of a novel 3D complex geometry.

# 2. Textile Experimental Characterisation

## 2.1 Introduction

Modelling the forming process for engineering fabrics and textile composites using a mechanical approach, such as the finite element method, requires characterisation of the material's behaviour under large shear deformation. Three shear characterisation methods (picture frame PF), uniaxial and biaxial bias extension methods UBE and BBE have been used for characterising and investigating the shear behaviour and wrinkling phenomena of dry and commingled engineering fabrics. For these materials, coupling between in-plane tension and both shear compliance and the onset of wrinkling is to be expected. In this chapter a novel testing technique, the BBE test, is evaluated as a means to investigate this shear-tension coupling and fabric wrinkling. Novel methods of determining the wrinkling behaviour are demonstrated. The main difficulty with the technique lies in extracting the material contribution to the recorded signal from a universal test machine (Zwick Z2) and in normalising the subsequent data. To do this, an experimental method is demonstrated using a plain weave glass fabric, self-reinforced polypropylene and commingled glass/polypropylene fabric. BBE test results are compared against PF and UBE results.

## 2.2 Review of Previous Work

During the manufacture of composite parts, press forming of engineering fabrics can be used to create complex geometries, suitable for subsequent liquid composite moulding and cure [31]. During the press-forming process, in-plane tension is generally used to mitigate process-induced defects such as wrinkling and, to some degree, to control the final fibre orientation distribution across the component after forming [32-34]. Tension is controlled through boundary conditions applied to the perimeter of the material using a blank-holder [33-37]. The shear compliance of dry woven engineering fabrics has been shown to be related to the in-plane tensions acting along the two sets of tows within the fabric. This can be intuitively understood as due to the increased normal forces acting between overlapping tows (weave crossovers) which increase internal sliding friction during deformation of the fabric [32, 38]. Thus, for these materials, blank-holder conditions applied during the

forming process are expected to change the material's shear compliance and the fabric's forming response, such as its propensity to wrinkle [32, 39, 40].

### 2.2.1 Shear In-Plane Tension Coupling

A few attempts to characterise shear-tension coupling experimentally have been reported; early investigations involved pre-tensioning the fabric prior to placement in a PF rig using biaxial pre-tensioning devices [41, 42]. These studies indicated a significant increase in shear stiffness with increasing pre-tension. Typical values of the scale factor produced from results published in the literature are provided in Table 2.1. Note that the scale factor provides only a rough estimate of the coupling measured using the PF test because large scatter in the data makes it difficult to determine definitive values. Further developments have since involved fitting a PF rig with load-cells along the side bars allowing the measurement and control of yarn tension during the test [43-45]. The latter technique attempts to address the issue of changing tension during the PF test due to two contributions: fabric misalignment and changing crimp. Improved accuracy might be expected in the results of [45] as the tensile stress in previous investigations [41, 42, 44, 45] was applied via a pre-tensioning technique whereas the instrumented PF rig used in these tests allowed tensioning during the experiments.

A previous attempt to use a biaxial test setup to measure shear-tension coupling has been reported [46]. Here prescribed displacement boundary conditions in two orthogonal directions were used during the test. Shear tension-coupling was reported, though large scatter in the data and variable transverse loading during the tests make comparison with other investigations difficult. Galliot and Luchsinger [47], [48] recently proposed a new biaxial experimental and theoretical method of determining the shear compliance of coated fabrics. Shear-tension coupling of woven dry engineering fabrics has not yet been investigated using this technique, though the authors suggest this as possible future work. Thus, it appears to be generally accepted that shear-tension coupling in woven engineering fabrics does exist, though, to date, there has been no definitive quantitative experimental characterisation of this coupling. Despite this, shear-tension coupling has been successfully introduced into FE simulations; Lee and Cao [49], [50] modified a non-orthogonal constitutive model [51, 52], making shear stiffness parameters a function of tensile strains along the two fibre directions. Rather than using experimental data, input parameters were

determined from predictions of meso-scale FE simulations of a plain-weave unit cell. The meso-scale simulations showed that as the tensile strain increased, the shear resistance also increased [53]. The size of the coupling used in the modified non-orthogonal constitutive model is significantly larger than that suggested by previous experimental investigations using PF tests (see Table 2.1).

Table 2.1. The ratio (coupling factor) of the forces measured during PF, numerical simulations and BBE tests at different applied values of the force per unit length along the edge of the fabric.

| Reference and source | Weave-material | Shear angle (°) | Applied pretensions (N/mm) | Applied tensions (N/mm) | Approximate scale factor |
|---|---|---|---|---|---|
| Figure 10 [39] | Plain-glass | 10 | 0 and 2.8 | - | 2.8 |
| Figure 10 [39] | Plain-glass | 20 | 0 and 2.8 | - | 2.1 |
| Figure 5b [54] | 2 x 2 twill-glass PP | 10 | 0 and 3.27 (warp) 5.03 (Weft) | | 2.0 |
| Figure 5b [54] | 2 x 2 twill-glassPP | 20 | 0 and 3.27 (warp) 5.03 (Weft) | | 1.9 |
| Figure 15 [43] | Plain-glass PP | 10 | - | 0 and 4 | 4.8 |
| Figure 15 [43] | Plain-glass/PP | 20 | - | 0 and 4 | 2.8 |
| Figures 16 and 18 [44] | Plain-glass/PP | 10 | - | 0 and 0.18 | 3 |
| Figures 16 and 18 [44] | Plain-glass/PP | 20 | - | 0 and 2.1 | 4.8 |
| Figure 6 [53] | Plain-NOCM | 10 | - | 0.007 and 0.163 | 12 |
| Figure 6 [53] | Plain-NOCM | 20 | - | 0.007 and 0.163 | 20 |
| Figure 2.40 3:1 specimen | Plain glass | 10 | - | 0.071 and 1.43 | 23 |
| Figure 2.40 3:1 specimen | Plain glass | 20 | - | 0.071 and 1.43 | 36 |
| Figure 2.42 3:1 specimen | Commingled | 10 | - | 0.071 and 1.43 | 25 |
| Figure 2.42 3:1 specimen | Commingled | 20 | - | 0.071 and 1.43 | 41 |

In the current investigation, the ability of a BBE test [55-57] to produce a reliable experimental characterization of the shear-tension coupling of woven engineering fabrics is examined and a procedure to extract the material response from the test is proposed. Results are compared with the more familiar PF and UBE tests. On the other hand, correctly predicting wrinkling during the forming of engineering fabrics is a difficult issue. Experimental characterisations of wrinkling of woven dry engineering fabrics using both PF and UBE tests have been performed previously, aiming to correlate wrinkling onset to

the fabric structure using simplified analytical models [39, 40]. However, it is clear that the occurrence of wrinkling is not just a function of the fabric structure but also of the stress field applied to the fabric during forming. Like shear stiffness, the out-of-plane bending stiffness is likely to be a function of the in-plane tensile stress. The current biaxial technique allows investigation of wrinkling behaviour under arbitrary in-plane tension conditions and, while it can't provide a direct characterization of this bending stiffness [58, 59], the modulus could be inferred using an inverse modelling approach.

## 2.3 Material

Three materials, a typical plain weave dry glass fabric, plain weave self-reinforced polypropylene and twill commingled glass/polypropylene were chosen for the investigation. For convenience the four materials used in this investigation will be referred to as the wrGF, srPP, cgPP and pccgPP (woven roving glass fabric, self-reinforced polypropylene, commingled glass/polypropylene and a pre-consolidated 2x2 twill weave, co-mingled glass / polypropylene composite). However, only three materials, wrGF, srPP and cgPP were used in Chapter 2. The material's geometrical properties are illustrated in Table 2.2. The three fabrics are shown in Figure 2.1. The woven fabrics that used in this investigation are plain and twill weave. Although satin weave is more formable than plain and twill weave, it is not used here due to its high degree of asymmetry and low stability.

Table 2.2. The geometrical properties of the wrGF, srPP, cgPP and pccgPP

| Parameters | Material name | | | |
|---|---|---|---|---|
| | wrGF | srPP | cgPP | pccgPP |
| Weft tow width (mm) | 2.18 +/-0.038 | 2.55 +/- 0.1 | 3.91 +/- 0.129 | 5.06 +/-0.45 |
| Warp tow width (mm) | 2.12 +/- 0.052 | 2.52 +/- 0.06 | 3.84 +/- 0.077 | 5.71 +/-0.59 |
| Areal density ($g/m^2$) | 311 +/- 5.5 | 123 +/- 2.7 | 1485 | 760 |
| Fabric thickness (mm) | 0.206 +/- 0.012 | 0.305 +/- 0.015 | 1.05 +/- 0.036 | 0.57+/-0.015 |
| Warp thickness (mm) | 0.101 +/- 0.002 | 0.152 +/- 0.021 | 0.48 +/- 0.196 | - |
| Weft thickness (mm) | 0.105 +/- 0.010 | 0.157 +/- 0.002 | 0.52 +/- 0.008 | - |
| Product code | ECK12, Allscot | Armordon | Twintex® T PP | Twintex® T PP |

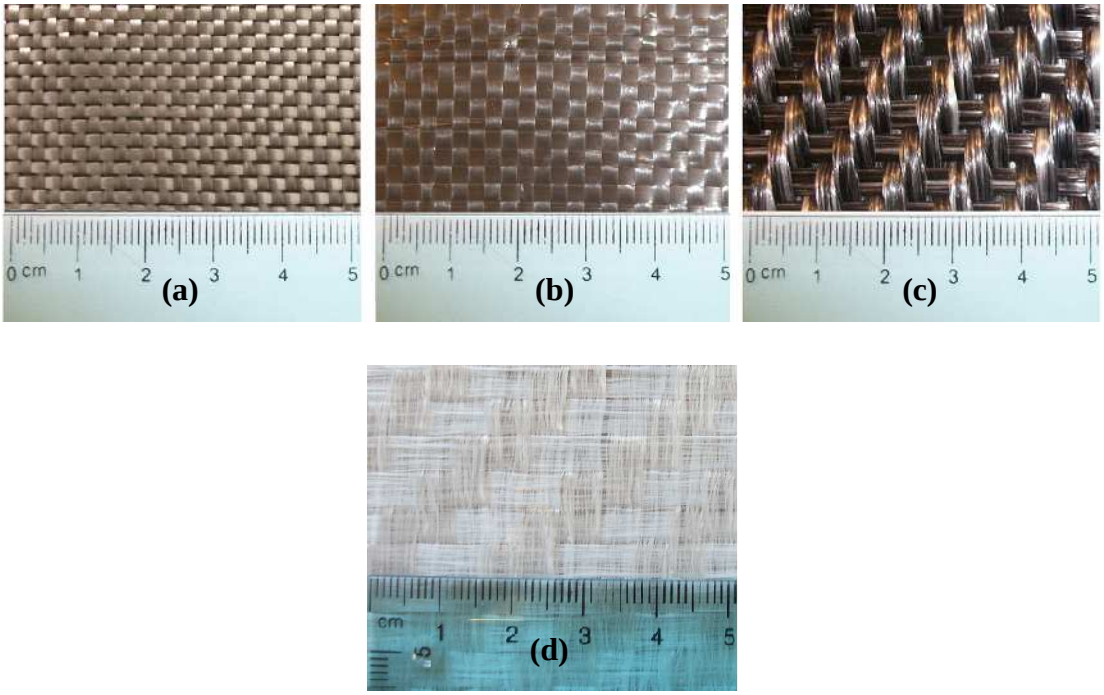


Figure 2.1. (a) wrGF (b) srPP and (c) cgPP and pccgPP

## 2.4 Experimental Setup

A universal test machine (Zwick Z2) with a 250kN load-cell was used to measure the vertical axial force in all tests and all experiments were conducted at a speed of 200 mm/min. Tests were recorded using a digital camera (Canon Powershot A 700) and sample kinematics were measured manually using the image analysis software *ImageJ* [60]. Lines were drawn along individual tows on the samples prior to testing to facilitate image analysis. Tests on the two wrGF and srPP were conducted in a darkened lab to facilitate a backlighting technique, whereas tests on the cgPP were conducted in a well-lit environment. wrGF and srPP samples were backlit using a white screen positioned behind the setup. The screen was illuminated using four bright spotlights positioned to provide a strong and even light intensity across the screen. In doing so, the translucent nature of wrGF and srPP could be exploited, allowing identification of wrinkles in subsequent image analysis of recorded movies; wrinkles appear dark due to the increased thickness of the sample along the line of sight from the camera to the screen. The opaque nature of the cgPP meant this method could not be employed for this material. Three repeats were conducted for each test condition.

### 2.4.1 PF Test Setup

One of the most popular methods of characterizing the shear behaviour of textile composite is the picture frame (PF) test [46, 61]. However, this method has drawbacks [56]. Misalignment of the yarns in the PF rig is a major cause of error. In addition, the tensile stress that is likely to take place at the clamped edged of the fabric, due to the influence of the boundary conditions, is another factor that might contribute to the increase in the shear stiffness [23, 44, 62]. On the other hand, shear angles higher than 40° can be obtained using the PF method, whereas this can not be obtained using UBE or BBE tests, unless with higher transverse force for BBE [42, 55].

Three samples have been tested for each material. The side length of the PF rig used here is 170 mm, while the sample length is 130 mm (see Figure 2.2). The samples are placed and clamped with care to avoid misalignment. Holes are then drilled in the exact position to avoid distorting the specimens. Prior to placing and clamping the sample, cross-lines were drawn at the centre for further image analysis. After fixing the sample on the machine, a special purpose rectangular aluminium bar was used to keep it initially squared. This bar was taken off as soon as the test started. Prior to starting the test, a translucent sheet with a concentrated strong light behind it was hung behind the specimens in a dark environment. Finally, the test was started by pulling the upper corner with a velocity of 200 mm/min until the last given displacement was reached.

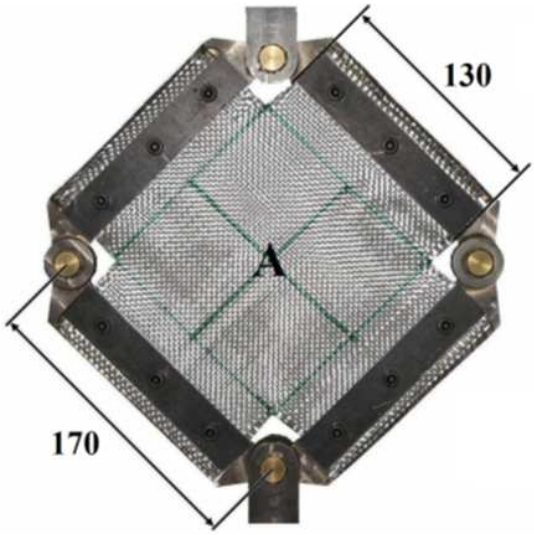


Figure 2.2. Photograph of a PF sample. The crossed lines indicate the direction of the orthogonal tows.

### 2.4.2 UBE Test Setup

The other popular method of characterizing the shear behaviour of textile composites is the UBE test [38, 42, 52]. However, this method also has drawbacks [55]. The UBE test is much easier to perform than the PF test. Three samples were cut for each type of material with size ratio $\lambda = L/W = 2$, where $L$ is the length of the specimen and $W$ is the width. The samples were cut in a way that makes the warps and wefts lie at ± 45° with the clamps (see Figure 2.3). This arrangement helps to produce pure shear until a slippage deformation mechanism takes place. Following this, lines were drawn at the centre of the specimens for further image analysis as shown in Figure 2.4. In order to obtain precise results, care was taken to ensure that the angle between the marked lines at the centre of the sample was initially 90°. A digital video camera has been used to record the tests for further image processing. The measured shear angles are determined from computer screen using *imageJ* software [60]. More detailed descriptions of the PF and UBE tests can be found elsewhere [62-64].

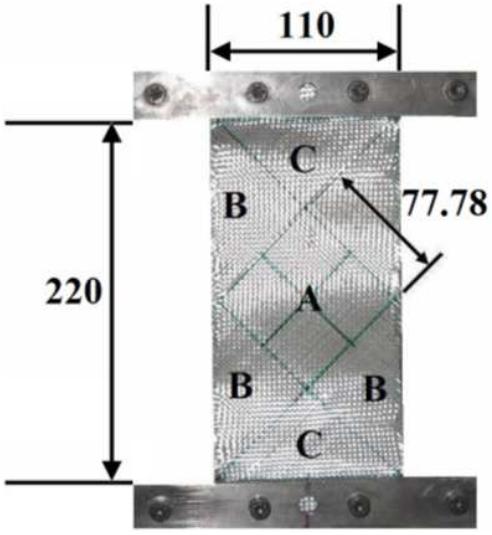


Figure 2.3. Photograph of a UBE sample. Regions A, B and C indicate areas that, under ideal trellis shear kinematics, would have shear angles of h, h/2 and 0, respectively. The crossed lines indicate the direction of the orthogonal tows.

### 2.4.3 BBE Test Setup

The BBE experimental test set-up is shown in Figure 2.4. Despite the difference in lengths of the longitudinal and transverse clamps shown in Figure 2.4, specimens were attached along the same fraction of the perimeter length on either side of the specimen, as indicated by the yellow lines drawn along the clamp lengths in Figure 2.4. The fabric was cut along

the remainder of the specimen perimeter and was therefore unconstrained along these edges.

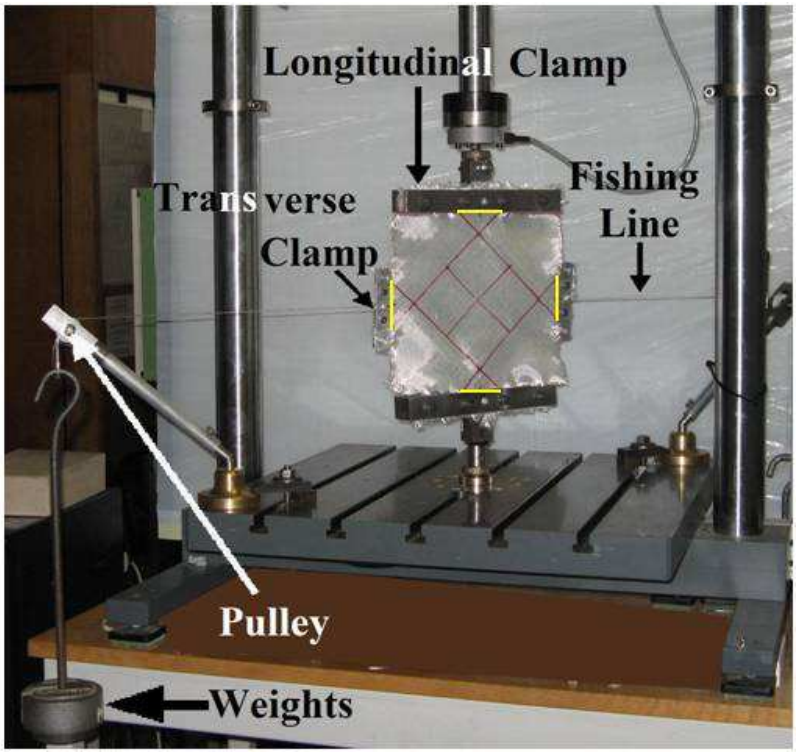


Figure 2.4. Experimental setup used for the BBE test. In addition to the two usual longitudinal clamps connecting the top and bottom of the specimen with the testing machine, there are also two transverse clamps connecting the sides of the specimen to hanging weights. The yellow lines drawn in the photograph indicate the lengths along which the specimen perimeter is clamped. The rest of the perimeter is unconstrained.

The effective specimen clamping areas are shown as dark grey areas in Figure 2.5. A balanced transverse load was attached to either side of the specimen using a set-up involving nylon fishing line, lightweight aluminium transverse clamping plates (45 g each), and bearing-mounted pulley-wheels. Pulley-wheel supports were securely clamped to the test bed using copper mounts and steel clamps; supports were mounted on shafts orientated at 45° to reduce the bending moment at the fixture and also to increase the distance between pulleys and specimen (see Figure 2.4). Increasing the latter reduces the change in angle of the fishing line during the test, which has an influence on measured force results. Transverse loads of 5, 37, 50, 75 and 100 N were applied to the wrGF specimens, 5, 27, 50, 75 and 100 N were applied to the cgPP specimens during testing and 5, 50 and 100 N were applied to the srPP fabric by hanging appropriate weights on the nylon fishing line. Two different specimen sizes and geometries were selected, as shown in Figure 2.5. The clamping length used along the sides of the specimens is crucial in determining both the in-plane fibre tensions and the kinematics that occur throughout the

sample during testing and will therefore influence the force results obtained during the tests. Figure 2.5a shows a specimen with a side length three times the clamping length; Figure 2.5b shows a specimen with side length four times the clamping length. These values are chosen arbitrarily in order to examine the influence of sample geometry on test results. In this investigation the emphasis is on determining whether the BBE test technique can, first of all, be used to measure a shear–tension coupling. For convenience the two specimen geometries used in this investigation will be referred to as the 3:1 and 4:1 specimens (see Figure 2.5a and 2.5b). In Figures 2.2, 2.3 and 2.5, Regions A, B and C indicate areas that, under ideal trellis shear kinematics, would have shear angles of θ, θ/2 and 0, respectively. Such kinematics follow naturally if the constraint of fibre inextensibility is coupled with the test boundary conditions and the fabric is assumed to undergo pin-jointed net kinematics, i.e. no intra-ply slip.

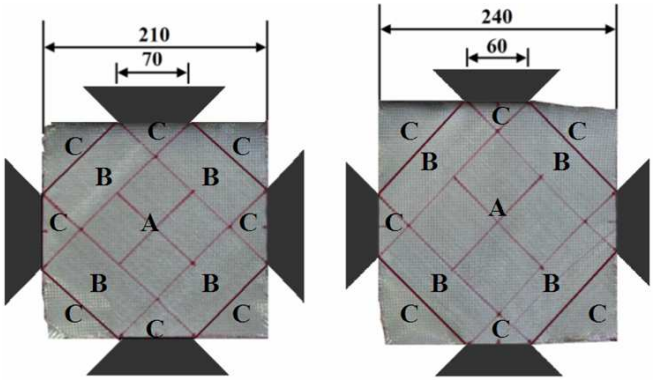


Figure 2.5. Two samples sizes are used in the BBE tests: (a) 210 x 210 mm with 70 mm clamping distance; here the side length is three times the clamping length (3:1) (b) 240 x 240 mm with 60 mm clamping distance; here the side length is four times the clamping length (4:1). The effective clamping areas are shown in grey.

### a) Evaluation of Sample Kinematics

In order to correctly interpret force results and subsequently develop accurate constitutive models, it is essential to record sample kinematics occurring in each of the three tests. For consistency the kinematics of all three tests are measured and compared with each other and also against the ideal predictions of pin-jointed net kinematics. Data points were collected every two seconds for image analysis. Several measures of the sample kinematics have been monitored. The shear angle, $\theta_m$, in Region A is often used as an objective measure of the shear strain in developing constitutive models for engineering fabrics and was recorded in all three tests. The cross at the centre of Region A was used to monitor the shear angle, though for UBE and BBE tests, once wrinkling made the measurement

problematic, the angle was taken from the four corners of Region A. Intra-ply slip is known to occur during UBE tests, resulting in increased compliance of the sample [63] (see Figure 2.6).

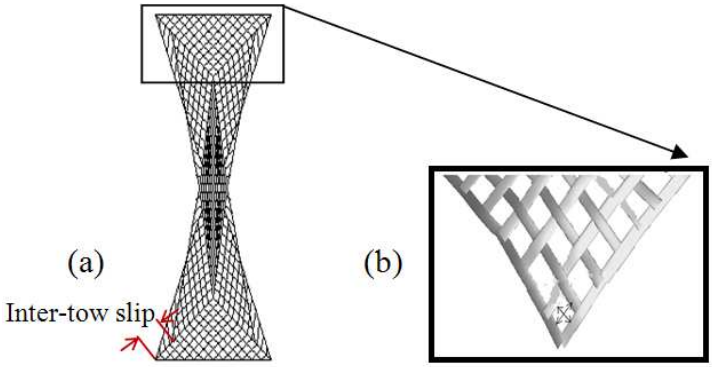


Figure 2.6. Two intra-ply slip mechanisms observed in UBE tests: (a) Inter-tow slip results in an increase in the side length of Region A [65] (b) Crossover slip results in a spreading and shearing of tows and an increase in the length C.

In order to detect intra-ply slip, additional quantities were monitored during the bias extension tests; referring to Figure 2.7 and the definition of symbols section, the lengths $C_{mu}$, $C_{mb}$, $L'_{mu}$ and $L'_{mb}$ are determined from test videos using the software *ImageJ* [60]. $C_{mu}$ and $C_{mb}$ indicate the measured value of the length of vertical diagonal across region C during UBE and BBE. $L'_{mu}$ and $L'_{mb}$ are measured straight side length of region A of UBE and BBE samples while $L''_{mu}$ and $L''_{mb}$ are measured curved side length of region A of UBE and BBE samples.

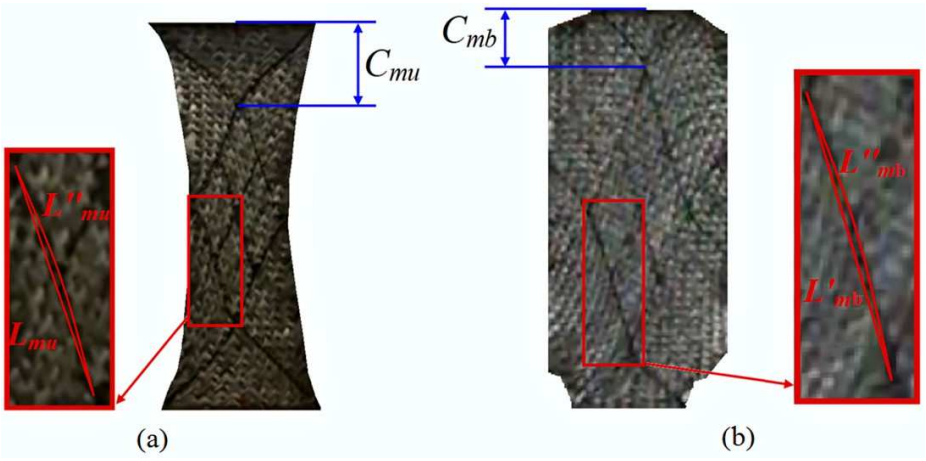


Figure 2.7. Example images of (a) UBE, and (b) BBE test specimens, at particular instants during testing. The lengths $C_{mu}$, $C_{mb}$, $L'_{mu}$, $L'_{mb}$ are measured every two seconds using image analysis of test video recordings, in order to quantify sample kinematics during tests.

Detection of wrinkling purely through analysis of 2-D images is of interest in that it reduces the need for more elaborate techniques such as the use of backlighting (used in this investigation) or digital image correlation (requires expensive equipment and application of surface patterns on the samples for tracking). To this end the quantities $L''_{mu}$ and $L''_{mb}$ are also measured and the ratios between the curved and straight lines along the perimeter of Region A in both the UBE and BBE tests, $L''_{mu}/L'_{mu}$ and $L''_{mb}/L'_{mb}$ are used to monitor the occurrence of wrinkles. The explanation for this ratio is illustrated in Figure 2.8, showing that tows along the edge of Region A tend to remain planar while those running through the wrinkle, which usually occurs vertically and entirely within the centre of Region A, travel out-of-plane.

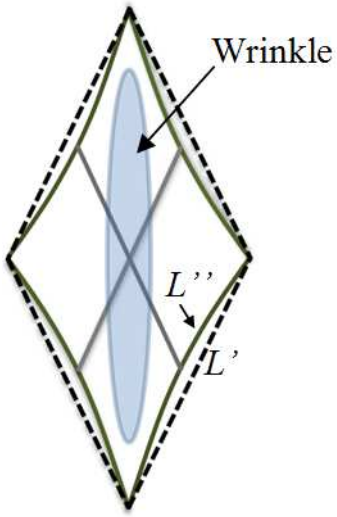


Figure 2.8. Illustration showing the exaggerated effect of a wrinkle on the shape of the perimeter of Region A. The grey ellipse indicates the area undergoing out-of plane wrinkling. The effect on the perimeter is to make it curve inwards.

The effect on the 2-D projection of the tows in the image plane is a shortening of tows running through the wrinkle and a consequent inward curving of the perimeter tows towards the centre of Region A (see Figure 2.7 for real observations). Thus, the ratio $L''/L'$ begins from unity and increases as wrinkling progresses. A final interesting quantity to measure during the tests is the ratio, $L''_m/L'_t$, the current measured curved length of the perimeter tow divided by its own initial (theoretical) value. This ratio is influenced primarily by (a) the change in length of the tows due to changes in crimp and (b) by inter-

tow slip. The former tends to decrease the ratio while the latter increases it (see Figure 2.6) [63, 65].

For the PF test, the theoretical shear angle, $\theta_{tp}$, is calculated using Eq (2.1)

$$\theta_{tp} = \frac{\pi}{2} - 2\arccos\left[\frac{1}{\sqrt{2}} + \frac{d_x}{2L_{tp}}\right] \tag{2.1}$$

where $d_x$ is the displacement of the crosshead and $L_{pt}$ is the side length of the PF rig. For UBE or BBE tests, Eq 2.1 is modified; instead of using the displacement of the crosshead to calculate the theoretical shear angle, modified displacements were used instead as follows,

$$\theta_{tu} = \frac{\pi}{2} - 2\arccos\left[\frac{1}{\sqrt{2}} + \frac{\left(d_x - 2\overline{\Delta C}_{mu}\right)}{2L_{mu}}\right] \tag{2.2}$$

and

$$\theta_{tb} = \frac{\pi}{2} - 2\arccos\left[\frac{1}{\sqrt{2}} + \frac{\left(d_x - 2\overline{\Delta C}_{mb}\right)}{2L_{mb}}\right] \tag{2.3}$$

where $\overline{\Delta C}_{mu}$ and $\overline{\Delta C}_{mb}$ represent the average increase in $C_{mu}$ and $C_{mb}$ measured from the top and bottom regions of the sample and are functions of $\theta_{mu}$ and $\theta_{mb}$. The purpose of introducing $\overline{\Delta C}_{mu}$ and $\overline{\Delta C}_{mb}$ in Eq (2.2) and (2.3) is to eliminate the stretching of Region C when predicting the ideal shear kinematics in Region A (see Figure 2.7).

**b) PF test kinematics**

Shear angle kinematics in PF testing are shown in Figure 2.9a, 2.9b and 2.9c where the measured shear angle, $\theta_{mp}$, is plotted against the theoretical shear angle, $\theta_{tp}$. Figures 2.9a, 2.9c and 2.9e show that the sample kinematics remains close to the ideal prediction up to 50º, 30º and 50º. The shear angle was measured until the onset of wrinkling because the distortion of the image due to the wrinkling prevented accurate angle characterisation. Figures 2.9b and 2.9d show the initiation of wrinkles at around 60º using the transmitted

backlighting technique. That is not clear in Figure 2.9f since no backlit was applied due to the dark colour of the twill fabric material.

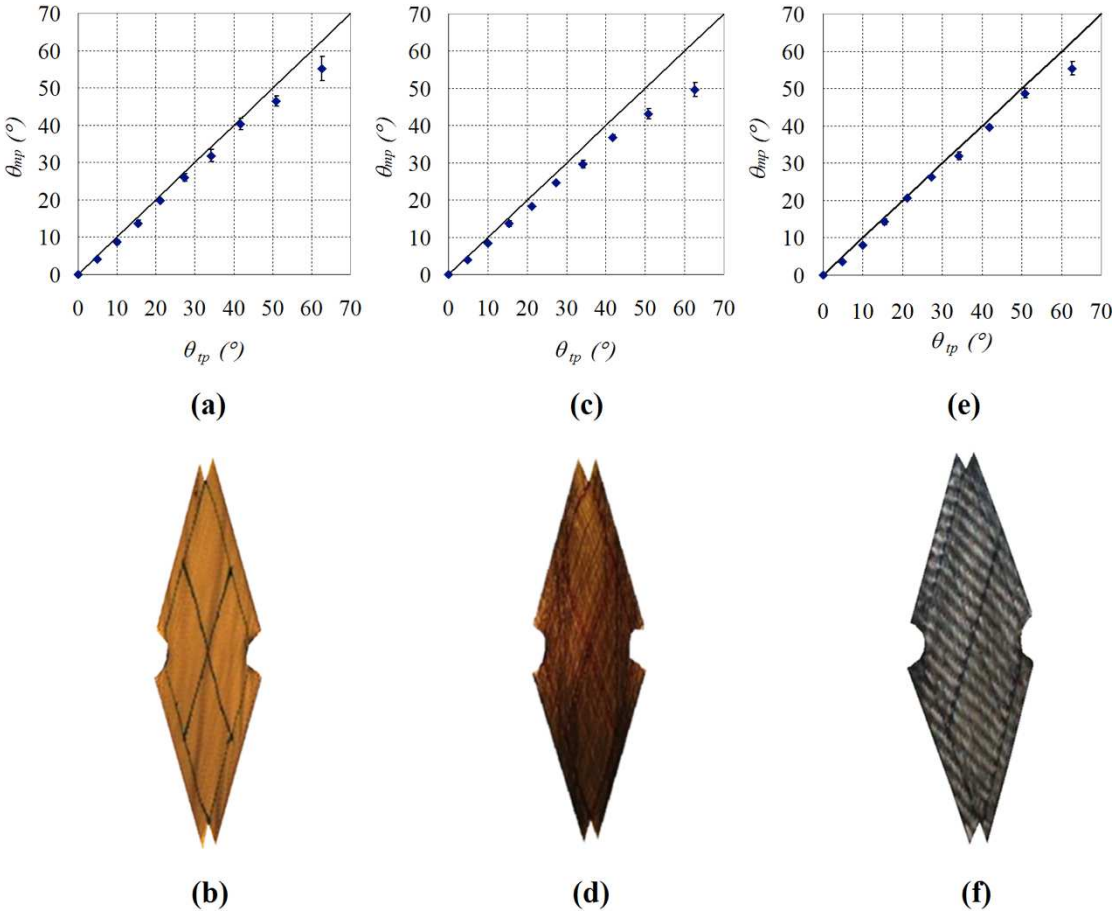


Figure 2.9. (a) $\theta_{mp}$ *vs* $\theta_{tp}$ for PF tests on glass plain-weave fabric (b) image of sheared specimen showing marked lines used to determine the shear angle (c) $\theta_{mp}$ *vs* $\theta_{tp}$ for PF tests on self-reinforced polypropylene plain weave fabric (d) image of sheared specimen showing marked lines used to determine the shear angle glass plain-weave fabric (e) $\theta_{mp}$ *vs* $\theta_{tp}$ for PF tests on co-mingled twill weave fabric (f) image of sheared specimen showing marked lines used to determine the shear angle co-mingled twill -weave fabric

If $\theta_{mp} = \theta_{tp}$ the data should fall on the straight line, thus Figure 2.9c shows that for the srPP plain weave fabric the sample kinematics quickly diverge from ideal kinematics while for the lighter plain weave glass fabric and co-mingled twill weave fabric, the kinematics of the two latter remain close to the ideal prediction up to $50^{o}$ (see Figure 2.9a and 2.9e) The non-ideal shear kinematics of the self-reinforced polypropylene plain weave fabric is thought to be due to the nature of the material. The specific contact areas of the crossed tapes are much greater in self-reinforced polypropylene plain weave fabric than in glass plain-weave fabric and co-mingled twill weave fabric. Moreover, the tapes of self-reinforced polypropylene plain weave fabric are just one flat tape, unlike the glass plain-weave fabric and co-mingled twill weave fabric tows where every tow consists of a huge

number of filaments that make the inter-tow shear and rotation between crossed tows much easier due to the micro-appendages vermicelli associated with each filament. Image analysis of shear angle data was stopped after the onset of wrinkling because the distortion of the image prevented accurate angle characterisation. The corresponding experimental shear force versus shear angle curves, $F_s(\theta)$ are initially approximated from the axial load, $F_m(\theta)$, using Eq (2.4).

$$F_s = \frac{F_m(\theta)}{2\cos(\pi/4 - \theta/2)} \tag{2.4}$$

Coefficients of 9th degree polynomial fits to the experimental $F_s$-$\theta$ curves for the wrGF and cgPP results are given in Table 2.3 for further use in FE numerical simulation in Chapter 4. The 9th degree polynomial fits were used to ensure optimum accuracy when fitting the experimental for input into the model.

Table 2.3. The experimental shear compliances $F_s$-$\theta$ 9th degree polynomial fits' coefficients of the PF wrGF and cgPP

| Coefficients | *Fs-θ* | |
|---|---|---|
| | wrGF | cgPP |
| 1 | -5.34E-13 | 1.19E-12 |
| 2 | 1.27E-10 | 1.84E-10 |
| 3 | -1.22E-08 | -5.29E-08 |
| 4 | 6.07E-07 | 4.30E-06 |
| 5 | -1.62E-05 | -1.71E-04 |
| 6 | 2.09E-04 | 3.65E-03 |
| 7 | -4.93E-04 | -4.08E-02 |
| 8 | -1.48E-02 | 2.65E-01 |
| 9 | 1.48E-01 | -3.06E-01 |
| 10 | -5.34E-01 | 1.31E+00 |

**c) UBE test kinematics**

Shear angles for the UBE tests are shown in Figures 2.10a, 2.10c and 2.10e. Up to 60º, 20º and 60º of shear (for the three materials), the kinematics in Region A are close to the ideal

case, even after the onset of wrinkles, i.e. the inter-tow slip mechanism depicted in Figure 2.6a is prevented from occurring by firm clamping of the specimen. Note that those ideal kinematics are determined using Eq. (2.2). This equation removes the extra sample compliance due to stretching of Region C. If Eq. (2.1) were used instead, the kinematics would appear to become non-ideal at much earlier shear angles. Beyond 60º, 20º and 60º the shear angles could no longer be measured experimentally due to intense wrinkling. As dark bands in the sample image indicate (see, for example, Figures 2.10b and 2.10d), the onset of sample wrinkling is at around $\theta_{mu}$ = 40º and 10º, much lower than in the PF tests.

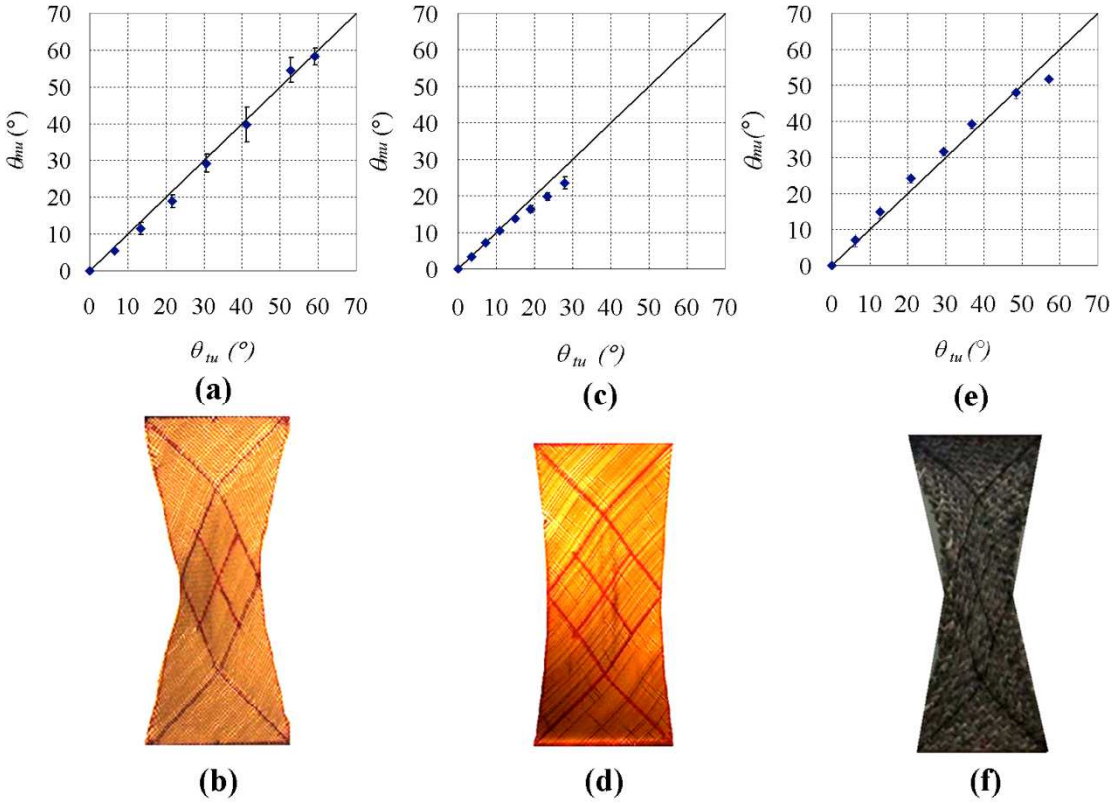


Figure 2.10. (a) $\theta_{mp}$ *vs* $\theta_{tp}$ for UBE tests on glass plain-weave fabric (b) image of sheared specimen showing marked lines used to determine the shear angle (c) $\theta_{mp}$ *vs* $\theta_{tp}$ for UBE tests on self-reinforced polypropylene plain weave fabric (d) image of sheared specimen showing marked lines used to determine the shear angle glass plain-weave fabric (e) $\theta_{mp}$ *vs* $\theta_{tp}$ for UBE tests on co-mingled twill weave fabric (f) image of sheared specimen showing marked lines used to determine the shear angle co-mingled twill -weave fabric.

Shear kinematics for the UBE tests are shown in Figure 2.10. The kinematics in Region A are close to ideal to up to 50$^o$ of shear for the co-mingled twill weave fabric, up to 60$^o$ of shear for the glass plain weave fabric and up to 20$^o$ of shear for the self-reinforced polypropylene plain weave fabric. Beyond 60$^o$, intense wrinkling meant that shear angles could no longer be obtained using image analysis, even from the corners of Region A. The

co-mingled specimen shows slight asymmetry about the central vertical axis (see Figure 2.6b) due to its asymmetric tensile behaviour in the warp and weft directions [23].

For bias extension tests, the onset of fabric wrinkling can also be evaluated from the plot of the ratio $L''_{mu}=L'_{mu}$ versus $\theta_{mu}$. Figures 2.11a, 2.11b and 2.11c show the values increasing before $\theta_{mu}$ = 30º, 5º and 40º, significantly lower than that suggested by the transmitted light measurements (see Figures 2.10b and 2.10d).

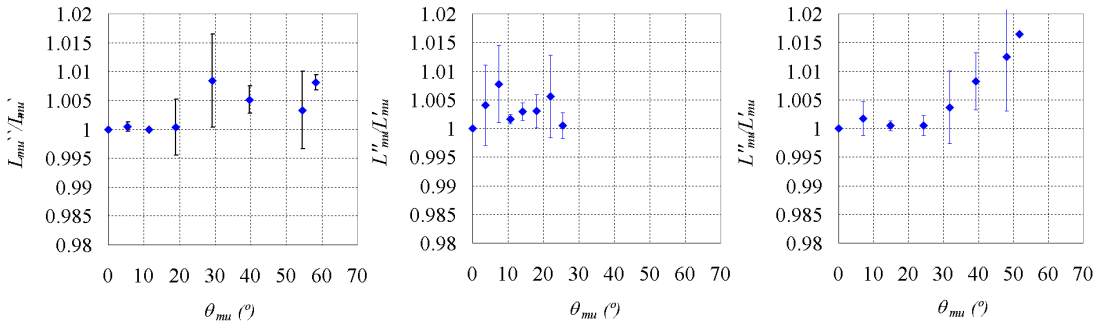


Figure 2.11. Ratio of the current curved perimeter length divided by the current straight perimeter length of Region A, $L''_{mu}=L'_{mu}$, (as shown in Figure 2.7 (a)) as a function of $\theta_{mu}$ for UBE tests for: (a) glass plain weave fabric. (b) Self-reinforced polypropylene plain weave (c) co-mingled twill weave fabric.

Figure 2.12 shows noticeably different behaviour of the ratio, $L'_{mu}/L'_{tu}$, for the three fabrics. This quantity is a combined measure of inter-tow slip and fabric crimping. The ratio is constant with increasing $\theta_{mu}$ for the cgPP twill weave fabric as shown in Figure 2.12c but steadily decreases with increasing $\theta_{mu}$ for the wrGF and self-reinforced polypropylene plain weave as shown in Figure 2.12a and 2.12b which can be attributed to the high level of crimping and low permeability for the co-mingled twill weave fabric that cause increasing $L'_{mu}$ which in order increase the $L'_{mu}/L'_{tu}$.

If fibre extension is assumed to be negligible, this suggests that (a) the inter-tow slip which has been observed previously [63] in Region A of woven prepregs is absent, indicating that woven dry fabrics hold together better during bias testing than prepregs, presumably because they are easier to clamp firmly and further (b) increasing crimp tends to shorten the in-plane length of the tows. The latter effect is difficult to model using a continuum

approach but is nonetheless relevant to the evaluation of forming predictions where draw-in of the perimeter of the deformed blank after press forming is used to assess the accuracy of simulations [66]. Figures 2.12a, 2.12b and 2.12c also show how the ratio $C_{mu}/C_{tu}$ increases steadily with increasing $\theta_{mu}$, probably due to both un-crimping of tows with increasing in-plane tension and, more importantly, due to cross-over slip in Region C (see Figure 2.6b). The heavier co-mingled twill weave fabric is slightly less prone to cross-over slip than the lighter glass plain weave fabric, though the difference in this regard is small.

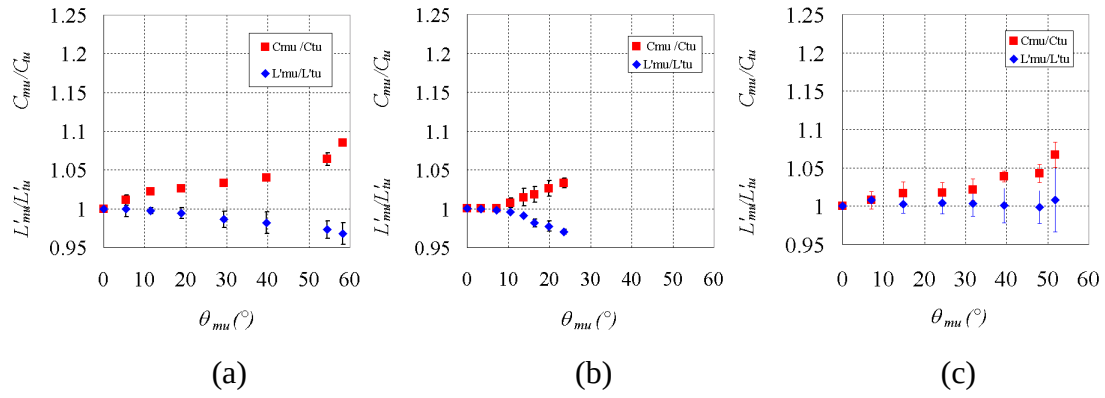


Figure 2.12. Ratio of the current curved perimeter length, divided by the initial straight perimeter length of Region A, $L'_{mu}=L'_{mu}$ and also the ratio of the current measured length divided by the initial theoretical length of Region C, $C_{mu}/C_{tu}$, as a function of $\theta_{mu}$ for UBE tests for: (a) glass plain weave fabric. (b) Self-reinforced polypropylene plain weave (c) co-mingled twill weave fabric.

The corresponding experimental shear force versus shear angle curves, $F_s(\theta)$ are initially approximated from the axial load, $F_m(\theta)$, using Eq (2.4). A 9$^{th}$ degree polynomial fit of the experimental shear compliances $F_s$-$\theta$ coefficients of the UBE wrGF and cgPP results was produced as illustrated in Table 2.4.

Table 2.4. The experimental shear compliances $F_s$-$\theta$ 9$^{th}$ degree polynomial fits' coefficients of the UBE wrGF and cgPP

| Coefficients | *Fs-θ* | |
|---|---|---|
| | wrGF | cgPP |
| 1 | -1.62E-23 | 2.50E-12 |
| 2 | 4.14E-21 | -6.46E-10 |
| 3 | -4.28E-19 | 6.79E-08 |
| 4 | 2.33E-17 | -3.78E-06 |
| 5 | 1.64E-07 | 1.22E-04 |
| 6 | -2.02E-05 | -2.32E-03 |
| 7 | 9.44E-04 | 2.55E-02 |
| 8 | -1.82E-02 | -1.50E-01 |
| 9 | 1.63E-01 | 4.58E-01 |
| 10 | 0.00E+00 | 1.97E-02 |

**d) BBE test kinematics**

The theoretical shear angle versus the measured shear angle $\theta_{tb}$ (calculated using Eq. (2.3)) versus $\theta_{mb}$ for the two specimen geometries are shown in Fig 13 for 3:1 geometry and in Figure 2.14 for 4:1 geometry. In Region A of both specimen geometries, the kinematics are close to ideal in Figures 2.13 and 2.14a, i.e. the inter-tow slip mechanism depicted in Figure 2.6a is prevented from occurring by firm clamping of the specimen. Image analysis above 50º for wrGF and cgPP and 10º for srPP was not performed because force results were unreliable beyond this shear angle due to fabric tearing (see Section 1.9). Again there is a noticeable difference in the kinematics of the three fabrics. The kinematics in Region A are close to ideal conditions for the first 25 $^{o}$ of shear in self-reinforced polypropylene, and for the first 50$^{o}$ of shear in the dry glass plain fabric and co-mingled twill weave fabric (see Figure 2.13c). However, the measured shear angle of the co-mingled twill weave fabric (3:1 BBE with 5N transverse force - Figure 2.13c) is slightly higher than the theoretical shear angle. This might be due to the asymmetric tensile behaviour in the warp and weft directions, the heavier fabric's greater resistance to the sudden changes of in-

plane tow direction, or assumption that the structure of twill fabric is more deformable than plain weave architectures.

On the other hand, there is a noticeable similarity in the kinematics of the 3:1 BBE and 4:1 BBE for the dry glass plain fabric and self-reinforced polypropylene as shown in Figures (2.13 and 2.14). Both are close to ideal kinematics but the measured shear angle for 4:1 BBE of self-reinforced polypropylene with 100N transverse force (Figure 2.14b) is slightly lower the theoretical shear angle. This might be due to the out-of plane buckling that takes place even when high in-plane tension is applied.

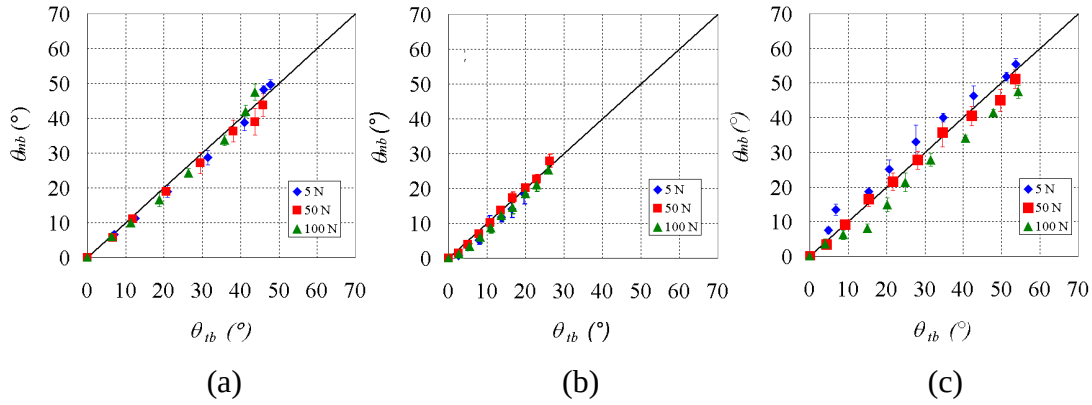


Figure 2.13. Shear angle kinematics ($\theta_{mb}$ versus $\theta_{tb}$) for 3:1 BBE tests using for the: (a) glass plain weave fabric. (b) Self-reinforced polypropylene plain weave fabric (c) co-mingled twill weave fabric

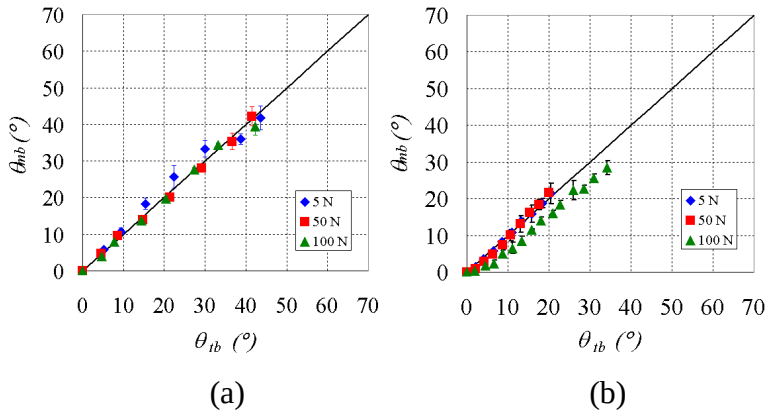


Figure 2.14. Shear angle kinematics ($\theta_{mb}$ versus $\theta_{tb}$) for 4:1 BBE tests using for the: (a) glass plain weave fabric. (b) self-reinforced polypropylene plain weave fabric

The onset of wrinkling was determined by the backlighting technique as shown in Figure 2.15 and 2.16. The corresponding shear angle was then plotted versus transverse load in Figure 2.17. As with the uniaxial tests, the wrinkling onset can also be determined by

examining the length of lines drawn on the surface of the specimen, e.g., the length ratio $L''_{mb}=L'_{mb}$. Figure 2.18 and 2.19 show this ratio as a function of $\theta_{mb}$ for the BBE test 3:1 geometry for glass plain weave fabric, self-reinforced polypropylene plain weave fabric and co-mingled twill weave fabric and for the BBE test 4:1 geometry for glass plain weave fabric and self-reinforced polypropylene plain weave fabric. Again Figures 2.18 and 2.19 show noticeably different behaviour of the ratio, $L'_{mu}/L'_{tu}$ for the three fabrics. In Figure 2.18, high shear angles up to 63° were obtained for dry plain glass fabric without wrinkles but according to the force graphs (Figure 2.22a), the fabric pulled apart much earlier and this might be the cause of wrinkling postponement. For self-reinforced polypropylene plain weave fabric, shear angles up to 14° were obtained and, for co-mingled twill weave fabric, shear angles up to 42° were obtained before the onset of wrinkling. In the latter case, the fabric does not pull apart but it wrinkles. This might be because this material is much thicker and heavier than the other two materials, which require much higher in-plane tension in order to avoid wrinkles.

Figure 2.19a and 2.19b shows similar trend to Figure 2.18a and 2.18b, shear angle up to 59° was obtained for dry plain glass fabric before the onset of wrinkling (see Figure 2.19a) and up to 11° was obtained for self-reinforced polypropylene plain weave fabric (see Figure 2.19b).

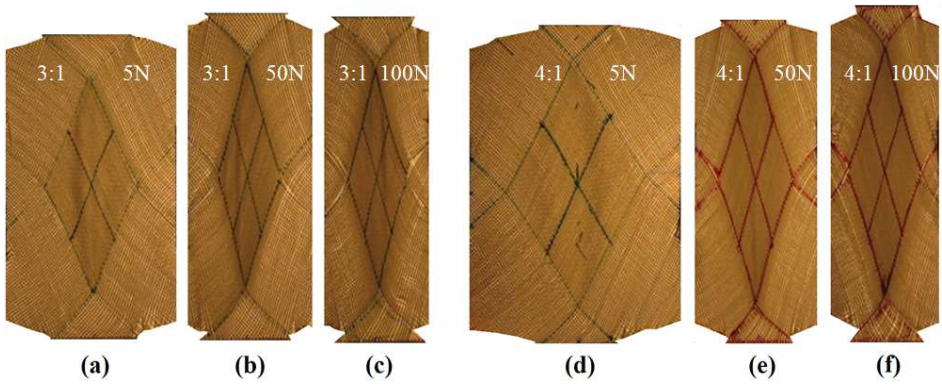


Figure 2.15. Backlit images showing onset of wrinkling in BBE tests. Specimen dimension and transverse force are given in each of the images. (a)–(c) correspond to the 3:1 specimens, (d)–(f) correspond to the 4:1 specimens. wrGF

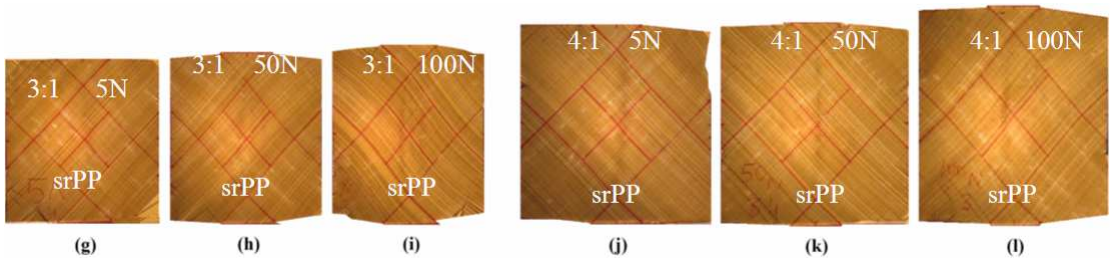


Figure 2.16. Backlit images showing onset of wrinkling in BBE tests. Specimen dimension and transverse force are given in each of the images. (a)–(c) correspond to the 3:1 specimens, (d)–(f) correspond to the 4:1 specimens. srPP

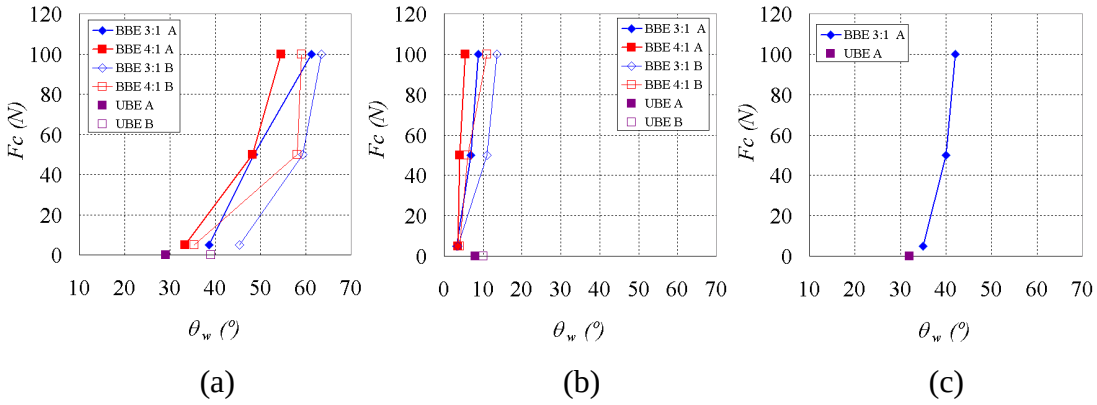


Figure 2.17. Wrinkle onset angle versus transverse force for the two geometries of the BBE test and the UBE test for: for: (a) glass plain weave fabric (b) self-reinforced polypropylene plain fabric (c) co-mingled twill weave fabric. As shown in the legend, technique A (closed points) is the wrinkle onset determined using the L''/L' ratio and technique B (open points) is the onset determined using the transmitted backlighting method

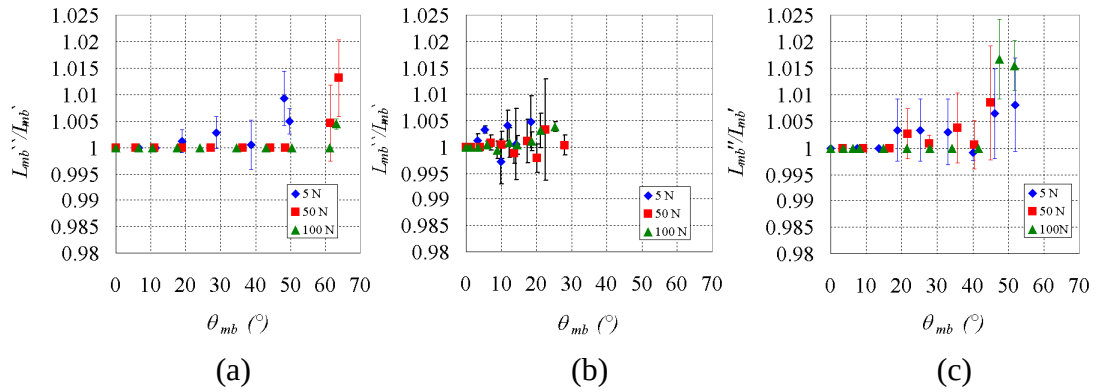


Figure 2.18. Wrinkling across the specimen can be monitored using the ratio $L''_{mb}=L'_{mb}$ versus $\theta_{mb}$ for 3:1 BBE results, the ratio increases with the growth of out-of-plane wrinkles for the (a) glass plain weave fabric (b) self-reinforced polypropylene plain fabric (c) co-mingled twill weave fabric.

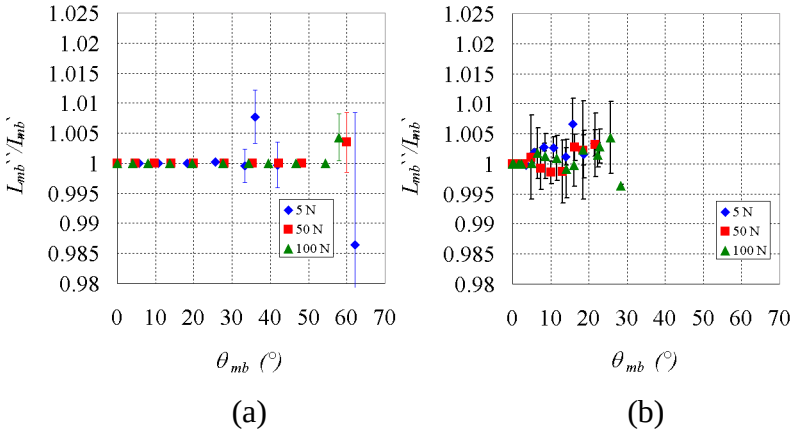


Figure 2.19. Wrinkling across the specimen can be monitored using the ratio $L''_{mb}=L'_{mb}$ versus $\theta_{mb}$ for 4:1 BBE results, the ratio increases with the growth of out-of-plane wrinkles for the (a) glass plain weave fabric (b) self-reinforced polypropylene plain fabric.

The onset of wrinkling is again indicated by the increase of the ratio above unity, and the corresponding shear angles are also compared in Figure 2.17. For the purpose of comparison, results from the UBE tests are also shown in Figure 2.17. The data show a clear and significant increase in the shear angle at the onset of wrinkling as the transverse load is increased. The two methods for determining the value of the wrinkle onset show similar trends, though the ratio method $L''=L'$ is shown to be a more sensitive technique than the transmitted backlighting method that is use a for dry glass plain weave fabric and self-reinforced polypropylene plain weave fabric. As for the specimen geometry, there is no notable difference between the two geometries for determining the wrinkling behaviour. It is interesting to note that PF test results of dry glass plain weave fabric indicate the same wrinkling angle as BBE tests conducted using transverse loads of at least 50 N, i.e. around 60º. As no pre-tension was applied to the PF test sample, this indicates that in-plane fibre tension increases during the course of the PF test, effectively suppressing the occurrence of wrinkles. The reason for this is discussed at length in [43-45].

Finally, Figures 2.20 and 2.21 shows the relationships between the ratios, $L'_{mb}=L'_{tb}$ and $C_{mb}/C_{tb}$, and the angle $\theta_{mb}$ for a BBE test geometry of 3:1 and 4:1 respectively, using glass plain weave fabric, self-reinforced polypropylene plain fabric and co-mingled twill weave fabric. Once again, a reduction of the ratio, $L'_{mb}=L'_{tb}$, below unity indicates an absence of inter-tow slip in Region A, and a shortening of the in-plane length of the tows due to increased crimping in glass plain weave fabric and self-reinforced polypropylene plain

fabric (see Figures 2.20 and 2.21). However, the ratio $L'_{mb}=L'_{tb}$ fluctuated around unity and increased a little at the end of the curves for the co-mingled twill weave fabric (see Figure 2.20c). This might be due to a presence of inter-tow slip. Crossover slip, $C_{mb}/C_{tb}$, is seen to be much more pronounced in the biaxial tests compared to uniaxial tests (see Fig 12), due to the higher forces involved. It is also higher in the 4:1 specimen than in the 3:1 specimen, indicating improved specimen integrity as the specimen side length/clamping length ratio decreases (see Figures 2.20 and 2.21). As expected, the amount of cross-over slip is directly related to the size of the transverse force applied to the specimens.

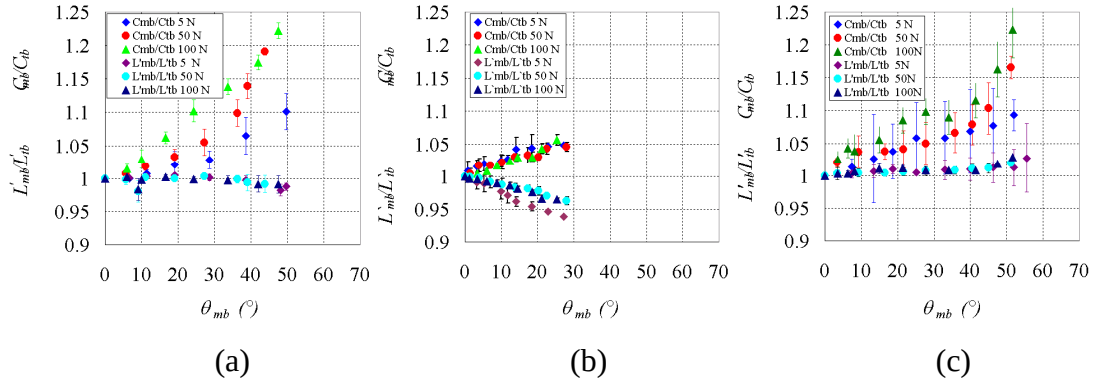


Figure 2.20. Inter-tow slip and tow contraction due to crimping can be monitored using the ratio, $L'_{mb}=L'_{tb}$ while cross-over slip in Region C can be monitored using the ratio, $C_{mb}/C_{tb}$ versus $\theta_{mb}$ for 3:1 BBE specimen tests for: for the (a) glass plain weave fabric (b) self-reinforced polypropylene plain weave fabric (c) co-mingled twill weave fabric

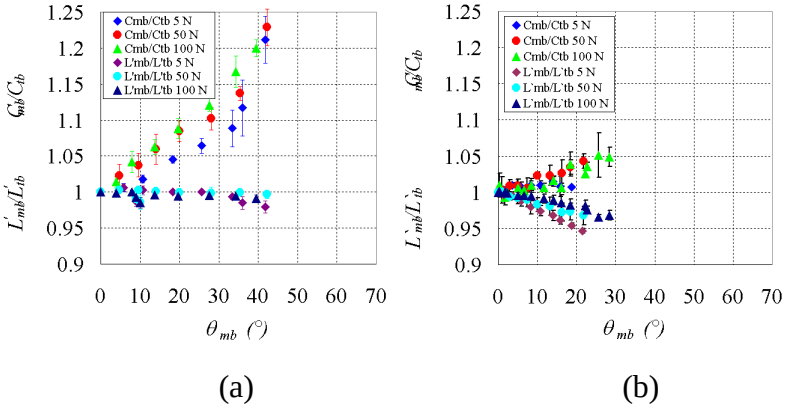


Figure 2.21. Inter-tow slip and tow contraction due to crimping can be monitored using the ratio, $L'_{mb}=L'_{tb}$ while cross-over slip in Region C can be monitored using the ratio, $C_{mb}/C_{tb}$ versus $\theta_{mb}$ for 3:1 BBE specimen tests for: for the (a) glass plain weave fabric (b) self-reinforced polypropylene plain weave fabric (c) co-mingled twill weave fabric.

### 2.4.4 Analysis of BBE force results

During BBE tests, the total signal recorded by the loadcell, $F_T$, is comprised of four different contributions:

$$F_T = F_m + F_r + F_f + F_{mis} \tag{2.5}$$

where $F_m$ is the material deformation force, $F_r$ is the reaction force due to $F_c$, the transverse load. $F_f$ is the frictional resistance of the system and $F_{mis}$ is the force due to misalignment of the sample in the test set-up. Three repeat tests were conducted and their averages were reported for each of five transverse loads: 5, 37, 50, 75 and 100 N for glass plain weave fabric and self-reinforced polypropylene plain weave fabric and 5, 27, 50, 75 and 100 N for co-mingled twill weave fabric (see Figure 2.22 for 3:1 BBE and Figure 2.23 for 4:1 BBE) error bars indicate standard deviation. Since $F_T$ includes various force contributions, it is important to determine $F_m$ from $F_T$. To do this, other contributions should be determined and then subtracted from $F_T$. Such procedures are described in Subsections 5.7.2 and 5.7.3.

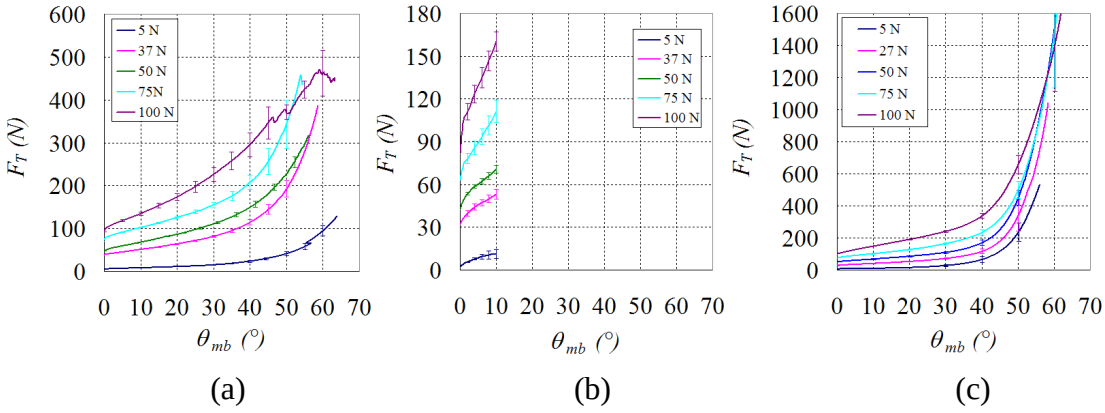


Figure 2.22. Total force, $F_T$, versus shear angle, $\theta_{mb}$ before removing the contribution from the transverse loads for 3:1 specimen tests. The applied transverse loads are given in the legend: for the (a) glass plain weave fabric (b) self-reinforced polypropylene plain weave fabric (c) co-mingled twill weave fabric.

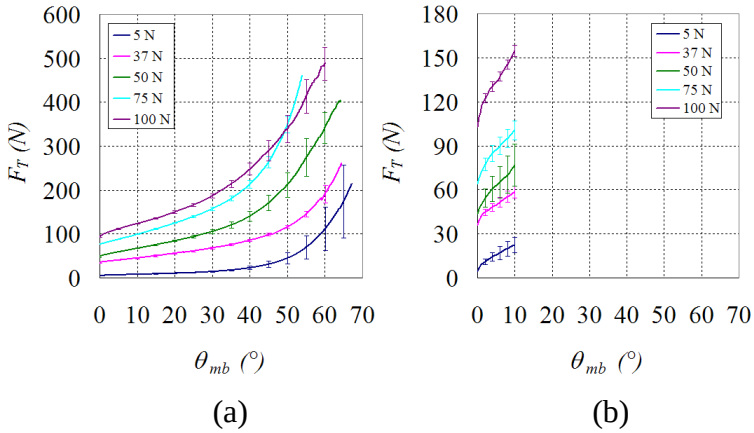


Figure 2.23. Total force, $F_T$, versus shear angle, $\theta_{mb}$ before removing the contribution from the transverse loads for 4:1 specimen tests. The applied transverse loads are given in the legend: for the (a) glass plain weave fabric (b) self-reinforced polypropylene plain weave fabric

### a) Determining the reaction force, $F_r$

For ideal kinematics, $F_r$ can be related to $F_c$ analytically by considering the stress power of the system [55]. If the side length of Region A, $L'$, is known, the only information required to determine, $F_r$ is $d_y$, the vertical displacement of the test machine crosshead (note that here $x$ indicated the horizontal direction and $y$ indicates the vertical direction). By referring to Figure 2.24 and using trigonometry it can be shown that,

$$\frac{d_y}{2} = L'\cos\left(\frac{\pi}{4} - \frac{\theta}{2}\right) - L'\cos\left(\frac{\pi}{4}\right) \tag{2.6}$$

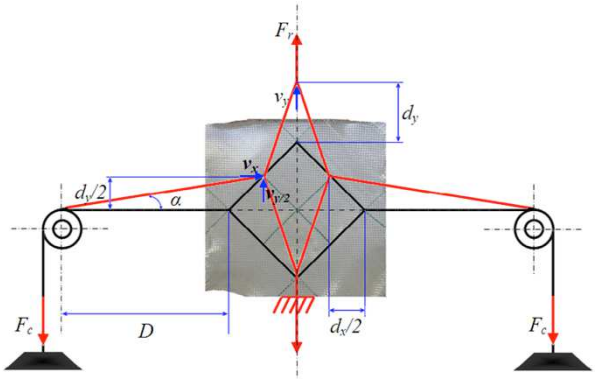


Figure 2.24. Construction lines showing idealised kinematics superimposed over image of actual test specimen. The change in the orientation of the lines connecting the transverse loads to the sides of the specimen is indicated by the angle α.

Differentiating Eq. (2.6) with respect to time, gives:

$$v_y = \dot{\theta} L'\sin\left(\frac{\pi}{4} - \frac{\theta}{2}\right) \tag{2.7}$$

where $v_y$ is the vertical velocity of the test machine crosshead. Similarly, using trigonometry it can be shown that

$$\frac{d_x}{2} = L'\cos\left(\frac{\pi}{4}\right) - L'\sin\left(\frac{\pi}{4} - \frac{\theta}{2}\right) \tag{2.8}$$

where dx is the horizontal displacement of the side corner of Region A. Differentiating Eq. (2.8) with respect to time, gives,

$$v_x = \dot{\theta} L' \cos\left(\frac{\pi}{4} - \frac{\theta}{2}\right) \tag{2.9}$$

where $v_x$ is the horizontal velocity of the side corner of Region A. If zero friction is assumed in the pulley wheel, then the force exerted by the fishing-line is simply $F_c$. In the ideal case, the force acting on the side corners of Region A is directed co-linearly along the direction of the fishing-line. By resolving both the velocity of the side corners, and the tensile force acting along the fishing-line, into x and y components, the power exerted in moving the transverse load can be calculated and equated with the power required to pull the crosshead, i.e.

$$F_r v_y = 2F_c \cos\alpha . \frac{v_x}{2} + 2F_c \sin\alpha . \frac{v_y}{2} \tag{2.10}$$

where the angle that the fishing-line makes with the horizontal, α, can be found as

$$\alpha = \arctan\left(\frac{d_y}{2D + d_x}\right) \tag{2.11}$$

where the length, $D$, is horizontal distance between the centre of the pulley wheel and the corner of Region A (see Figure 2.24). Rearranging Eq. (2.10) gives

$$F_r = F_c\left(\frac{v_x}{v_y}\cos\alpha + \sin\alpha\right) \tag{2.12}$$

As expected, when $\alpha$ = 0, Eq. (2.12) predicts $F_r = F_c$. However, when testing actual specimens Eqs. (2.11) and (2.12) are no longer valid as the specimen undergoes only a rough approximation of ideal kinematics, as shown in Section 2.4.4 (a). Thus, $v_x$ can no longer be derived from $d_y$ and the upward velocity of the centre of the specimen is no longer given by $v_y/2$. This means that the horizontal and vertical velocity components of the side corner of Region A have to be measured using image analysis. To distinguish actual quantities from ideal ones, a * superscript is used, i.e. $D^*$, $d^*_x$, $d^*_y$, $v^*_x$ and $v^*_y$, for the motion of the side corner of Region A. These quantities are obtained by measuring the displacement of the side corner of Region A in the $x$ and $y$ directions as a function of time, fitting polynomial functions and then differentiating these functions. The resulting polynomials for the displacements and velocities can then be introduced in Eq. (2.13) and (2.14) to determine $F_r$, i.e.

$$F_r = F_c\left(\frac{v^*_x}{v_y}\cos\alpha + \frac{v^*_y}{v_y}\sin\alpha\right) \tag{2.13}$$

$$\alpha = \arctan\left(\frac{d^*_y}{D^* + d^*_x}\right) \tag{2.14}$$

**b) Determining the friction force, $F_f$**

Using a stiff four-truss linkage with no friction at the joints (achieved by inserting a square linkage of carbon yarns) the reaction force, $F_r$, due to the transverse load, $F_c$, can be measured. Any difference between the theoretical prediction and the measured force can be assigned to friction in the system and is mainly attributed to the friction of the pulley wheel bearing. This friction was characterized for several transverse loads, $F_c$, as a function of $d_y$, thereby producing a polynomial surface plot for $F_f$ (see Figure 2.25).

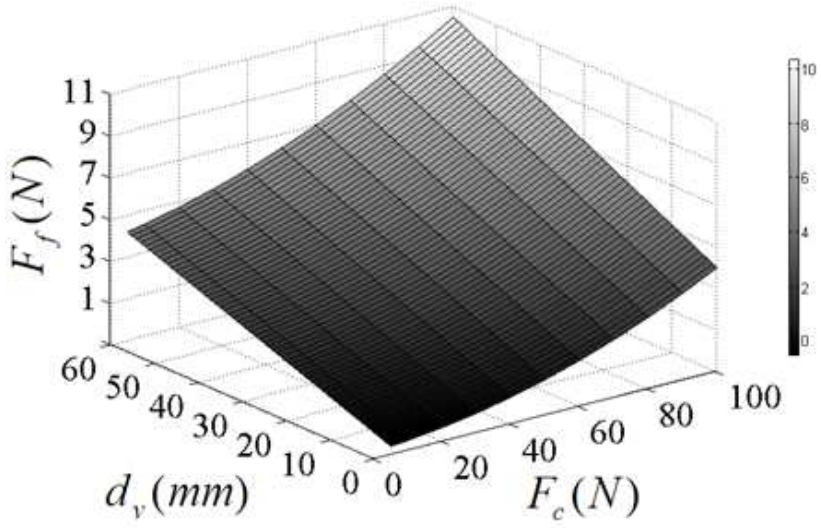


Figure 2.25. Polynomial surface fit of the friction force as a function of the transverse load and crosshead displacement. The friction force is used in Eq. (4) to find the material force.

A polynomial fitted to this surface using Matlab™ is given by Eq. (2.15). Results for this set-up suggest that $F_f$ is only a small percentage of the total signal, e.g., <4% for 5 N transverse force, <10% for 50 N transverse force and <15% for 100 N transverse force.

$$\begin{aligned} F_f &= -0.66 + 7.8\times10^{-3}F_c + 7.9\times10^{-2}d_y \\ &+ 3.8\times10^{-4}F_c^2 + 3.0\times10^{-4}F_c d_y - 1.2\times10^{-3}d_y^2 \end{aligned} \tag{2.15}$$

where $F_f$ is the friction force in the pulleys, $F_c$ is the transverse force and $d_y$ is the axial displacement. Once $F_f$ known, it can be subtracted from $F_T$, see Eq. (2.5), leaving only $F_m$

and $F_{mis}$ as unknowns. Here we assume the misalignment force, $F_{mis}$, for both specimen geometries, can be neglected. Future work is planned to check this assumption. Finally, $F_m$ versus $\theta_{mb}$ curves for the various transverse loads are given in Figures 2.26 and 2.27. The results reveal a strong shear–tension coupling and are of very similar form to those predicted numerically in [53]. The corresponding experimental shear force versus shear angle curves, $F_s^i(\theta)$ are initially approximated from the axial load, $F_m(\theta)$, using Eq (2.4). The superscript $i$ is the experiment number ($i$ = 1 to 5) with each experiment using a different transverse load ($i$ = 1 corresponds to 5N, $i$=2 corresponds to 37 or 50N etc). A 9$^{th}$ degree polynomial was used to fit the experimental shear compliance $F^i_s$-$\theta$ coefficients of the BBE 3:1 test. The wrGF and cgPP results were produced, as illustrated in Tables 2.5 and 2.6 respectively, for further use in the FE numerical simulations.

Table 2.5. the experimental shear compliances $F^i_s$-$\theta$ 9$^{th}$ degree polynomial fits' coefficients of the BBE 3:1 wrGF with different transverse forces

| *Fs-θ* | | | | | |
|---|---|---|---|---|---|
| Coefficients | $F_c$ (N) | | | | |
| | 5 | 27 | 50 | 75 | 100 |
| 1 | 1.04E-12 | 1.35E-12 | 2.35E-12 | 1.95E-12 | -1.60E-12 |
| 2 | -3.23E-10 | -4.71E-10 | -8.43E-10 | -7.61E-10 | 4.40E-10 |
| 3 | 4.12E-08 | 6.41E-08 | 1.17E-07 | 1.12E-07 | -4.67E-08 |
| 4 | -2.79E-06 | -4.49E-06 | -8.32E-06 | -8.47E-06 | 2.26E-06 |
| 5 | 1.09E-04 | 1.78E-04 | 3.34E-04 | 3.62E-04 | -3.98E-05 |
| 6 | -2.49E-03 | -4.08E-03 | -7.68E-03 | -8.94E-03 | -3.34E-04 |
| 7 | 3.17E-02 | 5.17E-02 | 9.78E-02 | 1.22E-01 | 1.91E-02 |
| 8 | -2.03E-01 | -3.29E-01 | -6.20E-01 | -8.27E-01 | -1.87E-01 |
| 9 | 6.92E-01 | 1.20E+00 | 2.15E+00 | 3.19E+00 | 2.84E+00 |
| 10 | -5.06E-02 | 0.00E+00 | 0.00E+00 | 1.03E-01 | -6.54E-03 |

Table 2.6. the experimental shear compliances $F^i_s$-$\theta$ 9$^{th}$ degree polynomial fits' coefficients of the BBE 3:1 cgPP with different transverse forces

| *Fs-θ* | | | | | |
|---|---|---|---|---|---|
| Coefficients | $F_c$ (N) | | | | |
| | 5 | 37 | 50 | 75 | 100 |
| 1 | -3.20E-14 | 3.51E-17 | 3.12E-17 | 2.71E-17 | 2.32E-17 |
| 2 | 8.19E-12 | -1.33E-14 | -1.17E-14 | -1.01E-14 | -8.59E-15 |
| 3 | -8.44E-10 | 2.51E-12 | 2.22E-12 | 1.93E-12 | 1.64E-12 |
| 4 | 4.36E-08 | -3.09E-10 | -2.72E-10 | -2.34E-10 | -1.96E-10 |
| 5 | -1.08E-06 | 3.33E-08 | 2.97E-08 | 2.60E-08 | 2.23E-08 |
| 6 | 4.05E-06 | -2.56E-06 | -2.18E-06 | -1.79E-06 | -1.41E-06 |
| 7 | 6.17E-04 | 3.13E-04 | 2.92E-04 | 2.70E-04 | 2.49E-04 |
| 8 | -7.58E-03 | 2.76E-03 | 6.92E-03 | 1.11E-02 | 1.52E-02 |
| 9 | 2.78E-02 | 3.87E-01 | 7.84E-01 | 1.18E+00 | 1.58E+00 |
| 10 | 0.00E+00 | 0.00E+00 | 0.00E+00 | 0.00E+00 | 0.00E+00 |

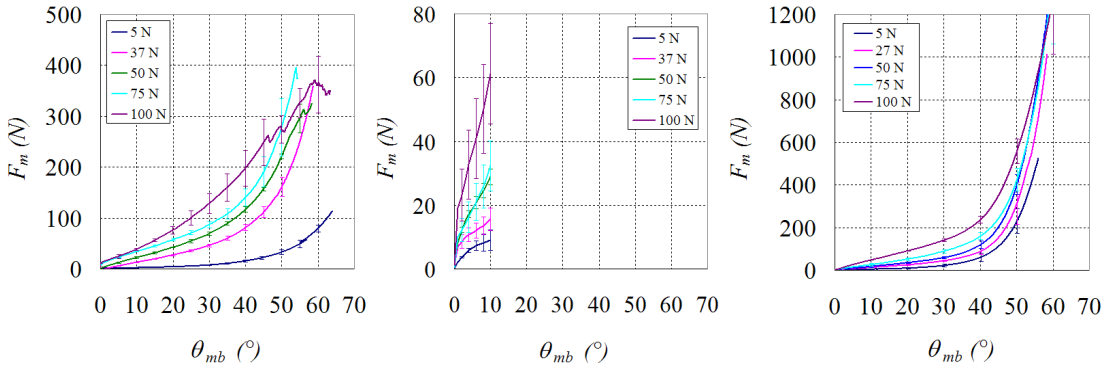


(a) (b) (c)

Figure 2.26. Material force, $F_m$ of 3:1 BBE as a function in $\theta_{mb}$ for various transverse loads ($F_c$ = 5, 37, 50, 75 and 100 N for glass and self-reinforced plain weave fabrics and $F_c$ = 5, 27, 50, 75 and 100 N for co-mingled twill weave fabric) for the (a) glass plain weave fabric (b) self-reinforced polypropylene plain weave fabric (c) co-mingled twill weave fabric.

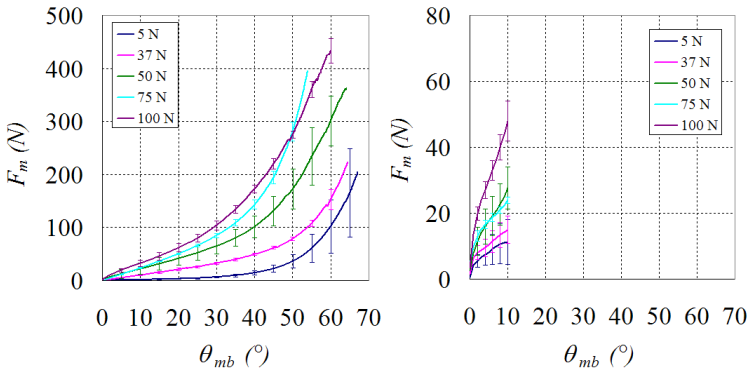


(a) (b)

Figure 2.27. Material force, $F_m$ of 4:1 BBE as a function in $\theta_{mb}$ for various transverse loads ($F_c$ = 5, 37, 50, 75 and 100 N for glass and self-reinforced plain weave fabrics) for the (a) glass plain weave fabric (b) self-reinforced polypropylene plain weave fabric

Test data obtained using the 100 N transverse load become unreliable at high shear angles due to tearing of the specimens and demonstrate the limits of the test technique. To quantitatively compare the size of the coupling with that measured in previous investigations, the ratio of the material force, $F_m$ of glass plain weave fabric and co-mingled twill weave fabric, at 10º and 20º for the 3:1 specimen is calculated and given in Table 2.1. The force per unit length is estimated by dividing the transverse force by the clamping length along the edge of the specimen. According to Table 2.1 and referring to results of [53] an increase in applied in-plane tension by a factor of 23 (i.e. 0.163/0.007)

results in an increased shear force of about 10 times at 10º and 20 times at 20º. In the current investigation, an increase of in-plane tension by a factor of 20 results in an increased shear force of 23 times for glass plain weave fabric and 25 times for co-mingled twill weave fabric at 10º and 36 times for glass plain weave fabric and 41 times for commingled at 20º. Considering the rough approximations used in this comparison, the agreement is reasonable and provides experimental validation of the multi-scale modelling strategy employed in [53].

## 2.5 Comparison of PF, UBE and BBE test results

In Figures 2.28 and 2.29, normalised material force results versus measured shear angle of BBE tests with a 5 N transverse load have been compared with PF and UBE test results using side length and energy normalisation method for the three materials.

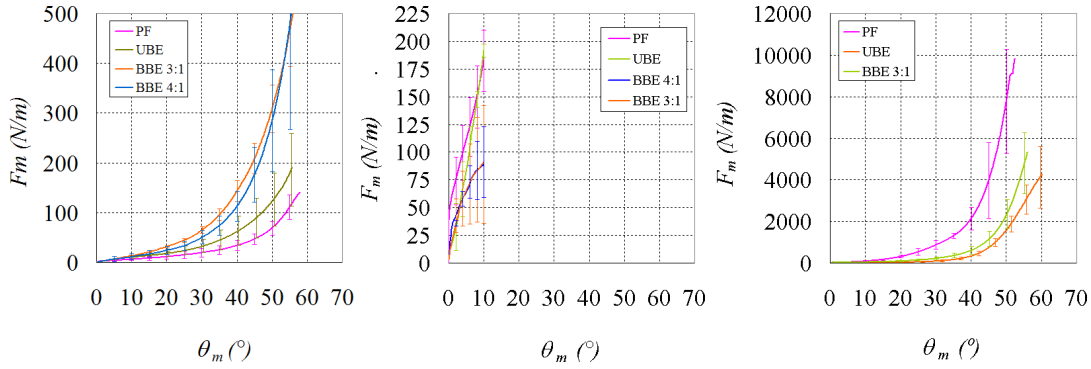


Figure 2.28. Normalized load as afunction of the measured shear angle of the PF, UBE and BBE tests with the latter using a transverse load of 5 N. The three tests are normalised by the side length of Region A. (a) glass plain weave fabric (b) self-reinforced polypropylene plain weave fabric (c) co-mingled twill weave fabric.

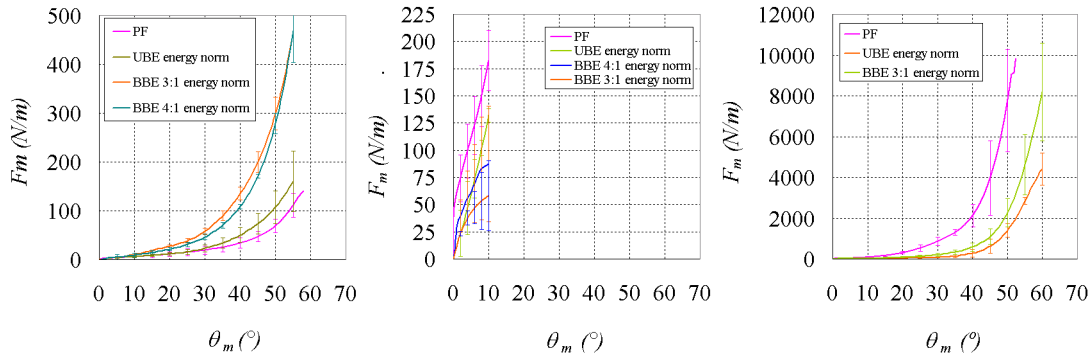


(a) (b) (c)

Figure 2.29. Normalized load as a function of the measured shear angle of the PF, UBE and BBE tests with the latter using a transverse load of 5 N. Two different normalisation procedures have been used: PF tests normalised by the side length of Region A while the UBE and BBE tests are normalised using an energy method described in Harrison, et al. [56], [67] (a) glass plain weave fabric (b) self-reinforced polypropylene plain weave fabric (c) co-mingled twill weave fabric.

PF results of glass plain weave fabric and self-reinforced polypropylene plain weave fabric represent the average of the lowest three results (i.e. smallest shear force) among six repeat tests for glass plain weave fabric and three repeat tests for self-reinforced polypropylene plain weave fabric. Three of the repeat samples of the glass plain weave fabric were discarded due to obvious contributions of clamped boundary effects to the measured force. On the other hand, UBE results of co-mingled twill weave fabric represent the average of the lowest three results [42, 46]. This clear difference in the wrGF and cgPP material behaviour could be attributed to the structure or crimping pattern. To compare the force results of the three different tests, a normalisation technique has to be used. In Figure 2.28, the data are normalised simply by dividing with the side length of Region A, while in Figure 2.29. an energy normalization technique developed in [55, 67] (which does not account for a shear–tension coupling) is applied to the UBE and BBE results. The latter technique aims to account for the contributions of Region B to the measured force, and it produces accurate results as long as shear–tension coupling effects are negligible. This is seen to be the case for the PF and UBE tests at low shear angles, where the data produces an almost perfect match. As the shear angle increases above 25° in glass plain weave fabric, the UBE test results increase at a faster rate, probably due to the steadily increasing in-plane tension in the fabric of the UBE test. In contrast, glass plain weave fabric tows in the PF test are ‘shielded’ from tensile stresses by the side bars of the PF, at least in the absence of misalignment or crimping effects [43]. Also, the UBE test results in co-mingled twill weave fabric increase at a slower rate than the PF results. This might be due to a

presence of misalignment or side boundary condition effect [42, 46]. The BBE test results of glass plain weave fabric show a significant difference from both the PF and UBE tensile data. This is due to the higher in-plane stresses experienced by the tows in the samples, as a result of using a 5 N transverse load and larger size specimens. On the other hand, the PF test results of self-reinforced polypropylene plain weave fabric and co-mingled twill weave fabric demonstrate a considerable raise over the other two tests results, and this might be as a result of misalignment and rigid boundary condition effects. Thus, it can be seen that for low in-plane stresses, the results of the three tests are close but quickly begin to diverge as the in-plane tension in the fabric increases, which is to be expected if a shear–tension coupling exists.

The normalised results of material force versus measured shear angle of the BBE tests using a 5 N transverse load, the PF method, and the UBE test, based on side length and energy normalisation methods for the co-mingled twill weave fabric has been also compared against the normalised results of PF and UBE tests conducted by [41] for the same material (see Figure 2.30).

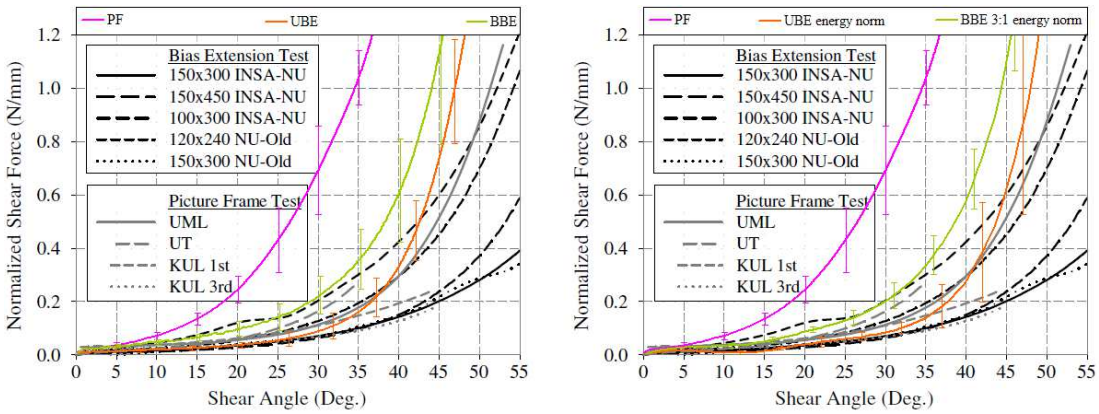


(a) (b)

Figure 2.30. Comparing the normalized load as function of the measured shear angle of the PF, UBE and BBE tests with the latter using a transverse load of 5 N that obtained in this work (colour curves) against the benchmarked results in [41]. (a) the three tests normalised by the side length of region A (b) PF test result was normalised by side length of region A and the UBE and BBE test results were normalised using an energy method.

The UBE and BBE test results for the two normalisation techniques were located within the same range of the benchmarked results (see Figure 2.30a and 2.30b). However, there is a significant gap between the current normalised PF result and the benchmarked results [41]. The reason for this large discrepancy is clearly the strict boundary condition of the PF device where it has been found impossible to prevent pretension and tow meander when fixing a given sample to the PF rig [44, 45].

## 2.6 Conclusions

BBE testing is shown to be an accurate method of characterising wrinkling onset and fabric shear compliance versus in-plane tension for woven biaxial engineering fabrics. Such characterisation is extremely difficult to conduct using regular PF or UBE tests. The technique requires a very simple experimental setup and analysis can be performed using freely available image analysis software. Two methods of monitoring wrinkling have been demonstrated: observing changes in the transmitted backlighting intensity through the samples and by analysis of tracer lines marked on the specimens prior to testing. Results show similar trends: an approximate doubling of the wrinkle shear angle with increasing in-plane tension. The transmitted backlighting intensity has been found to be less sensitive than the analysis of tracer lines in determining wrinkling onset. The latter technique has the added advantage of being useful for both translucent, e.g. glass, and opaque, e.g. carbon, fabrics. A strong dependence of shear compliance on in-plane tension has been demonstrated with the measured shear force increasing by a factor of about 30 to 40 times at a shear angle of 20° when comparing data measured using a small (5 N) compared to a high (100 N) transverse load. Comparison of shear force versus shear angle data with equivalent numerical results generated by other researchers is good [50]. The test is a first step towards a reliable method for parameter identification of shear–tension coupled constitutive models [53] and can be used inversely to fit out-of-plane bending stiffness model parameters [32, 59]. Normalisation of results using an energy method [55, 67] for comparison with PF and UBE tests, show the equivalence of the tests when low in-plane tensions are applied. Specimen geometry was found to influence the deformation kinematics of the samples with the 3:1 specimen holding together better than the 4:1 specimen. The 3:1 specimen created larger shear force versus measured shear angle results than the 4:1 specimen, despite being of smaller total area. It can be concluded that the BBE test technique is an effective method of measuring both the fabric's shear–tension coupling and the onset of wrinkling, at least for plain weave engineering fabrics. However, a method

of normalising the test results for any given sample geometry must be developed if the unique underlying material response of the fabric is to be accurately characterised.

# 3. Characterisation and Modelling Variability of Tow Orientation in Engineering Fabrics and Textile Composite

## 3.1 Introduction

Variability of tow orientation is unavoidable for biaxial engineering fabrics and their composites. Since the mechanical behaviour of these materials is strongly dependent on the fibre direction, variability should be considered and modelled as exactly as possible for more realistic estimation of their forming and infusion behaviour and their final composite mechanical properties. In this study, a pre-existing numerical code implemented in Matlab, 'MeshGen' [68, 69] has been enhanced to introduce new capabilities to model realistic full-field variability of the tow directions across flat sheets of biaxial engineering fabrics and woven textile composites. The original MeshGen algorithm [68] is based on pin-jointed net kinematics and can produce a mesh of arbitrary perimeter shapes with variability in vertical and horizontal directions, suitable for subsequent computational analysis such as finite element forming simulations. While the shear angle in each element is varied, the side-length of all unit cells within the mesh is constant. This simplification ensures that spurious tensile stresses are not generated during deformation of the mesh during forming simulations. The directional variability that can be generated from MeshGen [68] is achieved by stretching the given mesh vertically or horizontally, which results in producing a mesh with unrealistic variability i.e. the MeshGen [68] is unable to simulate the actual variability characteristics such as wavy tows and variability with normal distribution that mimic the inherent variability in actual engineering fabrics and their composite. Consequently, an improvement of the existing MeshGen algorithm [68] has been carried out here to obtain a means of producing mesh with realistic variability. Variability is controlled using six parameters that can take on arbitrary values within certain ranges, allowing flexibility in mesh generation. The distribution of tow angles within a pre-consolidated glass-polypropylene composite and commingled glass/polypropylene, self-reinforced polypropylene and glass fabrics has been characterized over various length scales. Reproduction of the same statistical variability of tow orientation as measured from these materials is successfully achieved by combining the *VariFab* code with a simple genetic algorithm.

## 3.2 Review of Previous Work

Product variability and discard rates of manufactured goods are closely related to the inherent variability of the materials from which they are made. Tow and fibres within actual advanced composites inevitably contain at least some degree of stochastic deviation away from their ideal architecture. The development of accurate process design tools that can account for this type of variability is aimed at reducing the cost of the pre-manufacture assessment and optimization of parts by minimising design iterations and prototyping. Variability in the architecture of advanced composites can be introduced at numerous stages in the manufacture process such as weaving or stitching of the fabrics, pre-impregnation of prepregs, pre-consolidation of co-mingled thermoplastic textile composites or handling and cutting of fabrics off the fabric roll. Understanding the resulting inherent variability in the architecture is important in that it can influence subsequent stages in the manufacture process. Examples include (i) variable infusion times and flow front irregularities [70-72] and possible formation of dry spots due to variable nesting [73] (ii) earlier wrinkling onset and variable final tow orientations during sheet forming [74-76] (iii) variable final mechanical properties such as stiffness [77, 78] compressive strength [79] or fatigue life [80] and (iv) changes in physical properties such as variable thermal conductivity [81]. The length scale over which variability has been characterized ranges from the entire sheet down to fibre orientations at the micro-scale, and the importance of considering not just global statistics but also spatial correlations of variability has been discussed [70, 75, 78].

Endruweit, et al. [71] and Endruweit [82] used manual digital image analysis to measure tow directions across the surfaces of four different 2-D engineering fabrics taken directly from the roll, including a non-crimp fabric and three woven fabrics. Variability of tow direction was correlated with the mobility of the fabric, a property related to the relative spacing between tows. Normal distributions were found, the loosely structured non-crimp fabric showed the most variability with a standard deviation of $7.9^{o}$ about the average, much higher than for the two more tightly packed 5-harness satin weaves and the plain weave, with mean inter-tow angles and corresponding standard deviations of 90.1 ±0.4, 89.4 ±0.5 and 91.2 $\pm 1.7^{o}$ respectively. Automated and semi-automated Fourier image processing techniques have been applied in the recognition of weave patterns [83] and to analyse the spectrum of frequencies within the fibre waviness of uniaxial composites [77,

84]. Characterisation techniques to analyse full-field variability have also been developed for both uniaxial composites [85] and textiles [75, 86]. Skordos and Sutcliffe [75] used a combined Fourier transform and image correlation approach to investigate variability across the surface of a carbon/epoxy 5-harness woven prepreg. Fourier transforms of the grey-scale image provided initial estimates of local tow directions and subsequent correlation techniques were used to refine this estimate and characterize tow spacing over small areas of just a few unit cells. By gathering information for 460 samples taken from a total area of 395 x 350 mm, they were able to use an autocorrelation method to pick out long-range variations in tow directions across the entire area of the sheet. Gan, et al. [86] recently developed a backlighting optical technique to investigate the variability of a woven and stitched fabric, identifying the centroid of tow crossover regions using built-in filtering techniques and a polar search algorithm to locate position and direction of neighbouring cells. Measurements across a sample area of up to 100 x 100mm allowed the determination of a full-field map of tow orientations. Data collection was approximately 50 times faster than equivalent manual analysis and revealed standard deviations in warp and weft orientations of approximately $5^o$ for the woven fabric and $2.5^o$ for the stitched fabric. Stochastic variation in interlock 3-D weaves using micro-CT has also been performed [78, 87]. For practical reasons, volumetric imaging techniques are usually limited to relatively small specimen dimensions. Representative samples measuring up to 8 x 25 mm containing 5 warp and 12 weft tows were characterized [87]. Meso-scale variations in tow direction of up to $5^o$ were recorded while much longer-range misalignment, measured by visual analysis, was much lower at around just $1^o$.

Measured variability has been incorporated into simulations and analytical predictions using a variety of techniques and at different length scales. For liquid infusion simulations Endruweit, et al. [71], [81] used a Monte Carlo technique to randomly assign variable tow angles across the finite element mesh to individual elements using statistics measured from actual fabrics. The method ignored the continuity in tow direction between elements and so was later replaced by an analytical method employing a spectral expansion of trigonometric functions to implement spatial correlation of tow direction from one element to the next [70]. For forming simulations, Long, et al. [74] used a Monte Carlo method to introduce a Gaussian distribution with a standard deviation of $5^o$ into the generator paths of kinematic draping simulations. The technique automatically ensured continuity in tow directions across the part. The technique of introducing variability during draping, as opposed to beginning with an initial sheet containing full-field tow angle variability is

subtly different to the actual forming scenario. Yu, et al. [76] attempted to avoid this by using the finite element method and adopted a similar approach to [71, 81]. However, assigning the shear angle in a stochastic manner caused discontinuity and disturbances in the tow-paths, leading to spurious tensile loads during forming simulations. Skordos and Sutcliffe [75] used a two-parameter stochastic process to generate a mesh with equivalent global statistics and importantly, with equivalent spatial correlations of tow angle variability as those measured in experiments. Variability has also been introduced into simulations at the meso-scale [72, 78, 80] taking advantage of the development of dedicated textile modeling codes. So far, this variability has focused on representative volume elements rather than long-range variability of tow paths. The aim of the current work is to: (a) characterize the variability of inter-tow angles in a range of engineering fabrics and (b) use the measured global statistics to reproduce representative variability with realistic spatial correlations, in meshes suitable for use in finite element forming simulations.

## 3.3 Material

Four materials have been analyzed in this investigation: a textile composite and three different engineering fabrics pccgPP, srPP, wrGF and cgPP (see Table 2.2 and Figure 2.1). Variability in these materials is analysed at different length-scales and, in particular for the glass fabric, following various types of handling. Nine square samples measuring 300x300 mm were carefully cut with scissors from each material. The pre-consolidated composite is frozen in place and so the cutting process has no influence on tow distribution. The srPP fabric has a small yield stress and high shear resistance at room temperature and likewise is unaffected by careful cutting; both accurately represent ‘off-the-roll’ states of the fabric. The glass fabric is very compliant and cutting introduces variability despite careful handling. One set of nine samples cut from the glass was carefully handled, and the variability measured in these sheets is a combination of off-the-roll variability plus variability due to careful cutting/handling. The other set was cut then intentionally mishandled to introduce further distortions. In doing so, the specimen shape became slightly irregular. These samples represent the result of careless handling and can be used to explore the full range of tow directional variability one might possibly see in composites manufactured textile composites.

## 3.4 Manual Image Processing and Statistical Analysis

In order to determine the statistical distribution of tow angles, hand-drawn grids following the tows of the samples (see Figure 3.1a) were used to determine the nodal coordinates of the corners of each grid-cell, using an image analysis code (*ImageJ*) [60]. Subsequently, nodal and element matrices were input into a Matlab™ code, generating a mesh consisting of quadrilateral elements (see Figure 3.1b). The angle at the left bottom corner of each cell was automatically determined and was output as a histogram (see Figure 3.2).

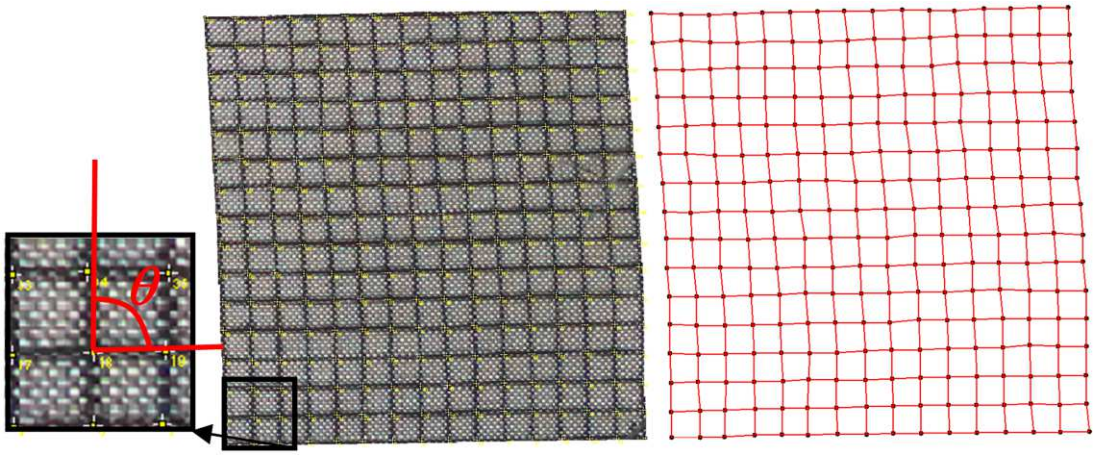


(a) (b)

Figure 3.1. (a) Image of variability in an actual 300 x 300mm textile sample (b) Image of the mesh produced from the Matlab code.

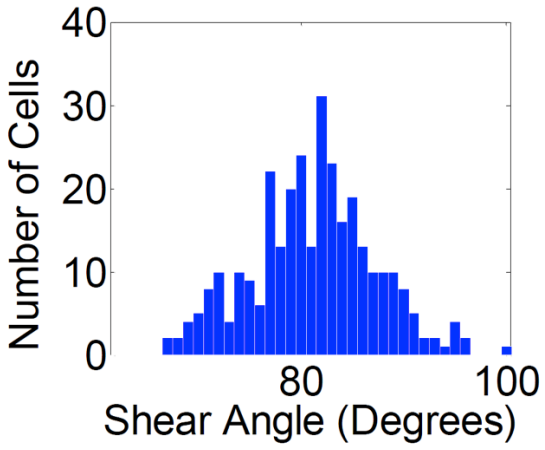


Figure 3.2. Image of typical distribution of angles from 1 of the specimens

Note that variability in the side length of the unit cell is ignored [75]. This simplification is required later when generating a regular mesh suitable for pin-jointed net kinematics.

Because the pccgPP, srPP and cgPP fabric were not distorted by cutting, the statistics of the 300 x 300mm samples could be used to produce the distribution for a ‘large’ sample measuring 900 x 900mm. On the contrary, the cutting process influenced glass fabric specimens. Discontinuities introduced in the spatial correlation of the tows at the location of the cut sample boundaries meant that statistics for a larger sample of glass fabric could not be determined from the statistics measured from the smaller samples. Normal distribution curves were fitted to the histograms of all fabrics and images of all the specimens were further subdivided to allow analysis at smaller length scales. In doing so, the global statistical variability was characterized as a function of length scale. For clarity, only the fitted distributions representing the 900 x 900 and 300 x 300mm sample sizes are shown in Figure 3.3a, 3.3b and 3.3e while only the 300x300mm sample sizes are shown in Figure 3.3c and 3.3d.

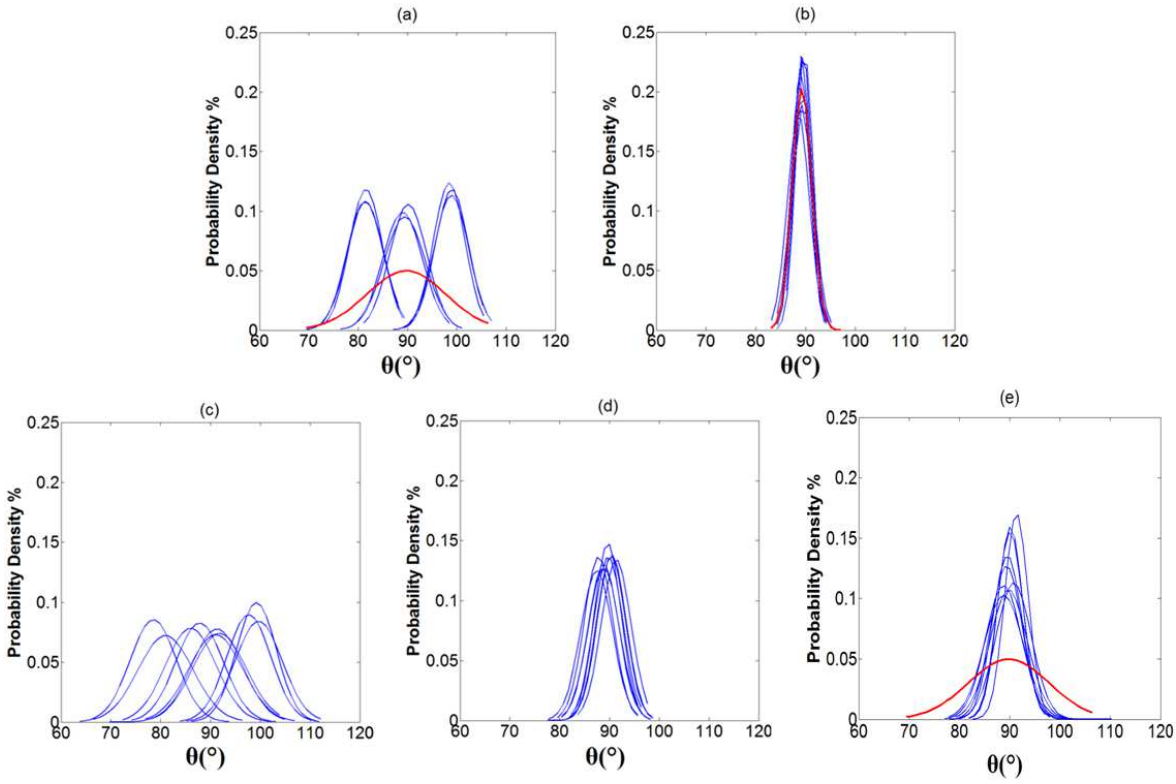


Figure 3.3. Shear angle distributions for (a) pccgPP, (b) srPP 'off-the-roll', (c) wrGF exposed to handling, (d) wrGF 'off-the-roll' and (e) cgPP

Various simple metrics can be used to characterise the statistical variability as a function of sample area. Here the standard deviation of the mean inter-tow angle versus sampling area is considered. The smallest sampling area used in this investigation is the area of the unit cells marked on the sheets, about 20 x 20mm for the composite and the srPP fabric, 16 x 16mm for the glass fabric and about 12.5x12.5 mm for cgPP. The measured inter-tow

angle of each cell is considered to be the mean value for that cell and so the standard deviation of all the means at this length scale is the standard deviation of all the cells in the entire sheet (the red distribution in Figures 3.3a, 3.3b and 3.3e). The largest subdivision of the full sheet considered here is that of the 300 x 300mm samples. The mean inter-tow angle at this scale is given by the fitted distributions for these samples. By subdividing the 300 x 300mm samples further into halves (dividing the squares using horizontal divisions), quarters and eights (again by dividing horizontally), the standard deviation at several intermediate length scales can be determined. Results for the srPP (Figure 3.4a), pccgPP (Figure 3.4b), wrGF 'off-the-roll' (Figure 3.4c) and cgPP (Figure 3.4d) fabric are plotted in Figure 3.4 (blue points).

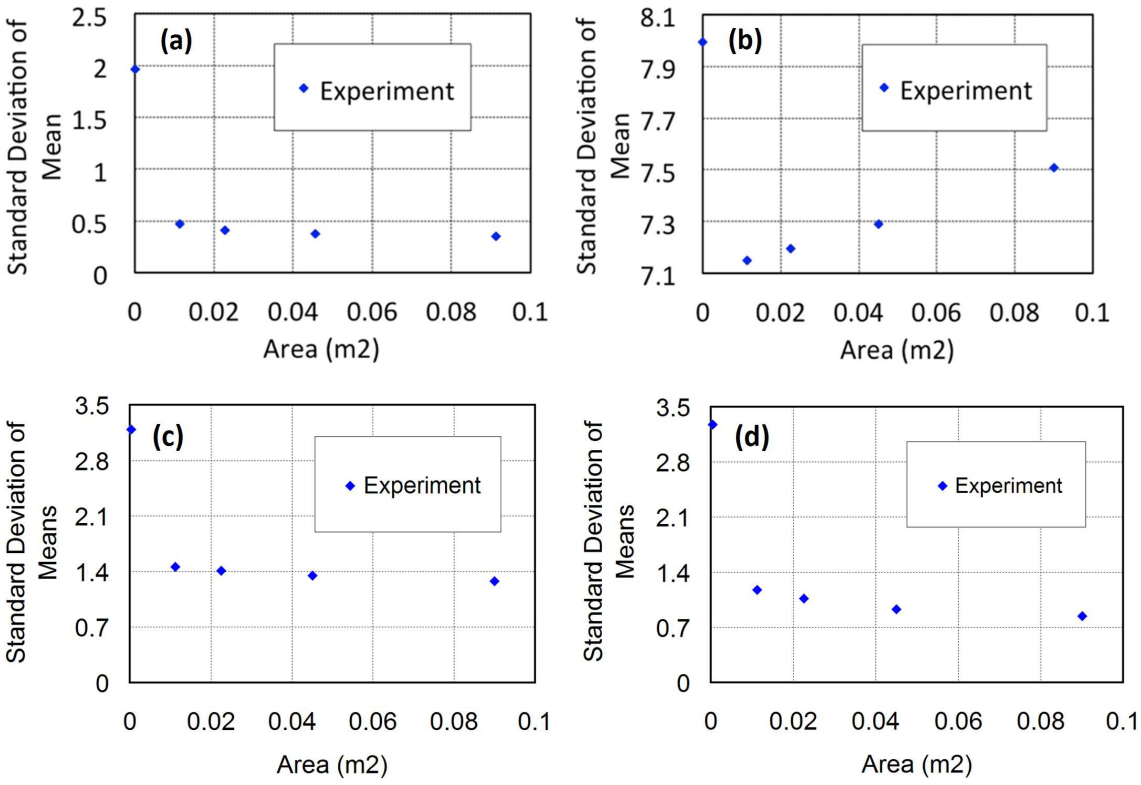


Figure 3.4. The standard deviation of the mean shear angle measured for several length scales. The smallest sampling area is that of the grid marked directly on the textile. The largest is 1/9$^{th}$ of the total area of the sheet. (a) srPP, (b) pccgPP, (c) wrGF 'off-the-roll' and (d) cgPP

In order to have confidence in the statistical data, it is important to quantify any other sources of variability that could be included in the measurements. The total measured variability is a combination of three distinct sources: (i) the error involved in determining the nodal positions on the hand drawn grid, (ii) the error involved in tracing the tow paths when drawing the grid and, (iii) the actual ‘real’ variability inherent in the sample.

Determining the latter is the objective of the analysis, while the first two sources (i) and (ii) are effectively ‘noise’ that can obscure the intended measurement.

To understand the relative importance of the noise compared to the desired measurement, a simple, two-step experiment was conducted using a pre-consolidated glass/PP specimen measuring 300 x 300 mm.

Step 1: Determining the variability inherent in measuring the nodal co-ordinates from the hand-drawn grid. To do this, the same grid was used to repeatedly determine the cell shear angle statistics of the sample on five separate occasions. As the sample is a solid composite and the same grid was used on each occasion, the same cell statistics should be reproduced in each set of measurements. Thus, any variability in the statistical results, such as in the average shear angle of the sample, can be attributed entirely to source (i) as described above.

Step 2: Determining the combined variability inherent in both measuring the nodal co-ordinates from the hand-drawn grid and in drawing the grid on the sample. To do this, a grid was drawn on the sample, the nodal coordinates were measured as described above then the grid was wiped clean from the specimen. The process was repeated five times. Variability in the statistical results, such as in the average shear angle of the sample, following this procedure is a result of both sources (i) and (ii) above. By comparing the results of Steps 1 and 2 and also the statistical results taken from different physical samples (e.g. Figure 3.4), an understanding of both the noise and the real sample variability can be determined. Figure 3.5a shows the average shear angle in each grid-cell (numbered 1–120), measured in Step 1 while Figure 3.5b shows the same data measured from Step 2. The error bars indicate the standard deviation of the shear angle calculated from the five different measurements on a given cell. Results can be analysed at both large and small length scales. At the large scale, the mean shear angle determined from all five measurements of the average shear angle across the specimen is 97.571°. The standard deviation of these 5 average results is 0.013°. This can be compared to equivalent measurements of 97.724° and 0.164° determined in Step 2. As expected more variation appears in Step 2 compared to Step 1. These standard deviations can be compared to those measured between different physical samples; for the least variable material srPP this is

around 0.4°, see Figure 3.4a while for the most variable material pccgPP this is around 7.5°. Thus, for the larger area measurements, it can be stated that most of the measurement noise comes from drawing the grid onto the specimen. For the least variable material this noise is significant, contributing about 40% of the measured signal, while for the most variable material the measurement noise is insignificant, contributing about 2% of the measured signal. Looking at the smaller scale, it is clear from Figure 3.5 that the error in determining the shear angle in any given cell is relatively large. The average standard deviation in the cell shear angle measurements found in Step 1 is 2.23° whereas in Step 2 it is 2.58°. This indicates that almost 90% of the noise at the smaller length scale comes from source (i). This is apparent in Figure 3.1 which shows the woven fabric and equivalent mesh side by side, and reveals a similar but inexact fit. This small scale noise is also apparent in Figure 3.4, indicated by the sharp rise in the standard deviation at the smallest length scales. The reason why this variability vanishes at the larger scale is that the error cancels when averaged over larger areas. For example, if the shear angle measured in one cell is too large due to the in correct positioning of a nodal point, this produces an equal and opposite change in the shear angle in the neighbouring cell and, when angles are averaged together, the error cancels. This means the average shear angle taken over a number of cells is insensitive to type (i) error. This explains why the standard deviation of the average shear angle is relatively small when considering larger areas.

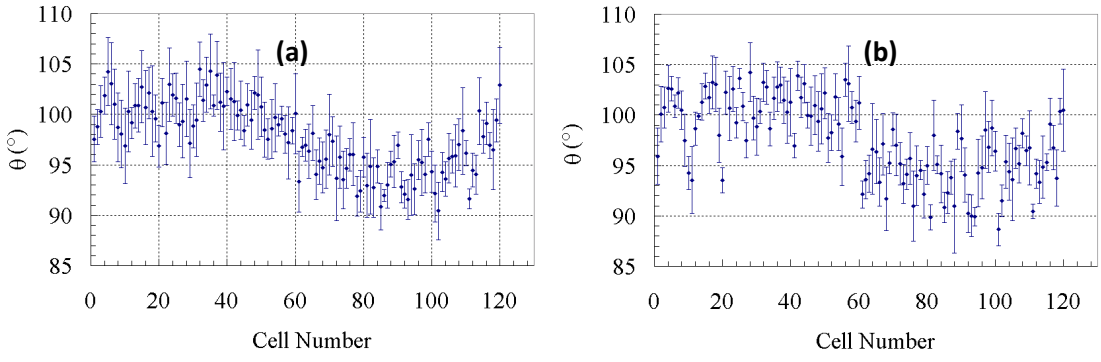


Figure 3.5. Statistical measurements of the shear angle in cells 1 to 120 of a grid marked on a pre-consolidated glass/PP specimen measuring 300 x 300 mm (a) the grid was marked on the specimen once, and shear angles were determined 5 times (b) the grid was marked on the specimen, shear angles were determined, the grid was wiped off of the specimen, the process was repeated 5 times. Error bars in both (a) and (b) indicate the standard deviation of the 5 measurements in each cell.

## 3.5 Automated Mesh Generation

A MatLab code MeshGen code [74] was designed to produce finite element meshes consisting of mutually constrained truss elements (representing the high tensile stiffness fibres) and membrane elements (representing the shear properties of the fabric) as that described in [76], suitable for use in finite element forming simulations written previously at the University of Glasgow, predominantly by [68]. The code is based on a kinematic algorithm that uses the same geometry-based mathematics as other pin-jointed net kinematic codes [74]. The code produces variability by introducing variable horizontal stretching/contraction of elements along the horizontal centreline of the mesh (see Figure 3.6a). In this section a brief overview of the functionality of this code is provided as MeshGen provides the starting point for novel work conducted on the topic of variable mesh generation in this thesis. The MeshGen code is able to produce three blank shapes (rectangle, circle and polygon) with regular (no variability) and irregular (with variability) meshes using a range of orientations of the principal material directions.

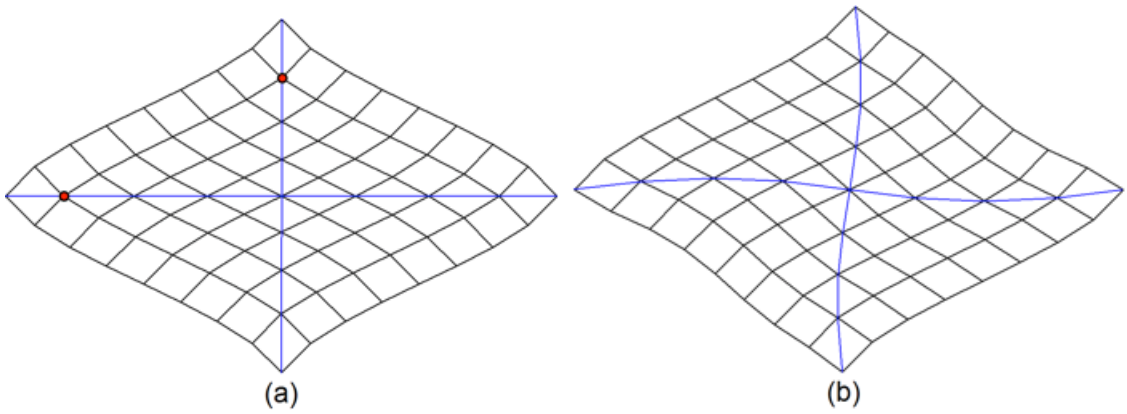


Figure 3.6. (a) Mesh with horizontal stretching of elements along the centreline. In this instance there is no vertical perturbation of nodes along the horizontal centreline [68] (b) Mesh with both horizontal stretching of elements along the centreline and a vertical and lateral perturbation along the nodes of the horizontal and vertical centrelines.

A mesh is generated from the origin outwards. From this large mesh a region with arbitrary perimeter shape can be selected at arbitrary positions (see Figure 3.7).

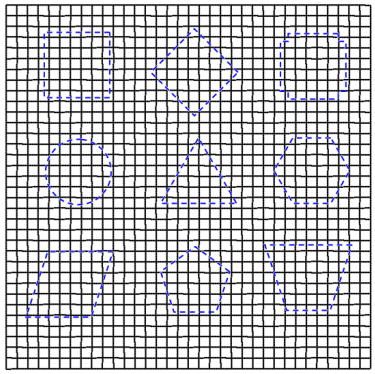

Figure 3.7. Selected regions that can be cut out of the larger mesh

An enhanced version of the code has been developed and named Varifab. The Varifab code produces variability by introducing additional perturbation of the nodes along the length of the horizontal and vertical centrelines as shown in Figure 3.6b, which shows clearly that the vertical and the horizontal centrelines are wavy, whereas the centrelines shown in Figure 3.6a are straight lines. Further improvement on the Varifab code has been carried out using simple genetic algorithm to automatically reproduce the actual variability measured from real textiles. The genetic algorithm code name is Varifab$^{GA}$. The starting point for mesh generation performed in this thesis is the MeshGen code [68, 69], though significant enhancements to the code have since been implemented during this work. The aim of enhancing MeshGen was to produce a software capable of automatically predicting realistic stochastic fibre angle distributions similar to those reported in Section 3.5. The first task was to understand the source code for MeshGen written in the MatLab programming environment. This proved challenging due to the absence of clear supporting documentation. Following study of the code, a single coherent explanation of the theory governing the original algorithm proved possible, the latter is presented, together with a description of the new enhancements implemented in MeshGen in this section.

The first enhancement of the MeshGen code performed in this work was to introduce additional perturbations of the nodes along the length of the horizontal and vertical centerlines (see Figure 3.6b). The new code Varifab developed by the author was to reflect the new variable nature of the meshes that could be predicted using the code following the enhancements performed in this work. Varifab produces variability by two methods (see Figure 3.6): (a) by introducing horizontal stretching/contraction of elements along the horizontal centerline of the mesh [69] and (b) by introducing additional perturbations of

the nodes along the length of the horizontal and vertical centrelines. The intention is to use these meshes in forming simulations such that the two directions of material anisotropy are aligned along the sides of the elements in the mesh e.g. [34, 75, 88, 89].

Perturbations of type (a) and (b) are transmitted to the rest of the mesh via pin-jointed net kinematics. Changing the amount of stretching, and the amplitude and wavelength of the perturbations can control the degree of variability. A mesh containing this variability is generated from the origin outwards. From this large mesh a region with arbitrary perimeter shape can be selected at arbitrary position (see Figure 3.7). This latter feature permits further control of the variability within the mesh.

The follows subsections show the implementations of the two codes 'MeshGen' and 'Varifab'. Implementation of stretching of mesh (MeshGen), implementation of perturbation of mesh by the author 'Varifab' and implementation of genetic algorithm by the author 'Varifab$^{GA}$'.

### 3.5.1 Implementation of stretching of mesh in MeshGen

The side length of the elements, $\Lambda$, and position of the perimeter of the mesh are variables input by the user. The degree of stretching/contraction along the horizontal centerline is also controlled by the user by specifying the diagonal length, $\mu_{\Delta}$, of elements at the centre of the mesh (see Figure 3.8a). Note that $\Lambda \leq \mu_{\Delta} \leq 2\Lambda$. Coordinates of nodes on the outermost upper left edge (indicated by filled red points in Figure 3.8) are determined using Eqs (3.1) and (3.2):

$$X = \begin{bmatrix} \left(-2\sum_{i=1}^{n} a_n(i)\right) \\ \left(-2\sum_{i=1}^{n} a_n(i) + a_n(n)\right) \\ \left(\left(-2\sum_{i=1}^{n} a_n(i) + a_n(n)\right) + a_n(n-1)\right) \\ . \\ row(n) + a_n(1) = S_a \\ S_a + a_n(1) \\ (S_a + a_n(1)) + a_n(2) \\ . \\ (row(2n) + a_n(n)) \end{bmatrix} \tag{3.1}$$

$$Y = \begin{bmatrix} (0) \\ (0 + b_n(n)) \\ ((0 + b_n(n)) + b_n(n-1)) \\ . \\ row(n) + b_n(1) = S_b \\ S_b + b_n(1) \\ (S_b + b_n(1)) + b_n(2) \\ . \\ (row(2n) + b_n(n)) \end{bmatrix} \tag{3.2}$$

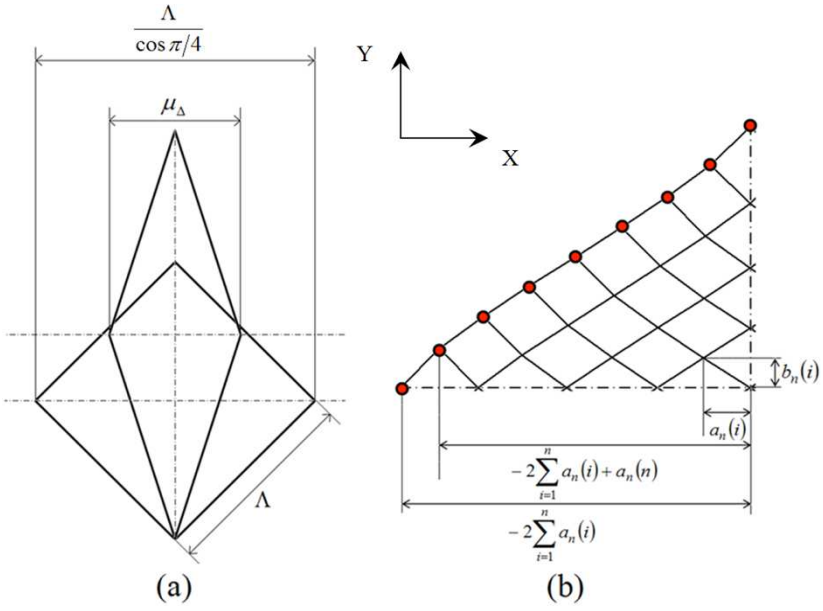


Figure 3.8. Varifab's geometrical parameters of (a) sketch of stretched sheet of fabric, (b) regular and irregular fabric unit cell.

where *X* and *Y* are arrays that are added to a matrix containing all the nodal coordinates of the expanding mesh (see Figure 3.6), *n* is the number of elements from the centre of the blank to either the right, left, top or bottom edge of the mesh (e.g. in Figure 3.6, *n*=4), *i* is the node number when counting outwards from the centre of the blank towards the outer edge of the mesh along the vertical or horizontal mesh centrelines (e.g. *n* = 3 for those nodes marked in red in Figure 3.3a) $a_n$ is an array containing the half lengths of the horizontal diagonal element lengths (see Figure 3.8b).

$$2a_n = \left\{\left(\mu_\Delta - \sqrt{2}\Lambda\right)\varepsilon_{k+1} + \sqrt{2}\Lambda\right\} \tag{3.3}$$

$b_n$ is an array containing the half lengths of the vertical diagonal element lengths (see Figure 3.8b):

$$2b_n = \sqrt{\frac{\Lambda^2 - {a_n}^2}{4}} \tag{3.4}$$

and $\varepsilon_i$ is an array defined by Eq (3.5) which gradually decreases the stretch/contraction of the elements towards 0 when moving from the centre towards the left corner of the mesh

$$\varepsilon_{k+1} = \sqrt{1 - \left(\frac{k}{n-1}\right)^2} \text{ , } k = 0,1,\cdots,n-1 \tag{3.5}$$

where $n \geq 3$. So far in this description, the horizontal and vertical diagonals of the cells (the blue lines in Figure 3.6) remain straight, leading to a limited degree of variability in the resulting mesh.

### 3.5.2 Implementation of enhanced perturbation of mesh in VariFab

To increase the degree of variability, a perturbation can be added to Eqs (3.1) and (3.2). The wavelength and vertical amplitude of the perturbation is controlled using a sinusoidal function:

$$\delta_k(t) = A\sin(\omega_k t) \tag{3.6}$$

where *A* is the peak amplitude of the perturbation and $\omega_k t$ controls the periodicity of the perturbation. The value of *t* can lie between 0 and 5 and controls the wavelength of the perturbation and $\omega_k t$ is an array;

$$\omega_k = \frac{k\pi}{j-1}, \quad k = 0,1,2... \; j-1 \tag{3.7}$$

of size equal to the number of all nodes within the blank (number of nodes= *j*). The perturbed (*x*,*y*) coordinates of each node can be determined using Eqs. (3.8) and (3.9)

$$X_{pert} = X_k + A\sin(\omega_k t) \tag{3.10}$$

$$Y_{pert} = Y_k + A\sin(\omega_k t) \tag{3.9}$$

where

$$0 \le A \le \left( \frac{X_{\max} - X_{\min}}{10} \right) \qquad 1 \le \omega t \le 5\pi$$

where $X_k$ and $Y_k$ are coordinates of nodes across the entire mesh, which are determined by a mapping technique once the upper left corner has been generated as described in Section 3.2.

### 3.5.3 Implementation of genetic algorithm to create VariFab$^{GA}$

An important goal of this work is to ensure that variability generated by the code accurately reflects the actual variability measured from real textiles (see Figure 3.4). To this end, 'Varifab$^{GA}$' has been designed using a genetic algorithm to automatically reproduce the same statistical distribution and spatial correlations of shear angles observed in actual engineering fabrics and textile composites. Six parameters are explored by the code including the stretched/contracted horizontal diagonal length, coordinates for the origin of the mesh and the amplitude and period of the perturbation. According to conventional genetic code nomenclature, any given set of input parameters is named an, 'individual', 'chromosome' or 'state' [90]. The chromosomes are thus comprised of a single row array including the parameters mentioned above. Each individual in a chromosome is named a 'gene' and is generated at random to lie within a predetermined range. Determination of the best individual chromosome from an arbitrary number of first generation chromosomes (typically 50) is based on selection criteria that use so-called 'fitness' or 'objective' functions [90]; see Eqs (3.10 & 3.11). These functions are used to reproduce a blank with the same statistical global variations as the measured data. The first fitness function is based on the mean inter-tow angle across the sheet:

$$FT_{mu} = \left| \frac{mu_m - mu_p}{mu_m} \right| \tag{3.10}$$

where $FT_{mu}$ is the fitness function of the mean of the angle across the sheet, $mu_m$ is the measured mean across a given specimen and $mu_p$ is the predicted mean for a mesh of the same area. The second function is based on the standard deviation of the means measured at various length scales, as discussed in Section 3.5.

$$FT_{std} = \left| \frac{std_m - std_p}{std_m} \right| \tag{3.11}$$

where $FT_{std}$ is the fitness function for the standard deviation of the mean inter-tow angle for a given sampling area, $std_m$ is the measured value of this quantity and $std_p$ is the predicted value of this quantity. By summing the fitness functions (Eqs 3.10 & 3.11) the best individual is selected by choosing the one with the smallest total value, a reproduction technique known as the Mutation technique [90]. As shown in Figure 3.9 the red spot indicate the statistics that obtained from characterising the variability (the standard deviation of the shear angle as function in the mean of the shear angle $std_m = f(mu_m)$), the blue stars are the first generation chromosomes, the green stars are the updated second generation chromosomes and the small yellow spots are the discarded second generation chromosomes. The second generation chromosomes are keeping updated until the two criteria are satisfied (Figure 3.9). The time of convergence is based on the number of stopping criteria and the complexity of the problem. The flow chart of 'Varifab$^{GA}$' is shown in Figure 3.10.

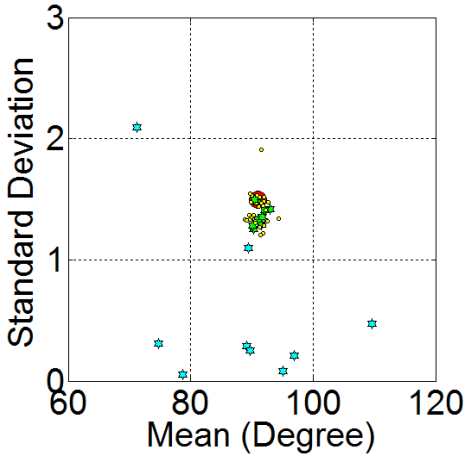


Figure 3.9. First and second generation chromosomes generation and updating

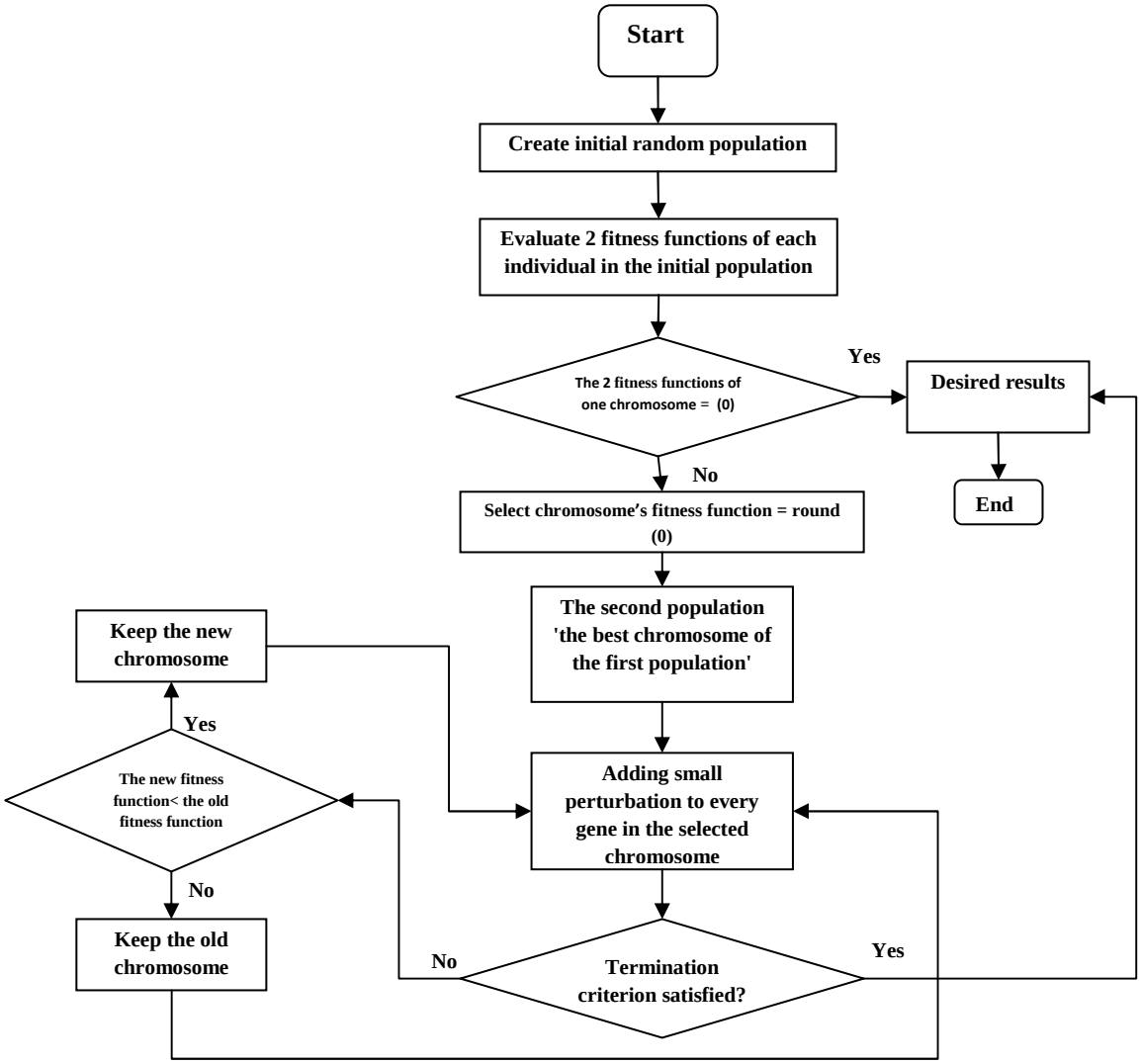


Figure 3.10. Flowchart process of VariFab$^{GA}$

In this work, two fitness limit criteria have been considered, Eqs. (3.12 & 3.13).

$$FC_{mu} = \left| mu_m - mu_p \right| \tag{3.12}$$

$$FC_{std} = \left| std_m - std_p \right| \tag{3.13}$$

where $FC_{mu}$ is the criterion of the mean and $FC_{std}$ is the criterion of the standard deviation. Eqs (3.11 and 3.13) can be used to incorporate data across various length scales. When analyzing the large 900 x 900mm sheets of glass/PP composite and srPP fabric, convergence has been obtained when up to 3 fitness functions have been used in any one simulation. In each case, two primary fitness functions, Eq (3.10) and Eq (3.11), involving data measured at the smallest scale, have been used together, with one more fitness function also based on Eq (3.11) but using data measured at a larger scale [90-96].

## 3.6 Comparison of experimental and numerical results

Comparison of experiment (Figure 3.4) and numerical predictions is shown in Figure 3.11. Excellent agreement (< 0.066 % difference in global statistical measures) is achieved when the two primary fitness functions plus a 3rd fitness function, based on the standard deviation of means of the 300 x 300, or 300 x 150mm sampling sizes, is used. When the 3rd fitness function is based on smaller sampling sizes (150 x150mm or 150 x 75mm) the convergence is less accurate. Comparison between the glass/PP composite and two predictions is shown in Figure 3.12. Results show similar long-range correlations in the variability, with the glass/PP composite possessing a wavelength and amplitude of about 900mm and 25mm while the two predictions have wavelengths and amplitudes of 660mm and 23mm and 1160mm and 36mm, respectively. Error bars (standard deviation of 4 measurements) show both these parameters vary across the sheets. Results demonstrate that the pin-jointed net kinematic coupled with the global statistics imposes a strong restriction on possible deformations, resulting in the prediction of realistic tow orientations across the sheet. As more fitness functions are added, the code becomes more deterministic and convergence becomes more difficult. To compensate, further possible modes of deformation could be added to the code, for example, by using a spectral expansion of several arbitrary wavelengths and amplitudes to determine the perturbation. This would allow the simultaneous use of more target functions to capture more information. More deformation modes would also improve the convergence. This is deferred to future work.

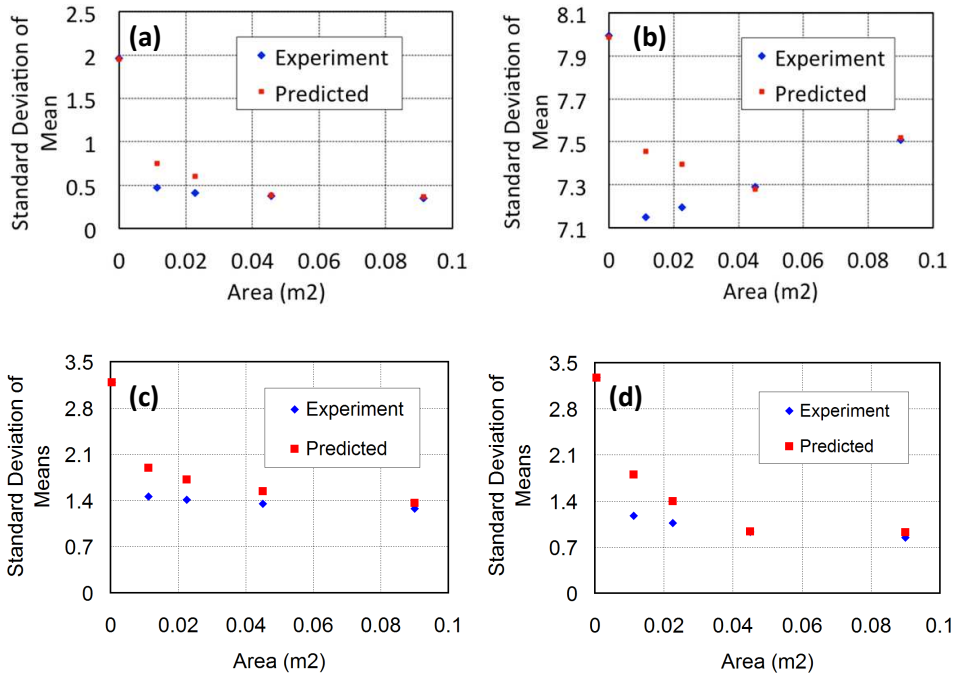


Figure 3.11. The measured results (Figure 3.4) compared aginst the predicted results (a) srPP, (b) pccgPP, (c) wrGF 'off-the-roll' and (d) cgPP

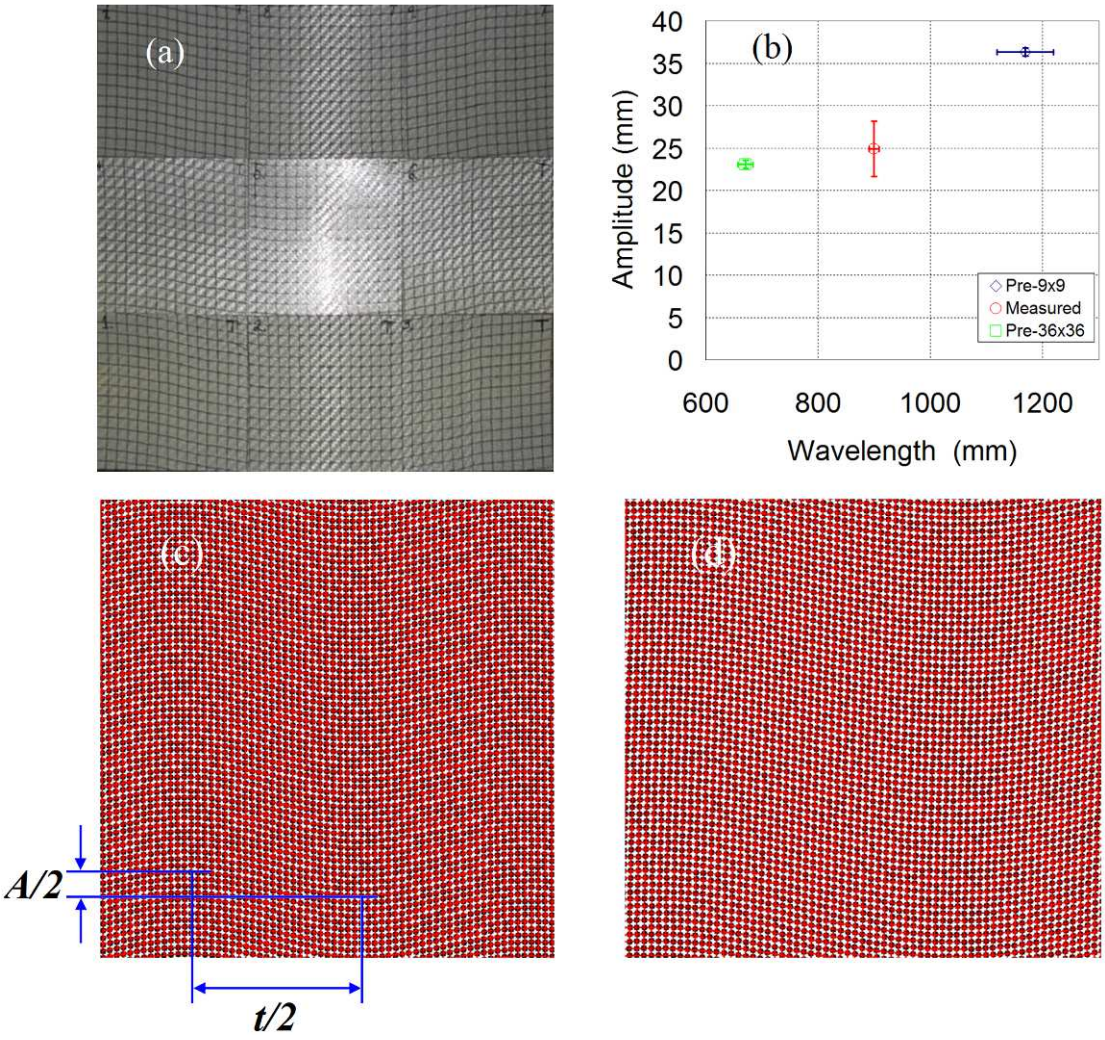


Figure 3.12. Example of tow directional variability in (a) 300 x 300 mm specimens pccgPP reassembled into a large sheet (b) wavelength and amplitude measured from figure 3.12 (a), 3.12 (c) and 3.12 (d), (c) prediction using the two primary functions with the 3rd based on the 300 x 150mm sample size (d) prediction using the two primary functions with the 3rd based on the 300 x 300mm sample size.

As a second comparison, Figure 3.13a shows a mesh predicted using statistics measured from one of the mishandled 300 x 300 mm glass specimens (see Figure 3.3d), for which the mean inter-tow angle is about 100°. Figure 3.13b shows the comparison between the measured and fitted statistics (circular points) along with the statistics of the predicted mesh (blue line). Good agreement between the measured and predicted variability is again achieved. Repeating simulations produces different meshes but with equally good fits to the measured statistics.

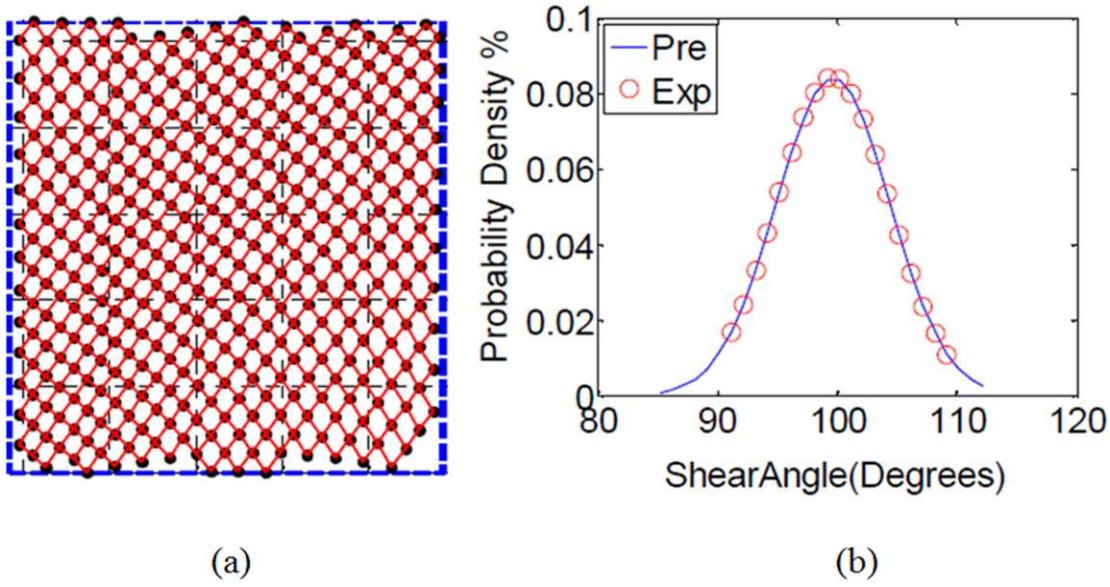


Figure 3.13. (a) Image of mesh with same distribution as one of the distributions shown in Figure 3.1 (b), (b) Experimental statistics (circles) used to generate Figure 3.1 with the predicted numerical distribution.

## 3.7 Semi-Automated Image Processing Method

### 3.7.1 Introduction and Review of Previous Work

The manual image analysis discussed in Section 3.5 of this chapter is a time consuming technique because the three steps of the manual procedure for 300 x 300 mm specimen consume the following time: hand-drawn grids following the tows of the samples (see Figure 3.1a) take about one hour, determining the nodal coordinates of the corners of each grid-cell (using e.g. *imageJ* software [60]) take about 45 minutes, and generating the nodal and element matrices take about 30 minutes. To decrease the effort and time, and to increase the accuracy, automating this process is necessary. A few researches related to this problem have been carried out previously [75, 86].

The technique that was used by Skordos and Sutcliffe [75] to determine the orientation variability across the surface of a carbon/epoxy 5-harness woven prepreg can be considered as a semi-automated technique, since lines have been drawn (on the centre of each image of the four hundred and sixty images on a 23x20 grid with 15mm spacing images), and superimposed on the tows at the centre of the images as the first step. Then the orientation was obtained automatically using the Fourier transform approach. Fourier

transforms of the grey-scale image provided initial estimates of local tow directions, and subsequent correlation techniques were used to refine this estimate and characterise tow spacing over small areas of just a few unit cells.

On the other hand, Gan, et al. [86] used a fully automated method to investigate the variability in tow orientations, tow width and tow spacing of three types of composite reinforcements: randomly orientated chopped strand mat, a balanced plain weave fabric and a biaxial stitched fabric. The method is based on converting the colour images to gray-scale images (in which the pixels are within the range of 0 - 225) to simplify the process, and then partitioning the source intensity (the intensity of the whole image) to transmitted intensity and blocked intensity using the gray thresh command available in Matlab. The transmitted intensity is the bright intensity of the spaces between the tows and the blocked intensity is the darker intensity of the crossed tows. From the blocked intensity of the tow cross-over regions, the tow orientation were determined by considered each tow cross over region as one separate node, and then the spatial orientation was determined from the position of the adjacent nodes as shown in Figure 3.14c.

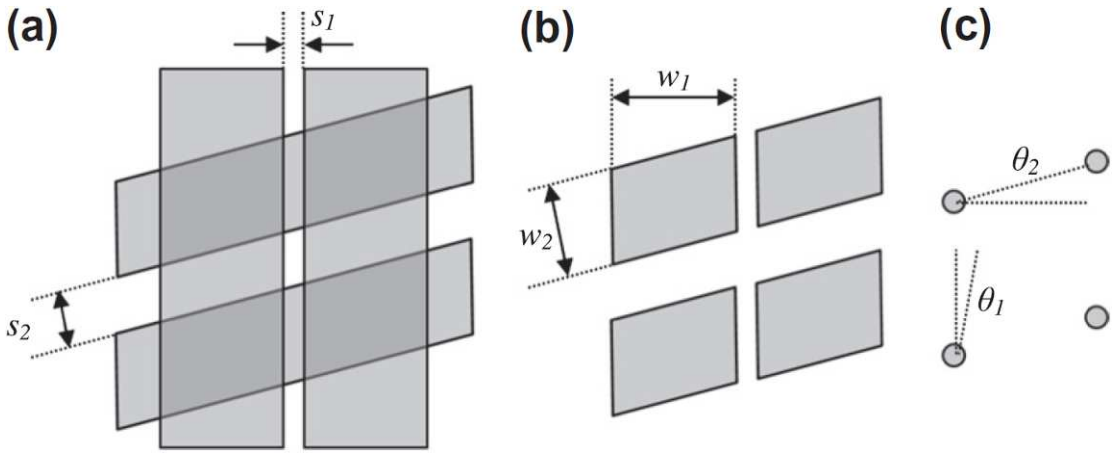


Figure 3.14. Procedures for determining tow width, spacing and orientation automatically (a) a gray-scale of plain weave fabric, (b) subtracting the cross-over regions and determining the tow width and spacing, (c) The nodes obtained from the tow cross over regions.

In this work, a semi-automated method has been developed to reduce efforts and time, and to increase accuracy. A numerical code, 'PreMesh', has been written within Matlab$^{TM}$ to characterize full-field variability of the tow directions across flat sheets of biaxial engineering fabrics and woven textile composites. The name semi-automated comes from the fact that the step of determining the coordinates at each corner of each unit cell (see

Figure 3.1a) and the step of generating the nodal coordinates of the corners of each grid-cell are automated and takes about one hour to complete. However, the step of drawing points rather than lines is a manual process that uses Paint software [97] as described in Section 5.1 of this chapter (see Figure 3.15). Although there is no significant difference in the time duration between the two methods, the semi-automated method saves effort in determining the coordinates at each corner of each unit cell, and the step of generating the nodal coordinates of the corners of each grid-cell.

The periodic structure of engineering fabrics is a key element for characterising variability based on detecting the edges of each unit cell using edge detecting methods [98-100]. In order to do this, an edge detection operation is introduced in the 'PreMesh' Matlab code.

While some fabrics show large contrast when photographed, making it possible to view the textile architecture easily, others show much less obvious patterns, as shown in Figure 3.15. For the fabric shown in Figure 3.15a the characterization process of the orientation variability might possibly be fully automated i.e. the coordinates of every unit cell might possibly be detected through edge detection. However, other types of fabrics are much less distinct showing no clear periodic structure (see Figure 3.15b for example). As a result, the variability characterization process for textile composites and engineering fabrics can be difficult. Here, a semi-automated method is developed and has been found to reduce manual effort by approximately 66% percent when compared to the fully manual process described in Section 3.5.

**(a)** 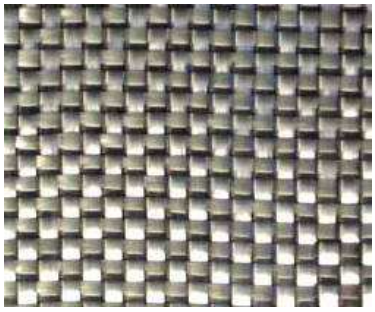 **(b)** 

Figure 3.15. (a) Warp and weft of different colour or intensity [50] (b) fabric of blur image, distinguishing the warp and weft is difficult ( Figure 2.1 (d) pccgPP)

### 3.7.2 Background Theory of Edge Detection

The operation of detecting the edges of an image is based on manipulating the basic unit in an image, a 'pixel'. The numeric characteristics of an image are the number of pixels that are processed in the computer memory as bytes (8bits/bytes). The image can be in grey or colour scale. Images with grey scale consist of {0 – 255} – one byte/pixel, whereas images with colour scale consists of red, green and blue colours with – three bytes/pixel (RGB of values 0 - 255). Edges in an image are distinguished by several factors, for example disconnection between surfaces, intensity of grey scale and lighting disconnection [99, 101, 102]. As shown in Figures 2.1b, 2.1c, and 3.15a, warps always appear very light while wefts always have a dark gray character. By taking into account this fact, an image can be de-composed into two threshold images namely: warps and wefts.

The techniques of determining edges in an image are the first and second derivative techniques. The first derivative of pixels across an image results in detecting the edges in the image from the pixels with values greater than the specified threshold. The simplest edge detection operation is based on grey scale gradient. The gradient of the intensity function *I* of an image is presented by the first derivative vector $\nabla I = \nabla f(x, y)$ [40].

$$\nabla I = \begin{bmatrix} \frac{\partial I}{\partial x} \\ \frac{\partial I}{\partial y} \end{bmatrix} \tag{3.14}$$

where $\frac{\partial I}{\partial x}$ is the first derivative of the intensity function in the x direction in an image and $\frac{\partial I}{\partial y}$ is the first derivative of the intensity function in the y direction. The magnitude of the intensity function is given below as:

$$|\nabla I| = |\nabla f(x, y)| = \sqrt{\left(\frac{\partial f(x, y)}{\partial x} i_x\right)^2 + \left(\frac{\partial f(x, y)}{\partial y} i_y\right)^2} \tag{3.15}$$

The orientation $\theta$ expresses the degree of the intensity of the edges.

$$\theta = \arctan\left(\frac{\frac{\partial f(x,y)}{\partial y} i_y}{\frac{\partial f(x,y)}{\partial x} i_x}\right) \tag{3.16}$$

Robert's Cross operator is considered to be the simplest and the quickest 2D spatial approximation gradient operator on an image [103]. The convolution kernel, which is a matrix of principles that identify how the adjacent pixels effect a given pixel's state in an image's edges, gives a good approximation of the derivatives of the operator as shown below [41, 42].

$$\frac{\partial f(x,y)}{\partial x} = \begin{bmatrix} 0 & 1 \\ -1 & 0 \end{bmatrix} \tag{3.17}$$

$$\frac{\partial f(x,y)}{\partial y} = \begin{bmatrix} 1 & 0 \\ 0 & -1 \end{bmatrix} \tag{3.18}$$

For higher grey scale, Prewitt operators are used. The 3x3 convolution kernels are shown below [102, 104, 105].

$$\frac{\partial f(x,y)}{\partial x} = \begin{bmatrix} -1 & 0 & 1 \\ -1 & 0 & 1 \\ -1 & 0 & 1 \end{bmatrix} \tag{3.19}$$

$$\frac{\partial f(x,y)}{\partial y} = \begin{bmatrix} -1 & -1 & -1 \\ 0 & 0 & 0 \\ 1 & 1 & 1 \end{bmatrix} \tag{3.20}$$

Sobel operation is also used to detect edges on higher grey scale and for edges running on horizontal and vertical directions [104-106].

$$\frac{\partial f(x,y)}{\partial x} = \begin{bmatrix} -1 & 0 & 1 \\ -1 & 0 & 2 \\ -1 & 0 & 1 \end{bmatrix} \tag{3.21}$$

$$\frac{\partial f(x,y)}{\partial y} = \begin{bmatrix} -1 & -2 & -1 \\ 0 & 0 & 0 \\ 1 & 1 & 1 \end{bmatrix} \tag{3.22}$$

### 3.7.3 Methodology of Semi-Automated Technique

The first step of characterising the inherent variability of any engineering fabric using the semi-automated method is by cutting a square piece of engineering fabric to an appropriate size, and drawing points on each corner of the unit cells as shown in Figure 3.16. Drawing the points can be done directly on the fabric using marker pen or by taking a photo and then drawing points using MS Paint (Microsoft Paint software) [106].

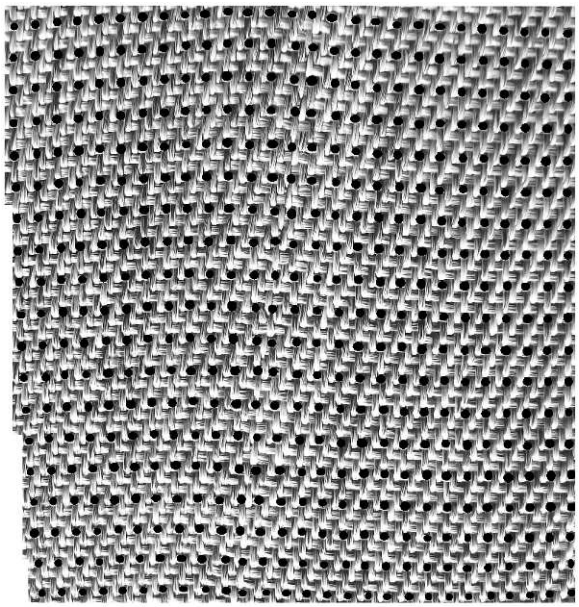

Figure 3.16. Drawing points on the crossed yarns of woven roving glass fabric sheet

Images can be in colour or grey scale as mentioned earlier; non-grey scale image consists of three colour matrices, each matrix correspond to three intensities for each pixel: red, green and blue intensities. The second step is converting images from colour scale to gray scale by detaching the green intensity of every pixel and these results in a gray scale image with intensity that is represented between 0 and 225. The conversion of the image has been conducted by using ***rgb2gray*** function available in Matlab, and then the brightness was increased to a higher level by multiplying the greyscale matrix (I) by an appropriate factor. This was done to hide all the features of the material and show the black spots (see Figure 3.17).

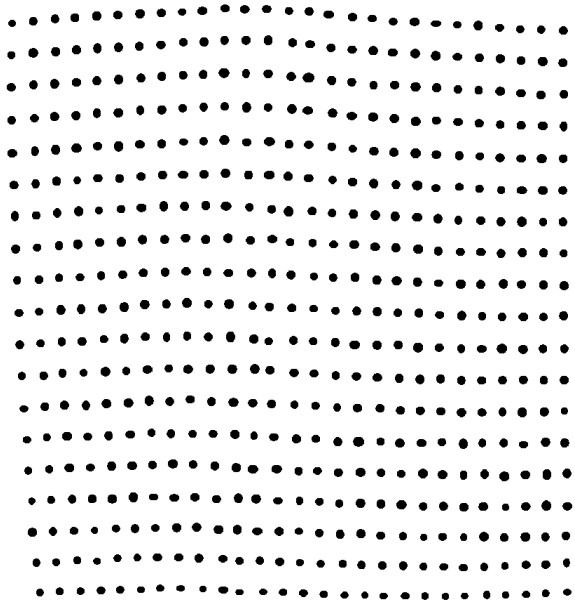

Figure 3.17. Increasing the brightness of woven sheet's image to a suitable level

In order to determine the edges of the black points, the 'Roberts Cross edge detecting method' has been used; a differential operator method initially proposed by Bovik [107]. The Robert's operator is based on the gradient magnitude, see Eq. (3.14). The kernel masks, Eqs (3.17) and (3.18), are applied on the greyscale image. Well-defined edges are detected by considering the following properties: (i) image's edges and background should be obvious i.e. very little or completely no noise is contributed and (ii) an appropriate level of intensity for the edges should take place i.e. the level of the intensity of edges in an image must be as apparent as possible for recognition by human vision [69].

Once the edges are detected (see Figure 3.18), determination of the central coordinate of each circular point has to be carried out using *bwboundaries*, a pre-defined function available in Matlab$^{TM}$. This function is used to determine the coordinates of each point on the outer perimeter of a given region in a binary image.

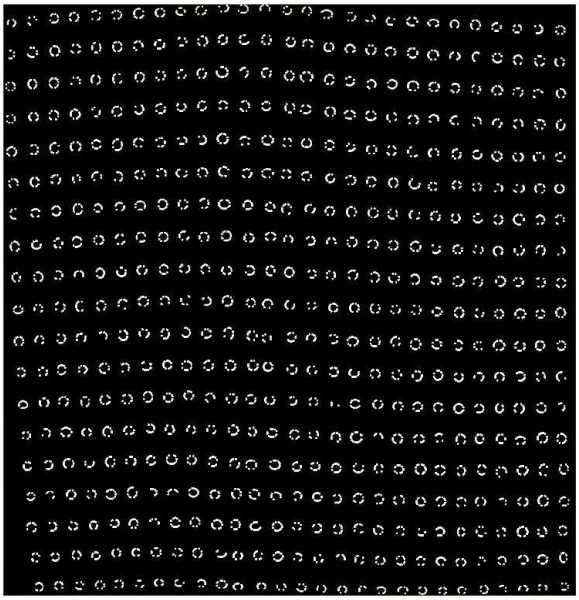

Figure 3.18. The binary image and the detected edges of the points.

Next, an average of the coordinates of all points surrounding the perimeter of the approximate circular shape was calculated to obtain a single coordinate at the centre of the shape. These co-ordinates represent corner nodes of quadrilateral elements (see Figure 3.19). Using the nodal points, the node and element matrices were determined to create a mesh. Using this information, the mean and the standard deviation of the shear angle could be calculated. The programming steps of the 'PreMesh' code are shown in the flow chart in Figure 3.20.

The statistics of two 300 x 300mm samples of cgPP fabric exposed to frequent handling were characterized using the semi-automated method and the manual image processing method. Normal distribution curves of the semi-automated method and the manual image processing method were fitted to the histograms of the two samples as shown in Figure 3.19. As can be seen from Figure 3.21, there is a significant difference of the probability density and the standard deviation of the shear angle between the manual and semi-automated method. However the mean of the shear angle of the two methods are close. These differences are attributed to the method of determining the coordinates of each black spot in Figure 3.16. The semi-automated method is more accurate in determining the coordinates since it based on averaging the coordinates of all the points at the edges of each geometrical shape, which is the result of the edge detection method (see Figure 3.18) and this results in a single point at the centre of the geometrical shape. However, since the

manual method of assigning the coordinate of each black spot is based on the user's focus and skills, the coordinates are more difficult to determine accurately.

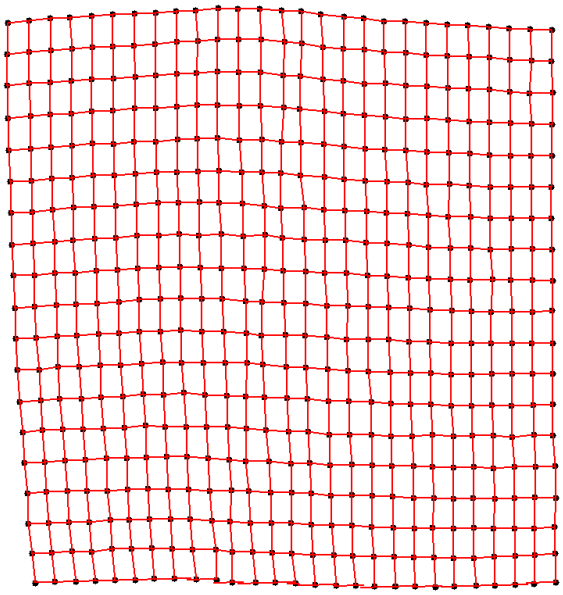

Figure 3.19. Image of the mesh produced from the MatLab code PreMesh

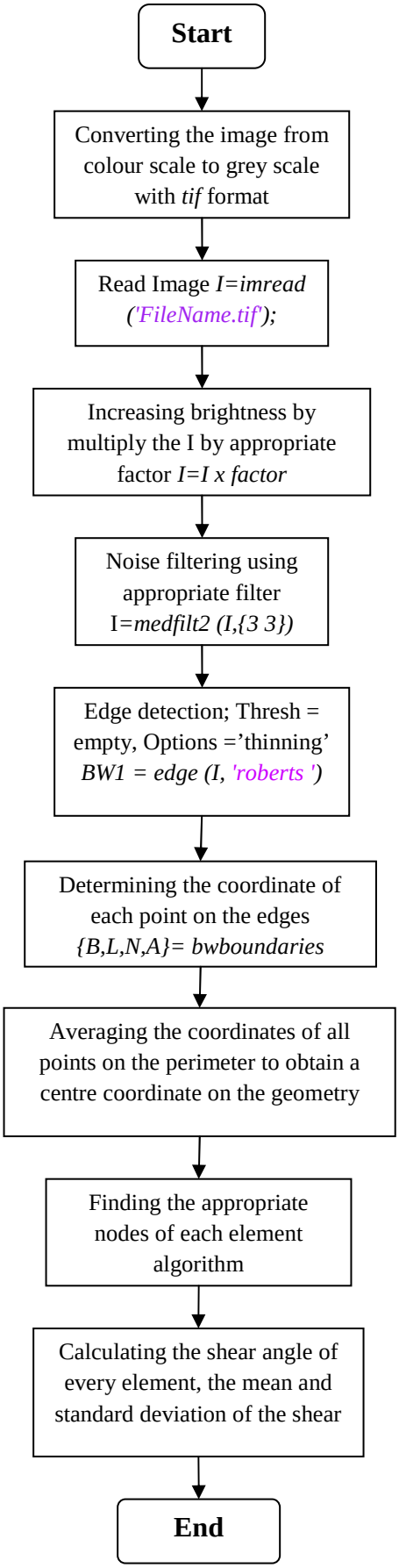


Figure 3.20. The flow chart of edge detection process using Roberts edge detection method

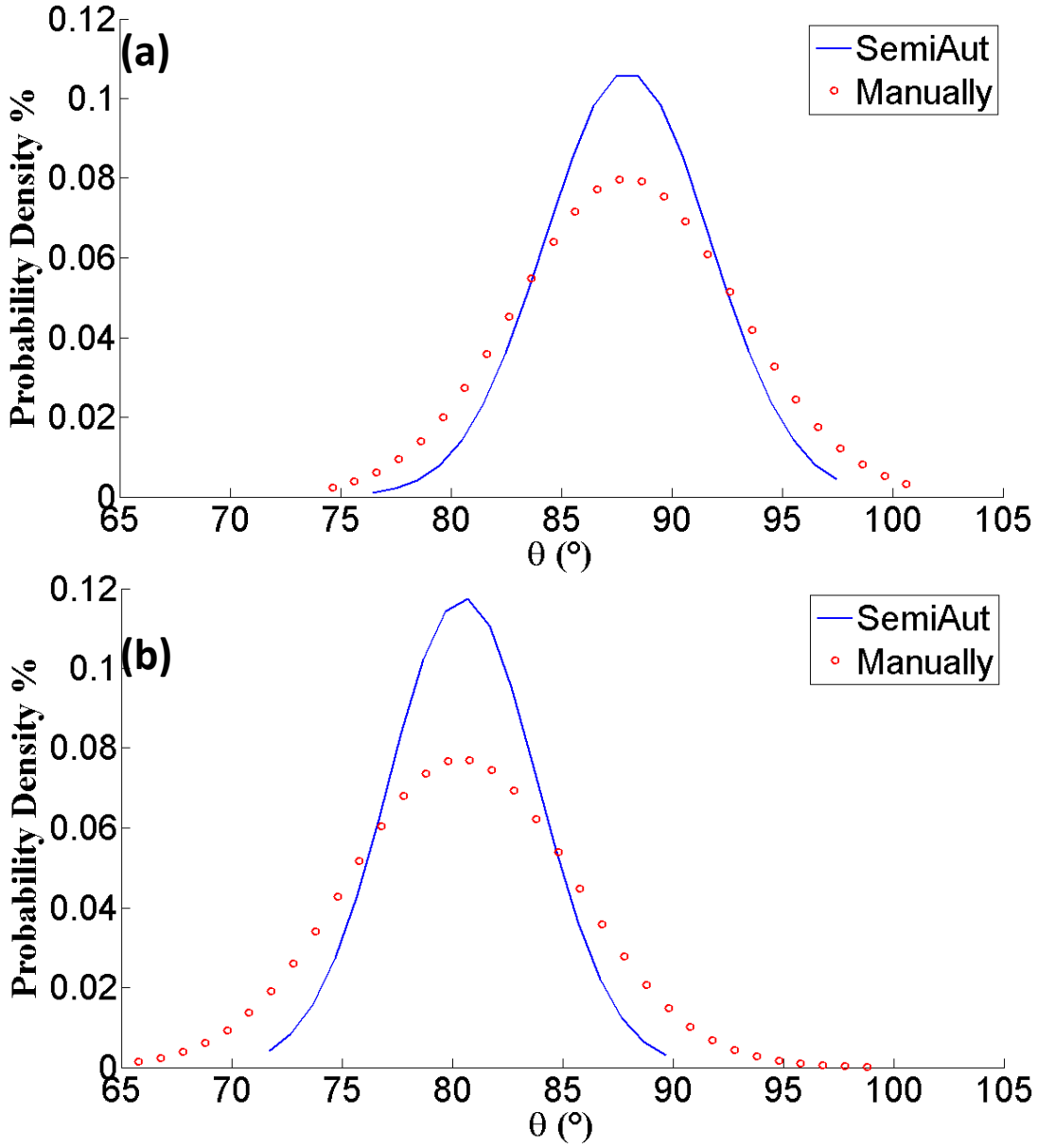


Figure 3.21. Shear angle distributions calculated using the semi-automated method for cgPP exposed to handling

## 3.8 Conclusions

Image analysis has been performed to investigate the variability of the tow orientation in a textile composite and two engineering fabrics. The results show a broad range of variability and the least and most distorted materials show standard deviations of about $2^{o}$ and $8^{o}$ respectively. A numerical code based on pin-jointed net kinematics has been enhanced by introducing additional perturbations of the nodes along the length of the horizontal and vertical centrelines to produce realistic variability 'Varifab'. A simple genetic algorithm was developed to reproduce full-field inter-tow angle of the measured global and spatial inherent variability of four materials (engineering fabrics and textile

composite). By combining this code into a genetic algorithm, realistic tow angle distributions have been predicted based only on simple statistical metrics as the input data.

Finally, a novel semi-automated image processing method used to characterise the inherent variability of engineering fabrics and textile composite and based on the edge detecting technique has been developed to increase accuracy and to save time and effort. The new method is very promising in terms of increasing accuracy and saving manual effort. However, there is no significant reduction in time due to the algorithm that is used to find the appropriate nodes of each element.

# 4. Modelling the Effect of Tow Meander on the Shear Compliance and the Shear-Tension Coupling of Woven Engineering Fabrics

## 4.1 Introduction

In this chapter, two developments in modelling the forming behaviour of advanced composites have been implemented in finite element simulations. The first development has been to incorporate the effect of fibre misalignment into large strain shear simulations. This has involved taking the output of the VariFab$^{GA}$ code described in Chapter 3 and using this to automatically generate variable finite element meshes and associated input files suitable for use with a pre-existing non-orthogonal constitutive model (NOCM) implemented in Abaqus Explicit$^{TM}$ [108-110]. Shear characterisation tests, including PF, UBE and BBE tests have all been simulated using this technique. The second development is designed to enhance the shear part of the NOCM (S-NOCM) by incorporating the experimentally measured influence of tension on shear compliance (see Chapter 2). The enhanced constitutive model (ES-NOCM) is implemented using the original NOCM material user subroutine as a starting point. Before describing this work a review of the relevant literature on the modelling of advanced composites during forming is provided.

Textile composites can be modelled using two main approaches: the kinematic (or mapping) approach and the mechanical approach. The main difference between these two approaches lies in the fact that no constitutive model is needed for the kinematic approach since information on stresses and deformations are not required, whereas constitutive models are required for the mechanical approach.

## 4.2 Review of Kinematic Modelling for Forming of Advanced Composites

The first attempts to model forming of textile composites was carried out using kinematic models or 'pin-jointed net' algorithms. This approach is used extensively in industry to simulate the forming of textile composite [111, 112]. The basic principle of this approach is that; the structure of the material is modelled as an inextensible pin-jointed net. Draping is usually achieved by picking a starting point on the fibre generator paths, and from this point the entire local fibre mapping is obtained using trigonometry strategies. Trellis deformation can be measured by calculating the angle between the fibre directions. Using a kinematic mapping approach, the overall shear deformation across 3D parts can be computed by specifying the geometrical shape of the part, the initial contact point on the part from which to drape the sheet and the initial reference orientations of the principal material directions. Nevertheless this approach just considers the kinematics of the fabric with no possibility to predict the mechanical stresses. Moreover, the solution can vary dramatically depending on the given starting point or path of the two generator lines [113].

## 4.3 Review of Mechanical Modelling for Forming of Advanced Composites

The mechanical approach is used to model the shear deformation mechanism of textile composites and engineering fabric materials during the draping and forming processes. In this approach, a constitutive model is required for calculating the mechanical behaviour of the material and to include a realistic boundary condition. The advantage of this method is that the mechanical behaviour of the material in the draping or forming process can be represented accurately. However, the complexity of calculating the non-linear behaviour and the contact conditions results in large CPU times compared to the kinematic method. Modelling the forming processes of textile fabrics can be considered across a range of length scales. Different FE approaches have been adopted as a result of the multi-scale nature of the textile architecture. These are usually classified into continuous and discrete approaches [114-116].

### 4.3.1 Discrete Approach

One type of mechanical approach used in modelling textile composite material is the 'discrete' or 'meso-structural' (the non-homogeneous) approach. Boisse, et al. [116] defined the modelling as discrete only if the yarns can slide past one another. At the meso-scale, warp and weft yarns can be modelled using dedicated textile modelling codes, for example, Wisetex [117] or Texgen [118, 119] or even using standard commercial solid modelling codes [120, 121]. Solid models are generated and can be imported into commercial finite element software [122, 123], for example, Abaqus. Despite the fact that this method is expensive in terms of time and computation, simulation of a complete model of the PF test using this unit cell model has been performed [114]. Moreover, Creech and Pickett [124], [125] modelled an entire part from the meso-scale level for an non-crimp fabric NCF as well as plain, twill 2/1 and twill 2/2 weave fabrics. Ballhause, et al. [126] invented the 'Discrete Element Method' which is used for modelling a fabric and fabric reinforced matrix. In this method the yarns are not allowed to slide past one other, and the unit cells are modelled as concentrated mass points with elements interacted between these points, where the role of different elements represents the relevant microstructure behaviour.

Attempt to model every individual fibre at the microscopic level have also been carried out [127-132]. This method is more expensive than the previous mentioned method in terms of time and computation. The modelling of a rope using this method was carried out recently by Vu [133], and this is the first attempt at modelling a simple braided synthetic rope.

Advantages of this bottom-up approach are as follows. Loading and material characteristics such as yarn geometry, yarn density, fibre material and weave style can be modified easily and their influence on the macroscopic behaviour can be predicted. This approach could eventually reduce or even eliminate the need to perform experimental tests. Defects or undesirable deformation mechanisms such as wrinkling and intraply slip can be predicted more realistically than using homogenised continuum-based methods. The ability to alter the yarn geometry could one day provide a very useful facility for manufacturing new fabrics with innovative structures. The vast increase in computational speed suggests a promising future for this approach.

### 4.3.2 Continuum Approach

In this approach the fabric sheet is assumed to deform as a continuum. Most materials can be considered as being a continuum at some level, such as metals in plasticity theory and composite materials consisting of matrix and reinforcement fibres in laminate theory. One of the main advantages of using a continuum approach is that the textile composite can be modelled using standard structural elements such as membrane or shell elements, which significantly reduces computational requirements compared to a discrete approach. To do this, the mechanical and kinematical behaviour, such as the change of the reinforcement orientations during shear, have to be considered within the constitutive model.

Defining a stress tensor at a point in a fabric is not possible without considering a fabric as a continuum. This approach involves using a few simplifying assumptions. Nevertheless, plausible local mechanical properties of the reinforcement can be conveyed using continuous constitutive models. The effectiveness of the approach improves as the 'intra' and 'inter-yarn' sliding and slipping becomes negligible. Since textile composite forming is generally a one-way process, elastic continuum approaches are generally valid as a first approximation when modelling engineering fabrics, despite the fact that their true behaviour is more accurately described by dissipative processes such as plastic deformation (dry fabrics). Still, some researchers have developed visco-elastic models for pre-impregnated materials [134-136] while others have developed elastic-plastic constitutive models for composite materials undergoing both loading and unloading cycles [137-141]. Elastic continuum approaches for large strains can be classified into two categories: hyper- and hypo-elastic approaches. Any mechanical model for bi-directional fabrics must be able to track the change in fibre direction during deformation.

#### a) Hyperelasticity

A hyperelastic material has a strain energy function such that the material derivative of this function is equal to the stress power per unit volume. It is useful for modelling rubber-like materials that can undergo large elastic deformations and is path-independent and fully reversible [142]. Engineering fabrics and reinforced polymers composites are materials that exhibit anisotropic linear elastic behaviour in finite deformation. The anisotropic behaviour in engineering textiles is a result of the two families of fibres. When these materials are subjected to finite deformations, significant changes occur in the directions of

anisotropy. The strain energy function per unit volume is often some scalar-valued function of the deformation gradient, in the two direction anisotropy invariants of the structural tensor [143].

Boisse, et al. [114] and Aimene, et al. [143] were the first to develop a hyperelastic constitutive model for woven engineering fabrics. The strain energy function in their constitutive model is a function of the right Cauchy-Green strain tensor and the two components of the structure tensor (the two yarn directions). It consists of the summation of two tensile energy functions and one in-plane shear energy function [144]. Consequently, the strain energy function proposed is a function of three mathematical invariants chosen based on the deformation mechanisms: the tension in the two directions of the reinforcements and the in-plane shear deformation. The tension and in-plane shear are uncoupled in this model. Good agreement between the experimental and the predicted results can be achieved using this approach. Peng, et al. [145] also recently developed a similar anisotropic fibre reinforced hyperelastic material model for woven engineering fabrics. The mathematical procedures used to develop the constitutive model were similar to that followed in [114, 143]. Vidal-Salle, et al. [146] studied the capability and the limitations of the hyperelastic model developed in [114, 143] by conducting a virtual forming test of a hemisphere geometry. Despite the fact that out-of-plane bending stiffness was not taken into account in this particular investigation, the local out-of-plane-buckling and stretching were well represented.

**b) Hypo-elasticity (Non-orthogonal Constitutive Models)**

A hypoelastic material is defined as one where the stress rate is a homogeneous linear function of the strain rate. The stress is history dependent. Different examples of hypo-elastic approaches are reviewed in the follows three subsections.

Several non-orthogonal constitutive models for textile composites and their preforms have been developed to predict the mechanical response during forming and to track the anisotropy of the yarns through large deformations [52, 108, 110, 147]. The approach was demonstrated initially by Yu, et al. [108]. The model is based on continuum theory by analysing the stresses along the principal material directions. The macro-scale material

properties of a plain-weave textile can be obtained from a repeat unit cell of the material's meso-structure. The shear and the tensile stiffness of the fabric are predicted based on the covariant reference frame associated with the fibre directions. These fibre directions are tracked during deformation and care is taken when updating the stresses in order to ensure objectivity of the stress predictions. In the non-orthogonal constitutive model the shear and tension are uncoupled. Essentially the full constitutive model is the sum of two separate sub-models, one relating to the tensile stresses due to stretching of the fibres, the other relating to the shear stresses due to the trellis shearing of the fabric. Further improvements of the model were implemented by Yu, et al. [109]; the effect of shear compliance and the weave structure of woven fabric were taken into account. Use of the refined constitutive model was demonstrated in the forming simulation of woven FRT. The refined model [109] was found to be more accurate in predicting wrinkling compared to the previous version of the model [108].

The model was subsequently modified in Yu, et al. [110] for the asymmetric shear behaviour of the non-crimp fabrics. The asymmetry is due to the structure of the fabric stitching which creates a very different shear response in the positive and negative shear directions. More details of the derivation of the shear part of the non-orthogonal constitutive model were carried out previously in [110]. The shear constitutive equation on the non-orthogonal constitutive model is shown here Eq.(4.1).

$$\Delta\sigma = \begin{bmatrix} \Delta\sigma_{xx} \\ \Delta\sigma_{yy} \\ \Delta\sigma_{xy} \end{bmatrix} = \begin{bmatrix} 0 & 0 & 2G_1 g_1^1 g_2^1 + G_2(g_1^1 g_2^2 - g_1^2 g_2^1) \\ 0 & 0 & 2G_1 g_1^2 g_2^2 + G_2(g_1^1 g_2^2 - g_1^2 g_2^1) \\ 0 & 0 & G_1(g_1^1 g_2^2 - g_2^1 g_1^2) \end{bmatrix} \begin{bmatrix} 0 \\ 0 \\ \Delta\theta \end{bmatrix} \tag{4.1}$$

$$G_1 = \frac{1}{h}\left\{ \frac{dF_s}{d\theta}\sqrt{g^{11}} + F_s\sqrt{g^{11}\left(g^{11}-1\right)} \right\} \tag{4.2}$$

$$G_2 = \left(\frac{F_s}{h}\right)\sqrt{g^{11}} \tag{4.3}$$

Where $G_1$ and $G_2$ are the shear modulus that $G_1$ related to the shear force $dF_s$ and shear angle $d\theta$ (see Eq. (4.2)) and $G_2$ related to the shear force $F_s$ and shear angle $\theta$ (see Eq. (4.3)). $g_1^1, g_1^2, g_2^1 \text{ and } g_2^2$ components of unit covariant base vector, $g_1$ and $g_2$ based on a orthogonal frame. $g^{11}$ diagonal component of metric tensor $= g^1.g^1$.

Later in 2006 [148], [88] and [33] replaced the tensile contribution of the NOCM with linear elastic truss elements. The approach of modelling the fibre reinforcement with truss elements was adopted previously [149-151]. The motivation for this alteration was related to numerical stability. Cherouat and Billoët [35] were perhaps the first to develop a FE meso-model of pre-impregnated composite material using a combination of two finite elements: truss elements to model the isotropic non-linear behaviour of warp and weft and membrane elements to model the isotropic viscoelastic behaviour of resin. Duhovic, et al. [152] also used this approach in developing a FE model of a stitched woven fabric material by a combination of truss and shell elements, and the yarns properties were modelled using the truss element while the yarn shear, yarn sliding, and yarn compression were modelled using the shell element. The effect of different stitching patters on the deformation of the woven material was investigated by conducting a number of forming experiments and simulations. A new stitching element was developed to model the interaction between the shell element (fabric) and stitching element through connecting the nodes of stitching element with the nodes of the shell element. The predicted shear deformation results presented quite good agreements with the experimental shear deformation results.

Willems [23] also found the tensile part of the NOCM does not work properly, therefore a new model was developed the tensile affine elastic model T-AEM. The two elements (the truss and the membrane elements) were mutually constrained by sharing common nodes (see Figure 4.1). The model [148] was used in determining optimum forming strategies to reduce or eliminate wrinkles [153], enabling the user to optimize forming parameters such as stamping rate, blank-holder holding force profile, blank size and forming temperature. This combination of membrane and truss element is often referred to as a 'semi discrete' approach.

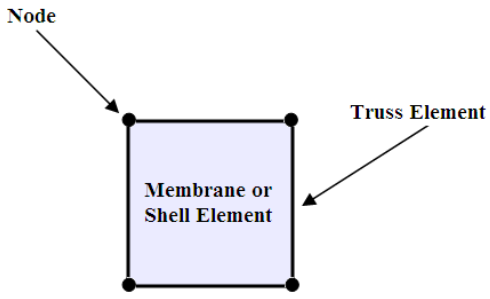


Figure 4.1. A semi-discrete finite element modelling approach

Peng and Cao [51] developed a non-orthogonal constitutive model similar to that developed by [108, 110]. The main difference between the models of Yu, et al. [108], [110] and that of Peng and Cao [51] is that in Yu, et al. [108], [110] the stiffness matrix components in the model are obtained by considering the fabric's meso-structure. Whereas in Peng and Cao [51] the material matrix components are obtained by fitting to experimental data. Both approaches use continuum theory to track the fibre directions.

### c) Hypoelastic Model for Uni and Bi-directional Composite Material

Hagège, et al. [154] also employed a hypo-elastic approach to model the tows within knitted composite reinforcements undergoing large strains. The approach was used to model one principal material direction and used the rotation tensor to compute the rotational derivative in order to update the local reference frame. The orthogonal axes were updated using the rotation reinforcement tensor keeping the angle between the orthogonal axes intact. The approach was extended to account for two reinforcement directions by Khan, et al. [155]. Here the two directions of the reinforcement were non-orthogonal due to changes in the angle between the material directions during forming (in-plane shear). The Lie time derivative [144] was used to determine the rate of change of the stress tensor and to track the principal material directions. The stresses on the two principal material directions tracked and calculated on the updated frames during test. The covariant $g_i$ and contra-variant $g^j$ affine frames are used to develop the stress algorithm. The frames $g_i$ and $g^j$ are orthogonal with respect to each other i.e. the mixed Kronecker delta=0 when i=j. The stresses with respect to its orientation are calculated in the appropriate mixed frame and transferred to the Apaqus Explicit working frame at the end of each increment.

### d) Rate-Dependent Viscous Modelling

A viscous rate/temperature constitutive model for modelling the mechanical behaviour of viscous textile composites have been developed by [134]. It is also called the model multi-scale energy model. The model is based on a summation of the shear energies dissipated during shearing of the textile composite. The model can predict the shear behaviour at any rate and temperature by relating the properties to the rheological behaviour of the matrix, and the fibre geometrical and mechanical properties. The viscosity parameters of the epoxy resin that was used in the model was obtained experimentally by characterising it as a function of shear strain rate and temperature. The input data required for the MSEM is the

epoxy resin rheological parameters and the fabric geometrical data such as tow width, space between tows, fibre volume fraction, and matrix volume fraction. Validation of the model has been carried out by [134] on thermoplastic and thermoset prepregs with different rates and temperatures. Good agreement has been achieved between experimental and predicted results.

Harrison, et al. [88] investigated the performance of two macro shear models; the NOCM [108-110] and his stress power model [148, 156], which is based on viscous assumptions implemented within two finite element codes (implicit and explicit) for viscous textile composites. The predicted results from the MSEM (shear force vs. shear angle vs. shear strain rate) at specified temperatures are used as input data fed into the two models by means of an interface numerical tool. Using this interface between the two macro shear models and MSEM, one can successfully simulate the effect of rate change on the viscous textile rate-dependant material by using PF test simulations.

## 4.4 Explicit Finite Element Solving Techniques

Explicit and implicit techniques of direct integration methods are used to solve finite element equations. In terms of solution accuracy, the implicit finite element method provides more accurate solution of the equilibrium equation. However, it is computationally expensive and has some convergence difficulties when contact is introduced in the forming simulation. On the other hand, the explicit finite element method is more stable for contact problems, less computationally expensive, and suitable for non-linear problems with large deformation. However, it cannot provide a solution that is as accurate as solution from the implicit method. As a result, the explicit finite element method is considered as the appropriate finite element analysis technique in forming problems. Throughout this research, the explicit finite element method was used in all finite element simulation [157]. The governing equation of the explicit finite element technique is

$$F_t(t) + F_D(t) + F_E(t) = R(t) \tag{4.4}$$

where, $F_t(t)$ are the inertia forces at time *t*, $F_D(t)$ are the damping forces at time *t*, $F_E(t)$ are the elastic forces at time *t* and $R(t)$ is the externally applied load at time *t*. Eq. (4.4) is to be satisfied at the discrete times e.g. ($0, \Delta t, 2\Delta t, 3\Delta t, \ldots\ldots, t-\Delta t, t, t+\Delta t\ldots$). Although in

static analysis $\Delta t$ is used too, inertia forces and damping forces are not included. The basic procedures for obtaining the solutions at the discrete times e.g. ($0, \Delta t, 2\Delta t, 3\Delta t, t-\Delta t, t, t+\Delta t$….) are as follows: the dynamic explicit method is based on the explicit central-difference integration rule where the equations of motion are integrated with respect to time using these rules:

$$M\,{}^{t}\ddot{U} + C'\,{}^{t}\dot{U} + {}^{t}F = {}^{t}R \qquad \text{equilibrium equation at time } t \tag{4.5}$$

$${}^{t}\dot{U} = 1/2\Delta t\,({}^{t+\Delta t}U - {}^{t-\Delta t}U) \tag{4.6}$$

$${}^{t}\ddot{U} = 1/(\Delta t)^2\,({}^{t+\Delta t}U - 2\,{}^{t}U - {}^{t-\Delta t}U) \tag{4.7}$$

where ${}^{t}F$ is the force corresponding to the internal element stresses at time $t$, $C'\,{}^{t}U$ is the damping forces at time $t$, $M\,{}^{t}\ddot{U}$ is the inertia force at time $t$, and ${}^{t}R$ is the externally applied load at time $t$. Eq. 4.6 shows the velocity at time $t$ and it was expanded to obtain the acceleration in Eq. 4.7.

Any method that uses the equilibrium equation at time $t$ to obtain the solution for the response at time $t + \Delta t$ is termed an explicit integration method. The important point to note is that there is no need to set-up a stiffness matrix, K, in the explicit method. Using equations (4.5-4.7) we can directly obtain equation Eq. (4.8) as shown below.

$$\left(\frac{1}{\Delta t^2}M + \frac{1}{2\Delta t}C'\right){}^{t+\Delta t}U = {}^{t}\widehat{R} \tag{4.8}$$

Since there are three equations (4.5-4.7) and three unknowns ${}^{t+\Delta t}U$, ${}^{t+\Delta t}\dot{U}$ and ${}^{t+\Delta t}\ddot{U}$, the three unknowns can be solved for, where ${}^{t}\widehat{R}$ is the effective load vector, and the hat means that there are a large number of terms to be taken into account, namely those corresponding to the inertia and damping in the system.

$${}^{t}\widehat{R} = {}^{t}R - {}^{t}F + \frac{2}{\Delta t^2}M\,{}^{t}U - \left(\frac{1}{\Delta t^2}M + \frac{1}{2\Delta t}C'\right){}^{t-\Delta t}U \tag{4.9}$$

where $\frac{2}{\Delta t^2}M\,{}^{t}U$ is an inertia contribution and $-\left(\frac{1}{\Delta t^2}M\right){}^{t-\Delta t}U$ is another inertia contribution, and the damping contribution is $-\left(\frac{1}{2\Delta t}C'\right){}^{t-\Delta t}U$. The method is used when M and C' are diagonal because in this case Eq. (4.9) is decoupled as shown in Eq. (4.10).

$$^{t+\Delta t}U_i = \left( \frac{1}{\frac{1}{\Delta t^2} m_{ii} + \frac{1}{2\Delta t} c_{ii}} \right) {}^{t}\widehat{R}_i \tag{4.10}$$

The individual displacement components or the displacement at each degree of freedom can be calculated one after another. Once the $\widehat{R}_i$ is evaluated from Eq. (4.9), when all the M and C are diagonal, then we substitute the individual components of the vector $\widehat{R}_i$ corresponding to the degree of freedom *i* in Eq. (4.10). Finally, the nodal displacement $^{t+\Delta t}U_i$ is calculated. An important point to note is that there is no need to set-up a stiffness matrix K for this approach [157, 158].

The time increment size $\Delta t$ is estimated by dividing the smallest element length in the mesh over the dilatational wave speed $c_d$.

$$\Delta t = \frac{L_{min}}{c_d} \tag{4.11}$$

$$c_d = \sqrt{\frac{\widehat{\lambda} + 2\widehat{\mu}}{\rho}} \tag{4.12}$$

where $\rho$ is the density of the material, $\widehat{\lambda}$ and $\widehat{\mu}$ can be defined for isotropic elastic material as shown in Eqs (4.13) and (4.14).

$$\lambda = \frac{E\nu}{(1+\nu)(1-2\nu)} \tag{4.13}$$

$$\mu = \frac{E}{2(1+\nu)} \tag{4.14}$$

where *E* and *v* are Young's modulus and Poisson's ratio.

In an explicit dynamic analysis very small time-steps can lead to long computation times. An efficient way of reducing the computation time is by increasing the punch speed. However, this might generate inertial effects e.g. unrealistic material deformation or high frequency of numerical oscillations due to the significant increase in the inertia, Momentum = mass x velocity, which means that the inertia increases as the velocity is increased. In order to reduce or even eliminate these oscillations damping is required [159-162].

## 4.5 Effect of Tow Meander on the apparent Shear Compliance of Woven Engineering Fabrics

Variability of shear results is often observed when testing engineering fabrics due to both deformation of the specimen prior to testing and misalignment when placing the fabric in the test machine. Tow meander can be present within the fabric, even when taken directly off the roll from the material supplier [21, 39, 163]. Various researchers have investigated the effects of specimen misalignment on shear test results produced using a PF test. Lussier and Chen [164] conducted an experimental study on two different engineering fabrics; satin and plain weave. This study concentrated on the effect of misalignment on PF shear compliance. They found that the shear compliance increased significantly as the misalignment angle increased from 0 to 5°. Later, Peng and Cao [51] carried out experimental and virtual PF tests with different degrees of misalignment again due to small rotations of the test specimen. As expected, the recorded shear compliance was found to increase with the degree of misalignment for both experimental and the numerical results. Launay, et al. [44] discussed how increasing crimp during PF tests can result in large tensile stresses in the fibre directions and presented a modified PF rig able to control tension in the fabric's two reinforcement directions. By relaxing tensions in warp and weft tows as the test proceeds the shear compliance measured using this modified PF rig was found to converge on results obtained from UBE tests. Another suggestion to reduce the effect of misalignment on shear compliance was recently proposed by Milani, et al. [165] who suggested a modified PF specimen geometry. The strategy of the test relies on reducing the extent of the clamping length. The shear results of the modified test were closer to those produced using the UBE test, indicating that the modified geometry is less sensitive to sample misalignments. Recently Komeili and Milani [166] developed a finite element meso-scale model to explore the effects of variations in the geometrical (yarn spacing, width, and height and fibre misalignment) and material properties (longitudinal and transverse stiffness and the friction coefficient between the warp and weft yarns) on the fabric's shear stiffness. They concluded fabric misalignment is by far the most important source of variability on the measured shear compliance of the fabric.

Note that most previous numerical studies on the effects of misalignment have been performed by simply rotating the specimen with respect to the PF rig. In practice it is

known that misalignment error is due to both rotation of the specimen and the inherent variability of tow directions in the fabric. The latter cause of misalignment makes it very difficult to align the specimen with the PF rig. Consequently Wang [21] introduced a step of straightening prepreg samples before testing. Results showed how repeatability can be improved by this process. Unfortunately, this procedure is not possible for consolidated thermoplastic materials.

To investigate the effect of tow meander on the shear compliance, a method of introducing realistic tow meander into finite element simulations is demonstrated here and used to investigate the effect on PF, UBE and BBE shear tests results. Actual tow directional variability has been characterized for a plain weave dry glass fabric wrGF and commingled glass/polypropylene fabric cgPP using an image analysis method and these data have been used to model tow meander using Varifab$^{GA}$ in Chapter 3 and also in [163].

### 4.5.1 Predicting the effect of Misalignment on Shear Compliances

Tow meander of several real engineering fabrics, both straight off-the-roll and after handling, was characterised in Chapter 3. Using the statistical information obtained through this characterisation, a method of reproducing realistic tow meander across a finite element mesh has been developed and implemented in the software Varifab$^{GA}$, also reported in Chapter 3. In this chapter, variable meshes based on the tow meander data for both (wrGF and cgPP) have been generated. The NOCM [108-110] with shear and tension material parameters given in Table (2-5 in Chapter 2) is now utilized to predict the shear force versus shear angle curves from the three most important shear characterisation tests. The aim is to investigate the likely influence of tow meander on the resulting shear force versus shear angle results.

#### a) Assigning Initial Orientation

To properly account for tow meander in the numerical simulations, a method of assigning the initial fibre directions to each element in the finite element mesh is required. To illustrate the method, an example of one mutually-constrained element, consisting of both membrane and truss elements are considered (see Figure 4.2a). The initial shear angle $\theta_p$ of

every element is predicted by calculating the angle between the two principal material directions in the NOCM using Eq. (4.15).

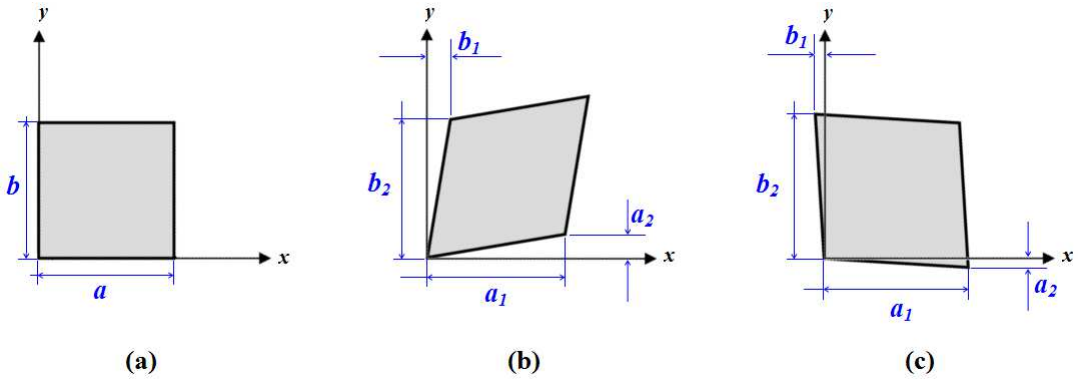


Figure 4.2. The structure of a combined element (a) the initial orientation at 0/90° (b) misalignment of the initial orientation with shear angle θ > 0° and (b) misalignment of the initial orientation with shear angle θ < 0°.

$$\theta_p = \frac{\pi}{2} - \frac{a\cos\left(a_1 b_1 + a_2 b_2\right)}{\sqrt{a_1^{\,2} + a_2^{\,2}}\sqrt{b_1^{\,2} + b_2^{\,2}}} \tag{4.15}$$

where $\theta_p$ is the angle between $a$ and $b$, $a_1$ and $b_1$ are the horizontal components of $a$ and $b$ and $a_2$ and $b_2$ are the vertical components of $a$ and $b$ as shown in Figure 4.2. The numerical technique of generating realistic tow meander across the specimen to reproduce a blank with the same global statistical variations as the measured data is described in Chapter 3, Section 3.6. Once a large mesh of size 900 x 900 mm is produced, with the same statistical global variations as the measured data, the mesh data (nodal co-ordinates, fibre directions and element shear angles) are saved in a database. In order to investigate the effect of tow meander on shear compliance when testing the same fabric in different shear tests, the initial sheet is used to cut several test specimens for each of the different characterisation tests. The appropriate blank shape is cut from the large blank using a simple Matlab code named 'BlankCut.m'. The procedure for cutting the test specimen or blank is as follows: (i) call the figure corresponding to the large sheet, (ii) assign the appropriate coordinates for the required blank and (iii) cut the required blank from the large blank using 'BlankCut.m' code (see Figure 4.3).

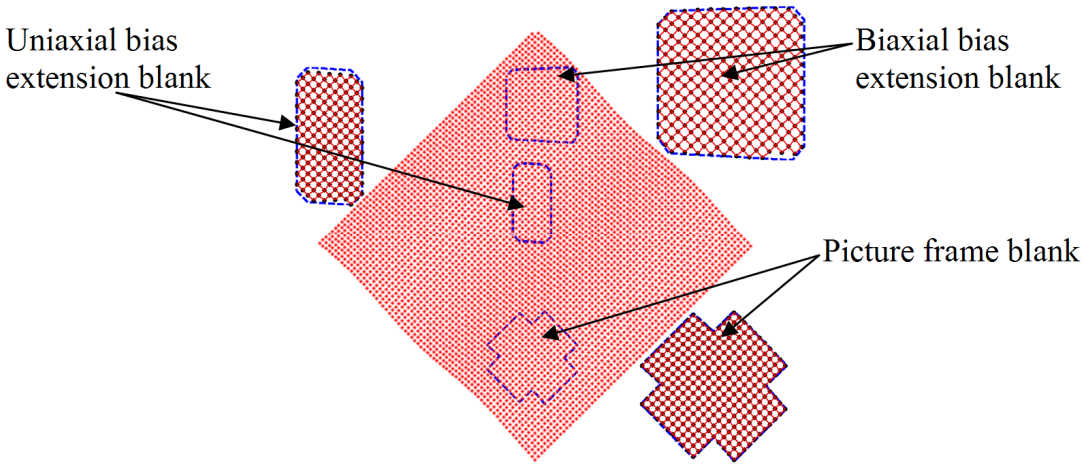


Figure 4.3. Cutting specimens of PF, UBE and BBE tests from large sheet Cutting blanks from large mesh sheet

Once the required sample size is cut from the large numerical blank (as shown in Figure 4.3), the vector components ($a_1$, $a_2$, $b_1$ and $b_2$) of the element's left and bottom sides as written within the element's local reference frame (with origin at the bottom left corner of the element - see Figure 4.2) of each element are computed automatically. Since each membrane element in the mesh (see Figure 4.3) has a different initial shear angle it has to be defined as a unique element set within the Abaqus input file. To do this a Matlab code 'InitAngle.m' has been written to generate two separate input files (*mat.inp* and *sec.inp*). The *mat.inp* input file defines the initial side length components ($a_1$, $a_2$, $b_1$ and $b_2$) for each membrane element while the *sec.inp* input file defines the section of each membrane element and assigns the element set (containing just the one membrane element) with a unique name for each element set. The input files are then included in the main input files of the simulations.

The fibre reinforcement was modelled using a simple 1-D linear elastic constitutive model in the truss elements. The shear part was modelled using the shear part of the NOCM. To model the test using the NOCM, a polynomial fit to the shear force versus shear angle curve is used as the input to determine the material's shear compliance. These input curves were obtained from the experimental tests (Chapter 2). The NOCM used in this particular investigation has no coupling between in-plane tension and shear compliance and so the model is unable to accurately model the actual test.

In the following section PF, UBE and BBE tests are modelled. Each test simulation is run three times with a unique specimen for each simulation. The specimen for each repeat simulation contains a unique degree of randomly assigned tow meander, generated using Varifab$^{GA}$. In so doing the influence of specimen variability is investigated for both the wrGF and cgPP materials.

### b) Modelling PF Test with Realistic tow meander

Abaqus/Explicit finite element software is used to conduct all FE simulation of this work. The PF rig used in this investigation was originally manufactured and modelled by Whyte [167]. The rig was modelled with four arms, each one containing 698 R3D4 rigid elements. The four arms are connected to each other by connector elements of type 'Cardan' [159]. Connection type Cardan provides a rotational connection between two nodes where the relative rotation between the nodes is parameterized by Cardan (or Bryant) angles. The blanks were modelled as mutually constrained truss and membrane structural elements (120 truss elements and 100 membrane elements). The truss elements represent the fibre reinforcement while the membrane elements represent the shear resistance of the fabric. Three numerical blanks for each material (wrGF and cgPP) are cut from the predicted large blanks with mesh variability (see Figure 4.4). The sizes of the PF blanks are corresponding to those experimental PF specimens used in Chapter 2.

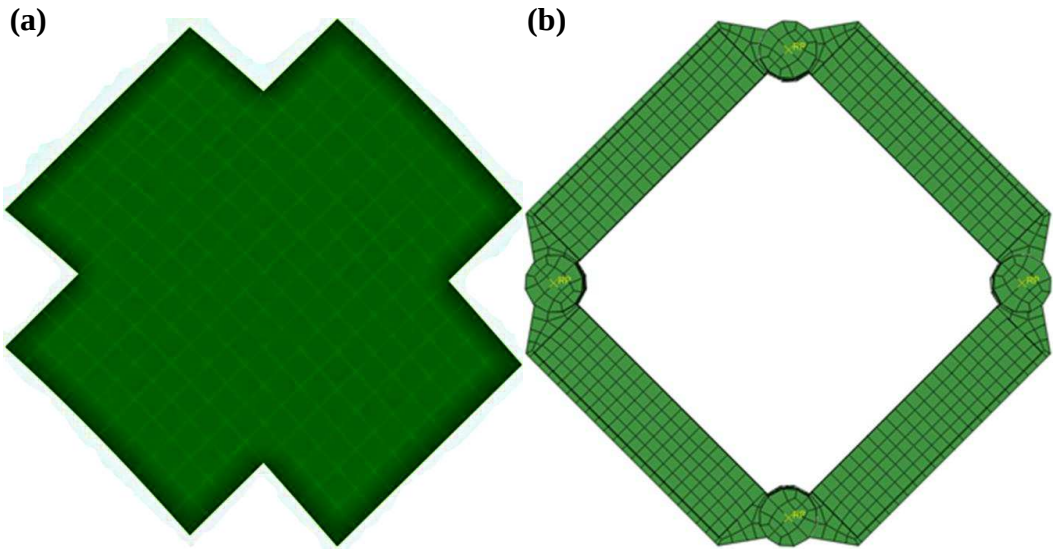


Figure 4.4. (a) Example of PF specimen with mesh variability and (b) PF rig constructed of rigid body elements

Shear material properties are obtained by fitting the representative experimental shear force-shear angle curves with 9 degree polynomial functions (Eqs. 4.16 and 4.17) to the two materials wrGF and cgPP respectively (the coefficients of the two polynomials shown in Table 2.3 in Chapter 2).

$$F_s = -5.3400E-13\theta^9 + 1.2700E-10\theta^8 - 1.2200E-08\theta^7 + 6.0700E-07\theta^6 - 1.6200E-05\theta^5 + 2.0870E-04\theta^4 - 4.9340E-04\theta^3 - 1.4800E-02\theta^2 + 1.4790E-01\theta - 5.3370E-03$$

(4.16)

$$F_s = 1.1900E-12\theta^9 + 1.8400E-10\theta^8 - 5.2900E-08\theta^7 + 4.3000E-06\theta^6 - 1.7089E-04\theta^5 + 3.6527E-03\theta^4 - 4.0834E-02\theta^3 + 2.6452E-01\theta^2 - 3.0563E-01\theta - 1.5347E-02$$

(4.17)

The tensile part in the NOCM was modelled by linear-elastic truss elements. A simple approximate homogenisation method has been used to calculate truss dimensions and mechanical properties. Using Eq. (4.18):

$$\frac{A_1}{A_2} = \frac{E_2}{E_1} \tag{4.18}$$

where $A_1$ is the cross sectional area per unit length of the ends of either the warp tows of a typical dry glass fabric and commingled glass/polypropelene (e.g. ~0.000086 $m^2$ per metre and 0.000288 $m^2$ per metre) and $A_2$ is the combined cross sectional area per unit length of the truss elements in the mesh, $E_1$ is the tensile stiffness of typical glass tows (e.g. 30-73 GPa [156, 166, 168-171] and $E_2$ is the stiffness of the truss elements used in the FE mesh.

The truss properties chosen for the truss elements here (stiffness = 6 GPa for wrGF and 14 Gpa for cgPP, length= 0.0135 m, circular cross-sectional area 0.0000025 $m^2$ gives an area per unit length, $A_2$, of 0.0001925$m^2$ for wrGF and cgPP) produce a sheet with a tensile response between about 2.2 and 5.4 times lower than an actual woven glass fabric 3.2 and 7.8 times lower than the commingled glass/polypropylene fabric. For simplicity the non-linear tensile behaviour in the tows due to fabric crimp (see for example [23, 172, 173]) is neglected. In this investigation, decreasing the tensile modulus of the truss elements in this way has been found to produce improved performance when modelling a shear-tension coupling and also tends to reduce simulation times when using the explicit FE method (due to the Courant stability condition). Previous researchers have also used this technique to improve computational efficiency [23, 174]. If this is done, care has to be taken to ensure

this reduction in stiffness has a negligible influence on the final complex forming simulation predictions. For example, in one forming case study, Willems [23] found that reducing the tensile stiffness by factor of 20 caused a 2° of change in the resulting shear deformation predictions. Poisson's ratio is assumed to be 0.0 for wrGF and cgPP respectively. The boundary conditions are modelled as being similar though slightly more strict than in actual PF tests; the blank is clamped to the PF rig using tie constraints, which means it cannot slip at all. The bottom joint in the rig was constrained in the three translational and the three rotational degrees of freedom while a displacement of 90 mm was applied to the upper joint in the *y* direction with constraints on the translation of the right and left joints in *z* direction with a free rotation condition around the *z* axis. Three predicted shear force-shear angle curves $F_c$-$\theta_p$ with variability are compared against the experimental $F_c$-$\theta_{mp}$ of the two materials as illustrated in Figures 4.5 and 4.6 respectively. In the figure legend *Exp* indicates the experimental results and *IrReg* indicates the predicted result using the irregular test specimens. The error bar on the experimental result is a standard division of three repeated PF tests.

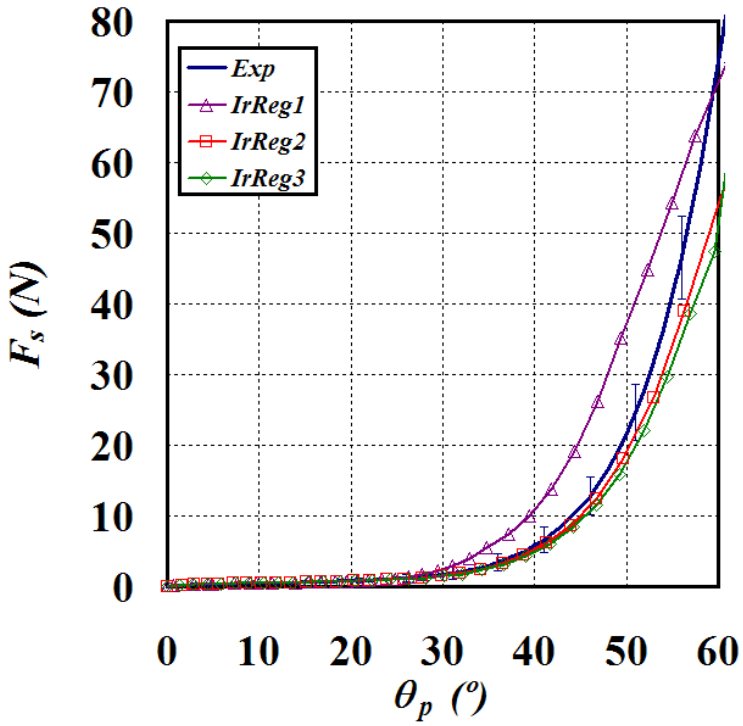


Figure 4.5. Experimental and predicted results with orientation variability $F_s$-$\theta_p$ of PF for wrGF. In the figure legend *Exp* indicates the experimental results and *IrReg* indicates the predicted result using the irregular test specimens.

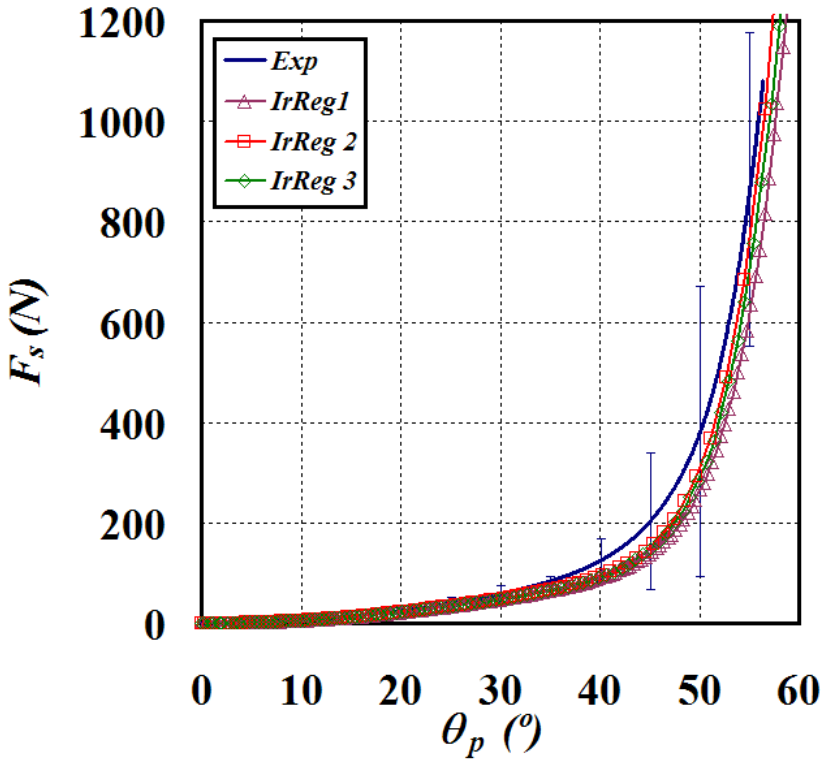


Figure 4.6. Experimental and predicted results with orientation variability $F_s$-$\theta_p$ of PF for cgPP. In the figure legend *Exp* indicates the experimental results and *IrReg* indicates the predicted result using the irregular test specimens.

The predicted mean $mu_p$ and the standard deviation $std_p$ of the angles between the tows of the three samples cut from large sheet are illustrated in Table 4.1.

Table 4.1. The normal distribution statistics of the three samples cut from the large sheet of the two materials

| Sample Name | wrGF | | cgPP | |
|---|---|---|---|---|
| | $mu_p$ | $std_p$ | $mu_p$ | $std_p$ |
| *IrReg1* | 90.07105 | 2.626733 | 88.66158 | 3.041468 |
| *IrReg2* | 86.04687 | 1.464828 | 87.72888 | 2.265209 |
| *IrReg3* | 90.0221 | 2.4766 | 88.95081 | 3.072438 |

The closest predicted result to the representative experimental result is *IrReg2* and *IrReg3* in the first case. However the predicted result of sample *IrReg1*, that has statistics close to no variability i.e. $mu_p$=90° and $std_p$=0, is far from the representative experimental result (see Figure 4.5). The predicted results of sample *IrReg1* and *IrReg3* are not close to each

other even though the statistics are almost identical (see Figure 4.5). Tow meander can reduce or increase the apparent shear resistance. In the second case (Figure 4.6) all the predicted results are close to each other and close to the representative experimental result, which a result of the close variability of the three samples (*IrReg1-3*) see Table 4.1.

### c) Modelling the UBE Test with tow meander

The FE simulation of the UBE is performed by modelling the UBE blanks with a mutually constraints 392 truss elements and 176 membrane elements. The size of the blank is the same as the size of the actual sample, 220 x 110 mm (see Figure 2.3 in Chapter 2). Three numerical blanks for each material (wrGF and cgPP) are cut from the predicted large blanks with mesh variability (see Figure 4.7).

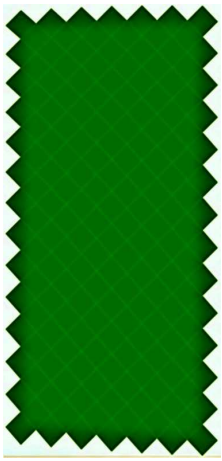

Figure 4.7. (a) Blank of hybrid mesh with mesh variability

The shear material properties are obtained by fitting the representative experimental shear force-shear angle curve of the UBE test with $9^{th}$ degree polynomials fitted to the experimental data (see Table 2.4). The truss properties chosen for the truss elements here (stiffness = 6 GPa for wrGF and 14 Gpa for cgPP, length= 0.01296 m, circular cross-sectional area 0.000001 $m^2$ gives an area per unit length, $A_2$, of 0.00009 $m^2$ for dry glass plain fabric and for commingled glass/polypropelen) produce a sheet with a tensile response between about 4.76 and 11.58 times lower than an actual woven glass fabric and 6.84 and 16.68 times lower than the commingled glass/polypropylene fabric. The boundary conditions are modelled as being similar to the actual uniaxial extension test. The upper node set (see Figure 4.8) was free to move in the positive *y* direction with a constant displacement of 45 mm while constraining the other five degrees of freedom. The bottom

node set was free to move in the negative *y* direction with a constant displacement of 45 mm while constraining the other five degrees of freedom (see Figure 4.8).

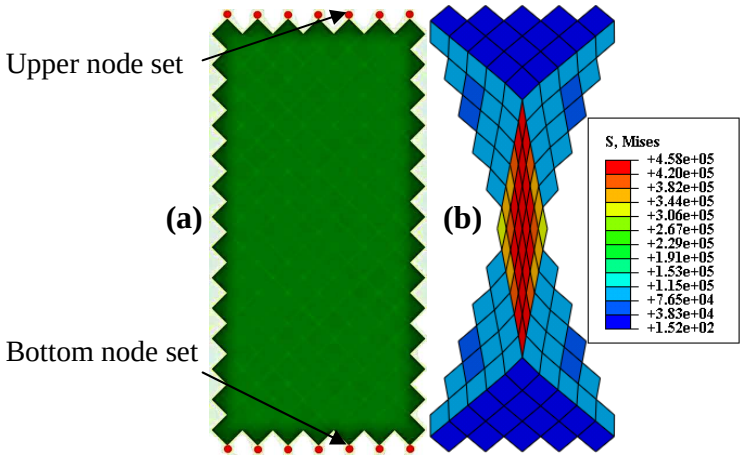


Figure 4.8. (a) Sketch of UBE blank show the upper and bottom node sets. (b) Deformed mesh of UBE simulation

The predicted $F_c$ versus $\theta_p$ shear results of the UBE test with no mesh variability show large differences compared to the experimental results for the two materials as shown in Figure 4.9a and 4.10a. This might due to the contribution from region B (see Figure 2.3 in Chapter 2) (or could possibly be due to error within the NOCM, though exploring this possibility would require an in-depth study of the NOCM and is beyond the scope of this investigation). In order to obtain good agreement between the predicted and experimental results a normalization method is required [67]. The normalization technique used here is based on iterating the input curve in order to achieve the correct final result from the simulation. By correctly normalising the experimental uniaxial bias-extension curves, the numerical simulations should produce approximately the same shear force versus shear angle predictions as those observed in experiments. To do this an approximate procedure is used here by the following a simple iterative method: (i) the input shear force versus shear angle curves are divided by the predicted shear force versus shear angle curves to produce a ratio (also a function of the shear angle) as shown in Figure 4.9b and 4.10b, (ii) polynomial functions, $R_p^i(\theta)$, are fitted to each ratio curve, (iii) input curves are multiplied by the ratio curves to produce a next generation of input curves, (iv) the process is repeated until reasonable agreement between numerical UBE test predictions and experimental results is obtained. Normally around three iterations are required before reasonable agreement between experimental and predicted results was achieved. Shear material properties are obtained by fitting the representative experimental normalised shear force-

shear angle curves with 9 degree polynomial fits (Eqs. 4.19 and 4.20) of the two materials wrGF and cgPP respectively for further use in FE forming simulations in Chapter 5. The coefficients of the curve fitting are illustrated in Table 4.2.

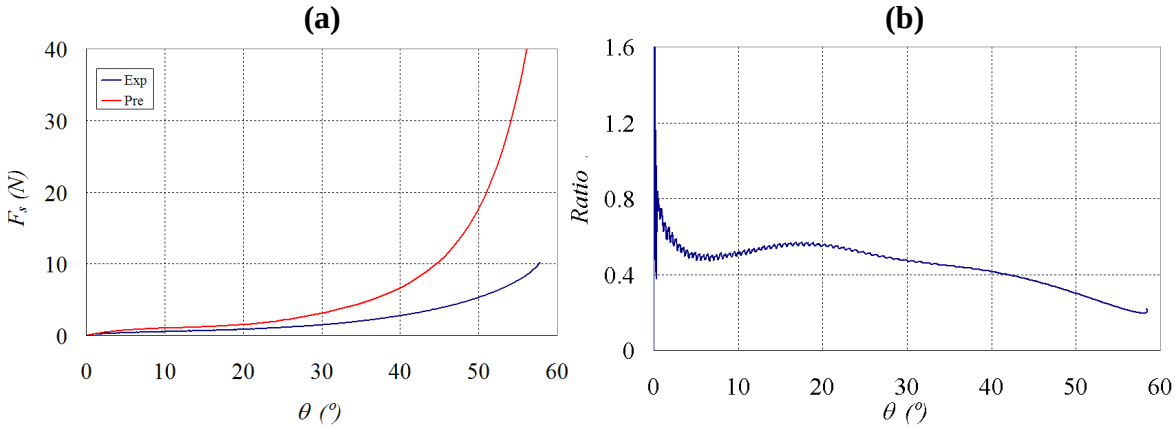


Figure 4.9. (a) The predicted and experimental $F_c$-$\theta_p$ of wrGF, the predicted $F_c$-$\theta_p$ obtained using un-normalized experimental $F_c$-$\theta_p$ input shear properties, (b) the ration of the input shear force versus shear angle curves which divided by the predicted shear force versus shear angle curves

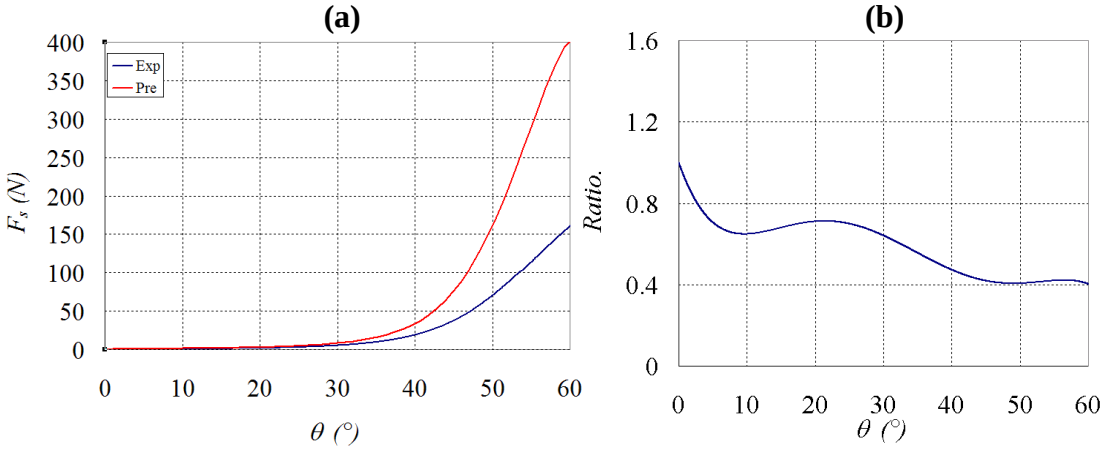


Figure 4.10. The predicted and experimental $F_c$-$\theta_p$ of the cgPP, the predicted $F_c$-$\theta_p$ obtained using un-normalized experimental $F_c$-$\theta_p$ input shear properties, (b) the ration of the input shear force versus shear angle curves which divided by the predicted shear force versus shear angle curves

$$F_s = 1.74E-24\theta^9 - 3.70E-21\ \theta^8 + 7.89E-19\theta^7 - 7.11E-17\theta^6 + 2.59E-08\theta^5 - 3.81E-06\theta^4 + 2.03E-04\theta^3 - 4.29E-03\theta^2 + 5.10E-02\theta + 0 \quad (4.19)$$

$$F_s = 1.70E-12\theta^9 - 4.24E-10\theta^8 + 4.39E-08\theta^7 - 2.46E-06\theta^6 + 8.13E-05\theta^5 - 1.60E-03\theta^4 + 1.84E-02\theta^3 - 1.12E-01\theta^2 + 3.30E-01\theta + 4.16E-03 \quad (4.20)$$

Table 4.2. the coefficients of the UBE normalised shear compliances of wrGF and cgPP

| Coefficients | wrGF | cgPP |
|---|---|---|
| 1 | 4.51E-23 | -1.11E-13 |
| 2 | -1.25E-20 | 3.25E-11 |
| 3 | 1.48E-18 | -3.73E-09 |
| 4 | -9.85E-17 | 2.10E-07 |
| 5 | 1.81E-08 | -5.79E-06 |
| 6 | -2.67E-06 | 6.25E-05 |
| 7 | 0.000142 | 0.000246 |
| 8 | -0.003 | -0.00935 |
| 9 | 0.035669 | 0.07959 |
| 10 | -1E-06 | -0.00001 |

Three predicted shear force-shear angle curves $F_c$-$\theta_p$ with variability compared against the experimental $F_c$-$\theta$ of the two materials are illustrated in Figures 4.11 and 4.12 respectively.

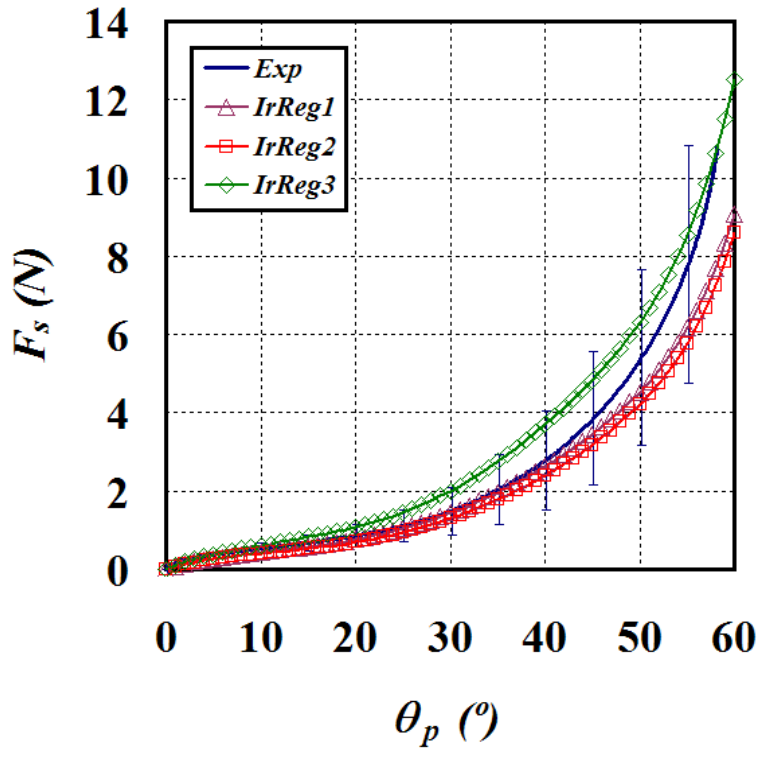


Figure 4.11. Experimental and predicted with orientation variability $F_s$-$\theta_p$ of the UBE of wrGF.

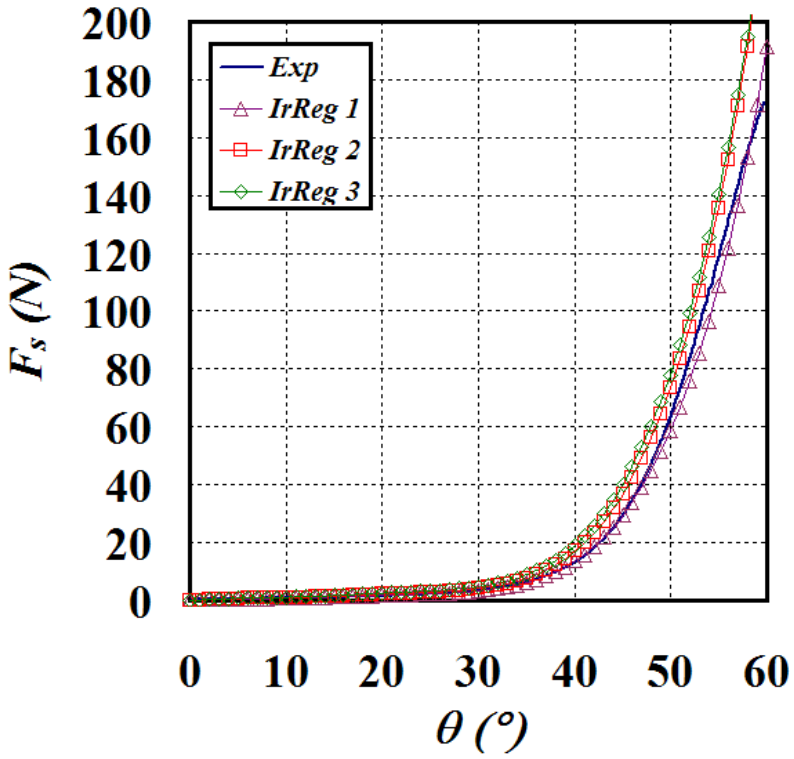


Figure 4.12. Experimental and predicted with orientation variability $F_s$-$\theta_p$ of the UBE of cgPP

The predicted mean $mu_p$ and the standard deviation $std_p$ of the angles between the tows of the three samples cut from the large sheet are illustrated in Table 4.3.

Table 4.3. The normal distribution statistics of the three samples cut from the large sheet of the two materials

| | wrGF | | cgPP | |
|---|---|---|---|---|
| Sample Name | $mu_p$ | $std_p$ | $mu_p$ | $std_p$ |
| *IrReg1* | 86.32 | 0.56 | 92.70 | 1.27 |
| *IrReg2* | 91.88 | 2.19 | 91.98 | 2.72 |
| *IrReg3* | 87.46 | 0.76 | 86.97 | 1.65 |

The closest predicted results to the representative experimental result are *IrReg1* and *IrReg3* in the first case. However, the predicted result of sample *IrReg2* that has very little variability, is far from the representative experimental result (see Figure 4.11), nevertheless it is still in the error bars' range. That indicates that the $mu_m$ of the representative experimental result is less than the ideal $mu_m$ (the $mu_m$ of the representative experimental result < 90°). In the second case (Figure 4.12) the closest predicted result to the

representative experimental result is *IrReg 3* that has statistics $mu_p$=92.70° and $std_p$=2.16 (see Table 4.3). It can be concluded that the representative experimental result is more than the ideal $mu_m$ (the $mu_m$ of the representative experimental result > 90°), which indicated that the sample might be exposed to stretching or mishandling horizontally before testing.

### d) Modelling the BBE Test with Realistic Orientation Variability

The BBE test which formed the subject of Chapter 2 has demonstrated interesting potential as a new method to characterise the shear behaviour of woven engineering fabrics [175]. The state of stress in the specimen of the BBE test is unlike that of the PF or UBE tests. For a well aligned specimen the deformation in a PF test involves just trellis shear with no strain along the fibre directions (neglecting the effects of increasing crimp, as discussed by Hivet and Duong [43]. Thus the shear compliance of the material obtained from a well-aligned PF test is measured in the absence of in-plane tension. In contrast, the BBE test gives the possibility of measuring the coupling between shear and in-plane tension.

One aspect of uncertainty discussed in the original experimental investigation on the BBE test [175] was the possible effect of sample misalignment, due to sample rotation and tow meander, on the results of the test. One concern was that any error due to misalignment might be amplified when greater transverse forces were applied to the specimen, due to greater contributions to the measured force from tensile stresses along the fibre directions. Though considered unlikely, it was suggested that this could be a possible alternative reason for the apparent increase in fabric shear resistance of the specimen with increasing in-plane tension.

A BBE test with sample dimensions measuring 210x210 mm and a clamping length of 70 mm is modelled using mutually-constrained truss and membrane structural elements (572 truss and 264 membrane elements) sharing the same corner nodes of the unit cell [88]. Simulations are conducted in two steps (i) application of a combined transverse force, $F_c$, equal to the loads used in [163] (5, 37, 50, 75 and 100N) to nodes at the edge of the central section of the right and left sides of the blank (Region C in [163], see Figure 4.13)) and (ii) pulling the sample from the upper and lower centrally located node sets at the middle

of the top and bottom side lengths of the blank (corresponding to the edge of Region C in [163]) (see Figure 4.13).

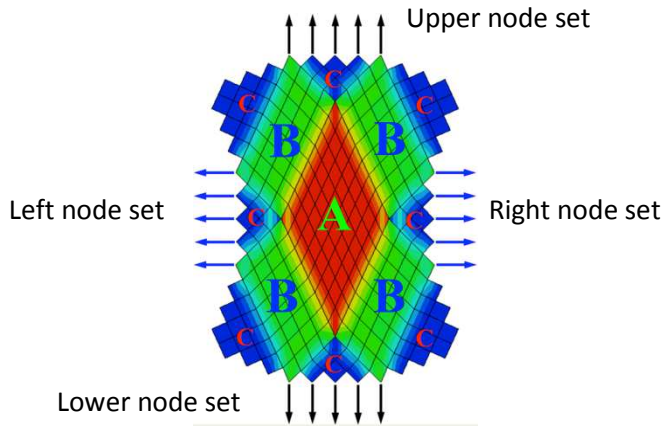


Figure 4.13. The three different deformations of A, B and C regions of the BBE FE model with force boundary conditions applied to the right and left, centrally located node sets and vertical displacements applied to the upper and lower centrally located node sets.

Output from the simulations includes the total predicted axial force, $F_{Tpr}$ (*pr* is an indication of prediction in all the following symbols), which is the combined vertical force of each node in the upper or lower central node set (Figure 4.13). $F_{Tpr}$ is a result of two contributions: one from the material, $F_{mpr}$, and another from the reaction force, $F_{rpr}$ caused by the applied transverse (or clamping) force $F_{cpr}$. As with the experiments discussed in Chapter 2, in order to extract the material force, post processing of the results is required. $F_{rpr}$ can be related to $F_{cpr}$ through consideration of the power of the system (see Eq. (4.22) and see Figure 4.14).

$$F_{Tpr} = F_{mpr} + F_{rpr} \tag{4.21}$$

$$F_{rpr} = \frac{F_{cpr} V_{xpr}}{V_{ypr}} \tag{4.22}$$

where $V_{ypr}$ is the vertical velocity of the blank at its upper and lower edges and $V_{xpr}$ is the horizontal velocity of the blank at both its side edges

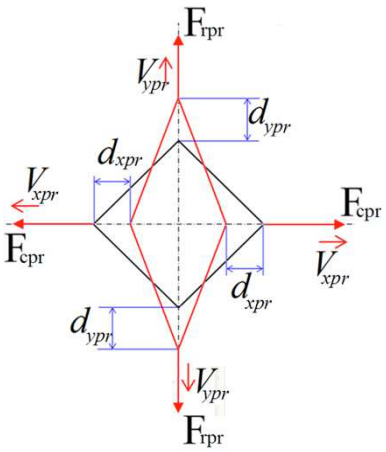


Figure 4.14. The distances moved vertically and horizontally by the corners of Region A and the reaction and transverse forces, $F_{rpr}$ and $F_{cpr}$.

While methods of modelling the shear-tension coupling have been reported recently by Abdiwi, et al. [176], the original NOCM is used here and, for now, an approximate method of modelling the test is employed, using 5 different polynomial shear force versus shear angle input curves to model the shear resistance for each of the 5 transverse loading conditions (see Chapter 2) (5, 37, 50, 75 and 100N for wrPP and 5, 27, 50, 75 and 100N for cgPP). The truss properties chosen for the truss elements here (stiffness = 6 GPa for wrGF and 14 Gpa for cgPP, length= 0.012375 m, circular cross-sectional area 0.000001 $m^2$ gives an area per unit length, $A_2$, of 7.143e-5 $m^2$ for dry glass plain fabric and for commingled glass/polypropylene) produce a sheet with a tensile response between about 5.56 and 13.53 times lower than an actual woven glass fabric and 8.63 and 21.02 times lower than the commingled glass/polypropylene fabric. In order to obtain good agreement between the experimental and predicted results, the measured shear force versus shear angle $F_s$-$\theta_m$ experimental shear compliances need to be normalized. Harrison [177] recently developed a theoretical technique for normalizing the BBE results; future work will involve application of this method to enable rapid and accurate normalization of BBE test results for use in a shear-tension coupled model. In this work, the same normalization method as used in (subsection 4.5.1 (c) in Chapter 4) has been employed. Using that process a good agreement between the experimental and predicted $F_s$-$\theta_m$ was achieved after about 2 to 3 iterations. The resulting coefficients of the 5$^{th}$ and 9$^{th}$ order polynomial input curves found using this iterative normalization process, for each of the tests are listed in (Table 4.4 and 4.5) of the two materials wrGF and cgPP respectively.

Table 4.4. the coefficients of the BBE normalised shear compliances of wrGF with different transverse forces

| Coefficients | $F_{cp}$ (N) | | | | |
|---|---|---|---|---|---|
| | 5 | 37 | 50 | 75 | 100 |
| 1 | -2.4E-09 | 2.04E-07 | 4.6E-07 | 2.75E-07 | 7.96E-08 |
| 2 | 6.9E-08 | -2.9E-05 | -7.8E-05 | -4.7E-05 | -8.7E-06 |
| 3 | 7.88E-05 | 0.001638 | 0.005313 | 0.003571 | 0.001155 |
| 4 | -0.00303 | -0.03595 | -0.15645 | -0.12609 | -0.06912 |
| 5 | 0.077822 | 0.584837 | 2.211267 | 2.276088 | 2.087169 |
| 6 | 0 | -1E-07 | -0.0001 | -0.0001 | -0.0001 |

Table 4.5. the coefficients of the BBE normalised shear compliances of cgPP with different transverse forces

| Coefficients | $F_c$ (N) | | | | |
|---|---|---|---|---|---|
| | 5 | 37 | 50 | 75 | 100 |
| 1 | 1.06E-12 | 1.28E-12 | 2.13E-12 | 3.58E-12 | 4.25E-12 |
| 2 | -2.74E-10 | -3.29E-10 | -5.49E-10 | -9.24E-10 | -1.10E-09 |
| 3 | 2.92E-08 | 3.50E-08 | 5.84E-08 | 9.83E-08 | 1.17E-07 |
| 4 | -1.66E-06 | -1.99E-06 | -3.32E-06 | -5.59E-06 | -6.64E-06 |
| 5 | 5.51E-05 | 6.61E-05 | 1.10E-04 | 1.86E-04 | 2.20E-04 |
| 6 | -1.09E-03 | -1.31E-03 | -2.18E-03 | -3.67E-03 | -4.36E-03 |
| 7 | 1.27E-02 | 1.53E-02 | 2.55E-02 | 4.29E-02 | 5.09E-02 |
| 8 | -8.58E-02 | -1.03E-01 | -1.72E-01 | -2.89E-01 | -3.43E-01 |
| 9 | 5.51E-01 | 6.61E-01 | 1.10E+00 | 1.86E+00 | 2.20E+00 |
| 10 | -1.10E-01 | -1.32E-01 | -2.19E-01 | -3.70E-01 | -4.39E-01 |

Three numerical blanks that were cut from the predicted large blanks with mesh variability (see assigning initial orientation section) (see Figure 4.15), are used in the BBE FE simulation to investigate the effect of realistic orientation variability on shear compliance. The predicted mean *mu* and the standard deviation *std* of the angles between the tows of the three samples (cut from the large sheet) for use in the BBE simulations are illustrated in Table 4.6.

Table 4.6. The normal distribution statistics of the three samples that cut from the large sheet of the two materials

| Sample Name | wrGF | | cgPP | |
|---|---|---|---|---|
| | $mu_p$ | $std_p$ | $mu_p$ | $std_p$ |
| *IrReg1* | 89.43 | 2.22 | 87.90 | 2.48 |
| *IrReg2* | 90.13 | 2.30 | 87.96 | 2.54 |
| *IrReg3* | 91.57 | 2.27 | 91.20 | 3.01 |

The BBE predicted shear compliances with different orientation variability of the two materials are illustrated in Figures (4.16-4.25) for wrGF and cgPP respectively.

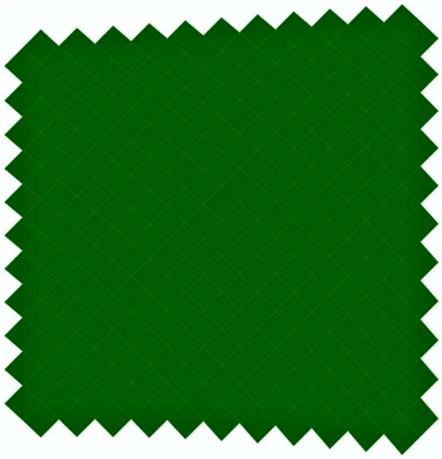

Figure 4.15. Blank of hybrid mesh with mesh variability

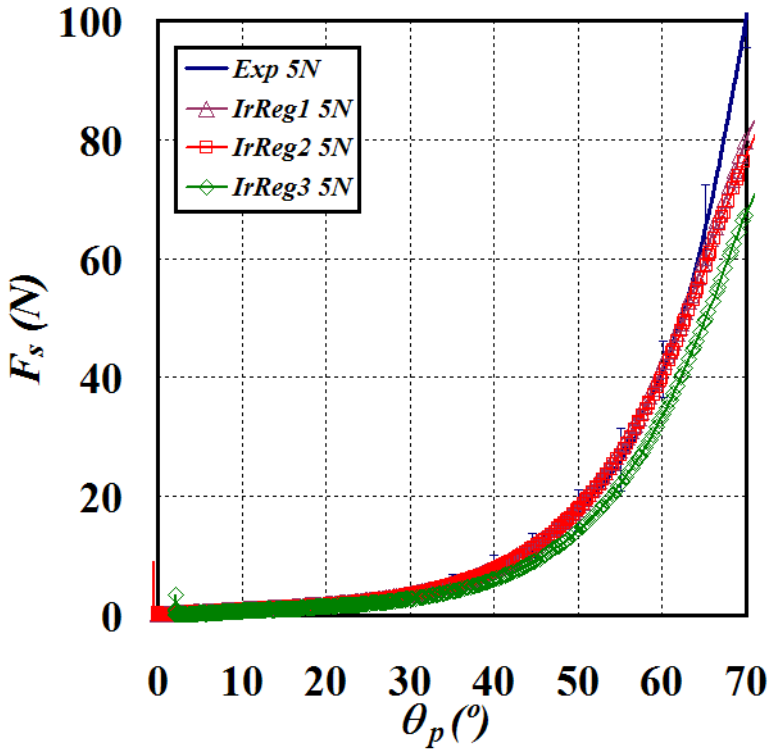


Figure 4.16. Experimental and predicted shear compliances of BBE with 5N transverse force with orientation variability of wrGF

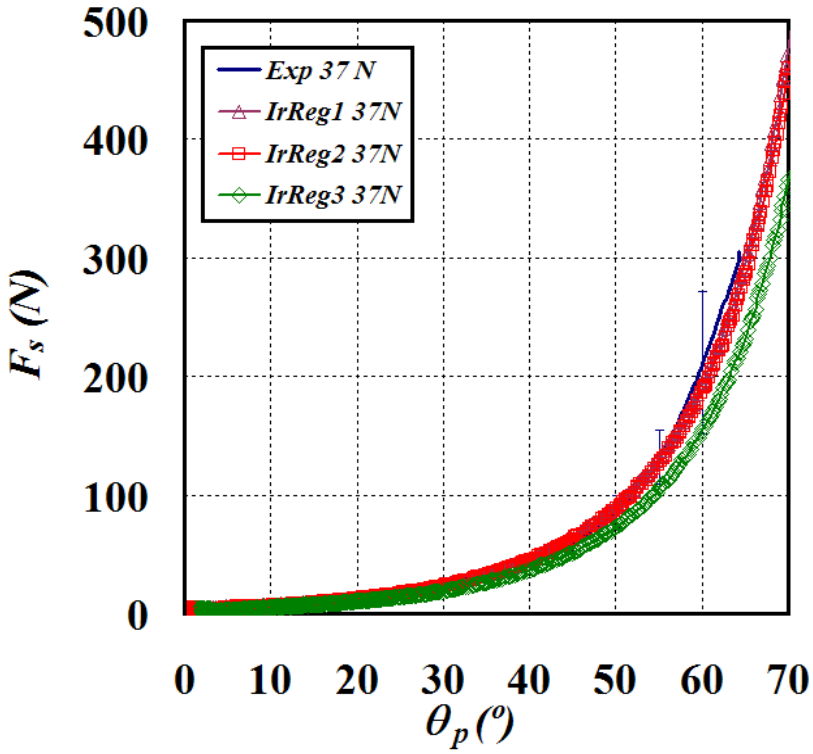


Figure 4.17. Experimental and predicted shear compliances of BBE with 37N transverse force with orientation variability of wrGF

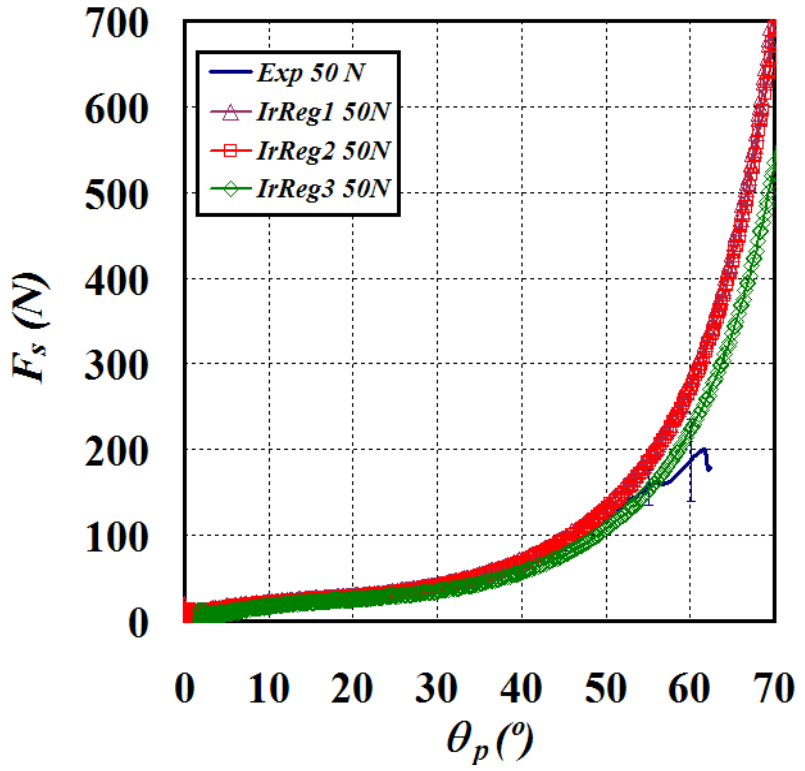


Figure 4.18. Experimental and predicted shear compliances of BBE with 50N transverse force with orientation variability of wrGF

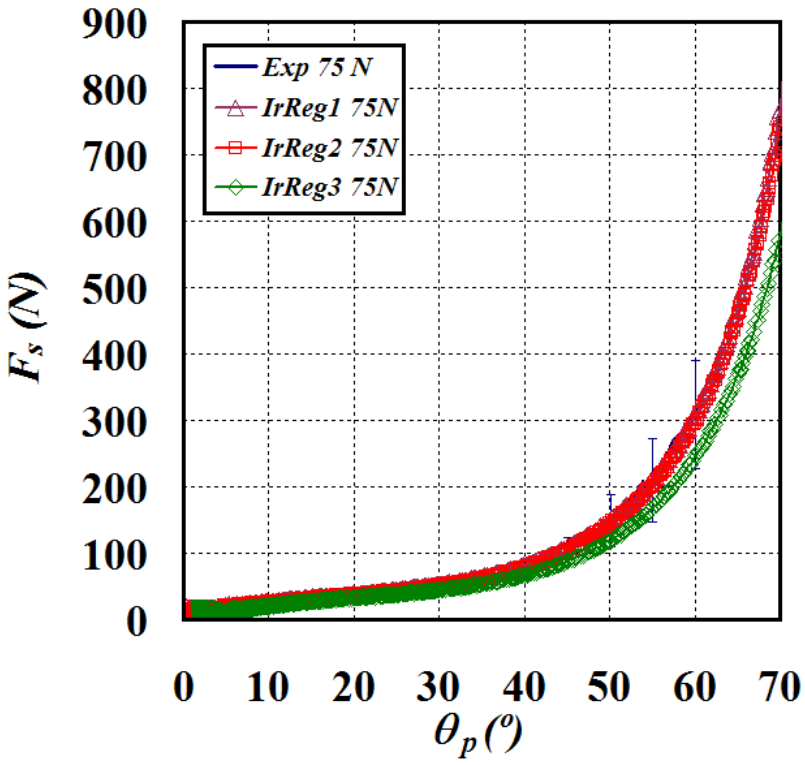


Figure 4.19. Experimental and predicted shear compliances of BBE with 75N transverse force with orientation variability of wrGF.

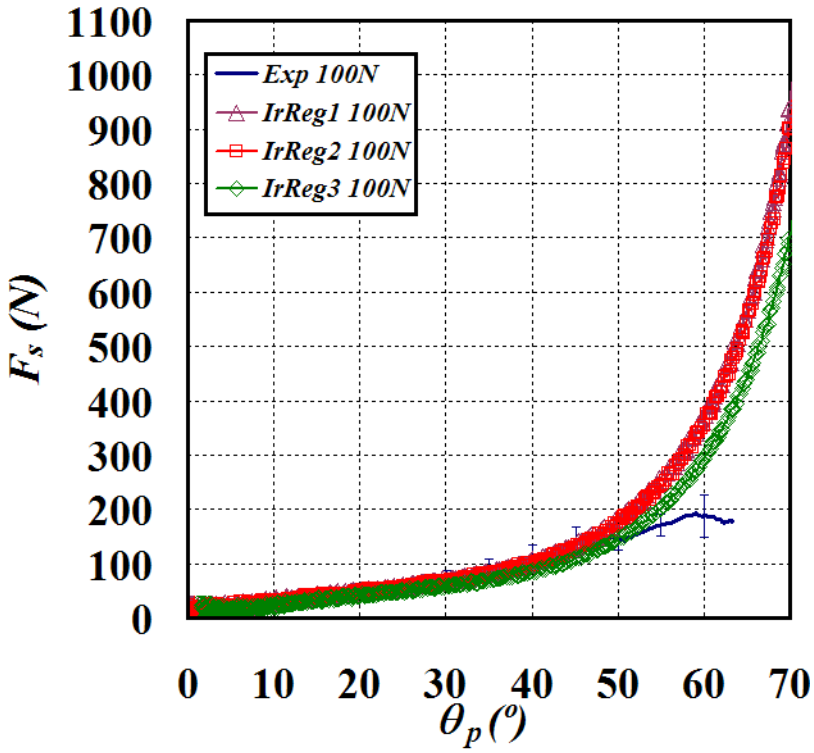


Figure 4.20. Experimental and predicted shear compliances of BBE with 100N transverse force with orientation variability of wrGF.

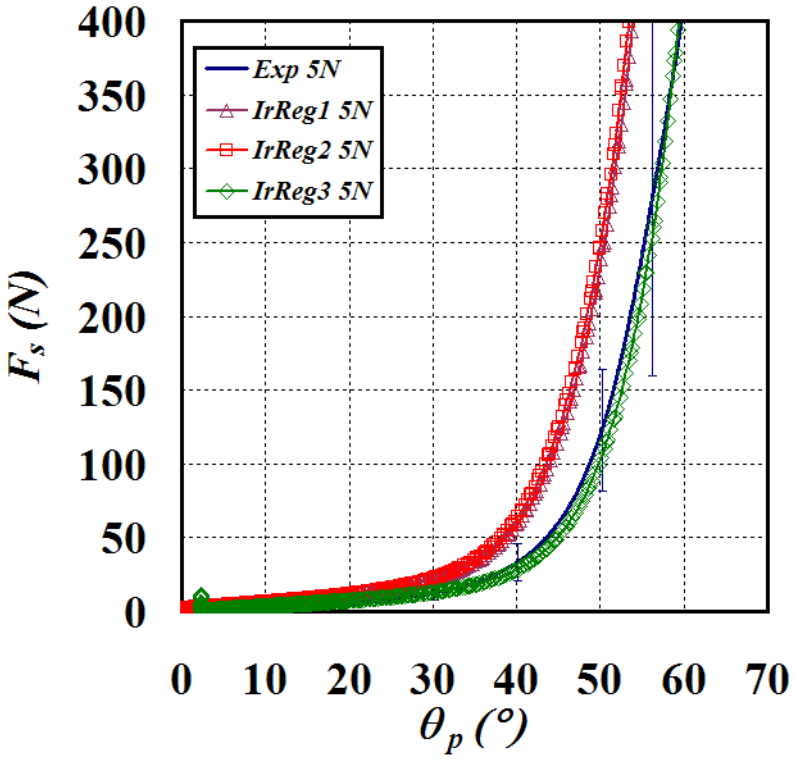


Figure 4.21. Experimental and predicted shear compliances of BBE with 5N transverse force with orientation variability of cgPP.

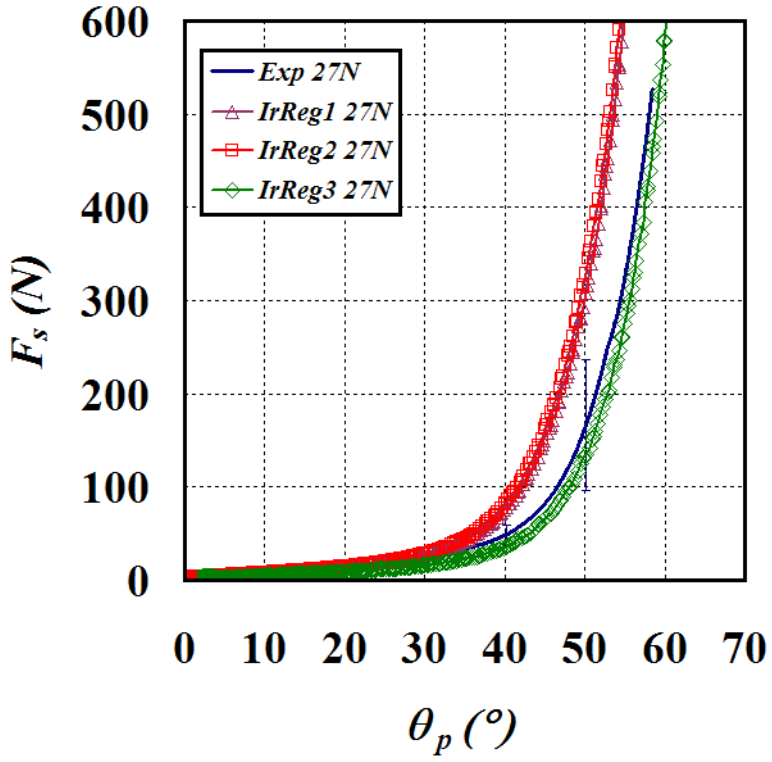


Figure 4.22. Experimental and predicted shear compliances of BBE with 27N transverse force with orientation variability of cgPP.

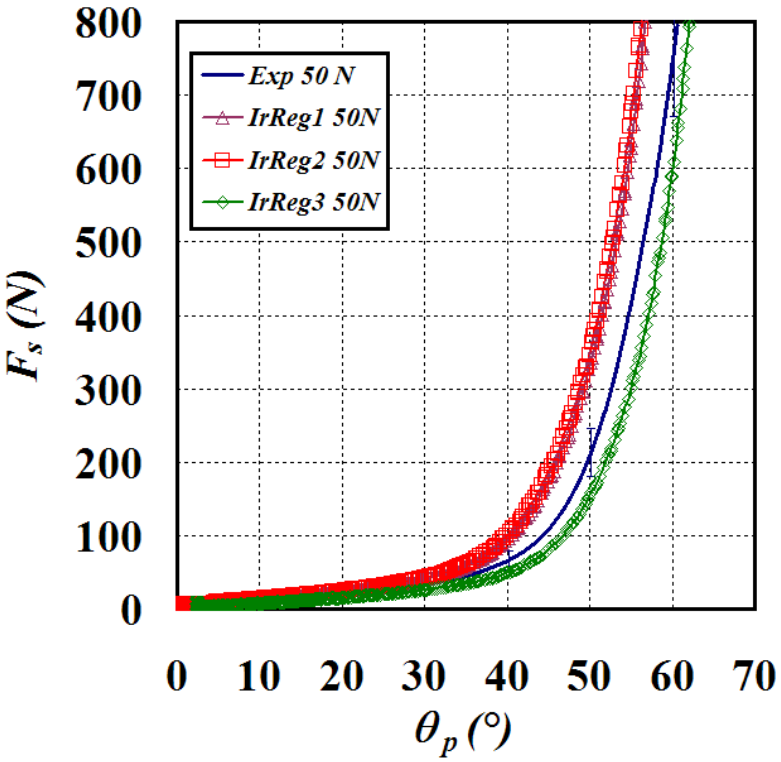


Figure 4.23. Experimental and predicted shear compliances of BBE with 50N transverse force with orientation variability of cgPP.

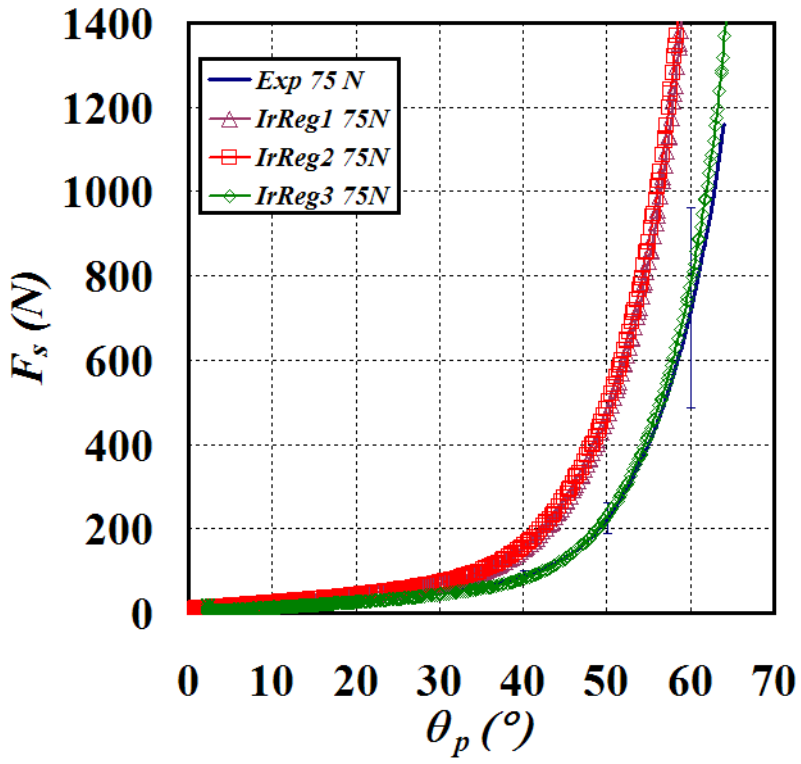


Figure 4.24. Experimental and predicted shear compliances of BBE with 75N transverse force with orientation variability of cgPP.

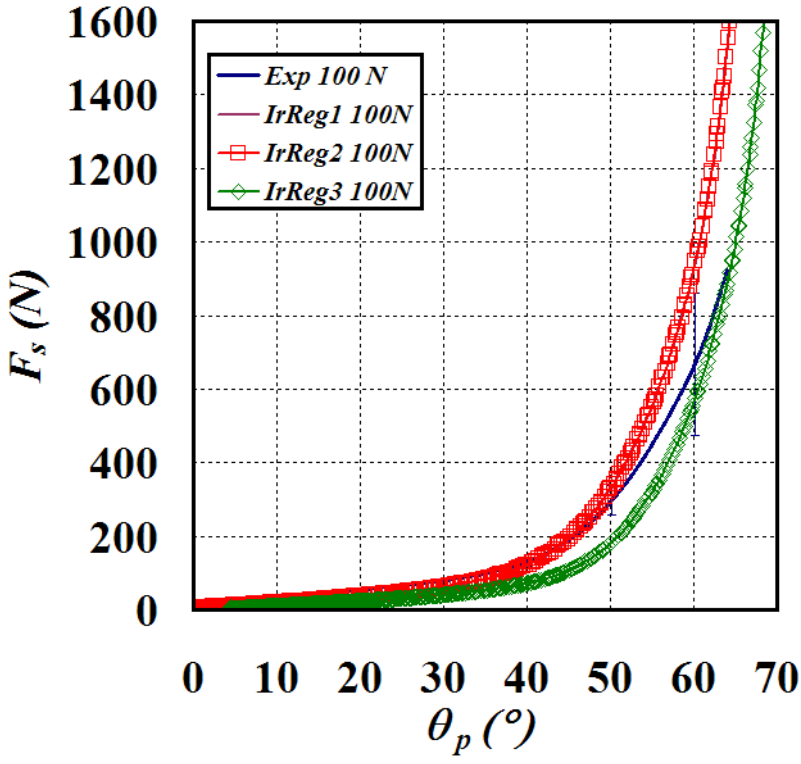


Figure 4.25. Experimental and predicted shear compliances of BBE with 100N transverse force with orientation variability of cgPP.

Simulation results show that *IrReg1* and *IrReg2* are close to the representative experimental result while *IrReg3* is further away, presumably as this test specimen contains a greater amount of pre-shear in the opposite sense of shearing induced by the test than the other two samples. The predictions are consistent with error bars measured in the actual experimental tests, suggesting that tow meander is a likely cause of variability in the BBE tests, a conclusion in agreement with those found by Hivet and Duong [43] and Milani, et al. [165] for PF tests. The absolute size of the variability in predictions increases with the transverse load; this is also to be expected as higher input shear force versus shear angle curves were fitted to each of the tests. The tow meander is shown to produce both higher and lower predictions than the experimental curve, suggesting that tow directional variability is not the cause for the increase in shear resistance attributed to the shear-tension coupling [175], i.e. the shear tension coupling is a real effect and is not attributable to tow directional misalignment.

## 4.6 Modelling the Shear-Tension Coupling of Woven Engineering Fabrics

The deformation kinematics of engineering fabrics during the forming process is dominated by trellis shear. However, tension along yarns also occurs as a result of the blank-holder load applied around the perimeter of the forming blank. Coupling between shear and in-plane tensile stresses is expected in woven engineering fabrics [32, 50, 53]. As such, consideration of the shear–tension coupling, when formulating constitutive models, can possibly result in improved accuracy in subsequent simulations of the forming process both in terms of shear angle and wrinkling predictions. With the exception of Lee, et al. [50] all of the current constitutive models for engineering fabrics assume no coupling between the shear resistance and the tension in a fabric although there is strong evidence to suggest that such a coupling does exist, e.g. see Chapter 2 [175]. In order to incorporate coupling in forming simulation, the shear component of an existing Non-Orthogonal Constitutive Model (S-NOCM) [109, 110] has been enhanced. The new method involves linking the shear compliance in the S-NOCM, which was originally just a function of the shear angle, $F_s=f(\theta)$, with both the shear angle and the tensile stresses along the fibre directions.

The FE model uses the same combination of mutually constrained truss elements (representing the high tensile stiffness fibres) and membrane elements (representing the

shear properties of the fabric) as that described in Section 4.3.2 (b) (see Figure 4.1). The truss element properties for BBE simulations were given in Section 4.5.5. The membrane elements have a initial thickness of 0.0002 m and 0.001 m for GPa for wrGF and cgPP respectively with a Poisson's ratio of 0. The shear stresses within the membrane elements are modelled using an enhanced version of the shear part of the original Non-Orthogonal Constitutive Model [114, 116, 151] (S-NOCM), as discussed in the following section. By replacing the tensile part of the original Non-Orthogonal Constitutive Model (T-NOCM) [114, 116, 151] with truss elements, the stress field within the membrane elements can be completely de-coupled from the tensile stresses occurring along the fibre directions within the membrane element. The shear stress in the membrane elements can consequently be precisely controlled as a function of any of the state dependent variables defined within the user-subroutine used to implement the constitutive model (e.g. shear angle, angular shear rate, temperature or strain along the fibre directions). This strategy has been used recently to create a rate-dependent or viscous constitutive model for thermoplastic advanced composites [35, 114, 178]. The original implementation of the S-NOCM VUMAT user-subroutine has been modified in order to implement a shear-tension coupled version of the model, as described in the next section.

### 4.6.1 Implementation of Shear-Tension Coupling in the S-NOCM

Implementation of the shear-tension coupled S-NOCM involves linking the shear parameters in the original S-NOCM model with the tensile stresses (or equivalently the tensile strains) acting along the warp and weft fibre directions in the fabric. Like the shear angle, the tensile strains are accessible as state-dependent variables within the Abaqus$^{TM}$ user-subroutine. In this section, a method of producing the same shear-tension coupling in the numerical model as that measured in actual woven engineering fabrics is described. The technique involves a four stage process, as follows:

***Stage one*** involves simulating the BBE test; details of the actual experiments of wrGF and cgPP can be found in (Chapter 2). A BBE test sample with dimensions 210 x 210 mm, and a clamping length of 70 mm is modelled (see Figure 4.26) using mutually constrained truss and membrane structural elements (572 truss and 264 membrane elements) as shown in Figure 4.1. Simulations are conducted in two steps. Step one involves application of a constant transverse load, $F_c^i$, equal to the loads used in (Chapter 2) (5, 37, 50, 75 and 100N for wrGF and 5, 27, 50, 75 and 100N for cgPP). The superscript *i* is the experiment number

($i$ = 1 to 5), with each experiment using a different transverse load ($i$ = 1 corresponds to 5N, $i$=2 corresponds to 37N etc). The transverse load is applied to nodes at the edge of the central section of the right and left sides of the blank (Region C in , see Figure 4.26). Step two involves applying a displacement controlled boundary condition on the upper and lower centrally located node-sets at the middle of the top and bottom side lengths of the blank (corresponding to the edge of Region C in [175], see Figure 4.26. The corresponding experimental shear force versus shear angle curves, $F_s^i(\theta)$, measured on a plain weave glass engineering fabric wrGF and a commingled glass/polypropelene fabric cgPP were used as input curves in the standard S-NOCM to conduct these preliminary simulations, here $\theta$ is the shear angle at the centre of Region A (see Figure 4.26). $F_s^i(\theta)$ are initially approximated from the axial load, $F_m(\theta)$, [175] using Eq. (4.23). In Stage 4 of the fitting process, this estimate is improved using a simple normalisation procedure.

$$F_s = \frac{F_m(\theta)}{2\cos(\pi/4 - \theta/2)} \tag{4.23}$$

Note that, to determine $F_m$, contributions to the measured total axial force, $F_T$, from the reaction force, $F_r$, which is caused by application of the transverse clamping load, $F_c$, must first be removed before applying Eq. (4.20). The method of doing this for experimental results is described in [175]. To do this for the numerical results, see Section 4.5.5 in this chapter, Eqs. (4.18 and 4.19).

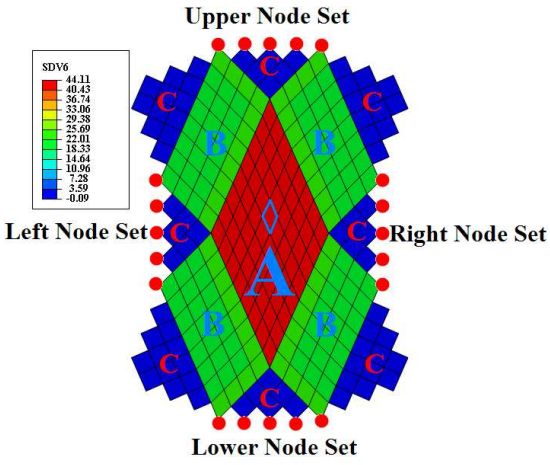


Figure 4.26. The BBE FE model. Force boundary conditions are applied to the right and left, centrally located node sets and vertical displacement boundary conditions are applied to the upper and lower centrally located node sets. The colour legend indicates the shear angle. The three different deformations occurring in Regions A, B and C of the test specimen are clearly visible. The shear angle in Region A is taken from the highlighted element.

***Stage two*** involves determining the average tensile strains, $\Psi$, along the warp and weft fibre directions, $\varepsilon_{warp}$ and $\varepsilon_{weft}$ as a function of the shear angle for $i$ = 1 to 5. The tensile strains are given as state-dependent variables within the VUMAT user-subroutine and have been verified to be the same as the tensile strains occurring along the truss elements bounding the corresponding membrane element. The average tensile strain across the entire specimen along the two fibre directions is determined as a function of the shear angle in Region A, by taking an average of $\varepsilon_{warp}$ and $\varepsilon_{weft}$ from a selection of elements across both Regions A and B. The average fibre tensile strain is plotted for each value of the transverse loads, $F_c^i$, as a function of the shear angle and a polynomial curve is fitted to the data from each of the five simulations, $\psi_p^i(\theta)$, the coefficients of which are stored for later reference by the enhanced S-NOCM code during the course of the simulations (the $p$ subscript indicates this is a fitted polynomial function). Thus, each shear force input curve, $F_s^i(\theta)$ has a corresponding average fibre strain curve $\psi_p^i(\theta)$.

*Stage three* involves implementing the shear-tension coupling in the VUMAT user-subroutine. To do this, code has been added within the original VUMAT user-subroutine for the S-NOCM to compare the value of $\Psi$ in each membrane element at each time increment against the values of $\psi_p^i(\theta)$ using the shear angle within the element (also given as a state dependent variable in the VUMAT user subroutine). Depending on the value of $\Psi$, the code assigns the appropriate shear force curve, $F_s^i(\theta)$ to the element using the algorithm given in the flow chart Figure 4.27. The shear stress within the element is then determined using the S-NOCM.

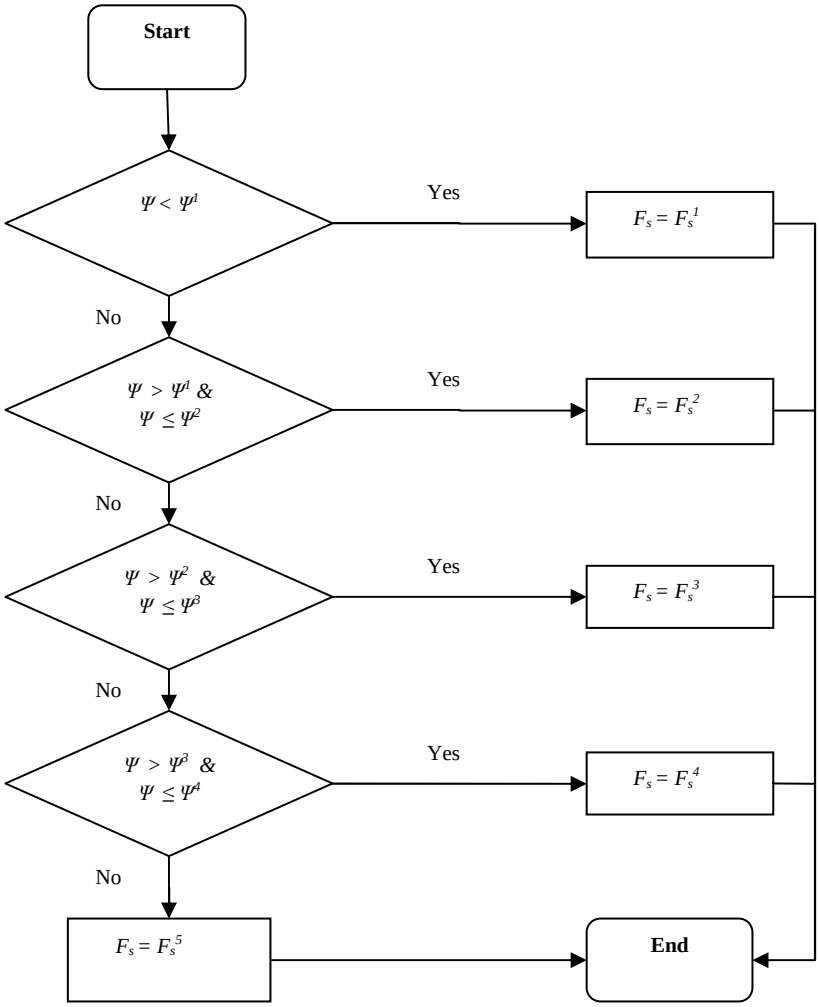


Figure 4.27. The flow chart of shear-tension coupling algorithm which runs for each membrane element at every time increment during a simulation.

Thus the shear force input curve is now a function of both the shear angle and the fibre strain within the membrane element. The process is illustrated in Figure 4.28, which shows actual shear force data measured in experiments, and values of the average tensile strain along the fibre directions predicted in the FE simulations of the BBE test (see Figure 28). The process of assigning the appropriate shear force versus shear angle curve is described and illustrated in Figure 4.28 using a specific example. Note that in Figure 4.28, only data correspnding to tranvserse loads of 5, 50 and 100N are shown in order to simplify the figure.

Consider an element that has a shear angle of $45^o$ at time *t*. The average tensile strain, $\Psi$, inside the element is determined, in this case the value is 0.03. An orange point indicates the ($\theta$, $\Psi$) co-ordinate in Figure 4.28. The algorithm shown in Table 4.7 is run to determine

where the average tensile strain in the element, $\Psi$, lies in relation to the average tensile strain versus shear angle polynomial curves, $\psi_p^i(\theta)$ (plotted as black lines in Figure 4.28). Once the appropriate polynomial is identified and assigned to the element (the assignment is indicated by a blue arrow in Figure 4.28), in this case $i$ = 3 for the 50N transverse load, then the corresponding shear force versus shear angle curve, $F_s^i(\theta)$ (plotted as red lines in Figure 4.28) is also assigned to the element, indicated by a red arrow in Figure 4.28. $F_s^i(\theta)$ is used to determine the shear stiffness of the membrane element using the S-NOCM, as has previously been described in detail in [110].

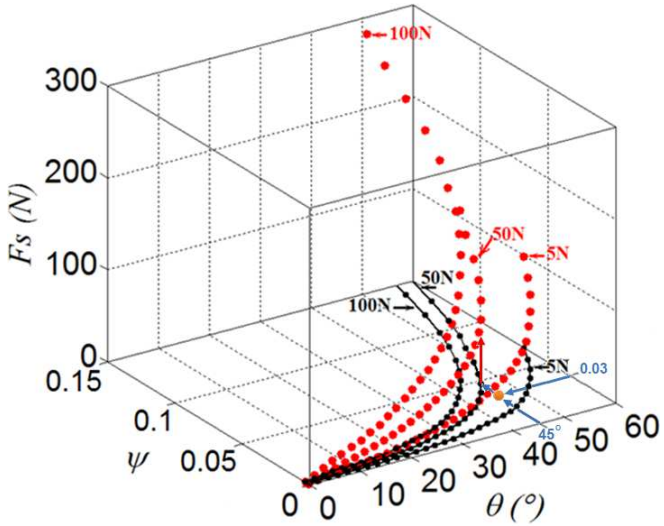


Figure 4.28. Shear force plotted against the shear angle, $\theta$, and the average fibre strain, $\psi$. Black lines indicate the average tensile strain versus shear angle polynomial curves plotted in ($\theta$,$\psi$) 2-D space, red lines indicate the corresponding shear force versus shear angle curves, plotted in the ($\theta$, $\psi$, $F_s$) 3-D space.

At this point it is possible to compare the results of the coupled S-NOCM, or 'CS-NOCM', against the experimental input data, as shown in Figure 4.29. Here, experimental data from (Chapter 2 of wrGF) are plotted as thin continuous lines with error bars (a different colour for each transverse load) and numerical predictions are plotted as thick continuous lines (the same colour as the corresponding experimental curve). Agreement between numerical prediction and experimental input curve is quite poor at this stage as the experimental shear force input curves supplied to the code are not yet normalised. A theoretical method to normalise BBE test results for materials with a strong shear-tension coupling was described in detail in [177]. The method requires custom software to retrieve the underlying normalised data via an automated iterative process. Future work will involve

use of this theory for accurate and fast normalisation. For now, a simpler approximate normalisation technique is described in the final stage, stage 4, of the fitting process.

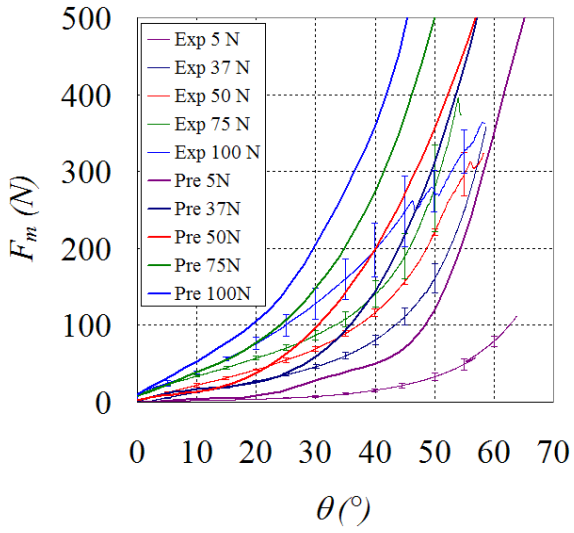


Figure 4.29. Comparison between the experimental and the predicted results using non normalized $F_s$-$\theta$ of BBE 3:1 in the CS-NOCM

***Stage 4*** involves normalising the experimental input curves such that the numerical simulations produce approximately the same shear force versus shear angle predictions as those observed in experiments. To do this, normalised input shear curves are obtained by the following iterative method: (i) the input shear force versus shear angle curves are divided by the predicted shear force versus shear angle curves to produce a ratio (also a function of the shear angle), (ii) polynomial functions, $R_p^i(\theta)$, are fitted to each ratio curve, (iii) input curves are multiplied by the ratio curves to produce a next generation of input curves, (iv) the process is repeated until reasonable agreement between numerical BBE test predictions and experimental results is obtained. Normally around three iterations are required. Figure 4.30 and 4.31 show the comparison between the original experimental results and the final predicted shear force versus shear angle curves after conducting this normalisation process for wrGF and cgPP. The agreement between numerical predictions and experimental data is clearly improved compared to Figure 4.29. The shear compliance $F^i_s$-$\theta$ and the strain functions' $\psi^i$-$\theta$ coefficients of BBE 3:1 FE simulation using coupling NOCM are illustrated in Tables 4.8-4.11 for wrGF and cgPP respectively.

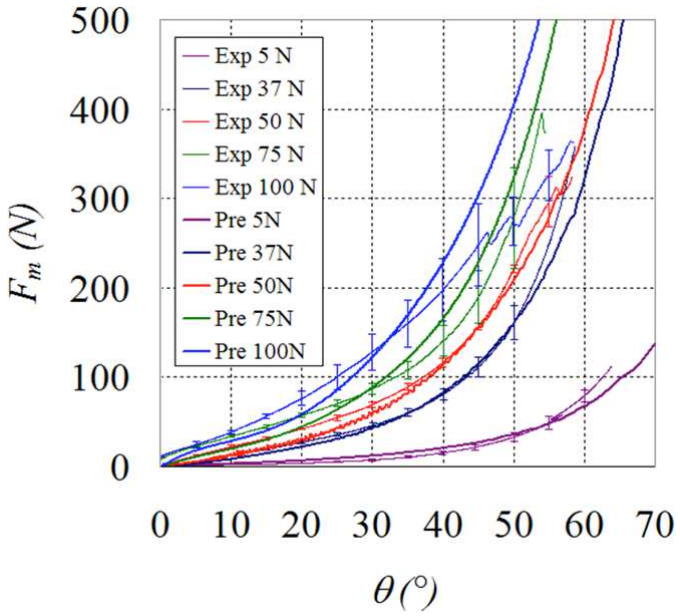


Figure 4.30. Comparison between the experimental and the predicted results of wrGF using the CS-NOCM and normalized $F_s$-$\theta$ input curves from the BBE 3:1 simulations.

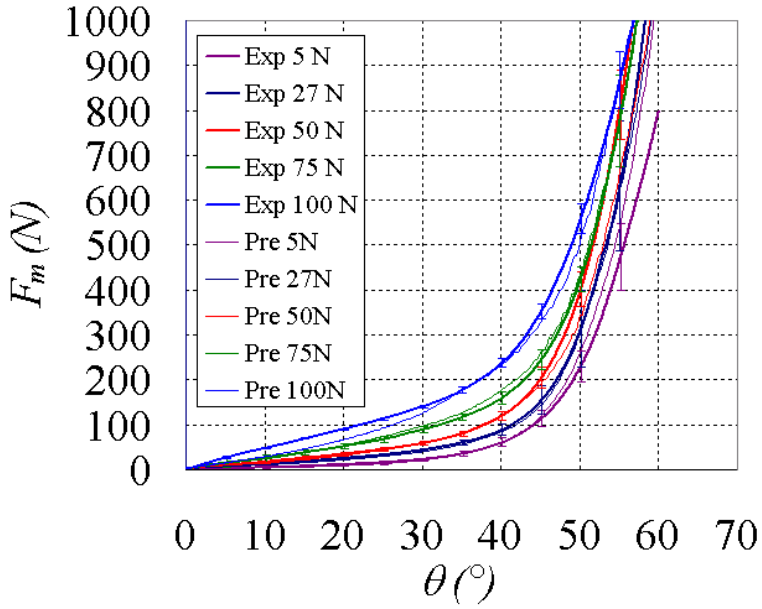


Figure 4.31. Comparison between the experimental and the predicted results of cgPP using the CS-NOCM and normalized $F_s$-$\theta$ input curves from the BBE 3:1 simulations

Table 4.8. The coefficients of the BBE normalised shear compliances of wrGF with different transverse forces

| $Fs$-$\theta$ | | | | | | |
|---|---|---|---|---|---|---|
| Coefficients | $F_c$ (N) | | | | | |
| | 5 | 37 | 50 | 75 | 100 | 125 |
| 1 | 6.52E-15 | 1.18E-12 | -7.00E-14 | -2.34E-12 | -2.99E-12 | -2.39E-12 |
| 2 | -1.86E-12 | -3.47E-10 | 3.86E-11 | 7.54E-10 | 9.12E-10 | 7.20E-10 |
| 3 | 2.17E-10 | 4.17E-08 | -7.87E-09 | -1.00E-07 | -1.14E-07 | -8.90E-08 |
| 4 | -1.33E-08 | -2.66E-06 | 7.86E-07 | 7.12E-06 | 7.58E-06 | 5.80E-06 |
| 5 | 4.60E-07 | 9.77E-05 | -4.23E-05 | -2.91E-04 | -2.86E-04 | -2.14E-04 |
| 6 | -9.11E-06 | -2.08E-03 | 1.25E-03 | 6.86E-03 | 6.18E-03 | 4.51E-03 |
| 7 | 1.01E-04 | 2.48E-02 | -1.96E-02 | -8.96E-02 | -7.30E-02 | -5.17E-02 |
| 8 | -4.74E-04 | -1.40E-01 | 1.58E-01 | 5.90E-01 | 4.36E-01 | 3.05E-01 |
| 9 | 4.78E-03 | 6.98E-01 | 3.55E-01 | -4.02E-01 | 4.46E-01 | 1.22E+00 |
| 10 | 0.00E+00 | 0.00E+00 | 0.00E+00 | 0.00E+00 | 0.00E+00 | 0.00E+00 |

Table 4.9. The coefficients of the BBE strain function as function in shear angle of wrGF with different transverse forces

| $\Psi_{i\text{-}n}$-$\theta$ | | | | | | |
|---|---|---|---|---|---|---|
| Coefficients | $F_c$ (N) | | | | | |
| | 5 | 37 | 50 | 75 | 100 | 125 |
| 1 | 4.04E-07 | 9.48E-08 | 4.42E-08 | -8.31E-08 | -3.28E-07 | -8.19E-07 |
| 2 | -7.58E-05 | -2.74E-05 | -1.37E-05 | 1.98E-05 | 8.32E-05 | 2.08E-04 |
| 3 | 5.93E-03 | 3.27E-03 | 1.75E-03 | -1.96E-03 | -8.79E-03 | -2.19E-02 |
| 4 | -2.54E-01 | -2.09E-01 | -1.19E-01 | 1.04E-01 | 5.02E-01 | 1.24E+00 |
| 5 | 6.55E+00 | 7.75E+00 | 4.75E+00 | -3.12E+00 | -1.66E+01 | -4.08E+01 |
| 6 | -1.03E+02 | -1.70E+02 | -1.13E+02 | 4.91E+01 | 3.17E+02 | 7.77E+02 |
| 7 | 9.68E+02 | 2.16E+03 | 1.61E+03 | -2.31E+02 | -3.18E+03 | -8.02E+03 |
| 8 | -4.79E+03 | -1.44E+04 | -1.23E+04 | -2.60E+03 | 1.28E+04 | 3.73E+04 |
| 9 | 1.18E+04 | 5.04E+04 | 5.38E+04 | 4.58E+04 | 2.73E+04 | -6.38E+03 |
| 10 | 1.12E+04 | 8.76E+04 | 1.20E+05 | 1.82E+05 | 2.44E+05 | 3.03E+05 |

Table 4.10. The coefficients of the BBE normalised shear compliances of cgPP with different transverse forces

| *Fs-θ* | | | | | |
|---|---|---|---|---|---|
| Coefficients | $F_c$ (N) | | | | |
| | 5 | 27 | 50 | 75 | 100 |
| 1 | 1.04E-12 | 1.35E-12 | 2.35E-12 | 1.95E-12 | -1.60E-12 |
| 2 | -3.23E-10 | -4.71E-10 | -8.43E-10 | -7.61E-10 | 4.40E-10 |
| 3 | 4.12E-08 | 6.41E-08 | 1.17E-07 | 1.12E-07 | -4.67E-08 |
| 4 | -2.79E-06 | -4.49E-06 | -8.32E-06 | -8.47E-06 | 2.26E-06 |
| 5 | 1.09E-04 | 1.78E-04 | 3.34E-04 | 3.62E-04 | -3.98E-05 |
| 6 | -2.49E-03 | -4.08E-03 | -7.68E-03 | -8.94E-03 | -3.34E-04 |
| 7 | 3.17E-02 | 5.17E-02 | 9.78E-02 | 1.22E-01 | 1.91E-02 |
| 8 | -2.03E-01 | -3.29E-01 | -6.20E-01 | -8.27E-01 | -1.87E-01 |
| 9 | 6.92E-01 | 1.20E+00 | 2.15E+00 | 3.19E+00 | 2.84E+00 |
| 10 | -5.06E-02 | 0.00E+00 | 0.00E+00 | 1.03E-01 | -6.54E-03 |

Table 4.11. The coefficients of the BBE strain function as function in shear angle of cgPP with different transverse forces

| $\Psi_{i\text{-}n}$-$\theta$ | | | | | |
|---|---|---|---|---|---|
| Coefficients | $F_c$ (N) | | | | |
| | 5 | 27 | 50 | 75 | 100 |
| 1 | 5.25E-07 | -1.75E-07 | 1.43E-08 | 3.49E-07 | 4.14E-06 |
| 2 | -1.28E-04 | 5.08E-05 | -2.00E-06 | -6.50E-05 | -8.49E-04 |
| 3 | 1.30E-02 | -5.78E-03 | 2.46E-04 | 5.01E-03 | 7.30E-02 |
| 4 | -7.16E-01 | 3.38E-01 | -2.86E-02 | -2.15E-01 | -3.40E+00 |
| 5 | 2.30E+01 | -1.10E+01 | 1.91E+00 | 6.00E+00 | 9.29E+01 |
| 6 | -4.33E+02 | 2.00E+02 | -6.52E+01 | -1.18E+02 | -1.50E+03 |
| 7 | 4.50E+03 | -1.90E+03 | 1.14E+03 | 1.58E+03 | 1.37E+04 |
| 8 | -2.27E+04 | 7.62E+03 | -9.69E+03 | -1.23E+04 | -6.45E+04 |
| 9 | 4.13E+04 | -5.26E+02 | 3.97E+04 | 5.40E+04 | 1.44E+05 |
| 10 | 3.23E+03 | 2.61E+04 | 4.78E+04 | 7.27E+04 | 9.94E+04 |

To test the effectiveness of the modelling approach two final BBE simulations of wrGF are conducted, this time using transverse loads increasing linearly in time from 5N to 100N rather than using constant transverse loads. In Figure 4.32a and 4.32b the grey curves are experimental results originally reported in [175] and the black curves are the numerical predictions following the approximate normalisation process decribed in Stage 4, when applying constant transverse loads of 5, 37, 50, 75 and 100N (the same information is shown in Figure 4.30). The blue curves in Figure 4.32a and 4.32b are the results predicted by the CS-NOCM when increasing transverse loads are applied over the course of the test. In Figures 4.32c and 4.32d the applied transverse load is plotted against $\theta$ rather than against time, creating slightly non-linear profiles.

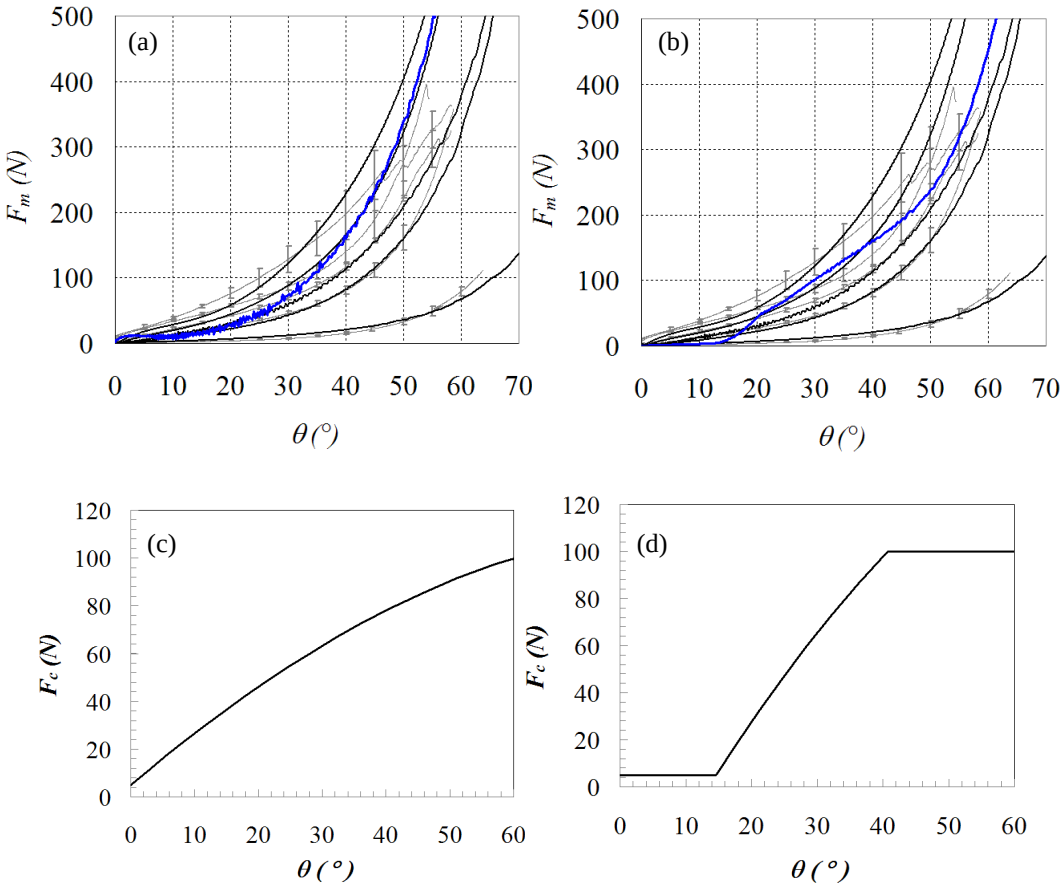


Figure 4.32. Evaluation of the coupled S-NOCM (a) and (b) the faint grey lines are the experimental results from [175], the black lines are the normalised predictions shown in Figure 4.6 and the blue lines are the predicted results when an increasing transverse load is applied to the sides of the specimen. The transverse loading profiles are shown in (c) and (d) respectively.

As expected the axial force predictions of the enhanced shear-tension CS-NOCM, made using increasing transverse loads, move across the normalised numerical predictions

generated using constant transverse loads (the black curves). The different transverse load versus shear angle profiles, $F_c(\theta)$, shown in Figures 4.32c and 4.32d, produce different axial force predictions, as can be seen by comparing Figures 4.32a and 4.32b. The result in Figure 4.32a is close to that which might be expected from the woven glass fabric used in the experimental investigation [175]. However, while the result of Figure 4.32b appears correct until around $30^o$, an unrealistic softening is apparent above this shear angle. Thus, at this point the predictions of the model have been found to be qualitively correct under simple loading conditions though can show unexpected behaviour under more complex loading. Possible explanations for the unexpected predictions could be related to the choice of elements used to create the average strain curves, $\psi_p^i(\theta)$. The resulting predictions have been found to be sensitive to this choice; future work may involve using a more refined mesh to model the BBE test and use a larger selection of elements to examine this sensitivity, the normalisation technique used in this work. The very simple normalisation procedure used here takes no account of the shear-tension coupling in the fabric. A more rigorous method was recently proposed in [177]. Future work will aim to employ this method to improve accuracy and reduce the uncertainty in the shape of the input curves passed to the CS-NOCM, the method of calculating the stress increment at each time step. A tangent stiffness matrix has been used to determine this stress increment, i.e.

$$\Delta\sigma_{ij} = \frac{d\sigma_{ij}}{d\theta}.\Delta\theta \tag{4.24}$$

The linearisation process is known to reduce the sensitivity of the technique of using multiple input curves to control the shear compliance of the membrane elements, a point discussed in detail in [88]. Nevertheless, the linearised increment was used in this first attempt to model to the shear-tension coupling, as the method has the advantage of being particularly robust. Future work will focus on improving the sensitivity of the approach, using the methods described in [88].

Despite the irregularities in the predictions of the shear-tension coupled model under certain in-plane loading conditions, it is clear that the technique proposed here produces a shear-tension coupling similar to that seen in actual experiments. Future work will focus on improving the accuracy of the method, though the model predictions are considered to be sufficiently accurate at this stage to begin to examine the question of whether or not, and

also under which conditions, the influence of a shear-tension coupling on the shear angle and wrinkling predictions of complex forming simulations is important.

## 4.7 Conclusion

A method of incorporating realistic tow meander into shear test simulations has been demonstrated. Results suggest tow meander is a significant cause of variability observed in actual BBE tests. Further, because the variability produces both decreases and increases in the measured force, it is apparent that tow meander is almost certainly not the cause of the increase in shear resistance observed in the three shear characterization experimental tests or, in other words, these simulations suggest the shear tension coupling observed in [175] is a real effect and not the result of sample misalignment or tow meander.

A method of modelling the coupling between shear compliance and in-plane tension in woven engineering fabrics has been demonstrated. The method is similar to that used previously to create rate-dependent 'viscous' behaviour using a hypo-elastic model [88] though here the average in-plane strain along the two tow directions, rather than the angular shear rate, is used to control the selection of the shear force versus shear angle curve for use in the non-orthogonal constitutive model (used to relate the shear force and shear stress) [50, 53]. A simple normalisation procedure has been proposed. The sensitivity of the modelling approach is assessed and found to give reasonable results, clearly showing a coupling between shear compliance and in-plane stresses and strains in the fibre directions. Future work will involve refining the modelling and normalisation process in order to improve the accuracy of the predictions. The shear-tension coupled model will be used to evaluate the importance of a shear-tension coupling on the predictions of complex forming simulations.

# 5. Forming Simulation of Woven Engineering Fabric

## 5.1 Introduction

The main aim of forming simulations is the virtual optimisation of forming processes and ultimately the optimisation of the parts' final mechanical properties through exploration of different forming conditions and fabric layups. The aim is to eliminate the empirical trial and error method, which can be very costly. Defects such as wrinkling and the final deformation of the material can be predicted in the design stage by using optimised models. A number of useful outputs can be obtained from forming simulations, such as the fibre directions, which are crucial in determining the mechanical properties of the final formed part and are also key elements in determining the permeability for liquid moulding of engineering fabric preforms. Process induced defects can also be predicted, such as the onset and propagation of wrinkling and the tearing of the fabric [111, 179-182].

In this chapter, novel kart wheel forming tools were designed and manufactured in the School of Engineering workshop at the University of Glasgow, to conduct forming tests on wrGF and cgPP weave fabric material. Then, FE forming simulations of the kart wheel were performed of 0/90 and ±45 orientations using two shear constitutive models: the shear non-orthogonal constitutive model S-NOCM and the coupling shear non-orthogonal constructive model, CS-NOCM. The effect of inherent variability has been also taken into account by using orientation variability measured from the two fabrics, as described in Chapter 3, and then using *Varifab*$^{GA}$ to automatically generate variable finite element meshes used in the FE forming simulations. After that, a comparison between experimental, predicted shear deformation results using the S-NOCM and predicted shear deformation results using CS-NOCM at specified locations on the deformed parts were carried out. Finally, a sensitivity study of the predicted shear deformations due to the alteration in the material and the process parameters (shear compliance, tension stiffness, blank-holder force, punch velocity and coefficient of friction) is reported.

In the following sections a review of prior investigations of the numerical modelling of the forming of advanced composites with complex geometries is provided in order to give an historical overview of the main innovations and current state of the art in this field.

## 5.2 Review of interesting developments in advanced composite forming

In investigating the validity, efficiency and limitation of the numerical modelling approaches that are used in modelling textile composite forming, researchers have utilized different geometries, such as a hemisphere [34, 146, 152, 168, 183-189], double-dome [53, 113, 170, 174, 190-194] , pilot helmet [153, 195, 196], cylinder [32, 197, 198], car hood [199] , cone-shapes [200], aerospace part [201] , tetrahedron [202], square box [111], an industrial complex part [203], a helicopter part [204], and a complex multi-cavity part [152] (see Figure 5.1). All the geometries contain double curvatures providing useful case studies in exploring the potential and limitations of different constitutive models under different forming conditions. Particularly extensive numerical and experimental studies have been carried out using hemispherical and double dome geometries [34, 53, 113, 146, 152, 168, 170, 174, 183-194]. Much of the recent benchmarking work concentrates on using the double dome geometry [53, 113, 170, 174, 190-194], due to some advantages of this geometry over the previous hemisphere benchmark geometry. For example, a hemisphere has one possible initial contact point which gives just one possible shear deformation result using either a kinematic or mechanical forming approach. In contrast, many initial contact points are possible on double dome geometry, which creates issues when using a kinematic forming approach in that different shear deformation results are produced for every starting contact point. The other advantage of double dome geometry is the possibility of investigating the material properties of the deformed part by cutting a piece of consolidated material from the flat surfaces that run along the sides of the geometry (see Figure 5.1b).

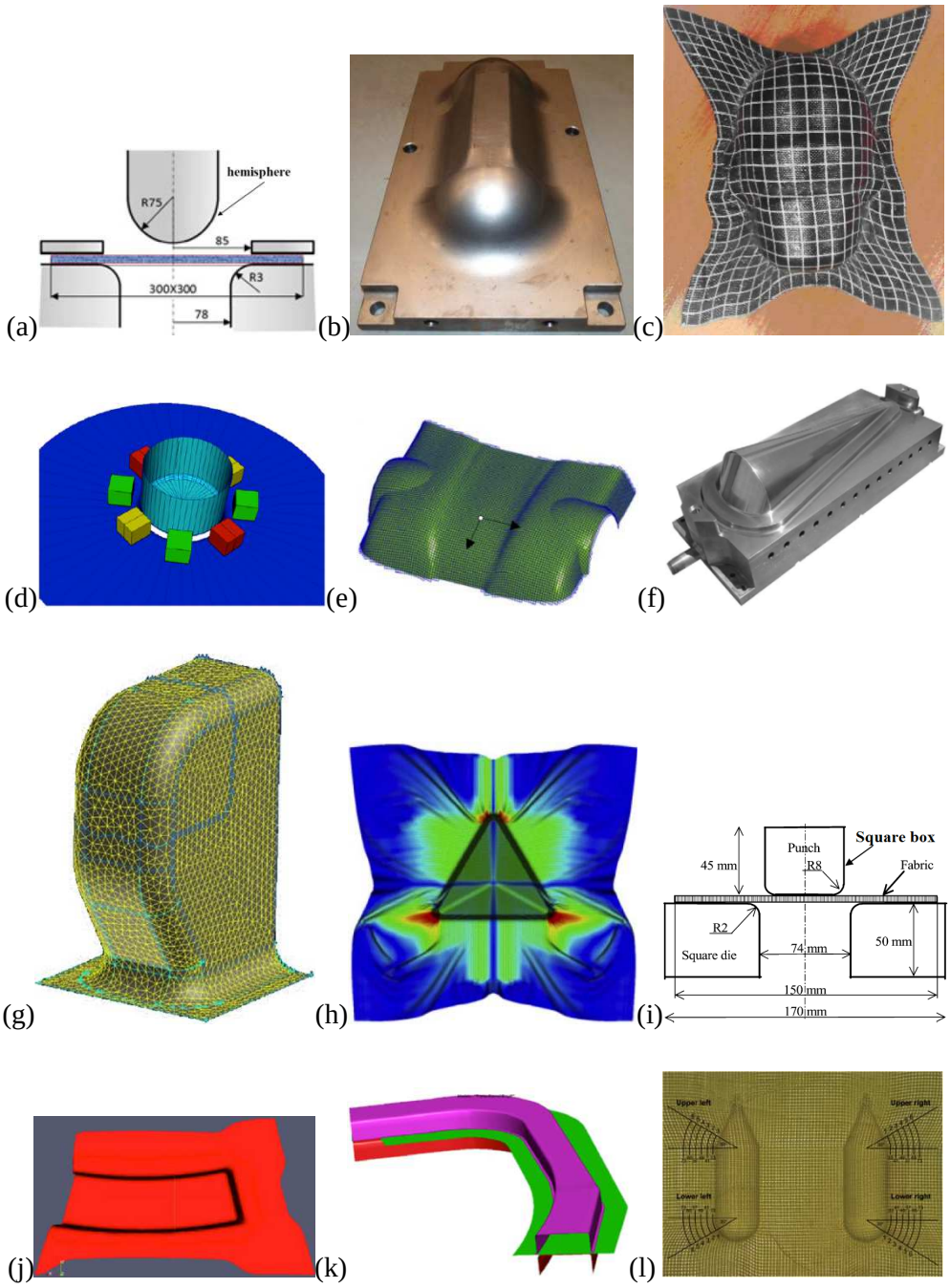


Figure 5.1. Shapes of different geometries were used in forming of advanced composite (a) hemisphere [183], (b) double-dome [174], (c) pilot helmet [153], (d) cylinder [32], (e) car hood [199], (f) cone-shapes [205], (g) aerospace part [200], (h) tetrahedron [201], (i) square box [111], (j) an industrial complex part [202], (k) a helicopter part [203] and (l) complex multi-cavity part [152]

Various researchers have investigated the effects of different constitutive models on local shear deformation and the draw-in shape of the hemispherical textile composite parts [34, 146, 152, 168, 183-189]. An early attempt to model the draping of fabric over a hemispherical mould was carried out by Dong, et al. [184] using an hypoelastic constitutive model. Their updated material model, which tracked fibre directions,

successfully modelled the draw-in shape and the shear deformation, whereas significant discrepancies were observed when using a non-updated material model. Yu, et al. [108], [109, 110] used a hypoelastic model in a forming simulation of asymmetric NCF material using a hemispherical (die and punch) model. The experimental shear deformation results were compared with the model predictions and they found that there were significant differences between the experimental results and the predicted shear deformation on certain position of the hemisphere. An hypoelastic constitutive model similar to that developed by [108-110] was developed by Badel, et al. [168] for the numerical forming simulation of a textile composite over a hemispherical mould. The experimental draw-in shape and shear deformation were in a good correlation with the predicted results, and the out-of plane wrinkling was also predicted accurately. Later, Sadough, et al. [187] conducted a simulation of a quarter hemisphere using the non-orthogonal constitutive model of Peng and Cao [51]. The predicted results were not compared against experimental results. However, comparison of the predictions of their explicit and implicit based FE models showed identical results though the computational time of the implicit code was about twenty times greater than that of the explicit code. In 2007 Skordos, et al. [188] used a visco-elastic model [151] to simulate the effect of different strain rates and in-plane tension on shear deformation and out-of plane buckling. The model predicts the shear deformation field, the maximum value of shear strain and the onset of out-of plane buckling successfully. However, the model underestimated the maximum wrinkling. Lin, et al. [34] utilized the predictive rate/temperature-dependent model of Harrison, et al. [206] which was novel in that shear force vs. shear angle vs. shear rate input data were predicted from the fibre volume fraction, yarn width and matrix rheology [134] and incorporated in the numerical optimisation simulation of textile composite forming. The effect of a localised loading condition on the blank holder and the effect of size and temperature of the blank on wrinkling and shear deformation distribution of a hemisphere were predicted. Optimising the loading distribution on the segmented blank-holder perimeter and use of appropriate temperature were found to be key factors in reducing or eliminating wrinkling. In order to optimise the numerical forming process of a textile composite, Vanclooster, et al. [189] incorporated a predictive frictional model implemented in the VFRIC user subroutine in Abaqus Explicit, based on experimental viscous tool/ply and ply/ply traction tests for modelling the fabric/tool and tool/tool contact in the hypoelastic constitutive model that was developed by Willems [23] through FE simulation. Numerical multilayer forming of dry fabric was investigated and the predicted draw-in shape was found to be very close to the experimental draw-in shape. Later in 2011 Thije ten [207] conducted experimental forming on multi-layered unidirectional

carbon/polyetherketoneketone laminates with a quasi-isotropic {0/90/45/-45}S lay-up and woven 8HS/PPS laminates at 360 C° using a steel punch and cold rubber die. The stack of unidirectional multi-layered laminate was modelled using one blank in which a single element could incorporate several different fibre directions in order to provide fast and accurate forming simulations, however this method means that predictions of delamination between UD layers is not possible. Nevertheless, comparison between the experimental and predicted results of the fibre distribution and the wrinkling pattern show a good agreement.

In 2006 Creech and Pickett [124] took advantage of modern high performance computers to model every individual tow and stitch of dry biaxial non-crimp fabrics at the meso-scale level. Their meso-scale model was used to simulate the forming of impregnated composite on a hemispherical mould. The meso-model demonstrated more accurate fabric deformation mechanisms than both kinematic mapping and mechanical continuum approaches, and excellent agreement of the shear deformation of the deformed hemisphere part between the experimental and predicted forming. Later Boisse, et al. [114], [208] modelled a simple unit cell consisting of few shell elements with 216 Dofs. The reinforcements (fibres, yarns, and unit cells of woven or knit) were considered as a set of elements. The reinforcements were linked together by contact or springs, and were explicitly described. The interaction contact between the yarns and the rotations with respect to each other were all taken into account. The model has been validated by carrying out a PF and a hemispherical forming simulation. The predicted results show natural yarn slippage, lateral yarn compaction, and wrinkling (see Figure 5.2).

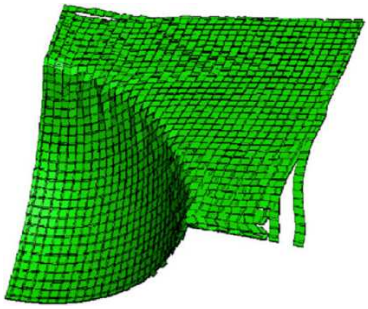

Figure 5.2. Numerically deformed hemispherical part using the 216 Dof shell element FE model

The model of Cherouat and Billoët [35] was validated by conducting a draping simulation on rectangular and circular tables and a forming simulation on a hemispherical dome. The

simulations showed good agreement with the test results in predicting wrinkling and shear deformation. Subsequent, in 2005 Sharma and Sutcliffe [151] developed a model similar to that of Cherouat and Billoët [35]; the difference was to replace the membrane element with a truss element connected diagonally to the vertical nodes.

The hyperelastic model of [143] was also used to successfully simulate the asymmetrical behaviour of an unbalanced fabric by taking into account the differences in the tensile behaviour of the two principal directions of the material (see Figure 5.3). Figures 5.4 shows the draw-in shapes modelled with and without shear compliances. The draw-in shapes predicted with shear stiffness shown in Figures 5.4e and 5.4f more closely predict the experimental draw-in shapes as shown in figures 5.4a and 5.4b than those without shear stiffness shown in figures 5.4c and 5.4d [143].

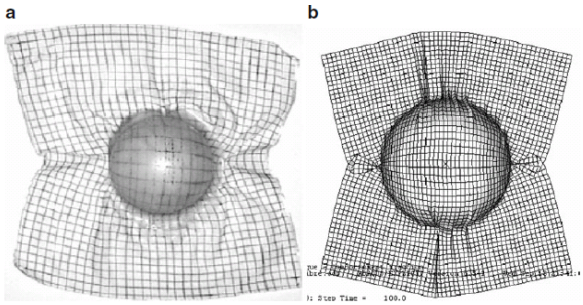


Figure 5.3. The draw-in-in hemispherical shape of non-crimp fabric using the hyperelastic model (a) experimental (b) numerical [143]

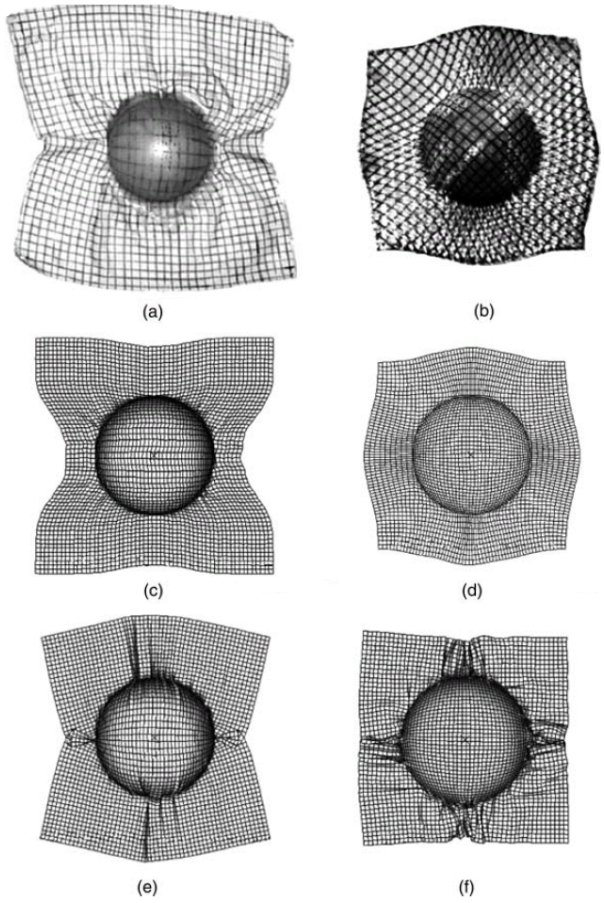


Figure 5.4. (a) The experimental hemispherical part with 0/90° (b) The experimental hemispherical part with ±45° (c) The predicted hemispherical part with 0/90° and without shear compliance (d) The predicted hemispherical part with ±45° and without shear compliance (e) The predicted hemispherical part with 0/90° and with shear compliance (f) The predicted hemispherical part with ±45° and with shear compliance [143]

The double-dome benchmark geometry was provided by Ford Motor Company (Dearborn, Michigan, U.S.A.) to benchmark the potential, efficiency, and limitation of different FE software modelling approaches as applied to the forming of a double-dome geometry [50]. The double dome geometry was proposed in a Woven Benchmark Exercise initiated at ESAFORM in 2003. A number of researchers [53, 113, 170, 174, 190-194] have used the double-dome benchmark geometry in their work to investigate the limitation and validity of their constructive models and to optimise the numerical forming process of textile composites.

Willems [23], [193] and [194] conducted numerical forming simulations of co-mingled glass-PP weave on a hemisphere and double dome geometry for optimizing the forming parameters using two constitutive models: the affine elastic model with the non-orthogonal

constitutive model (T-AEM /S-NOCM) and the affine elastic model with the shear elastic model (T-AEM/S-AEM). Shear deformation results of forming simulations obtained from both models agree well with the experimental results for the material with maximum tensile strain < 1.5%, however only the T-AEM/SAEM demonstrates reasonable shear deformation results when examining 10 times more stretchable material.

Since the mechanical approaches of modelling the material behaviour of textile composite based on FE method are computationally expensive but give good predictions, and the mapping approaches are poor in terms of predicting the deformation especially on moulds that have complex curvatures but are computationally fast, an intermediate mechanical approach that can take the advantages of each approach was introduced by Sharma and Sutcliffe [196] and named the progressive drape mode. Accordingly, the proposed model is an enhanced mechanical model of truss elements with membrane forces included and with low computational cost. Draping simulation has been applied on an hemispherical helicopter pilot helmet using the mapping fish net approach [209], and the results indicated that the enhanced model is able to perform an accurate draping when compared to experimental results, especially on the curvature surface around the ears of the helmet. The results from the progressive drape model were found to be more accurate than a kinematic model.

Later Vanclooster, et al. [113] and Vanclooster, et al. [192] also performed a comparative study between the kinematic and mechanical draping approaches [41]. They concluded that the shear deformation results predicted from the kinematic mapping approach were not in good agreement with the measured results when unsymmetrical forming arrangements are used. By contrast, the mechanical approach produces a more precise prediction and appears to be the best technique in terms of draping simulation.

Khan, et al. [190], Khan, et al. [155] and Khan, et al. [170] conducted experimental forming tests of dry woven fabric on double dome benchmarked moulds and numerical forming simulations using their hypoelastic constitutive model [155, 170]. The predicted draw-in shape and the shear deformation of the predicted forming simulation were found to be in good agreement with the experimental results. Peng and Rehman [191] validated the non-orthogonal constitutive hypoelastic model developed by Peng and Cao [51] by

conducting forming simulations of balanced plain weave composite with two initial orientations 0/90° and ±45° on a benchmark double-dome mould. The predicted draw-in shape and the shear deformation results from the non-orthogonal constitutive model were found to be in good agreement with the experimental results.

Lee, et al. [50] was the first to perform a macro-scale forming simulation of a balanced commingled glass/polypropylene plain weave fabric on double-dome mould using a non-orthogonal model that incorporated a shear-tension coupling. Predicted shear deformation results, punch force histories and draw-in shape from coupled and non-coupled constitutive models were compared, and they found that the result using the shear-tension coupling model was such that the shear deformation decreased and the punch force increased [53].

Recently Harrison, et al. [174] has carried out experimental and numerical forming tests of 0/90° pre-consolidated unidirectional cross-ply advanced thermoplastic composite on a benchmark double-dome moulds using the Stress Power constitutive model [88]. In-plane tension is applied on the tested blanks in the experimental and predicted forming simulation using clips and springs rather than a blank holder due to the need to heat the entire part, a goal that is difficult when using blank-holder. The predicted shear deformation results at points 11-20 (the locations used by Khan, et al. [170] for the 0/90 sheet orientation case) were compared with the experimental results obtained by Khan, et al. [170]. Also, results obtained using woven fabric, different boundary conditions and blank shape were compared to results of Harrison, et al. [174]. The predicted shear deformation results at points 1-10 were in close agreement with the experimental results, whereas only approximate agreement was observed at points 11-20 (see Figure 5.5).

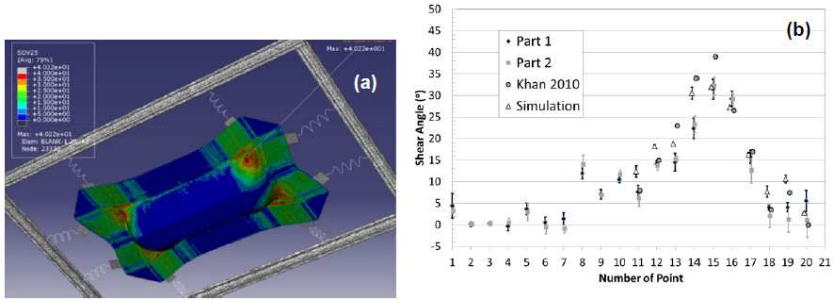


Figure 5.5. (a) The predicted shear deformation contour plot (b) Shear deformation of double-dome part from [174]

Long, et al. [195] used a simple finite element model [151], which consists of five truss elements (four elements on the perimeter of the unit square cell model with the tension in the tows, whereas the fifth element is in the horizontal diagonal and models the shear compliance) in modelling a woven carbon/epoxy prepreg helicopter pilot helmet using a thermoforming approach. The thermoforming approach is adopted from the metal and plastic thermoforming processes and uses a sophisticated segmented blank-holder. The segmented blank-holder when integrated with a binary genetic algorithm was used in optimising the pressure distribution so as to obtain a formed part free from, or with reduced, wrinkling. By allowing the peripheral elements to be subjected to compressive deformation, the out-of plane buckling was modelled. Optimising the pressure distribution profile on the 0/90° and ±45° woven blank perimeter using a genetic algorithm method leads to decreasing the maximum wrinkling deformation from 20% to 14% and 15% to 8% for both cases respectively (see Figures 5.6 and 5.7).

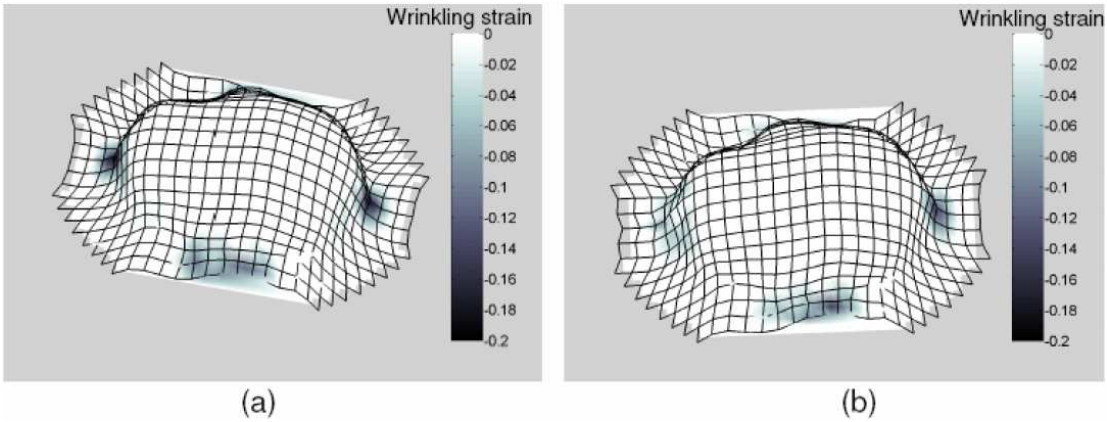


Figure 5.6. The 0/90° formed part (a) with non-optimised blank-holder force (b) with optimised blank-holder force[195]

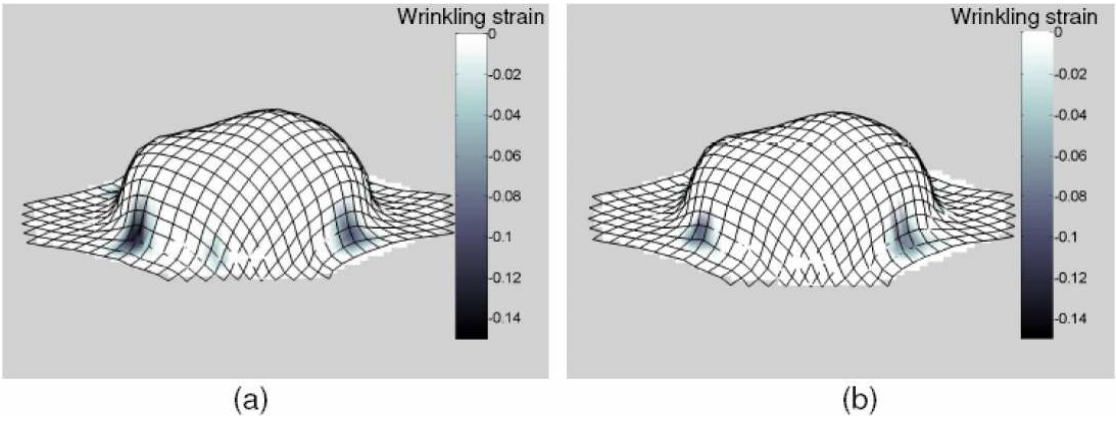


Figure 5.7. The ±45° formed part (a) with non-optimised blank-holder force (b) with optimised blank-holder force [195]

Studies of optimising the prediction potential of the formed part profile and wrinkling has been carried out by [32, 111, 181, 182, 197]. Yu, et al. [59] and later, in 2005 Boisse, et al. [111], [181, 182] used a semi-discrete approach to demonstrate the importance of correctly predicting the out-of-plane buckling. Hamila and Boisse [181] have added a shear compliance to the semi-discrete model and then conducted a draping simulation on a cylindrical geometry to predict wrinkling, which appears very clearly when shear compliance was added see Figure 5.8b. Wrinkling was not predicted when the shear compliance was not added (see Figures 5.8a).

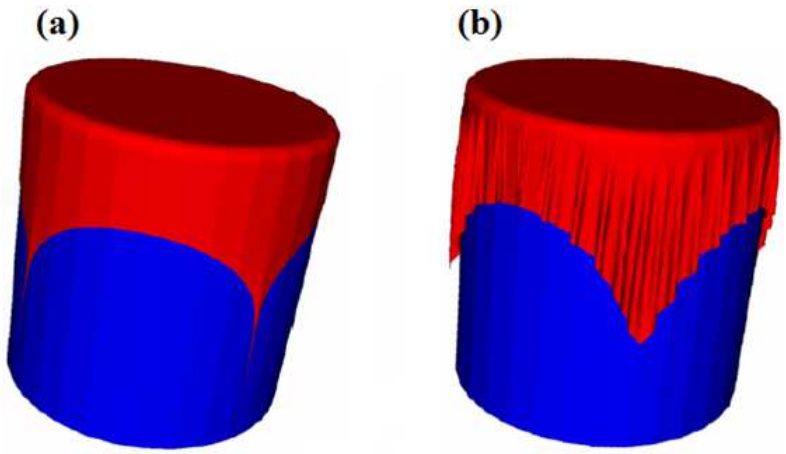


Figure 5.8. The final formed draw-in shape of the draped shape on cylinder (a) with just tensile compliance included and (b) with tensile and shear compliances [181].

Inflation of two air bags has been simulated by considering the following three cases in modelling the material of the bags: tensile stiffness only, tensile and shear stiffnesses, and tensile, shear and bending stiffnesses (see Figure 5.9) [182]. As can be seen clearly from Figure 5.9a, in shapes 1 and 2 with only tensile compliance, there are no wrinkles. In Figure 5.9b, shapes 1 and 2 with tensile and shear compliances have wrinkling, whereas in Figure 5.9c, shapes 1 and 2 with tensile, shear and bending compliances, have wrinkling and they appear to be more realistic.

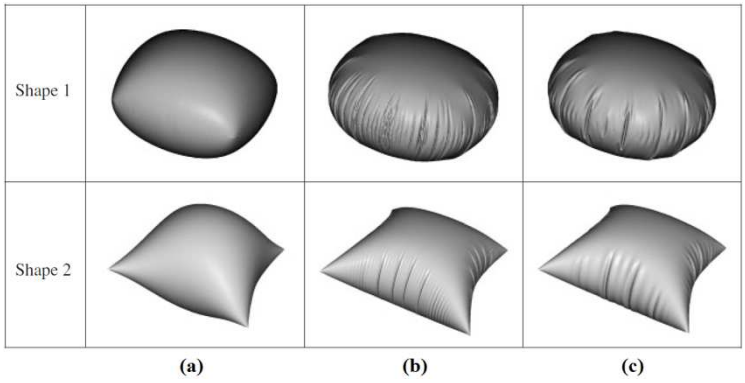


Figure 5.9. Three different constitutive models to inflate the airbags (a) only the tensile compliance (b) the tensile and the shear compliances (c) the tensile, shear and bending compliances [202].

Draping simulation of fabric on a circular cylindrical mould using the previously mentioned three constitutive models was also carried out in [202] (see Figure 5.10).

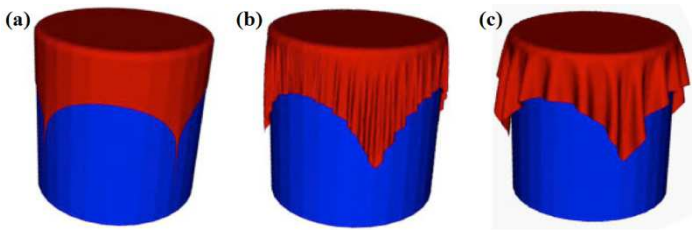


Figure 5.10. Three different constitutive models for draping a fabric blank on cylindrical mould (a) only the tensile compliance (b) the tensile and the shear compliances (c) the tensile, shear and bending compliances [197, 202]

Further improvement of the semi-discrete approach [111, 181, 182, 197, 202] has been performed by Boisse, et al. [32]. However, the material model that includes tensile, shear, and bending stiffness shows the shape of the wrinkles more naturally (see Figure 5.11 b) when compared to the experimentally deformed part (see Figure 5.11a). While the shape seems to be far from the natural appearance when bending compliance is absent (see Figures 5.11c and 5.11d) [32].

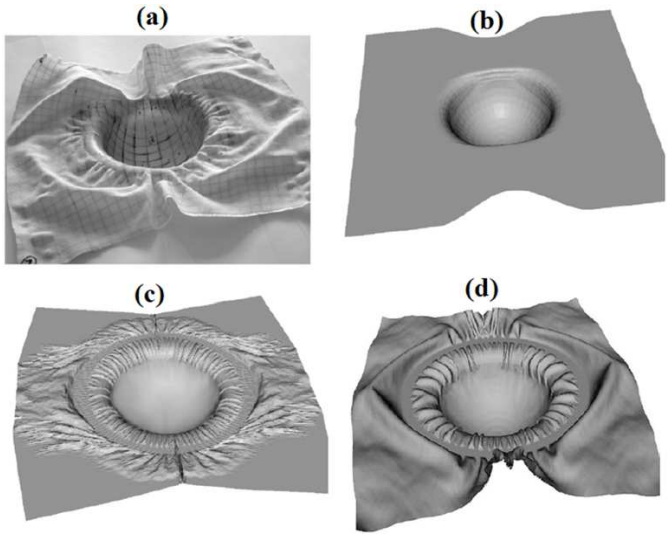


Figure 5.11. Three different constitutive models for forming the hemisphere (a) virtual formed part, (b) only the tensile compliance, (c) tensile and the shear compliances and (d) tensile, shear and bending compliances [32]

## 5.3 Design and manufacture of an advanced composite kart wheel using press forming

The aim of the current work on complex forming is to (i) use the pre-existing S-NOCM (with the mutually constrained structural truss/membrane elements) to design a useful component of high geometric complexity (beyond the predictive capability of kinematic codes), (ii) manufacture the component based on the predictions of forming simulations (iii) evaluate the predictions of the original S-NOCM and the predictions of the CS-NOCM (see Chapter 4) and (iv) introduce variability into forming simulations. In so doing, the goal is to demonstrate the potential improvements in accuracy and robustness of the mechanical modelling approach over the more common kinematic (or mapping) approach and also to understand the importance of the shear-tension coupling and initial material variability on final forming predictions. To the best of the author's knowledge, this is the first occasion in which a mechanical forming code has been used to optimise the design of a complex component.

The Carbon Revolution Company introduced to the market the first one-piece carbon fibre wheel (see Figure 5.12). There are some advantages in a carbon fibre wheel such as 'increasing acceleration, improved steering, handling and response, improved mechanical grip, reducing road noise and reducing fuel consumption' [210].


Figure 5.12. The world's first one piece carbon fiber wheels for automotive and aerospace applications [210]

An advanced composite car wheel was also introduced by a Japanese company (Weds Sport) [211]. The weight of one wheel is just 2.76kg (6.08 pounds). The cost of one set is from $10,000 to $12,000. The high cost of the wheel is attributed to the high cost of the manufacturing process, which depends on skilled labour i.e. a non-automated manufacturing process. In order to reduce the cost of such products, automated manufacturing processes such as stamp forming need to be used.

Manufacture of a kart wheel offers a challenging subject for textile composite forming and can therefore serve as an excellent case study with which to evaluate mechanical forming predictions. An initial 6-rib geometry of the kart wheel was suggested by [212], inspired by the nylon kart wheel shown in Figure 5.13.

(a) (b)

Figure 5.13. A plastic Kart wheel (a) one half of the wheel (b) the two halves of the wheel

### 5.3.1 Kart wheel design considerations

The objectives when designing the tooling are to eliminate tearing and wrinkling in the formed part and to maximise the number of ribs in order to provide increased structural integrity. The aim is to manufacture two identical halves of the wheel; these will subsequently be fastened together (see Figure 5.13b). Thus, the geometry has to be such that the two halves can be easily mated together after manufacturing. There are two constraints that must be adhered to when designing the mould tooling: (i) the tooling must be tapered with no vertical edges in order to allow stacking and consolidation of multiple formed layers and (ii) all the corners and edges must be filleted and rounded to avoid high strain regions when forming the sheet and to facilitate easy extraction and release of the part from the mould.

### 5.3.2 Preliminary simulations of possible kart wheel geometries

A virtual trial and error approach has been used to determine the optimum composite kart wheel geometry. In order to satisfy the design considerations mentioned earlier, a number of CAD forming tools have been built with different numbers of ribs and rib side angles (to make the rib sides taper). The tools (die, punch and blank-holder) are imported to Abaqus Explicit. The best tool design in terms of formability and the formed wheel's expected stiffness was chosen. Four possible geometries have been evaluated using the code with the aim of choosing the best geometry for subsequent manufacture. The simulations were conducted in two steps, (i) the blank holder force was applied in the first step. The blank holder force was 1000N (ii) the punch moves down to form the blank. The wrGF shear compliance of UBE tests (Table 4.2 in Chapter 4) and tension material properties of wrGF (see Section 4.5.1 (c) in Chapter 4) were used to conduct the simulations. The predicted shear deformation of the four geometries (geometry (a) with three straight ribs, geometry (b) with four straight ribs, geometry (c) with five straight ribs and geometry (d) with eight ribs with tapered angle = 5° and hole at the centre, the tapering and hole were found to reduce the shear angle significantly (see Figures 5.14-5.17)).

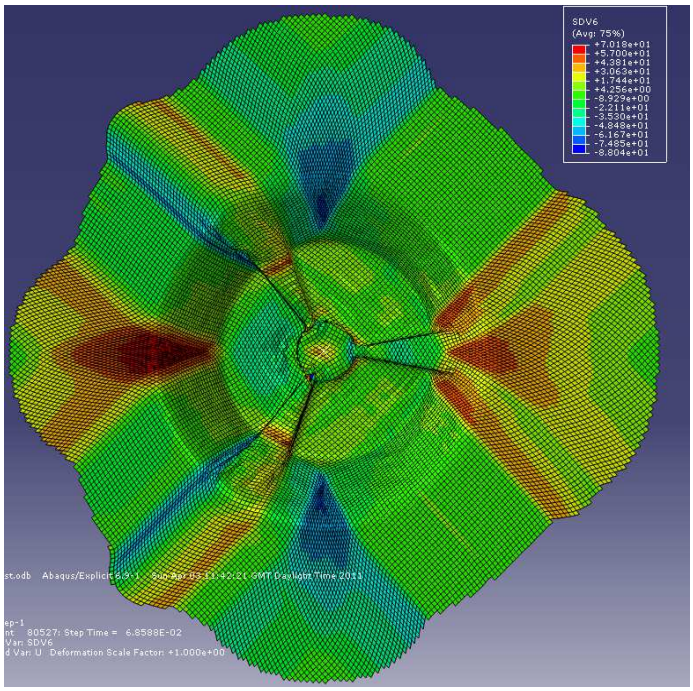


Figure 5.14. The shear angle contour plot of three-rib Kart Wheel

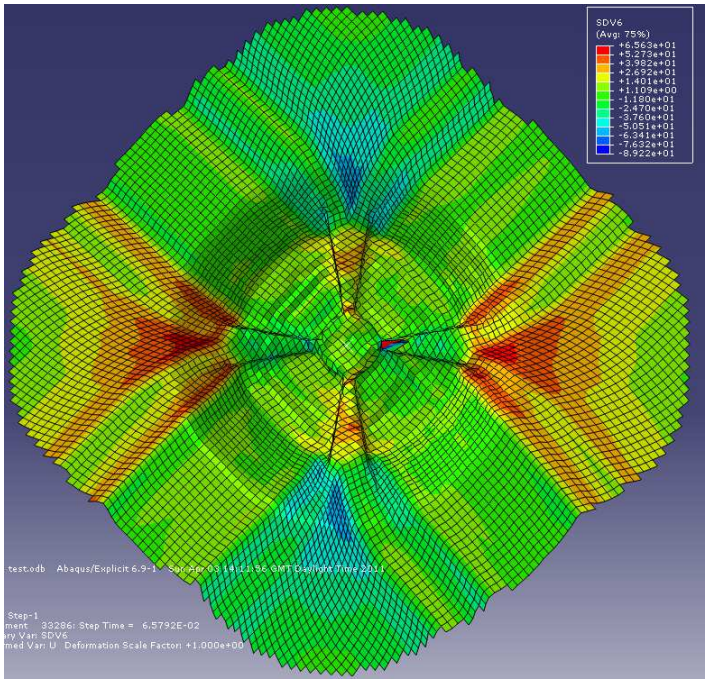


Figure 5.15. The shear angle contour plot of four-rib Kart Wheel

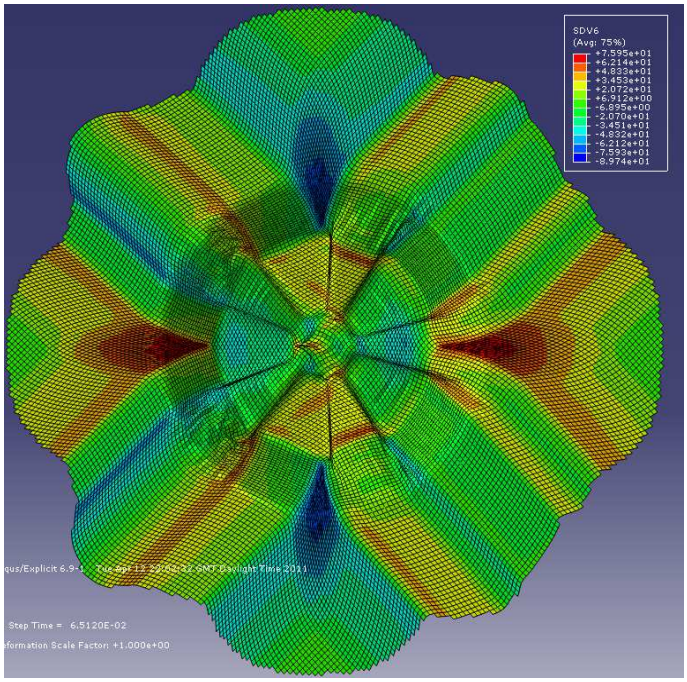


Figure 5.16. The shear angle contour plot of five-rib Kart Wheel

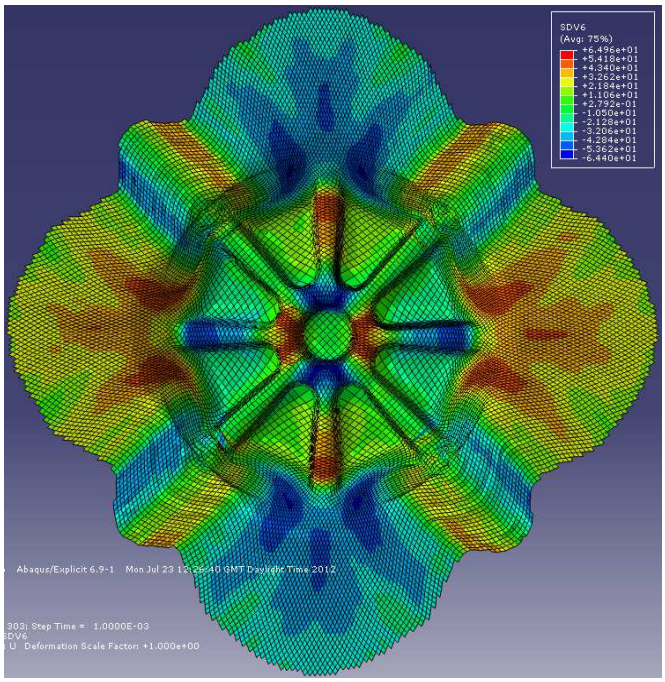


Figure 5.17. The shear angle contour plot of eight ribs deformed composite Kart Wheel

In terms of stiffness and formability, the wheel with eight ribs and a hole at the centre (Figure 5.17) was considered to be the best design when compared to the other three geometries due to two reasons: (i) the eight tapered ribs make the part stiffer and (ii) the predicted shear deformation was the lowest compared to the other three cases (Figures 5.14-5.17). Based on these results, a set of matched male/female kart wheel moulding tools was manufactured (see Section 5.3.3).

### 5.3.3 Experimental forming setup and process condition

#### a) Machining of tooling

Tooling for a kart wheel with eight taper ribs has been designed and manufactured (see Figure 5.18). A heating system is embedded within the tooling for heating up the thermoplastic or thermoset composite (consolidated plate, commingled fabric or prepreg). This comprises four cartridge heaters in both male and female tools and one cartridge heater in the long central pin. Cooling is achieved by circulating cold water or air inside the female and male tools for faster consolidation in the mould (see Figure 5.19). However, the water cooling system has not been used in the current work due to strict safety concerns.

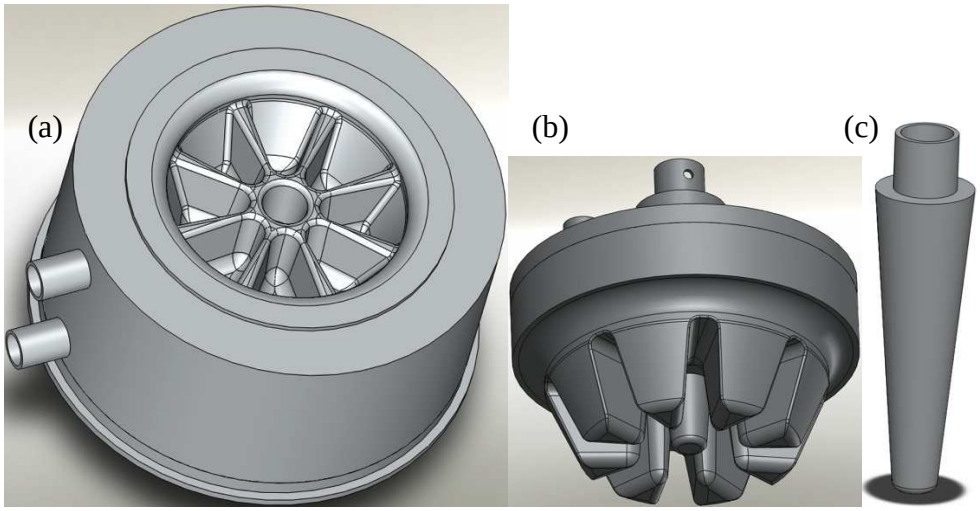


Figure 5.18. CAD assemblies and parts of Kart Wheel mould (a) female mould (b) male mould and (c) pin.

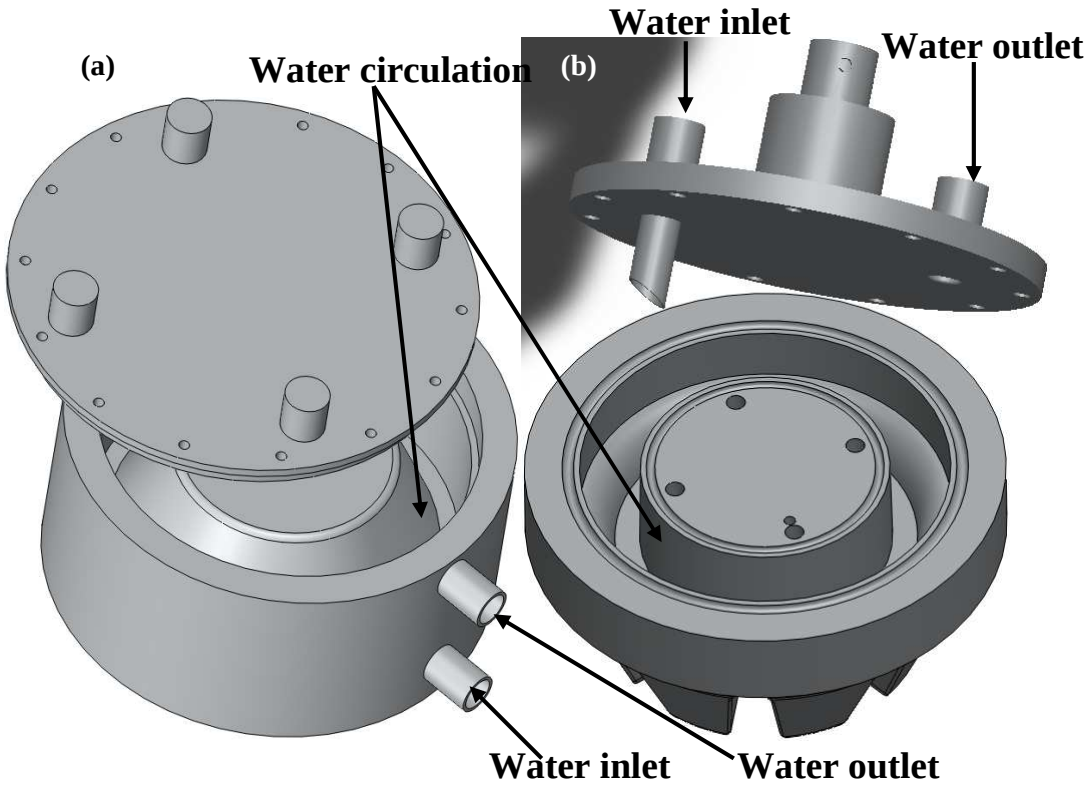


Figure 5.19. Water cooling system of (a) the male and (b) female tool

A segmented blank-holder first introduced by Adams [213] and used by Lin, et al. [34] has been re-manufactured for producing symmetric and asymmetric boundary conditions during forming (see Figure 5.20).

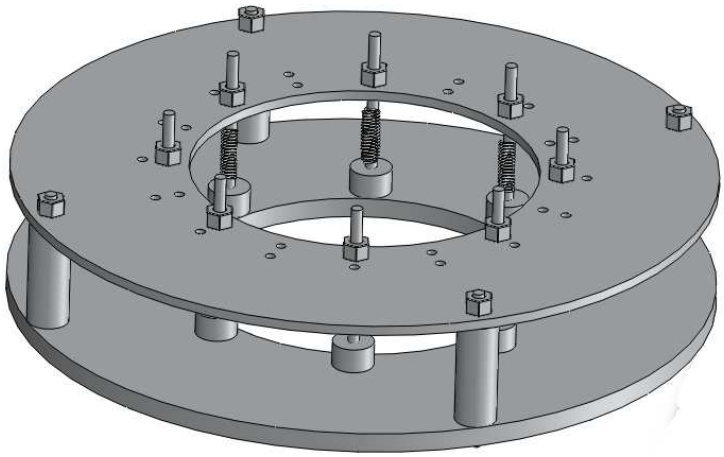

Figure 5.20. CAD assembly of the segmented blank-holder

### b) Steady State Thermal FE Simulations of the Forming Tools

Thermal simulations were performed in order to understand the thermal response of the tooling prior to manufacture. The purpose of the thermal simulation is to visualize the temperature field, which should be almost homogenous across the tooling surface, and to predict the heating time. The required simulation boundary conditions are the specified temperature $T=T(\delta,t)$, the surface heat flux $q=q(\delta,t)$ per unit area, and the surface convection $q=f(T-T^0)$ where $f=f(\delta,t)$ is the film coefficient and $T^0= T^0(\delta,t)$ is the sink temperature, $t$ is time and $\delta$ is the position [214]. The input data are: the sink temperature of the female tool, male tool, pin and the bottom plate of the blank-holder is set as room temperature which was presumed to be 20° C=293° K on the whole surface except places in direct contact with the cartridge heaters. The whole surface has a film coefficient of 34.0 W/m$^2$K and the temperature of the heaters is 200° C=473° K. A surface heat flux of -1 W/m2 is applied to the whole surface. A temperature distribution is shown in Figure 5.21.

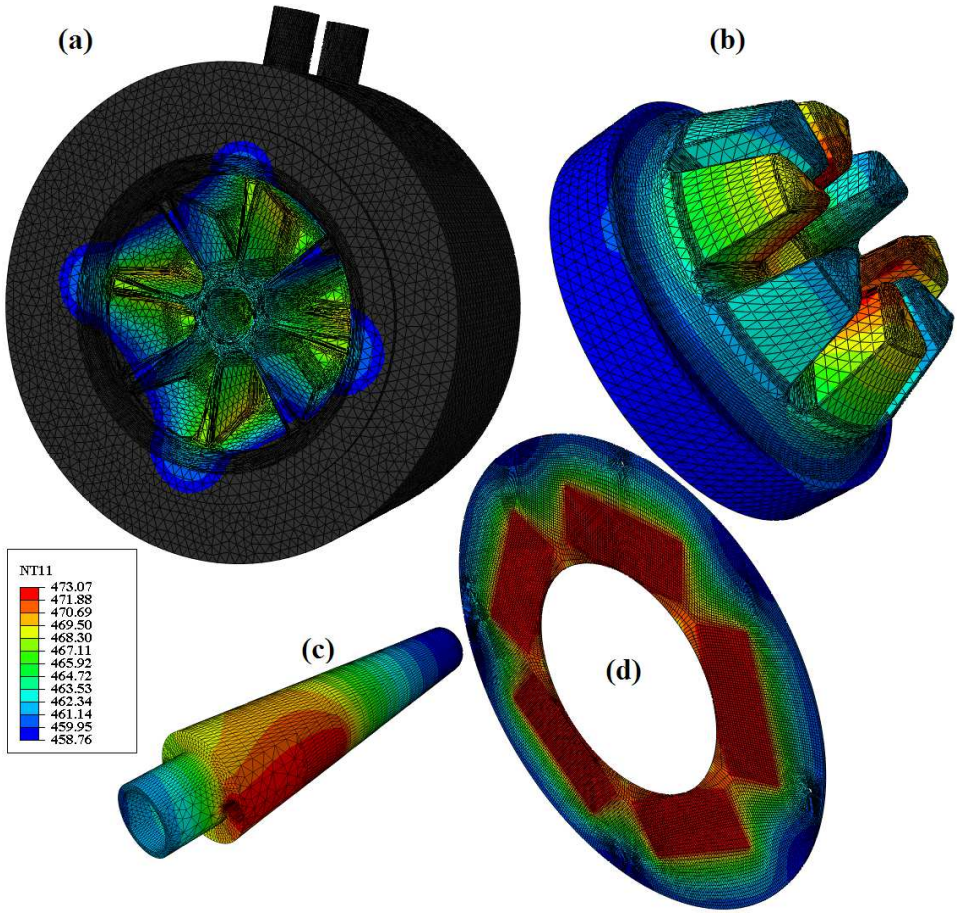


Figure 5.21. The temperature distribution contour plot of (a) the female tool (die) (b) male tool (punch), (c) long-pin and (d) the bottom plate of the blank-holder

### 5.3.4 Experimental forming procedure

Two materials have been analyzed in this investigation: the commingled glass/polypropylene twill weave fabric, cgPP, and the plain weave dry glass fabric, wrGF, described in Chapter 2 (see Section 2.3 for details)

The forming of the kart wheel part is based on a number of basic procedures.

1. Cut out square sheets measuring 350 x 350 mm of each material with orientations of 0/90º and ±45º.
2. Measure the inherent variability by drawing lines following the tows of the samples.
3. Create a grid pattern for subsequent image analysis.

The image analysis involved using the mouse-cursor to identify the corners of every grid cell within the *ImageJ* image processing environment [60]. The measured statistics (the average of the shear angle and the standard deviation) are used as input data for *Varifab*$^{GA}$ to produce FE meshes of mutually constrained membrane and truss elements containing equivalent variability to the actual sheets. The square fabric is then placed within the segmented blank holder (Figure 5.20) and the blank holder force is applied by the eight sets of springs and pads onto an aluminium pressure distribution plate, measuring 15 mm thick, which enables the blank holder load and load distribution to be varied. After this, the blank holder bottom plate is connected to the die flange (see Figure 5.22).

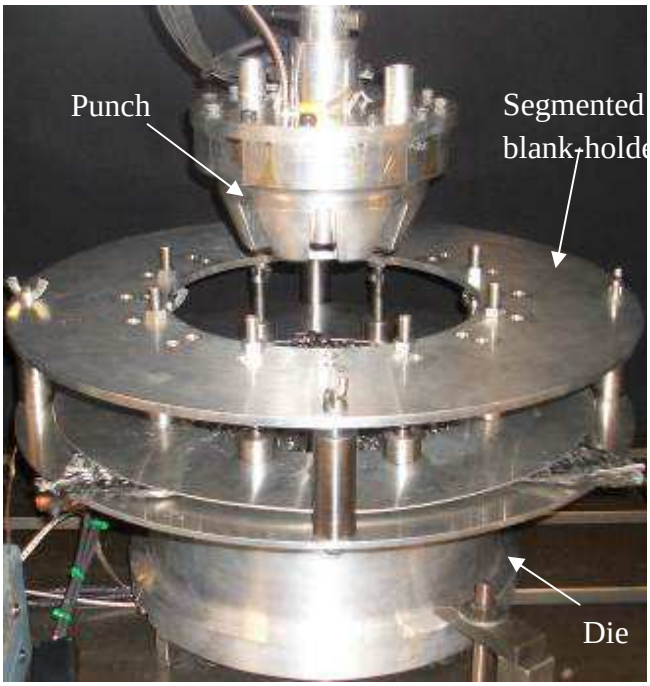


Figure 5.22. The forming station of the segmented blank-holder, the punch and the die

Both the wrGF and cgPP fabrics have been formed using the stamp-forming process. However, since wrGF is eventually consolidated using a thermoset matrix, whereas the cgPP is consolidated by heating and cooling its thermoplastic matrix, the procedures for performing the experiments on the two materials are different.

**a) Procedure for forming the cgPP material and observed defects**

The first step involves forming the central hole using the pin and consolidating the material within the hole by heating up the pin and the die using (the cartridge heaters) to heat the pin to 200 C$^{o}$, maintaining the temperature for about 15 minutes. The reason for forming the hole first using the long-pin and then forming the rest of the part using the full punch is due to the complexity of the geometry, which causes the material to tear and pull apart when trying to form the entire geometry in a single press-forming step using the full punch (see Figure 5.23).

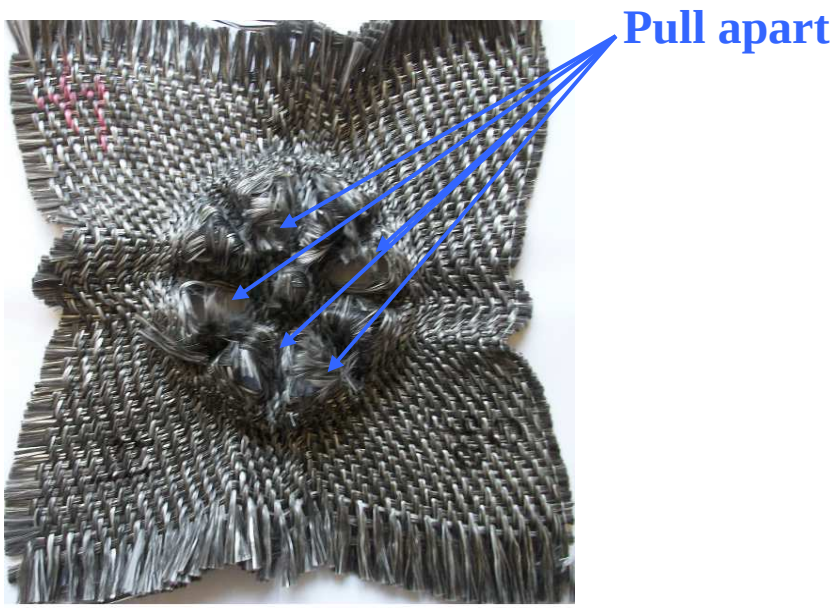


Figure 5.23. Pull apart of cgPP deformed part using the full punch in a single forming step

After forming the central hole, the system is cooled to room temperature by switching off the heaters and leaving the blank in the mould for about 30 minutes. The next step involves replacing the pin with the main punch and forming the rest of the blank. The remainder of the blank is partially consolidated by heating the punch up to 200 C$^{o}$ before cooling to room temperature by leaving it for about one hour under a load about 26000 N. Figure 5.24 shows the formed blank from above while still in the mould. The pin and punch speed is 200 mm/min and the blank holder force 125 N on every pad. The blank holder force used for this material cgPP is much higher than that used for wrGF because cgPP is stiffer and thicker than wrGF.

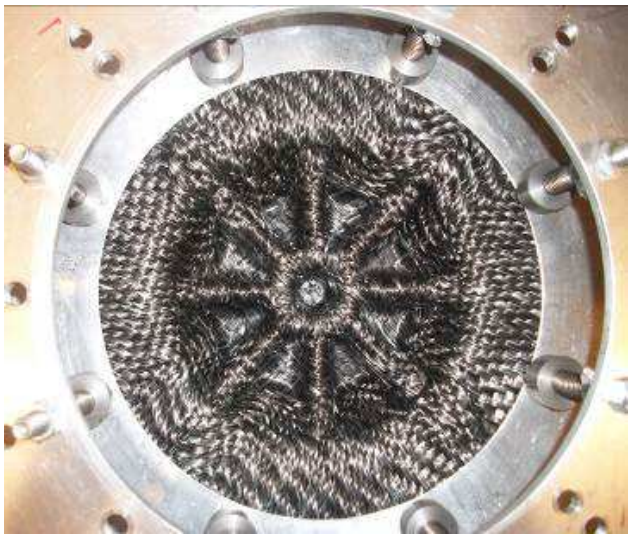

Figure 5.24. Formed part after removing from the moulds

To prevent yarn slipping after forming, blue adhesive tape was placed on three sides of a formed sample's perimeter, the other fourth side was already stitched by the fabric's supplier (see Figure 5.25). However, it was found that use of a stitched fabric perimeter caused severe fabric fracture and opening in localised regions of the formed part, as shown in Figure 5.25.

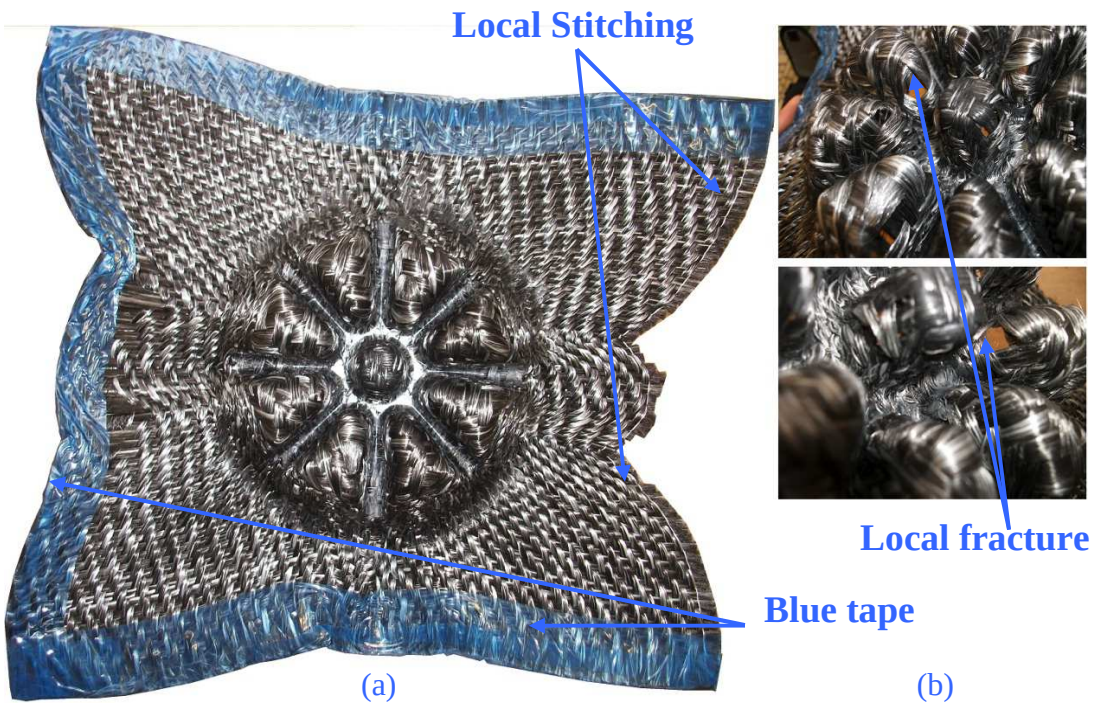


Figure 5.25. (a) Formed part with tapering and local stitching (b) local fracture and opening of the formed part

**b) Procedures of forming the wrGF material and observed defects**

First of all, a liquid PVA release agent (ALLSCOT) was applied to all surfaces of the blank-holder (Figure 5.20), pin (Figure 5.18c), punch (Figure 5.18b) and die (Figure 5.18a). The blank was then formed in two steps. The first step involved forming the central hole using the pin and then applying epoxy resin on the formed material within the hole, after which it is left to cure overnight. The second step involved replacing the pin (Figure 5.18c) with the main punch (Figure 5.18b) and forming the rest of the part, and then applying epoxy resin before again leaving it to cure overnight. The pin and punch speed was 200 mm/min and the blank-holder force 12.5 N on every pad.

The blank-holder force is a crucial parameter and plays a key role in forming, excessive blank-holder force cause tearing (the pin tool goes through the blank) (see Figure 5.26a). Insufficient blank-holder force permits wrinkling (see Figure 5.26b).

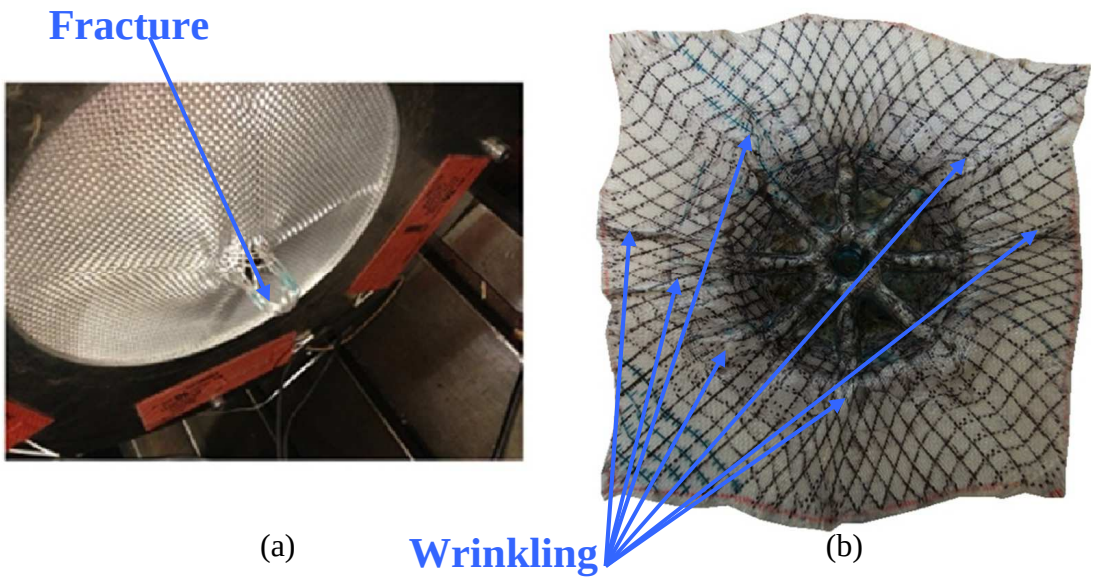


Figure 5.26. (a) Tearing of blank due to excessive blank holder force (b) wrinkling due to insufficient blank-holder force

## 5.3.5 Analysis of the experimental results

A brief review of the common methods of measuring shear deformation after forming advanced composites and engineering fabrics over complex geometries is provided before reporting the shear deformations measured in this investigation. Three methods of measuring shear deformations for advanced composites are reported in the literature

including manual, fibre volume fraction, visual shear deformation, grid deformation and digital image correlation measurements [215-218].

**a) Manual shear deformation measurement**

The engineering strain of a woven cloth has been measured manually using manual shear deformation measurements [112, 219]. In this method the shear deformation is measured directly from the deformed part using simple equipment such as protractor and triangles. However, this method is normally reserved for simple geometries and becomes time consuming for complex geometries.

**b) Visual shear deformation measurement**

The visual method was used by both Long, et al. [195] and Lin, et al. [34]. This method involves drawing lines along the orthogonal tows before forming to generate a grid. After forming the shear deformation can be evaluated visually. In the visual method used by Van Der Weeen [220] and Souter [221] a picture of the predicted deformed part is laid over the photo of the experimentally deformed part to facilitate direct comparison.

**c) Digital image correlation measurement**

Digital image correlation (DIC) is an optical strain measurement method used to measure displacement and strains across a surface using the deformation gradient tensor obtained from correlated images. Measurement of the displacement and the strains can be performed using commercial 3D digital image correlation systems e.g. ARAMIS and LIMESS systems [23] and LaMCoS [222]. The general components of any 3D DIC measurement systems are two CCD cameras and image correlation software. The two CCD cameras capture grey scale images of the item during deformation and calculate the reference and spatial displacement field of the item. The displacement can be calculated by comparing the position (the coordinate) of a particular intersection of the grid to subsequent images using an image correlation algorithm [23, 222]. The 3D DIC process of measuring the deformation starts by painting a grid or spraying a speckle pattern on the specimen. The current coordinates of the four corners of every cell in a 3D formed part can be determined by the grid intersection points. As a final point, the (x,y,z) coordinates of every point of intersected lines in the grid is extracted using image correlation software and then the shear angle can be calculated as the dot product of the vectors [23, 222].

## 5.4 Numerical Simulations: Model Setup and Forming

The FE software Abaqus Explicit was used to model the problem due to the technique's ability to analyse complex and changing contact conditions. The forming setup (see Figure 5.27) consists of a 350x350 mm square blank of mutually constrained elements with quadrilateral membrane elements (M4D4R) measuring 2x2 mm and truss elements (T3D2) along the perimeter of each membrane element (see Section 4.3.2 (b)). The die, punch and pin were all modelled using three and four nodded rigid body elements (R3D4 and R3D3). The reason for using three nodes rigid elements R3D3 in some regions instead of using four nodes rigid elements R3D4 in all the regions of the geometries was due to the complexity of the geometries. A deformable blank-holder was modelled using quadrilateral membrane elements (M4D4R); the pressure loading on the top of the blank holder was distributed across eight node sets as shown in Figure 5.28 (this technique has been used before by Lin, et al. [34].

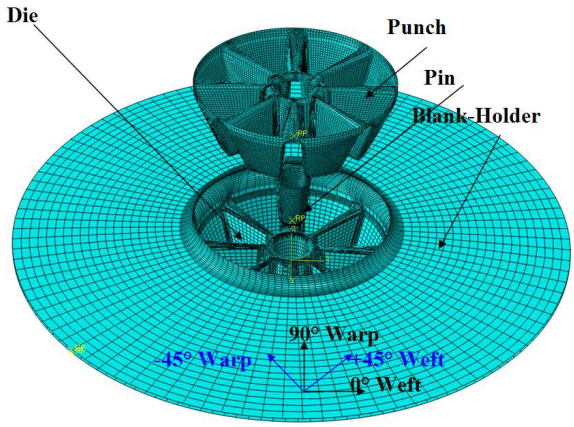


Figure 5.27. FE forming model setup

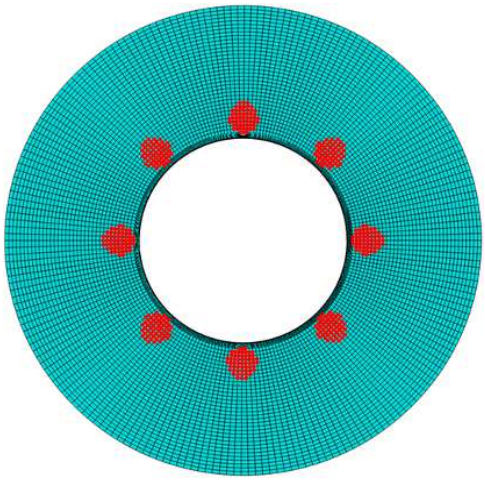

Figure 5.28. The deformable blank holder with loading positions on eight node sets

For the wrGF and cgPP the density of truss elements = 700 and 1500 kg/m$^3$ respectively and the density of membrane elements = 400 and 1000 kg/m$^3$ respectively. The densities were chosen after several attempts to obtain successful simulations with no excessive and unrealistic element distortion. The friction coefficient between tools and the blank was 0.3. Simulations of the eight-ribbed wheel were conducted in three steps (different to the preliminary simulation procedure to determine possible kart wheel geometries, see Section 5.1.1). The three steps are as follows: (i) the blank-holder force is applied, either 12.5 or 125 N on each pad for the wrGF and cgPP materials respectively, (ii) the pin moves down to form the central hole in the middle of the blank with a velocity of 15 m/s and (iii) the rest of the blank is formed by moving the full punch down with a velocity of 10 m/s. The velocities were chosen after several attempts to obtain the optimum simulation speed. Speeding up the simulations by decreasing the simulation time and increasing punch speed or scaling the mass by either increasing material density or reducing the modulus reduces the computational cost. However, there are certain limits that must not be exceeded by ensuring the ratio of the kinetic energy to internal energy is less than 10% [223]. This was verified in all simulations.

The reason for conducting three simulation steps for the eight ribbed wheel rather than two (such as with the preliminary simulations, see Section 5.1.1) was because, in the case of the preliminary simulations, the full punch travel was just 40 mm and there was no central hole for the first three cases (Figures 5.14-5.16)). To simulate the eight ribbed wheel to a depth of 50 mm, (the depth of the actual plastic wheel, see Figure 5.13) three simulation steps had to be introduced in order to prevent wrinkling, pulling apart (see Figure 5.23), bridging and element distortion in the simulations.

### 5.4.1 Model parameters

Commingled glass/polypropylene fabric (cgPP) and dry plain weave glass fabric (wrGF) were used to perform numerical forming tests. Two constitutive models, the original S-NOCM and the enhanced CS-NOCM have been used, see Chapter 4. The truss stiffness properties in tension and the cross sectional area for wrGF and cgPP are equal to those used in Chapter 4 Section 4.5.1 (d), taking into account the mesh density i.e. the tensile stiffnesses were decreased regarding to element length. The shear coefficients for the S-NOCM were obtained from the UBE tests while the coefficients for the CS-NOCM were

obtained from the BBE tests. The polynomial coefficients are given in Tables 4.8 and 4.10 of Chapter 4. This procedure is intended to discover whether the results obtained from the new BBE test method, incorporated within the enhanced CS-NOCM, make a difference to the predictions of the complex forming simulations.

The FE forming simulation was conducted using two initial blank orientations, namely, 0/90° and ±45°, corresponding to the orientations used in the forming experiments. In addition, the blanks were initially meshed with no variability using meshes consisting of mutually constrained membrane/truss elements generated using Meshgen (Chapter 3 and [68, 163]). Later, variable meshes created using Varifab$^{GA}$ were used in the forming simulations (Chapter 3 and [163]).

### 5.4.2 Simulations of Eight-Ribbed Wheel

An evaluation of the CS-NOCM compared to the S-NOCM in predicting the deformation of the wrGF and cgPP on the eight-ribbed kart wheel is presented in the following sections. Numerical forming simulations of wrGF and cgPP using two initial blank orientations ($0^o/90^o$ and $\pm 45^o$, see Figure 5.29) for four case studies will be investigated, namely:

1. forming simulation with no mesh variability using the original S-NOCM
2. forming simulation with mesh variability using the original S-NOCM
3. forming simulation with no mesh variability using the enhanced CS-NOCM
4. forming simulation with mesh variability using the coupling enhanced CS-NOCM

Results of each of these case studies are compared both against each other and against the experimental results. Afterwards a sensitivity study is presented in which the effects of blank-holder force, friction coefficient, punch speed and shear compliances, on the predicted deformation are investigated.

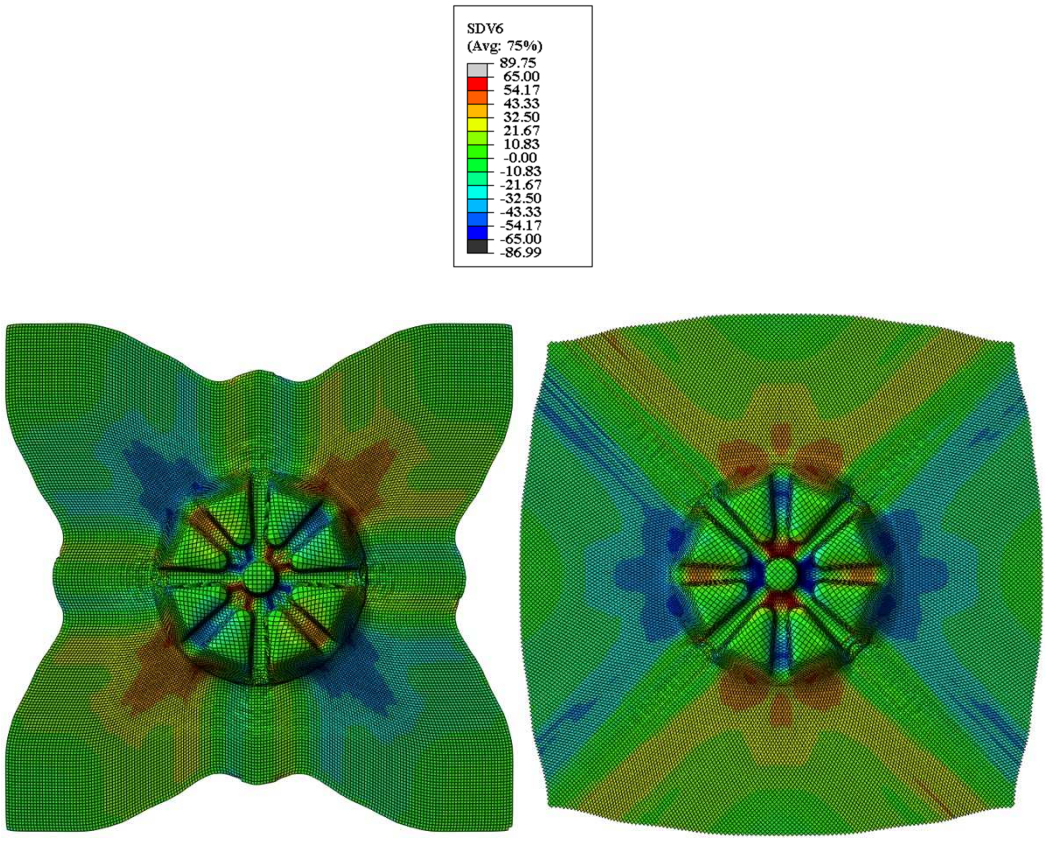


(a) (b)

Figure 5.29. FE simulation of (a) 0/90° initial orientation (b) ±45° initial orientation.

## 5.5 Comparison between Experiments and Numerical Predictions

Note that in order to permit direct comparison of simulation predictions, the limits of the colour legend in all simulations in the following sections are the same as the legend in Figure 5.29.

### 5.5.1 0/90° non-variable mesh predictions with unmodified S-NOCM

FE forming simulations of the cgPP and wrGF using a 350 x 350 mm blank with a 0/90° non-variable mesh were carried out using the original S-NOCM with shear resistance input curves measured by the UBE test (see Table 4.2 of Chapter 4). Simulating the cgPP and wrGF with a 0/90° non-variable mesh using the original S-NOCM and mutually constrained truss/membrane elements was initially found to cause severe element distortion during the early stages of the simulation. Various ideas to eliminate excessive element distortion such as increasing the mesh density, introducing artificial damping, reducing the blank/tool friction coefficient and increasing mass scaling by increasing the density were

attempted. Only by increasing the mass scaling of both membrane and truss elements by a factor of 10 could reasonable results be obtained. The ratio between the internal and kinetic energies have subsequently been checked and are found to be less than 10%, indicating that inertial effects are still negligible.

Sensitivity study of the effects of mass scaling on shear deformation was conducted in Section 5.6.4.

Contour plots of typical shear angle predictions (State Dependent Variable 6 in the user subroutine) for the two materials are depicted in Figures 5.30 and 5.31 alongside the actual experimentally formed fabrics. The predicted and the experimental shear angles are measured in 12 different locations of each quarter of the four quarters of the deformed wheels (the upper right quarter URQ, the upper left quarter ULQ, the lower right quarter LRQ and the lower left quarter LLQ) (see Figure 5.32). An average of each shear angle at corresponding locations of the four quarters are calculated (the experimental and predicted shear angles are given in Table A.1 and Table A.2 in Appendix A). A simple measurement technique was used to obtain results, with photos of the formed parts taken and *imageJ* software [60] used to measure the shear angle. Figures 5.33 and 5.34 show a quantitative comparison of the predicted shear angle with the experimental results of the formed textile composite wheel. The co-ordinates of the points of the four quarters used to make the comparisons are given explicitly in Table A.3 in Appendix A. Since the simulations were initially performed using non-variable meshes with a uniform blank holder force on all eight pads, as expected, symmetrically deformed parts are obtained in the numerical simulations. In the subsequent figures, '*Exp'* is short for experimental results and '*Pre'* is short for predicted results. Lines between points in all subsequent figures of the shear angle vs. points were included just for visual clarity.

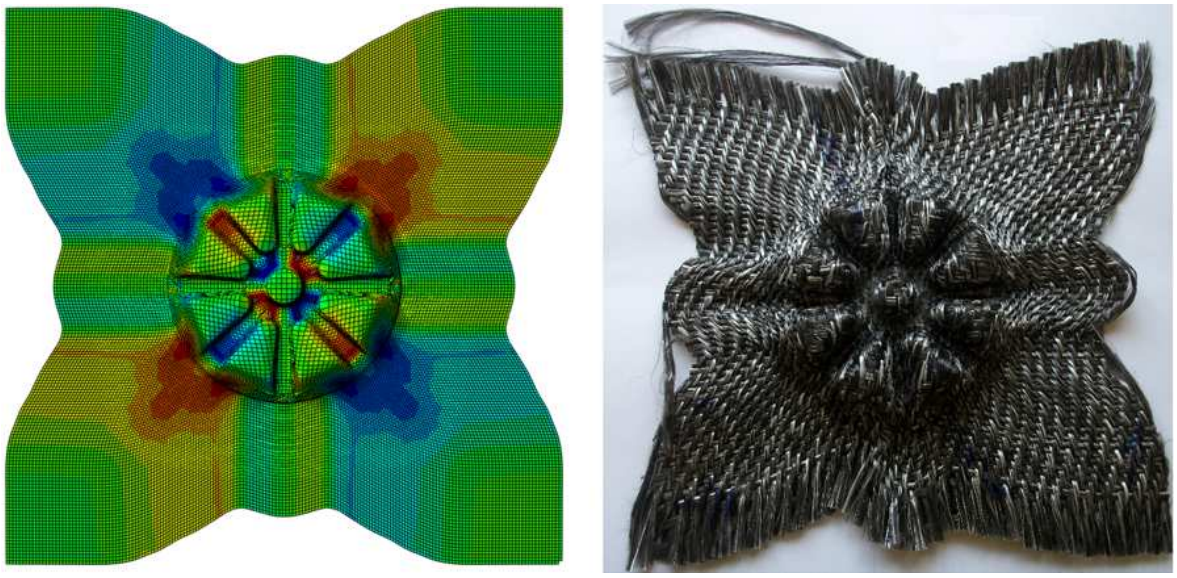

**(a)** **(b)**

Figure 5.30. (a) The contour plot of the predicted shear angle SDV6 (b) the experimental formed kart wheel (cgPP).

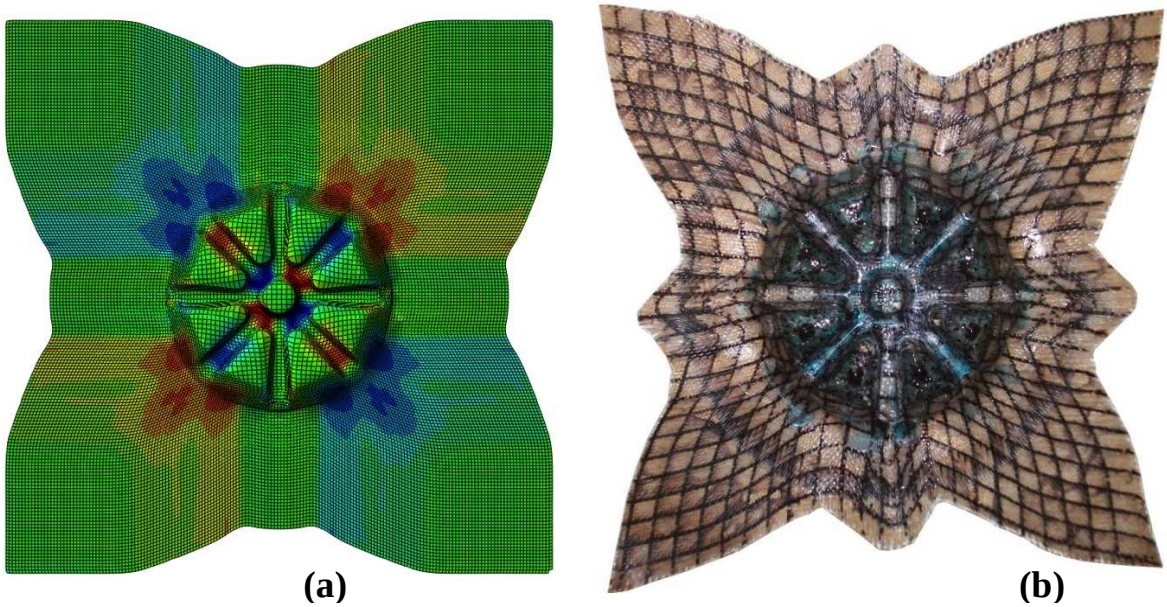

**(a)** **(b)**

Figure 5.31. (a) The contour plot of the predicted shear angle SDV6 (b) the experimental formed kart wheel (wrGF).

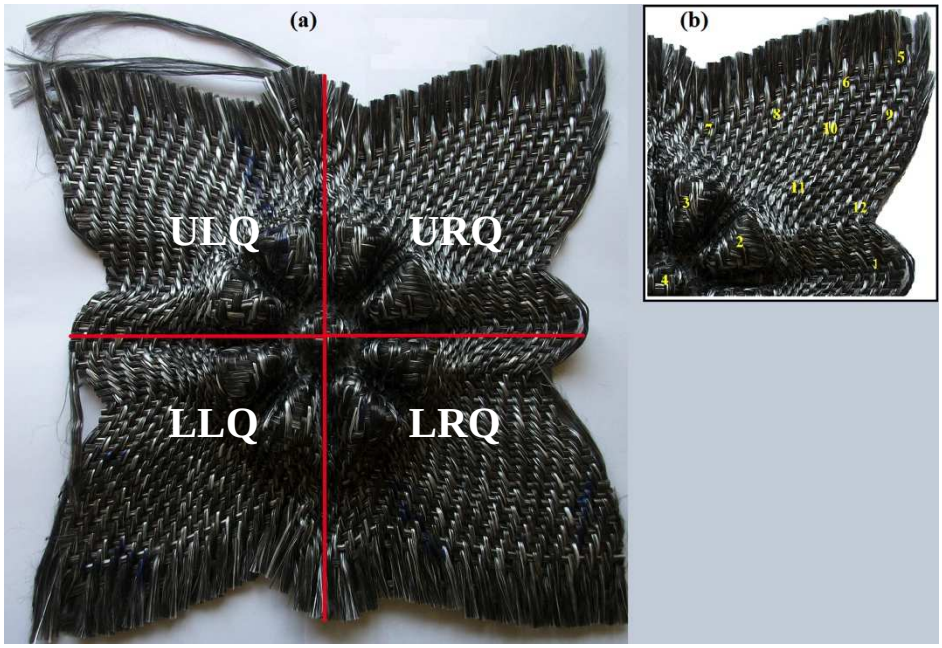


Figure 5.32. (a) The four quarters of the formed wheel (b) the 12 locations from which the shear angle were measured

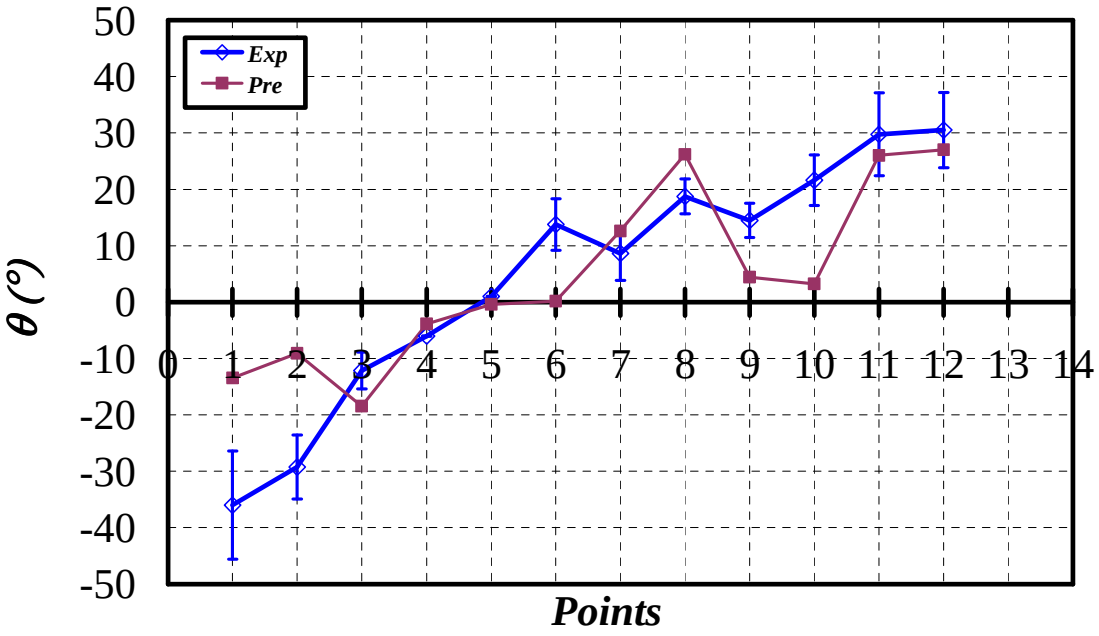


Figure 5.33. Comparison between experimental and predicted shear angle with 0/90° non-variable mesh using the S-NOCM (cgPP).

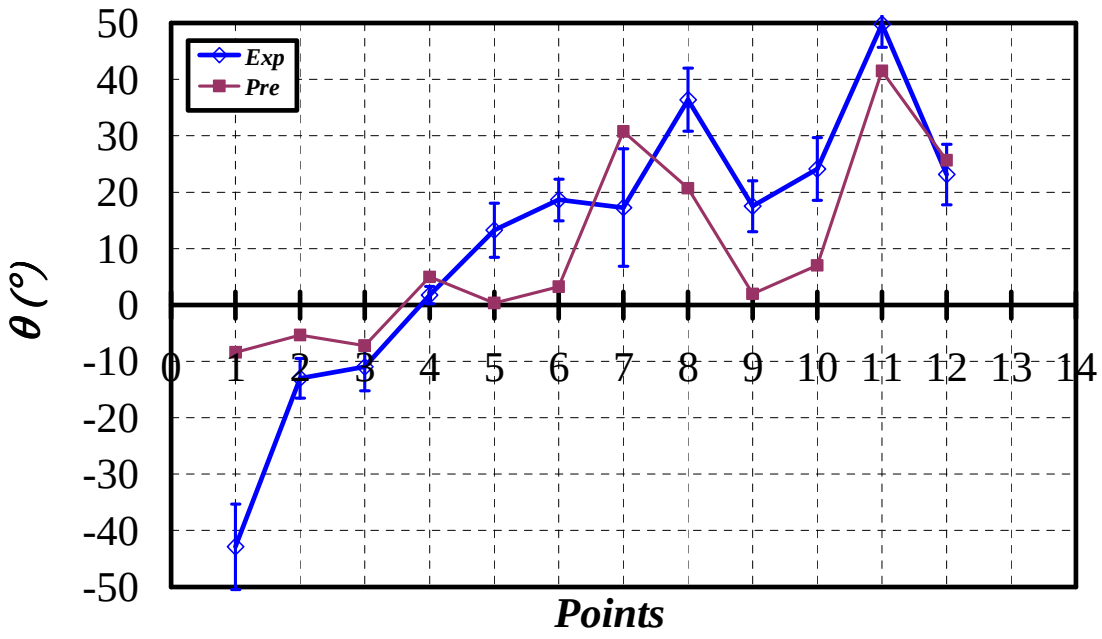


Figure 5.34. Comparison between experimental and predicted shear angle with 0/90° non-variable mesh using the S-NOCM (wrGF).

Comparison between experimental and predicted local shear deformation with 0/90° non-variable mesh using the S-NOCM show significant variation (see Figures 5.34 and 5.35) i.e. most of the shear angles are not in good agreement. Significant gaps between the experimental and predicted shear angles can be clearly seen in eight points out of the twelve points. This discrepancy can be attributed to various possible differences between the simulations and the experiments, including significant differences in the material response, such as a lack of shear-tension coupling in the S-NOCM and the simplified linear tensile behaviour in the truss elements compared to the non-linear coupled tensile response of the fabric [23, 172]. Numerical issues could also be to blame, such as the use of the fixed mass scaling option, which decreases the computational time and prevents element distortion but increases the material density by a factor of 10. This increase might affect the predicted results in a negative way even though the kinetic energy is still 1ess than 10% of the internal energy. In the ensuing investigation, the significance of these influences is examined.

### 5.5.2 ±45° non-variable mesh predictions with unmodified S-NOCM

FE forming simulations of the cgPP and wrGF using a 350 x 350 mm blank with a ±45° non-variable mesh were carried out using the original S-NOCM with shear resistance input curves measured by the UBE test (see Table 4.2 of Chapter 4). Again severe element distortion in the early stages of the simulations, similar to the case considered in Section 5.5.1, was encountered when simulating both the cgPP and the wrGF. The solution was again to increase the fixed mass scaling of both membrane and truss elements, though this time a factor of 20 was required to avoid excessive element distortion. The contour plots of the predicted shear angle (SDV6) are depicted in Figures 5.35 and 5.36 alongside the actual experimentally formed fabrics. Again, the experimental shear angles are measured in 12 different locations of each quarter of the deformed wheels (the upper right quarter URQ, the upper left quarter ULQ, the lower right quarter LRQ and the lower left quarter LLQ) (see Figure 5.37). An average of each shear angle at corresponding locations from all four quarters is calculated (the experimental and predicted shear angles are illustrated in Table A.4 and Table A.5 in Appendix A). Figures 5.38 and 5.39 show a quantitative comparison of the predicted and measured shear angles. The co-ordinates of the points of the four quarters used to make the comparisons are given explicitly in Table A.6 in Appendix A. The simulation results also indicate wrinkling of the sheet in the same regions as in the experimentally formed parts. The form of the predicted wrinkles is different to those observed in the actual parts, a point that may be explained due to the absence of out-of-plane bending stiffness in the simulations, which employ membrane rather than shell elements.

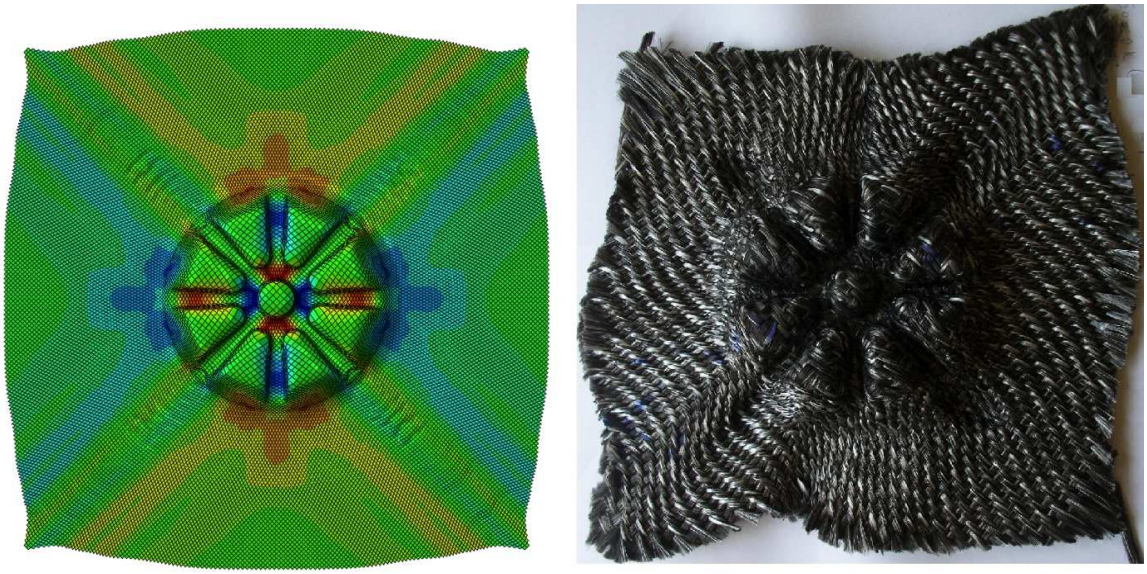

(a) (b)

Figure 5.35. (a) Contour plot of the predicted shear angle (SDV6) (b) the experimental formed kart wheel (cgPP).

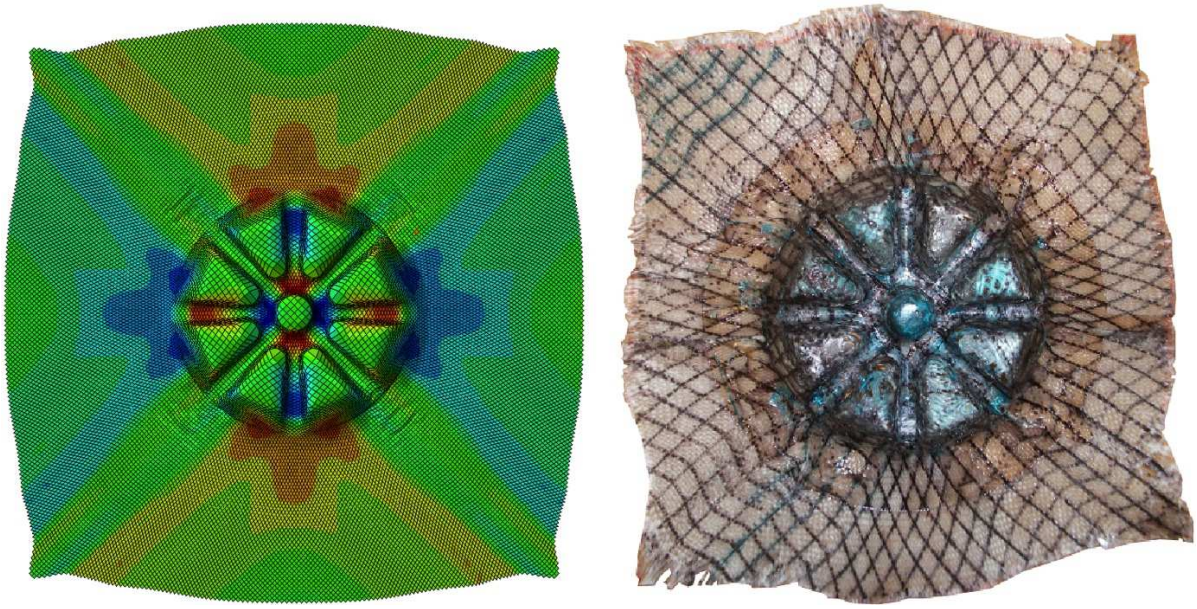

(a) (b)

Figure 5.36. (a) The contour plot of the predicted shear angle SDV6 (b) the experimental formed kart wheel (wrGF).

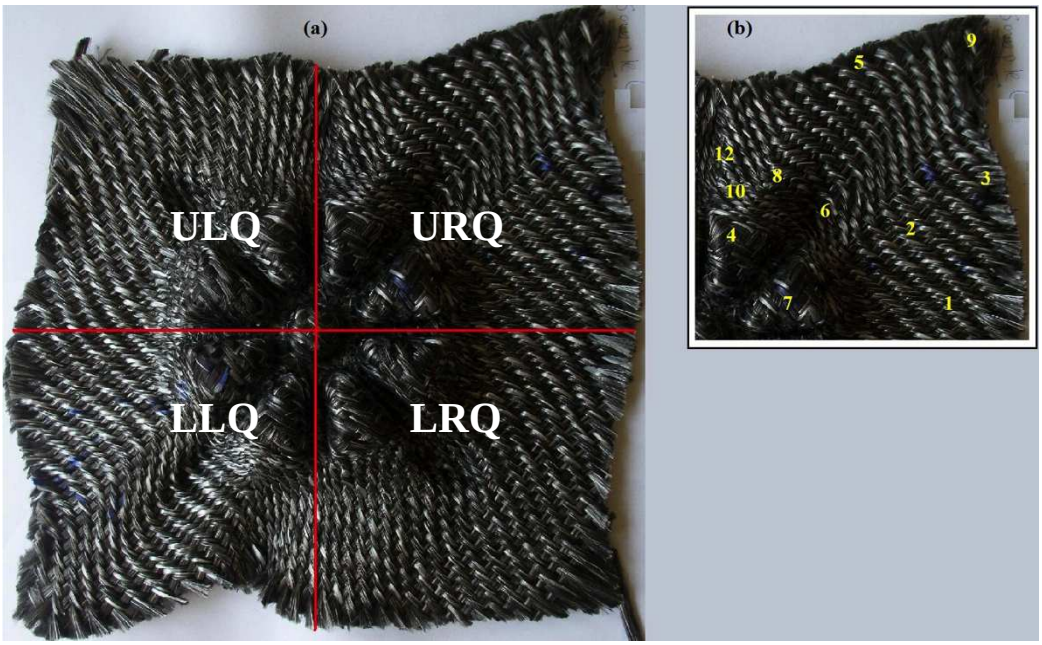


Figure 5.37. (a) The four quarters of the formed wheel (b) the 12 locations from which the shear angle were measured

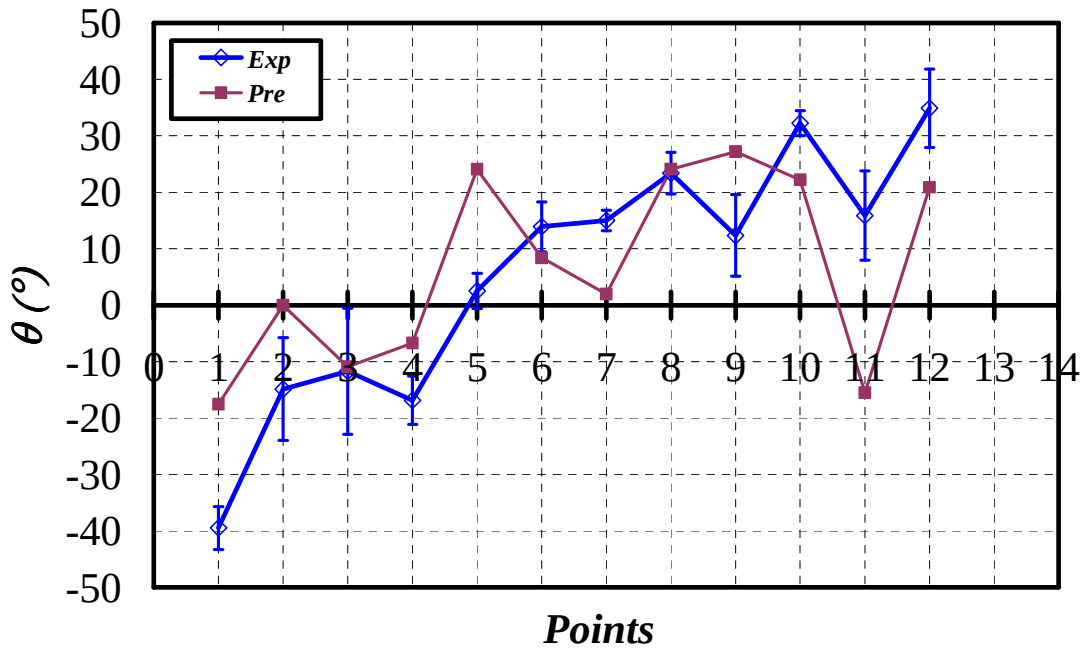


Figure 5.38. Comparison between experimental and predicted shear angle with ±45° non-variable mesh using the S-NOCM (cgPP).

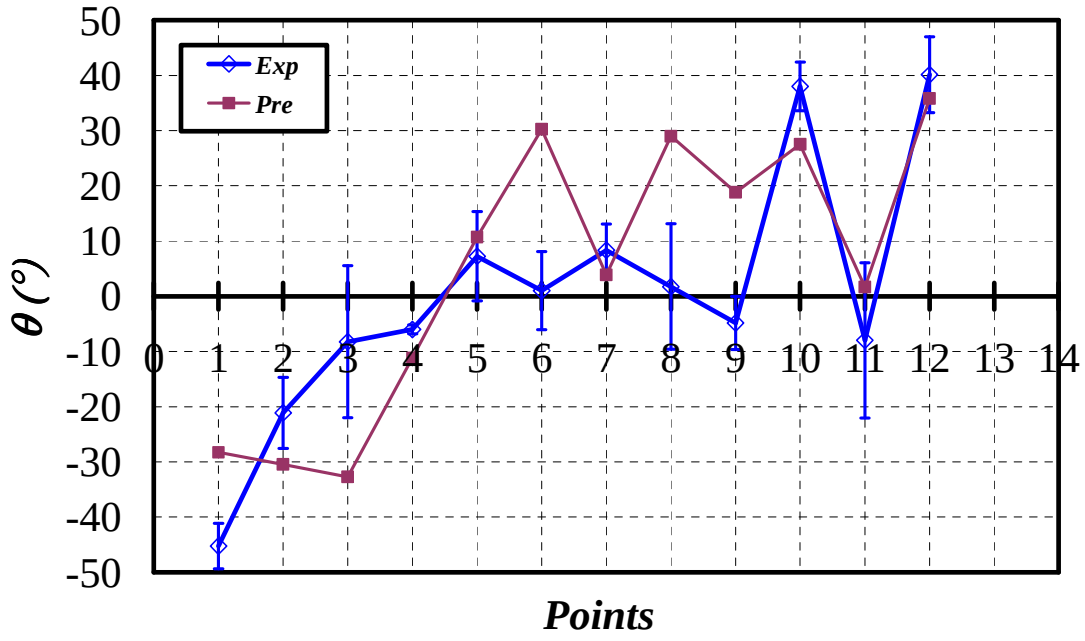


Figure 5.39. Comparison between experimental and predicted shear angle with ±45° non-variable mesh using the S-NOCM (wrGF).

Again, comparison between experimental and predicted local shear deformation with a ±45° non-variable mesh using the S-NOCM (see Figures 5.38 and 5.39) shows significant

differences and the possible reasons for these differences, discussed in Section 5.5.1, apply here also.

### 5.5.3 0/90° non-variable mesh predictions with enhanced CS-NOCM

FE forming simulations of the cgPP and wrGF using a 350 x 350 mm blank with a 0/90° non-variable mesh were carried out using the enhanced CS-NOCM with shear resistance input curves initially obtained from a BBE test and then normalised for use in the CS-NOCM (see Tables 4.8 and 4.10 of Chapter 4). Significantly, the simulations in this case were completed without the need to use fixed mass scaling (see Sections 5.5.1 and 5.5.2). The contour plots of the predicted shear angle (SDV6) are depicted in Figures 5.40 and 5.41. The contour plots in Figures 5.40a and 5.41a were obtained using the CS-NOCM, while the contour plots in Figures 5.40b and 5.41b were obtained using the S-NOCM, the latter are identical to Figures 5.30a and 5.31a and are included here to facilitate direct comparison of results. The predicted shear angles were measured using the same technique described in Section 5.5.1 from just one quarter of the simulation (see Figure 5.32, the coordinates of the measurement points are given in Table A.3 in Appendix A). The experimental shear angles were obtained previously, as described in Section 5.5.1 (see Tables A.1 and A.2 in Appendix 1). Numerical values for the predicted shear angles of the cgPP and wrGF simulations are given in Table A.7 in Appendix A. Figures 5.42 and 5.43 show quantitative comparisons of the predicted shear angles obtained using the CS-NOCM with those obtained using the S-NOCM (see Section 5.5.1) alongside the experimental results of the formed textile composite wheel. In the the figures, '*Exp'* is short for experimental result, '*Pre CS-NOCM'* is short for predicted result obtained using CS-NOCM and '*Pre S-NOCM'* is short for predicted result obtained using S-NOCM. Similar notation is used in the subsequent figures. Figures 5.42 and 5.43 suggest that the predicted results of the CS-NOCM are improved compared to the corresponding results obtained from the S-NOCM . This improvement might be attributed to either the inclusion of the shear-tension coupling and associated improved shear data measured using the BBE test (see Chapter 2) or possibly due to the absence of mass scaling, which was only included in the previous simulations in order to produce reasonable results. It is concluded that because of the more realistic shear behaviour predicted by the CS-NOCM, the latter is better than the unmodified S-NOCM in terms of numerical convergence in that it requires less manipulation of the simulation parameters in order to produce a valid result.

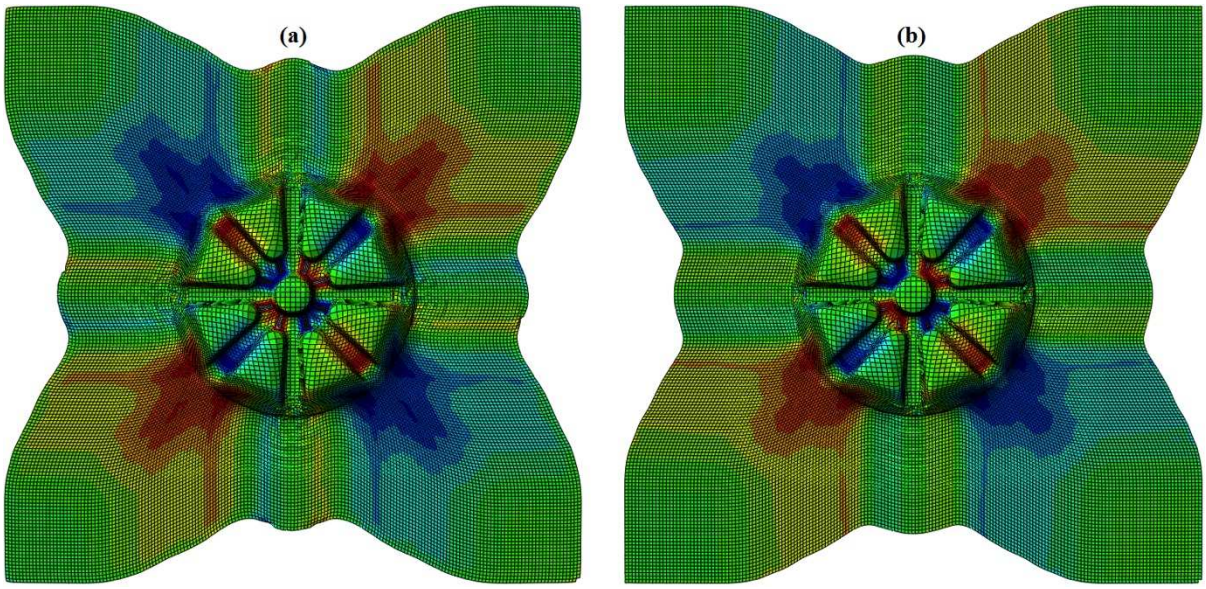


Figure 5.40. Contour plot of the predicted shear angle with a 0/90° non-variable mesh (a) using the CS-NOCM coupled model (b) using the S-NOCM (repeated from Figure 5.30a to ease comparison) (cgPP).

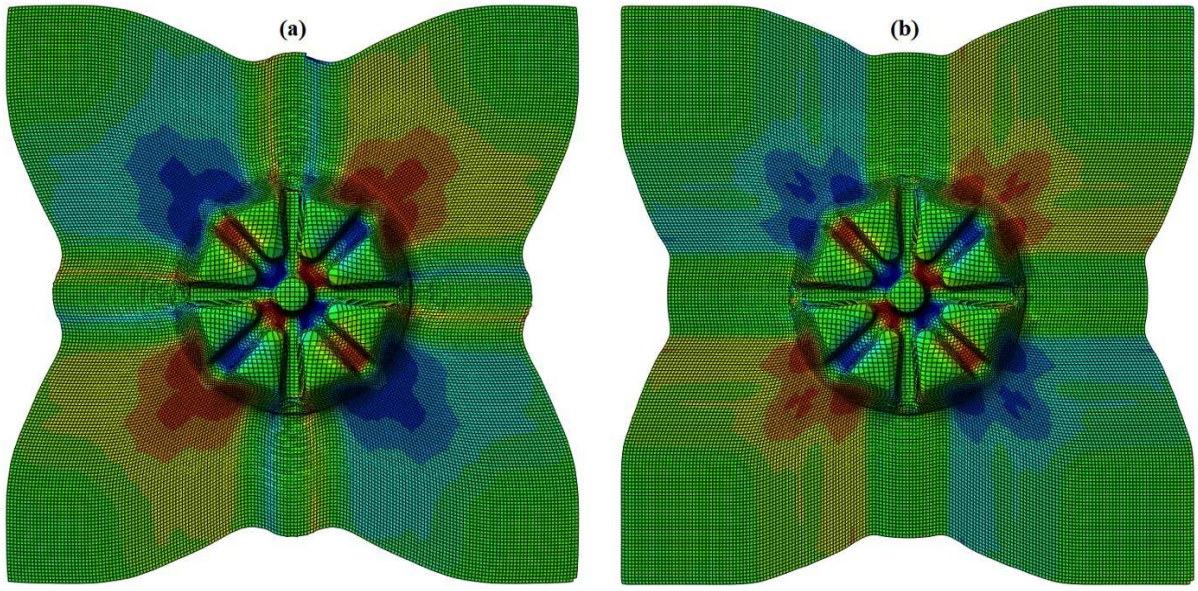


Figure 5.41. Contour plot of the predicted shear angle SDV6 with a 0/90° non-variable mesh (a) using the CS-NOCM coupled model (b) using the S-NOCM (repeated from Figure 5.30a to ease comparison). (wrGF).

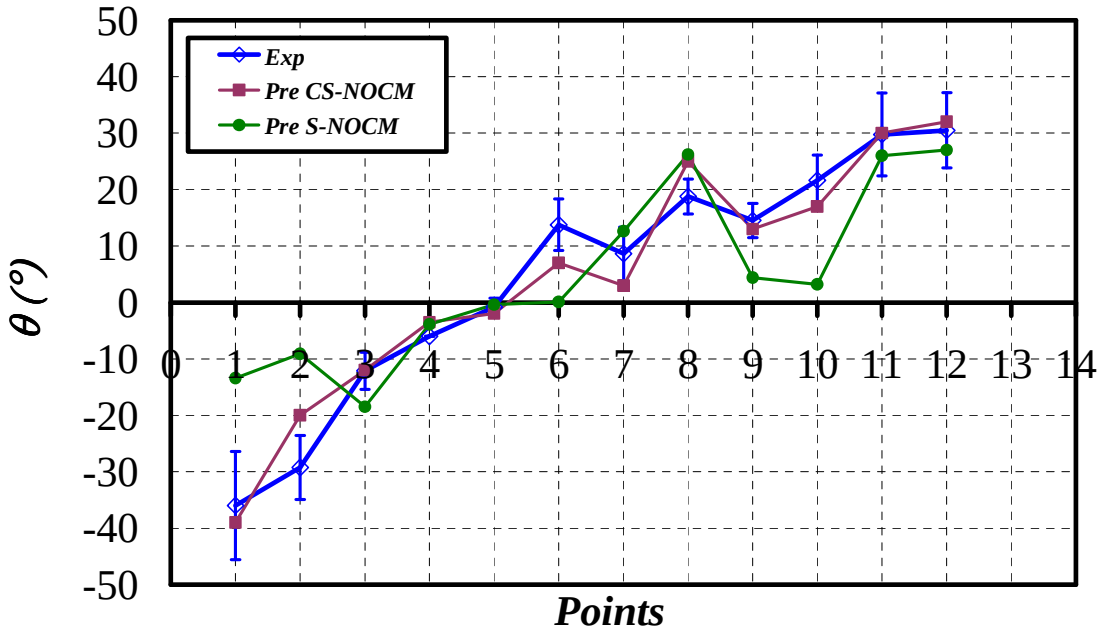


Figure 5.42. Comparison between experimental and predicted shear angle with a 0/90° non-variable mesh using both the CS-NOCM and S-NOCM (repeated from Figure 5.33 to ease comparison) (cgPP).

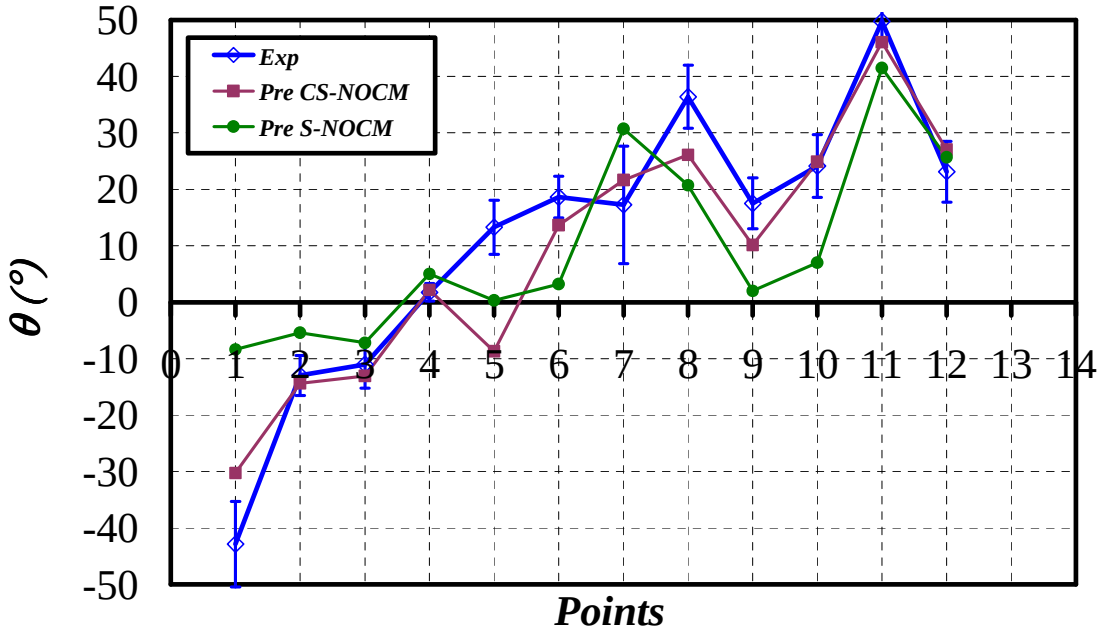


Figure 5.43. Comparison between experimental and predicted shear angle with a 0/90° non-variable mesh using the CS-NOCM and S-NOCM (repeated from Figure 5.34 to ease comparison) (wrGF).

### 5.5.4 ±45° non-variable mesh predictions with enhanced CS-NOCM

FE forming simulation of the cgPP and wrGF using a 350 x 350 mm blank with a ±45° non-variable mesh were carried out using the enhanced CS-NOCM with shear resistance input curves initially obtained from a BBE test and then normalised for use in the CS-NOCM (see Table 8 of Chapter 4). The simulations in this case were also completed without the need to add a fixed mass scaling factor (see Sections 5.5.1 and 5.5.2). The contour plots of the predicted shear angle (SDV6) are depicted in Figures 5.44 and 5.45. The contour plots in Figures 5.44a and 5.45a were obtained using the CS-NOCM, while the contour plots in Figures 5.44b and 5.44b were obtained using the S-NOCM and are identical to those in Figure 5.35a and 5.36a. The predicted shear angles were measured using the same technique used in Section 5.5.1 from just one quarter URQ (see Figure 5.37, the coordinates of measurement points in the URQ are given in Table A.6 in Appendix A). Experimental shear angle data were obtained previously, see Section 5.5.2 (see Tables A.4 and A.5 in appendix 1) (the numerical values of predicted shear angles of the cgPP and wrGF are given in Table A.8 in appendix A). Figures 5.46 and 5.47 show a quantitative comparison of the predicted shear angle obtained using the CS-NOCM with the predicted shear angle obtained using the S-NOCM (Section 5.5.1) alongside with the experimental results of the formed textile composite wheel. As in Section 5.5.3 the predicted results of CS-NOCM (see Figures 5.46 and 5.47) are improved considerably compared to the corresponding results obtained previously from S-NOCM (Section 5.5.1).

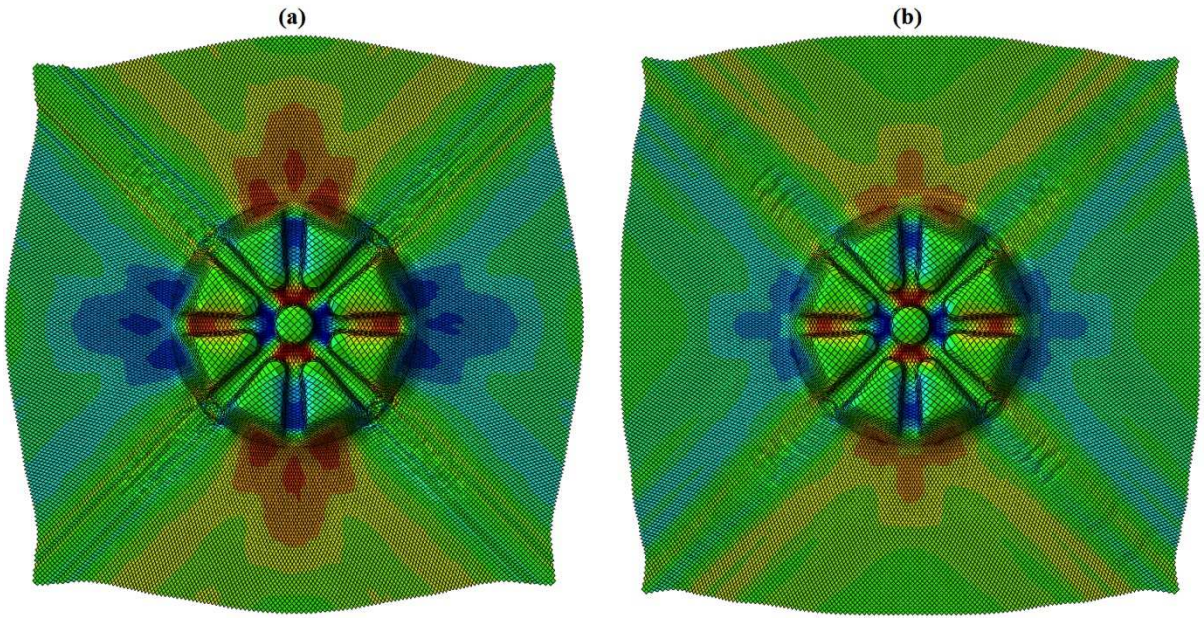


Figure 5.44. Contour plot of the predicted shear angle with a ±45° non-variable mesh (a) using the CS-NOCM coupled model (b) using the S-NOCM (repeated from Figure 5.30a to ease comparison) (cgPP).

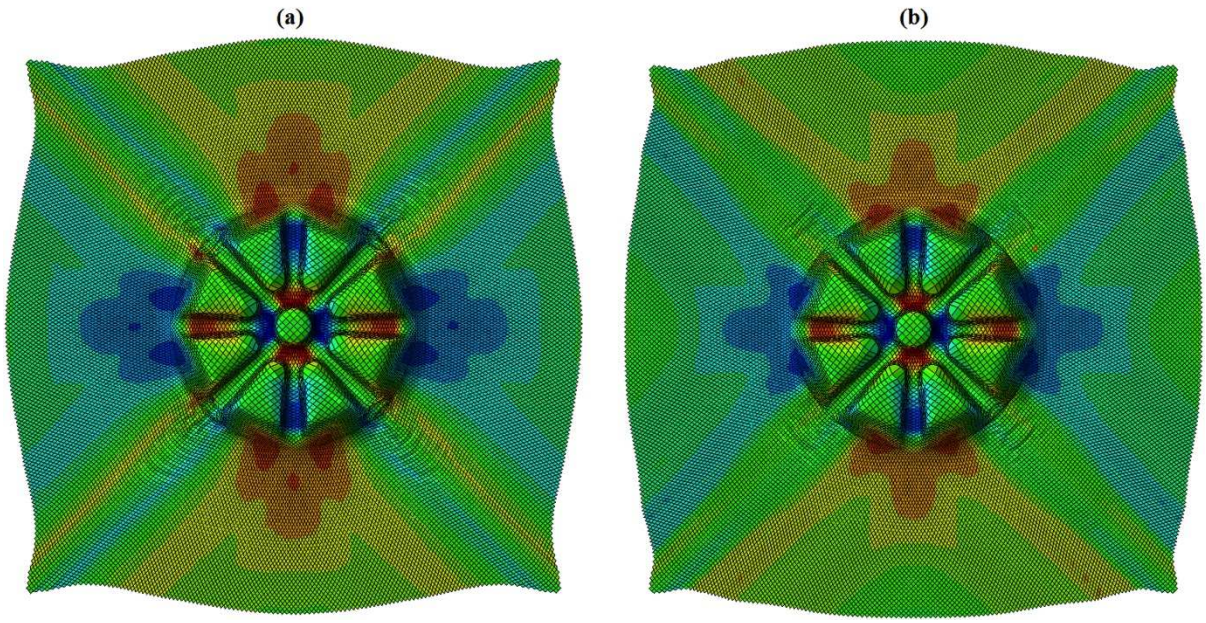


Figure 5.45. Contour plot of the predicted shear angle with a ±45° non-variable mesh (a) using the CS-NOCM coupled model (b) using the S-NOCM (repeated from Figure 5.30a to ease comparison) (wrGF).

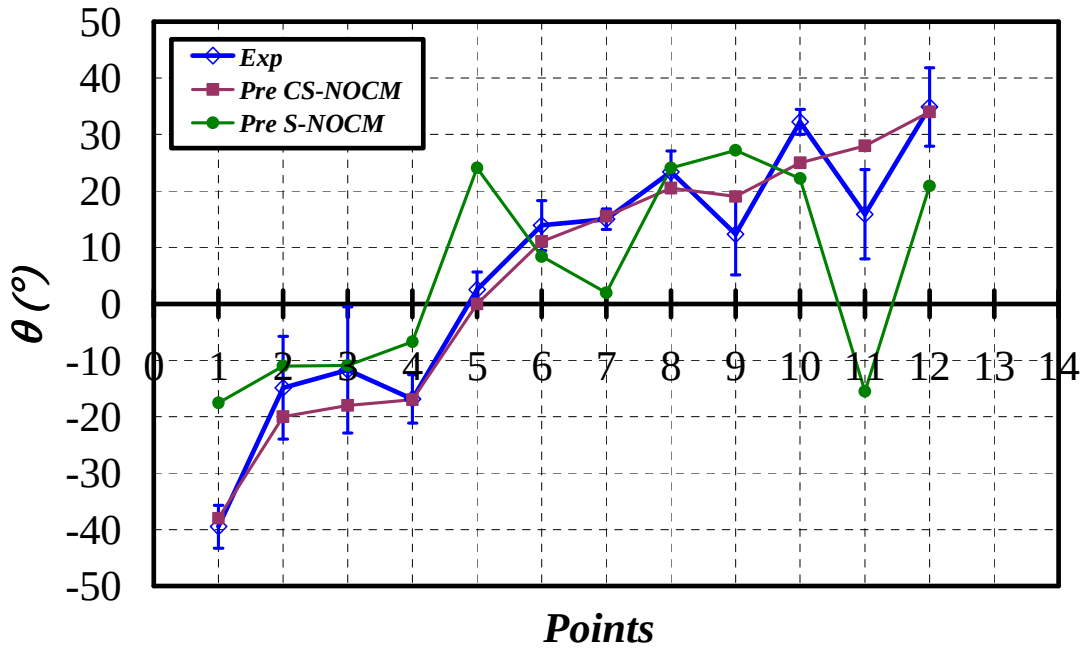


Figure 5.46. Comparison between experimental and predicted shear angle with ±45° non-variable mesh using the CS-NOCM and S-NOCM (from Figure 5.38 and repeated to ease comparison) (cgPP).

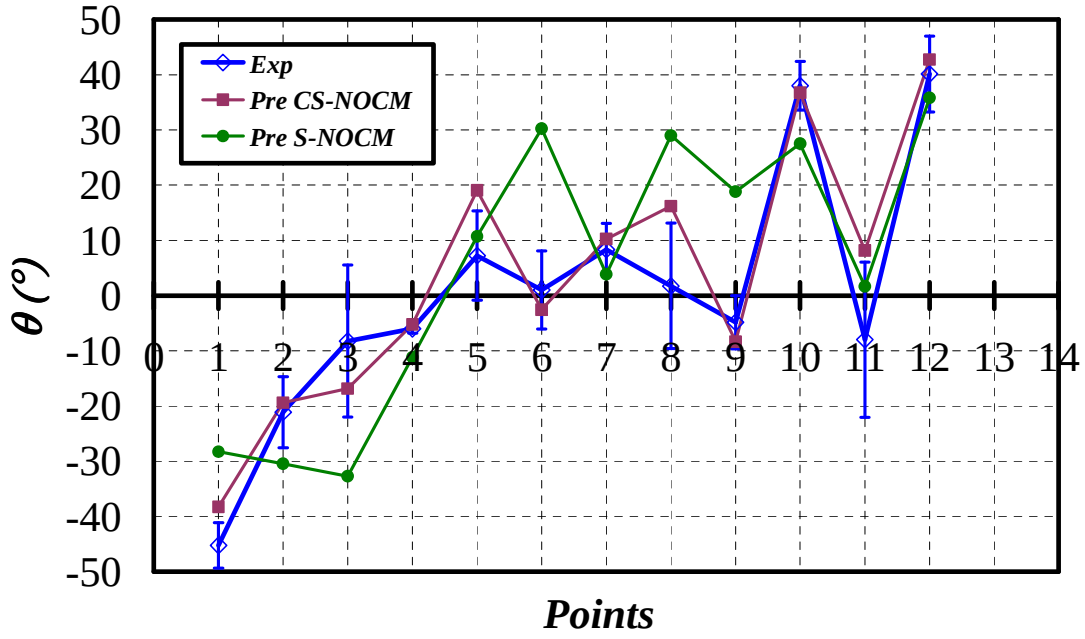


Figure 5.47. Comparison between experimental and predicted shear angle with ±45° non-variable mesh using the CS-NOCM and S-NOCM (from Figure 5.39 and repeated to ease comparison) (wrGF).

### 5.5.5 0/90° variable mesh predictions with enhanced CS-NOCM

FE forming simulations of cgPP and wrGF using 350 x 350 mm blanks with 0/90° variable mesh were carried out using the coupling model CS-NOCM. The variability of inter-tow angles of two 350 x 350 mm blanks with 0/90° orientation (see Figure 5.48) was characterised using a manual image processing method (see Section 3.4). The measured shear angle statistics (Table 5.1) were used to create cgPP and wrGF blanks with the same statistical data using the Varifab$^{GA}$ code (see Section 3.5.3).

The average side length of the cells in the two samples (Figure 5.48) is 10.2 and 13.4 mm for cgPP and wrGF respectively. Since the wheel geometry is very complex, the optimum element side length for forming the wheel using FE simulation was found to be about 2mm (small enough to capture the geometric complexity without mesh penetration though the tooling, but large enough to reduce simulation times to manageable levels). In order to obtain the orientation variability of the two fabrics on this length scale, linear extrapolations of the variability determined at two large lengths scales, for each of the fabrics, was used to provide a rough estimate. In order to generate two relations, one for each fabric, statistical distributions measured using two different grid spacing for each

fabric were used, namely, 10.2 and 10.2x2 for the cgPP and 13.4 and 13.4x2 mm for the wrGF. The orientation variability for the two samples with larger length scale was measured by considering four cells as one larger cell (see Figure 5.49). The orientation variability statistics of the cgPP and wrGF samples with larger cells are given in Table 5.2.

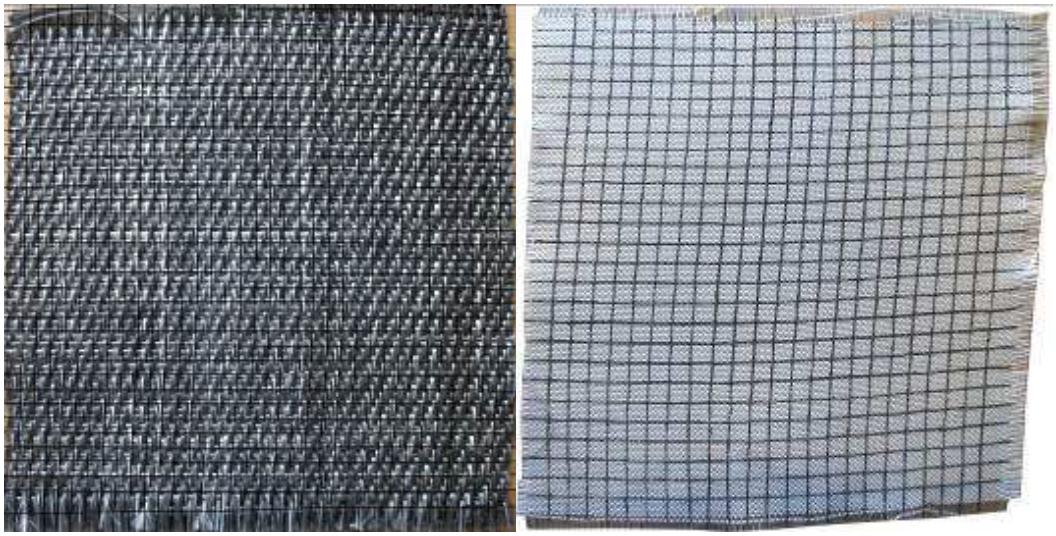

Figure 5.48. Example images of the variability seen in actual 350 x 350 mm textile samples. Average grid side lengths of 10.2 and 13.4 mm were marked for each cell of the cgPP (left) and wrGF (right) fabrics.

Table 5.1. The orientation variability statistics of the 350 x 350 mm cgPP and wrGF samples with 10.21 and 13.40 mm average side length

| cgPP | | wrGF | |
|---|---|---|---|
| *mu* | *std* | *mu* | *std* |
| 91.48 | 2.37 | 94.45 | 3.27 |

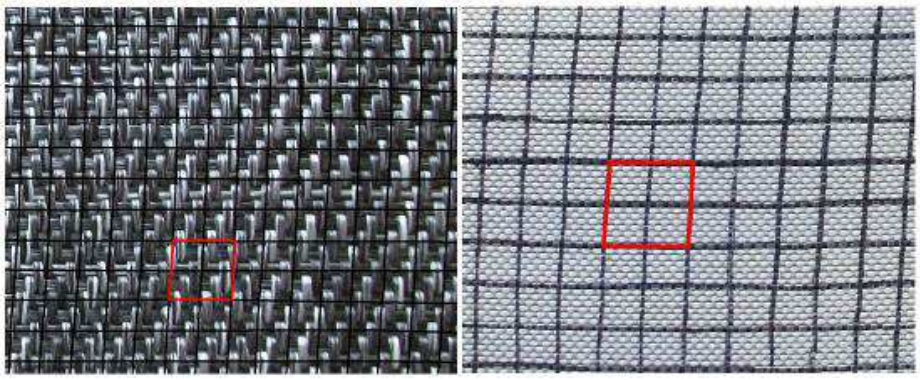

Figure 5.49. Close up of Figure 5.48, showing mages of the variability in an actual 350 x 350 mm textile samples with 10.2x2 and 13.4x2 mm average side length (one cell = 4 smaller cells for cgPP (left) and wrGF (right) )

Table 5.2. The orientation variability statistics of 350 x 350 mm cgPP and wrGf samples with 10.21x2 and 13.40x2 mm average side length

| cgPP | | wrGF | |
|---|---|---|---|
| *mu* | *std* | *mu* | *std* |
| 91.36 | 2.71 | 94.26 | 3.71 |

Linear relations of the average shear angle *mu* as a function of the cell side length *lc* are shown in Eqs. (5.1 & 5.2), and the linear relations of the standard deviation of the shear angle *std* as a function of the cell side length *lc* are shown in Eqs. (5.3 & 5.4) for the cgPP and wrGF materials respectively. The equations are based on the data in Tables 5.1 and 5.2.

$$mu = 0.0139 l_c + 91.342 \tag{5.1}$$

$$mu = 0.0164 l_c + 94.235 \tag{5.2}$$

$$std = -0.0405 l_c + 2.7914 \tag{5.3}$$

$$std = -0.0386 l_c + 3.7882 \tag{5.4}$$

The orientation variability statistics of the cgPP and wrGF samples with cell side length equal to 2 mm are calculated using Eqs. (5.1 to 5.4) and given in Table 5.3, the effect of extrapolating the results is quite small, suggesting that for these two samples there is only a small sensitivity of the variability with length scale.

Table 5.3. The orientation variability statistics of 350 x 350 mm cgPP and wrGf samples with 2 mm average side length.

| cgPP | | wrGF | |
|---|---|---|---|
| *mu* | *std* | *mu* | *std* |
| 91.62 | 1.96 | 94.67 | 2.74 |

Two blanks (membrane + truss elements) measuring 350 x 350 mm with a 2 mm side length of the membrane elements for both the cgPP and wrGF were modelled using the Varifab$^{GA}$ code and using the data in Table 5.3 as input parameters. Note that in these complex forming simulations and those of the next sections, the initial angle within the user subroutine in each element is $0^o$, i.e. the actual shear angle has not been initialised as it was in the variable meshes of the shear tests of Chapter 4 (by assigning each element to its own element set). This omission is for reasons of practicality; the computational requirements are significantly increased when using this approach and grow quickly with the number of elements within the FE mesh. Thus, the approach to include variability used in this chapter is a first step. More accurate predictions could be made in the future by initialising the shear angle in each element, though a significant increase in the currently available computational resource is required.

To be specific, the Abaqus simulation files (odb, pac, stt, message, abq……) become very large in terms of memory size, the simulation can take several days and even then no solution is guaranteed (there is often a lack of convergence). Thus, assigning initial shear angle variability in each element can make the simulation slow and the final Abaqus simulation files very large. For example, even for a small number of elements, such as the BBE simulation of Chapter 4 which employed just 264 membrane elements and 570 truss elements, with initial variability, the size of the final output files is 711 MB compared to 55MB without variability, about 13 times greater. Considering that forming simulations without initial variability produce .odb files the ABAQUS output database file, about 5 GB in size, the capacity with initial variability can be expected to be about 65 GB, assuming that a linear extrapolation is possible.

Returning to the variable simulations in this chapter, the shear properties are those used for the CS-NOCM (see Section 4.6.1) for the cgPP and wrGF materials as listed in Tables 4.8 and 4.10. The blank-holder forces are again 1000N for cgPP and 100N for wrGF. The contour plot of the predicted shear angle (SDV6) with variable and non-variable mesh (from Section 5.5.3, Figures 5.40a and 5.41a for cgPP and wrGF respectively), and a photo of the experimentally deformed part, are depicted in Figures 5.50 and 5.51 for cgPP and wrGF respectively. Figures 5.52 and 5.53 show a comparison between the average experimental and predicted shear deformation from the four quarters of the cgPP and wrGF materials respectively (see also Tables A.9 and A.10 Appendix A). Due to the variability in

the initial mesh, the shear deformation of the deformed part was measured from four quarters, at different 12 locations. The coordinates of the 12 locations of the shear angle in the four quarters are illustrated in Tables A.3 in Appendix A. In the subsequent figures, '*Exp*' is short for experimental results, '*Pre CS-NOCM-NV*' is short for predicted results obtained using CS-NOCM with non-variable mesh and '*Pre CS-NOCM-V*' is short for predicted results obtained using CS-NOCM with variable mesh.


Figure 5.50. Contour plot of the predicted shear angle of cgPP deformed part with a 0/90° initial orientation using (a) non-variable mesh (repeated from Figure 5.40a to ease comparison), (b) variable mesh and (c) the experimental deformed part

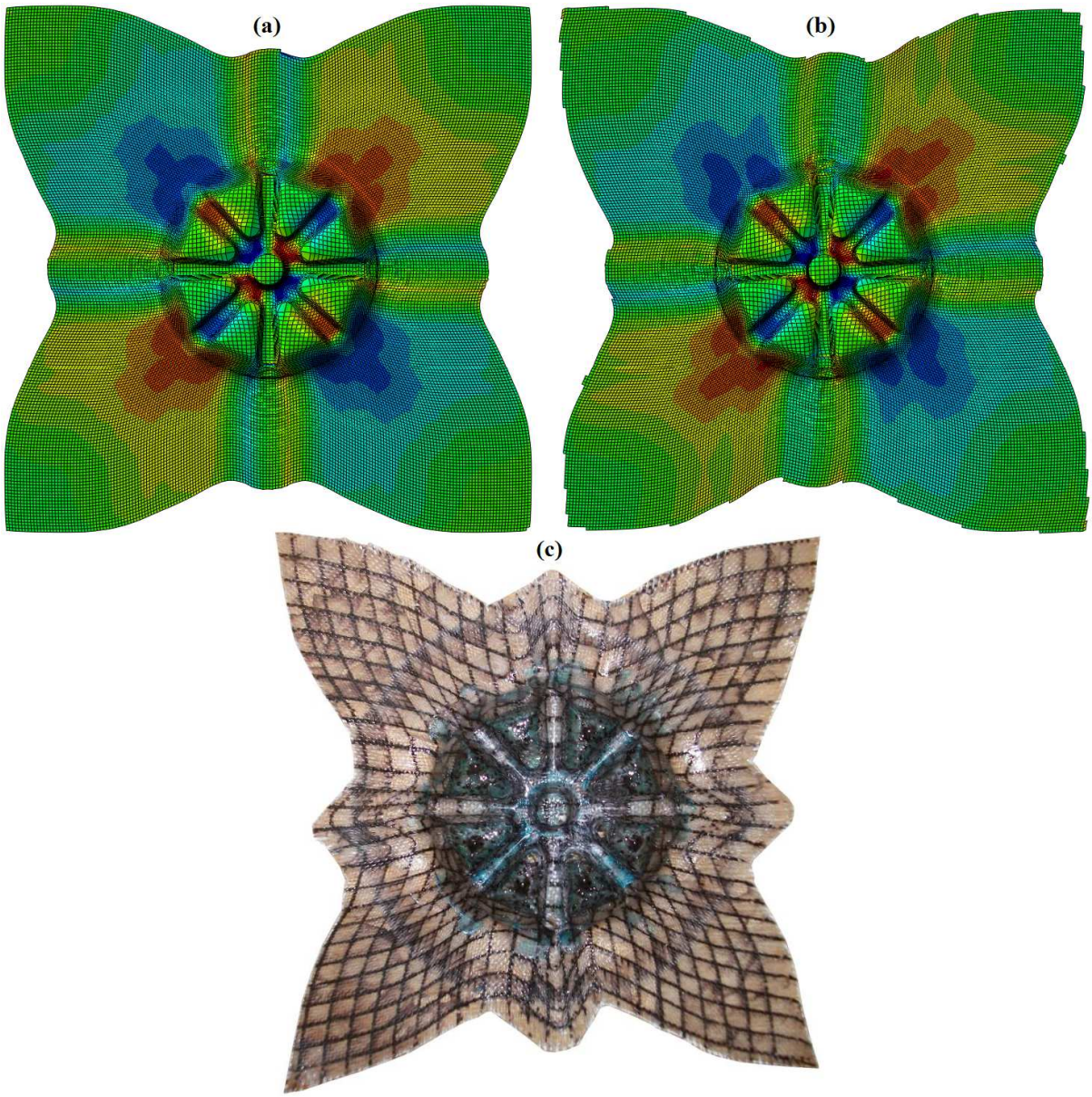


Figure 5.51. Contour plot of the predicted shear angle of wrGF deformed part with a 0/90° initial orientation using (a) non-variable mesh (repeated from Figure 5.41a to ease comparison), (b) variable mesh and (c) the experimental deformed part

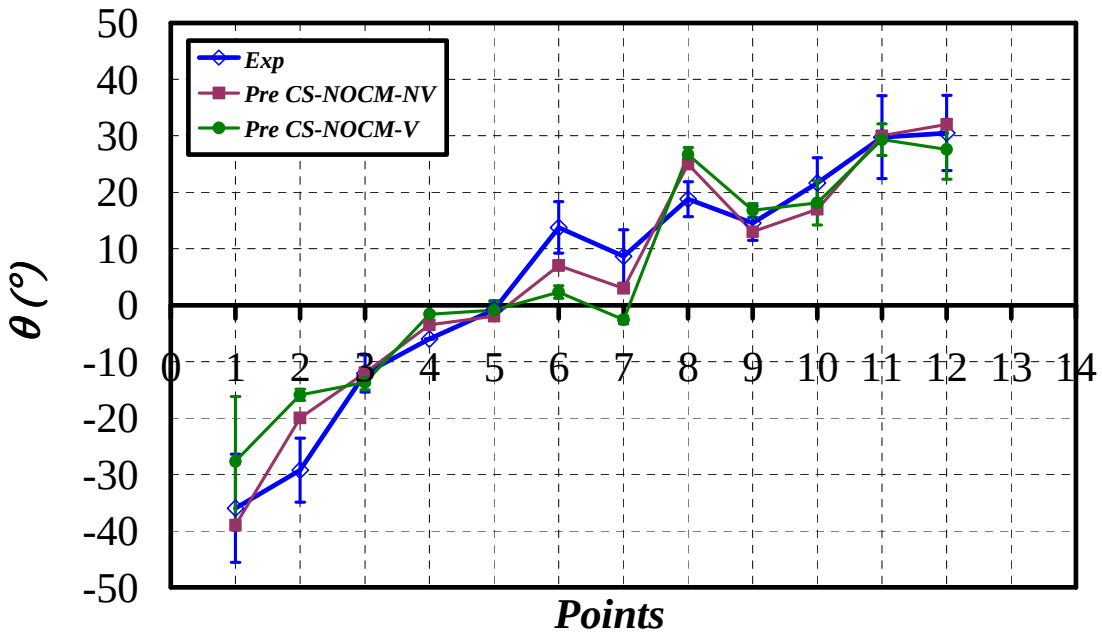


Figure 5.52. Comparison between the averaged experimental and predicted shear deformation from the four quarters of the cgPP with 0/90° variable mesh (Pre CS-NOCM-V) and non-variable mesh (Pre CS-NOCM-NV from Figure 5.42 and repeated to ease comparison).

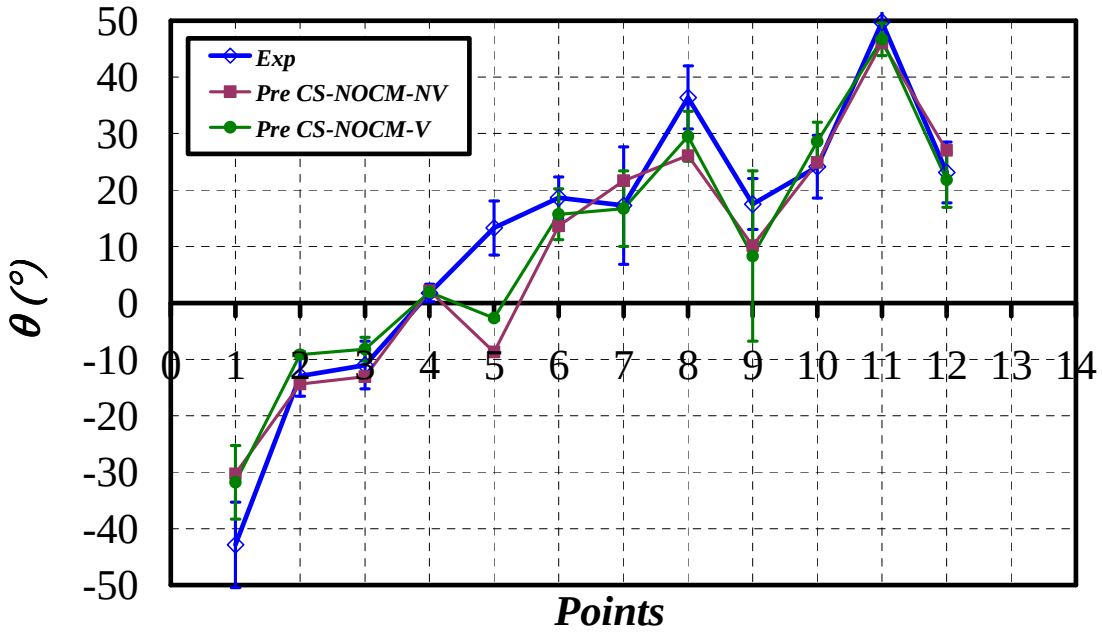


Figure 5.53. Comparison between the averaged experimental and predicted shear deformation from the four quarters of the wrGF with 0/90° variable mesh (Pre CS-NOCM-V) and non-variable mesh (Pre CS-NOCM-NV from Figure 5.43 and repeated to ease comparison).

### 5.5.6 ±45° variable mesh predictions with enhanced CS-NOCM

FE forming simulations of cgPP and wrGF using 350 x 350 mm blanks with ±45° variable mesh were carried out using the enhanced CS-NOCM. The variability of the inter-tow angles of two 350 x 350 mm blanks with ±45° orientation (see Figure 5.54) was characterised using a manual image processing method (see Section 3.4), and the measured shear angle statistics (Table 5.4) were used to create cgPP and wrGF blanks with the same statistical data using the Varifab$^{GA}$ code (see Section 3.5.3).

Figure 5.54. Example images of the variability seen in actual 350 x 350 mm textile samples. Average side lengths of 10.00 and 13.50 mm were marked for each cell of the cgPP (left) and wrGF (right)

Table 5.4. The orientation variability statistics of the 350 x 350 mm cgPP and wrGF samples with 10.00 and 13.50 mm average side length

| cgPP | | wrGF | |
|---|---|---|---|
| *mu* | *std* | *mu* | *std* |
| 94.91 | 2.83 | 91.73 | 5.47 |

The average side length of the cells in the two samples (Figure 5.54) is 10.00 and 13.50 mm for cgPP and wrGF respectively. The element side length is 2 mm as in Section 5.5.5. The orientation variability of the two fabrics on this length scale were obtained using same procedures followed in Section 5.5.5. The orientation variability statistics of the cgPP and wrGF samples with larger cells are given in Table 5.5.

Table 5.5. The orientation variability statistics of 350 x 350 mm cgPP and wrGf samples with 10.00x2 and 13.50x2 mm average side length

| cgPP | | wrGF | |
|---|---|---|---|
| *mu* | *std* | *mu* | *std* |
| 95.12 | 2.01 | 91.58 | 2.37 |

Linear relations of the average shear angle *mu* as a function of the cell side length *lc* are shown in Eqs. (5.5, 5.6), and the linear relations of the standard deviation of the shear angle *std* as a function of the cell side length *lc* are shown in Eqs. (5.7 and 5.8) for the cgPP and wrGF materials respectively. The equations are based on the data in Tables 5.4 and 5.5.

$$mu = 0.0119\, l_c + 94.891 \tag{5.5}$$

$$mu = -0.0063 l_c + 91.749 \tag{5.6}$$

$$std = -0.0457_c + 2.925 \tag{5.7}$$

$$std = -0..124 l_c + 5.721 \tag{5.8}$$

The orientation variability statistics of the cgPP and wrGF samples with cell side length equal 2 mm are calculated using Eqs. (5.5 to 5.8) and given in Table 5.6, the effect of extrapolating the results is quite small suggesting that for these two samples there is only a small sensitivity of the variability with length scale.

Table 5.6. The orientation variability statistics of 350 x 350 mm cgPP and wrGf samples with 2 mm average side length.

| cgPP | | wrGF | |
|---|---|---|---|
| *mu* | *std* | *mu* | *std* |
| 95.00 | 2.47 | 91.66 | 4.04 |

Two blanks (membrane + truss elements) measuring 350 x 350 mm with 2 mm side length of the membrane elements of cgPP and wrGF were modelled using Varifab$^{GA}$ code and using the data in Table 5.6 as input parameters.

The shear properties for these simulations are again those used for the coupled model (see Section 4.6.1) for the cgPP and wrGF materials, as listed in Tables 4.8 and 4.10. The blank holder forces are again 1000N for cgPP and 100N for wrGF. The contour plot of the predicted shear angle (SDV6) with variable and non-variable mesh (Section 5.5.4, Figures 5.44a and 5.45a for cgPP and wrGF respectively) and a photo of the experimentally deformed part are depicted in Figures 5.55 and 5.56 for cgPP and wrGF respectively. Figures 5.57 and 5.58 show a comparison between the averaged experimental and predicted shear deformation from the four quarters of the cgPP and wrGF materials respectively (see also Tables A.11 and A.12 Appendix A). The shear deformation of the deformed part was measured from four quarters, at 12 different locations. The coordinates of the 12 locations of the shear angle in the four quarters are given in Tables A.6 in Appendix A.

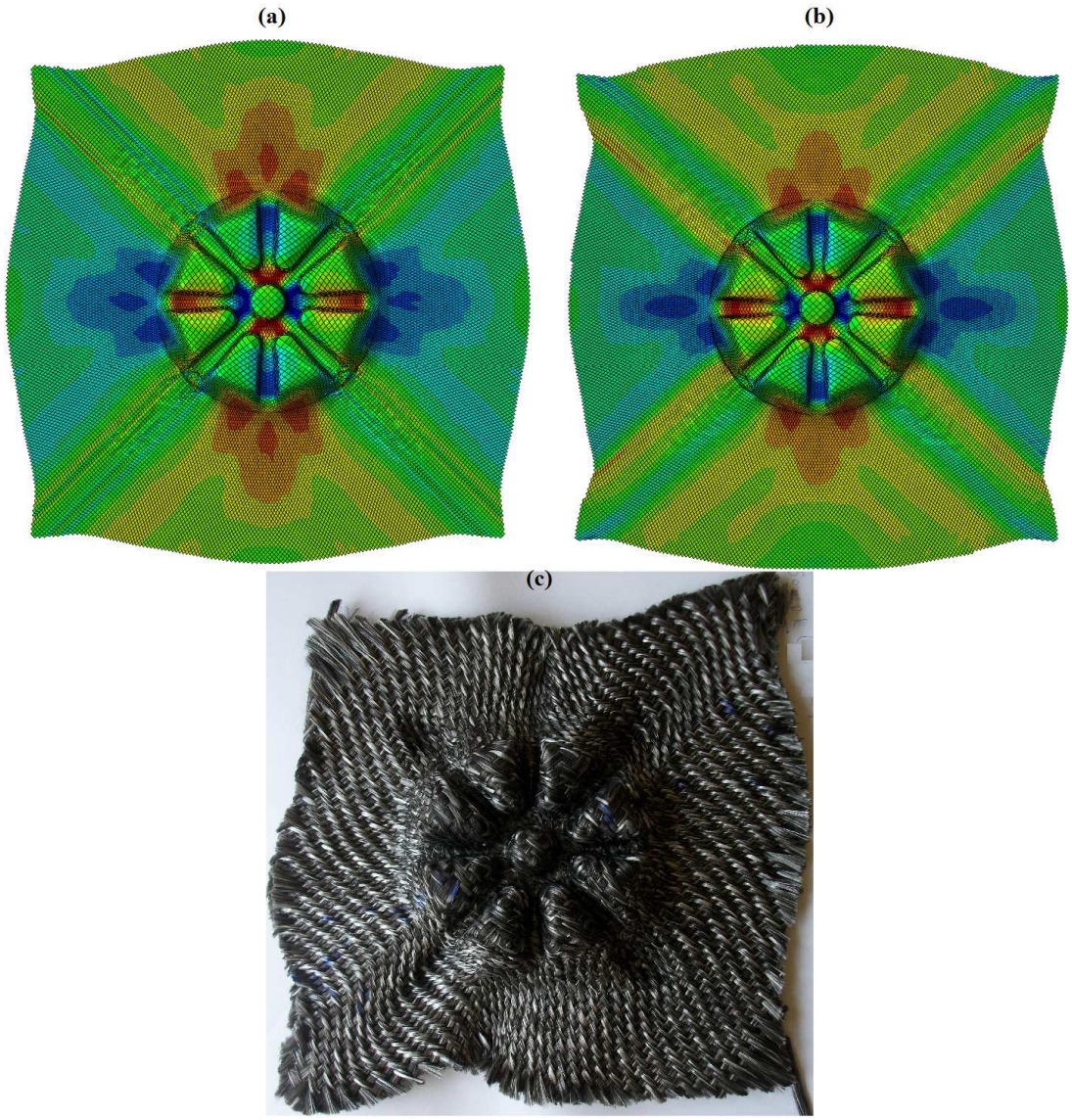


Figure 5.55. Contour plot of the predicted shear angle of cgPP deformed part with a ±45° initial orientation using (a) non-variable mesh (from Figure 5.44a and repeated to ease comparison), (b) variable mesh and (c) the experimental deformed part

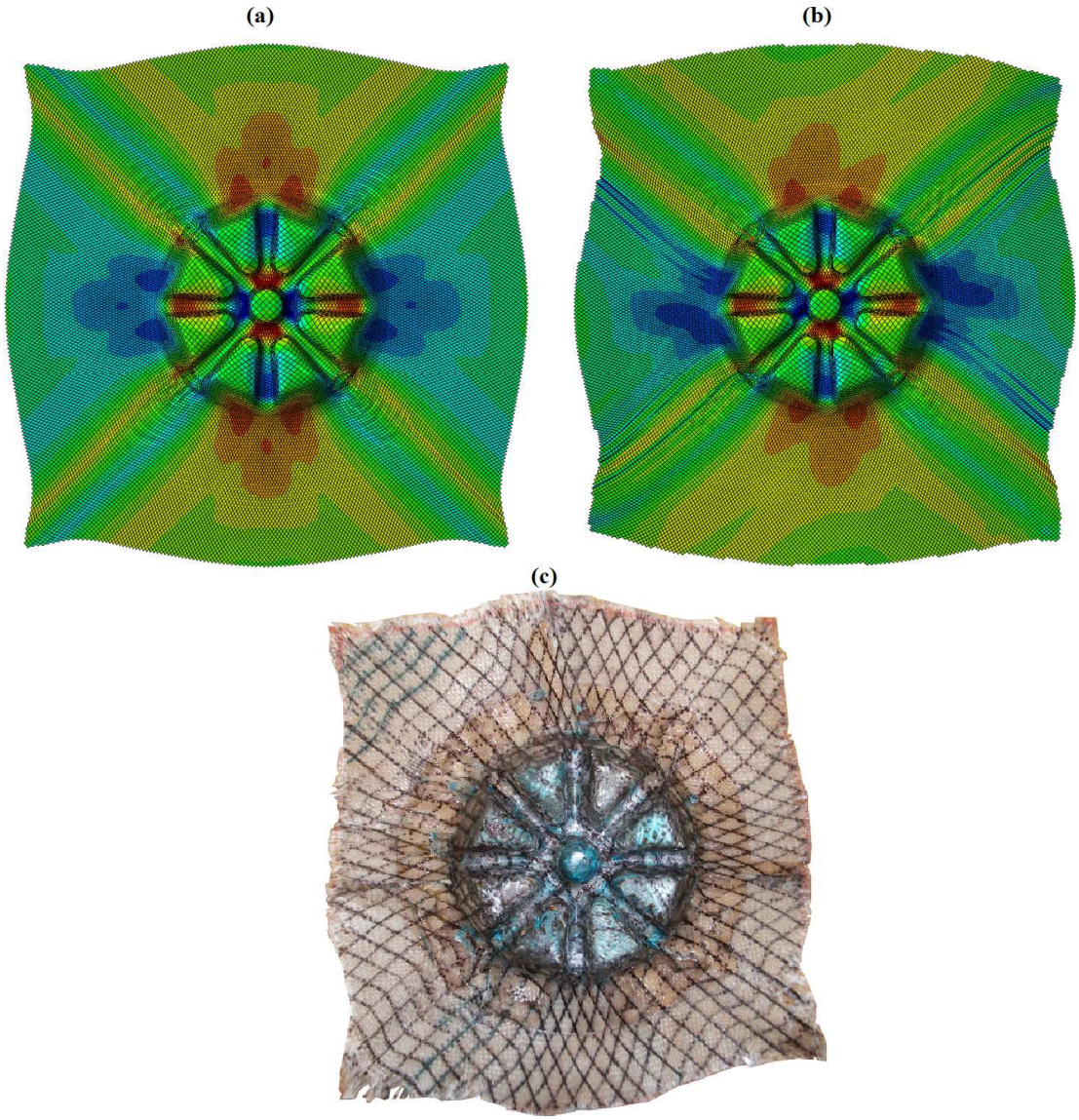


Figure 5.56. Contour plot of the predicted shear angle of wrGF deformed part with a ±45° initial orientation using (a) non-variable mesh (from Figure 5.45 (a) and repeated to ease comparison), (b) variable mesh and (c) the experimental deformed part

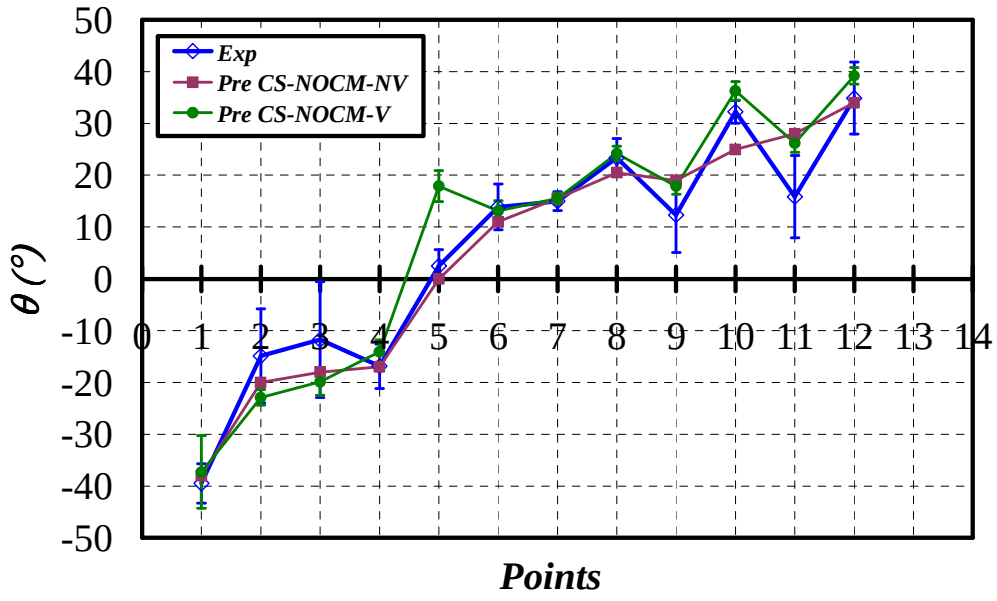


Figure 5.57. Comparison between the averaged experimental and predicted shear deformation from the four quarters of the cgPP with ±45° variable mesh (Pre CS-NOCM-V) and non-variable mesh (Pre CS-NOCM-NV repeated from Figure 5.42 to ease comparison).

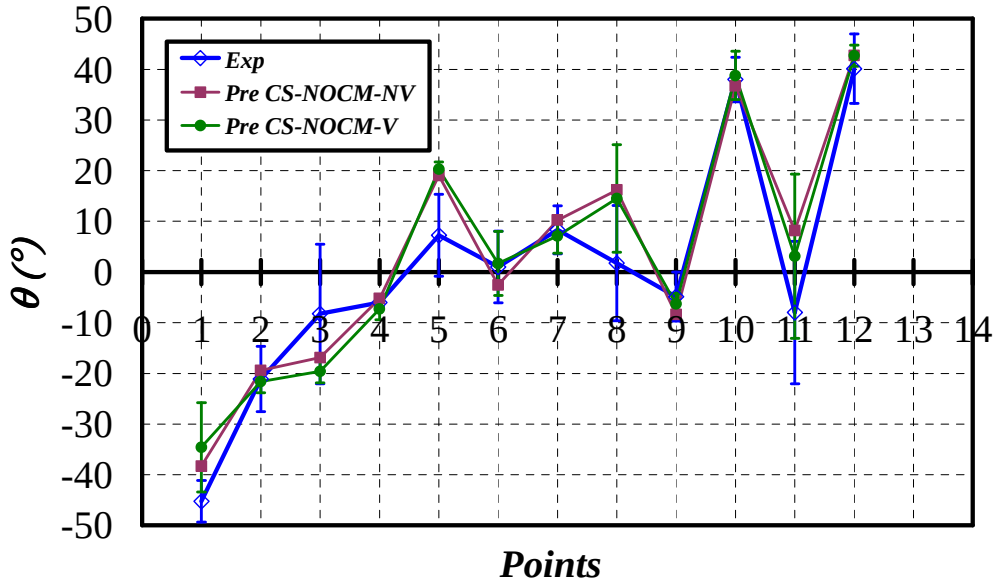


Figure 5.58. Comparison between the averaged experimental and predicted shear deformation from the four quarters of the wrGF with ±45° variable mesh (Pre CS-NOCM-V) and non-variable mesh (Pre CS-NOCM-NV repeated from Figure 5.43 to ease comparison).

Comparison of the local shear deformation between the predicted and experimental results of cgPP and wrGF with variable and non-variable meshes with two initial fibre orientations 0/90° and ±45° has been carried out (see Figures 5.52 and 5.53 for 0/90° and 5.57 and 5.58 for ±45°). In general, good agreement between the predicted and experimental results can be observed (see Figures 5.52 and 5.53 for 0/90° and 5.57 and 5.58 for ±45°) and in these cases error bars can now be included in the simulation results. At most measurement points the error bars overlap, however there are still variations at some points. Moreover, there is no stable trend for the predicted results of the variable and non-variable meshes(see Figures 5.52 and 5.53 for 0/90° and 5.57 and 5.58 for ±45°); in some cases the predicted results of the non-variable mesh are closer to the experimental results than those of the variable mesh and vice versa.

Nevertheless, comparison of both the global and the local shear deformation of the CS-NOCM appear to be quite good. Further enhancements may still be possible in the future by incorporating factors such as bending stiffness, the nonlinearity and biaxial tension coupling of the warps and wefts tows and by modelling friction contact between the tool and ply more accurately using the VFRIC user subroutine. It should be noted however that all these changes will lead to increases in simulation time but should be facilitated by the ever improving speed of computers.

### 5.5.7 The Effects of Different Tensile Stiffness in Warp and Weft Directions on Draw-in Shape

The differences in the draw-in shapes of the predicted and experimental results for the cgPP fabric (see Figures 5.50 and 5.55) may well be attributed to the significant differences in the crimp of the warp and weft tows which produce non-linear and coupled tensile stiffness in the two tow directions (see [23, 224]). To examine this hypothesis, FE simulations have been conducted using different tensile stiffness in the warp and weft directions, i.e. assigning different tensile properties to the truss elements in the horizontal and vertical directions. This has been done by sorting the truss elements in the horizontal and vertical directions into two different element sets using an in-house Matlab code ‘TensionAsymmetric.m’, and then assigning two different linear elastic stiffness values to the two different truss element sets using the solid section keyword. Simulations of the wheel have been performed using Young’s Modulus of the truss elements in the horizontal

and vertical direction of 16GPa and 2.26GPa and UBE shear compliance as illustrated in Table 4.2. Predictions for the two orientations of 0/90 and +/- 45$^{o}$ are shown in Figure 5.59.

It can be seen clearly from Figure 5.59 that assigning different tensile stiffness in the warp and weft direction produces an asymmetric perimeter shape for the +/- 45$^{o}$ case which is much closer to the cgPP experimentally formed component. By comparing the predicted perimeter shape in Figure 5.59 with those in Figures 5.40, 5.41, 5.44, 5.45, 5.50, 5.51, 5.55 and 5.56, it can be concluded that tensile stiffness is a key factor in modelling the exact draw-in shape of fabrics with different weave styles and asymmetric crimp. However, while improvements can be obtained by using unbalanced stiffness properties for the truss elements, accurate modelling of the wheel part cannot be achieved by simply using linear elastic properties. The nonlinear coupled tensile behaviour of woven engineering fabrics has been measured previously by [23, 111], Boisse, et al. [172], [224]. Thus, more accurate predictions could perhaps be provided by, for example, a hyperelastic model containing a mechanical coupling of the stiffness in the two fibre directions, as suggested in [145]. This could provide an interesting and useful focus for future work.

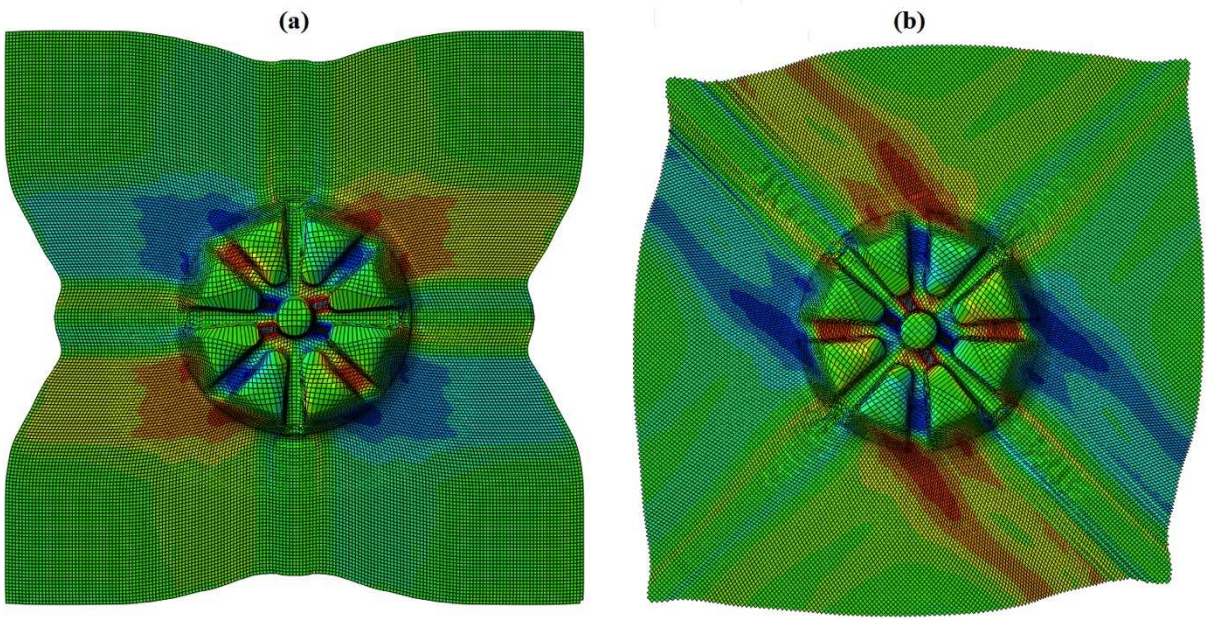


Figure 5.59. New draw-in shape of the deformed wheel part using different warp and weft tensile stiffness (a) deformed part with 0/90° initial orientation and (b) deformed part with ±45° initial orientation.

## 5.6 Influence of Material and Process Parameters on Shear Deformation

Before closing this complex forming investigation a final sensitivity study has been conducted to explore the influence of several factors on forming predictions. Material and process parameters considered in this sensitivity study include:

1. blank-holder force,
2. friction coefficient between tools and blank,
3. shear compliance,
4. mass scaling

### 5.6.1 Effect of Blank Holder Force

One of the very important factors in the forming process is the blank-holder force. Wrinkling propagation and reduction mainly depends on several parameters; one of them is blank-holder force. However, since excessively increasing or decreasing the blank-holder force can cause tearing of the sheet (see Figure 5.26a) or wrinkling (see Figure 5.26b), an optimized blank-holder force is an important issue in the forming process. In order to investigate the effect of different blank-holder forces on local shear deformation, an FE simulation has been carried out using the CS-NOCM and two blank-holder forces of 500N and 1000N for the two orientations of 0/90° and ±45° on the cgPP material. The contour plots of the two cases are quite similar as illustrated in Figures 5.60 and 5.61. 500N, the local shear deformation results are close to those of 1000N (as shown in Figures 5.62 and 5.63). Thus, it appears that halving the blank-holder pressure has only a small influence on the fabric's shear behaviour.

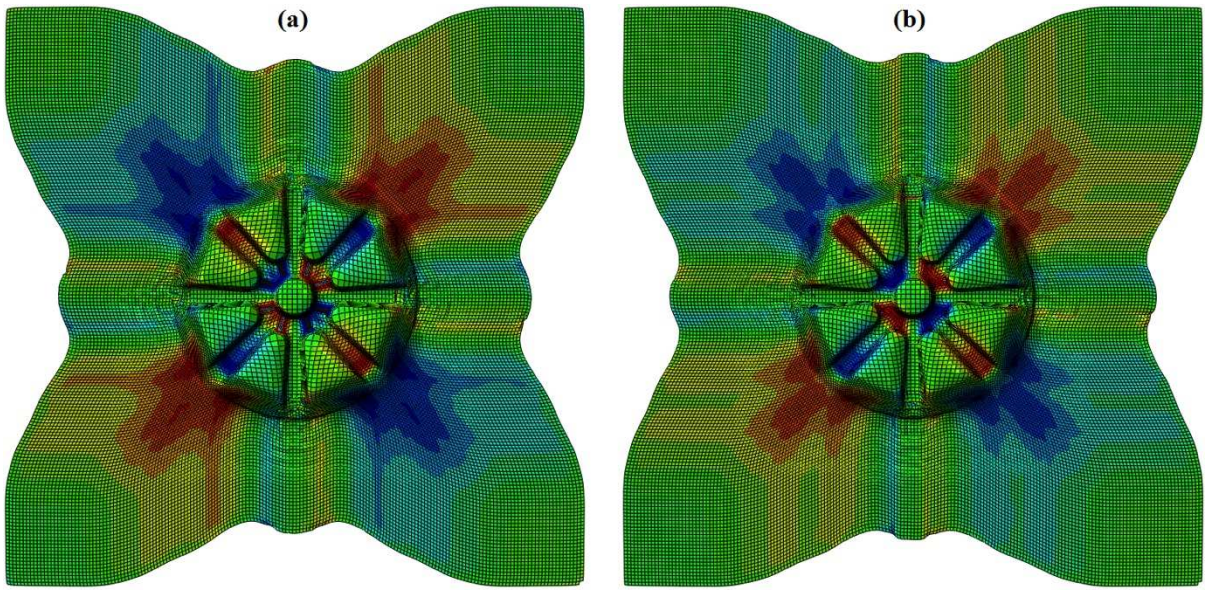


Figure 5.60. The contour plot of the shear deformation of cgPP with 0/90° non-variable mesh using CS-NOCM (a) BHF = 1000N (from Figure 5.40 (a) and repeated to ease comparison) and (b) BHF = 500N

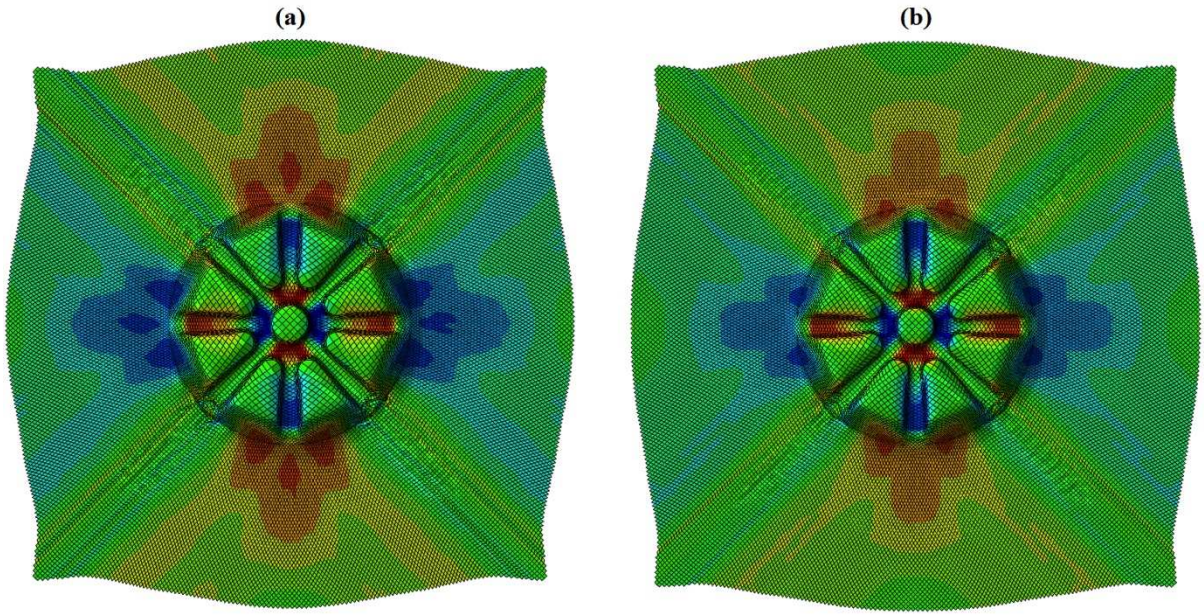


Figure 5.61. The contour plot of the shear deformation of cgPP with ±45° non-variable mesh using the CS-NOCM (a) BHF = 1000N (repeated from Figure 5.44a and to ease comparison) and (b) BHF = 500N

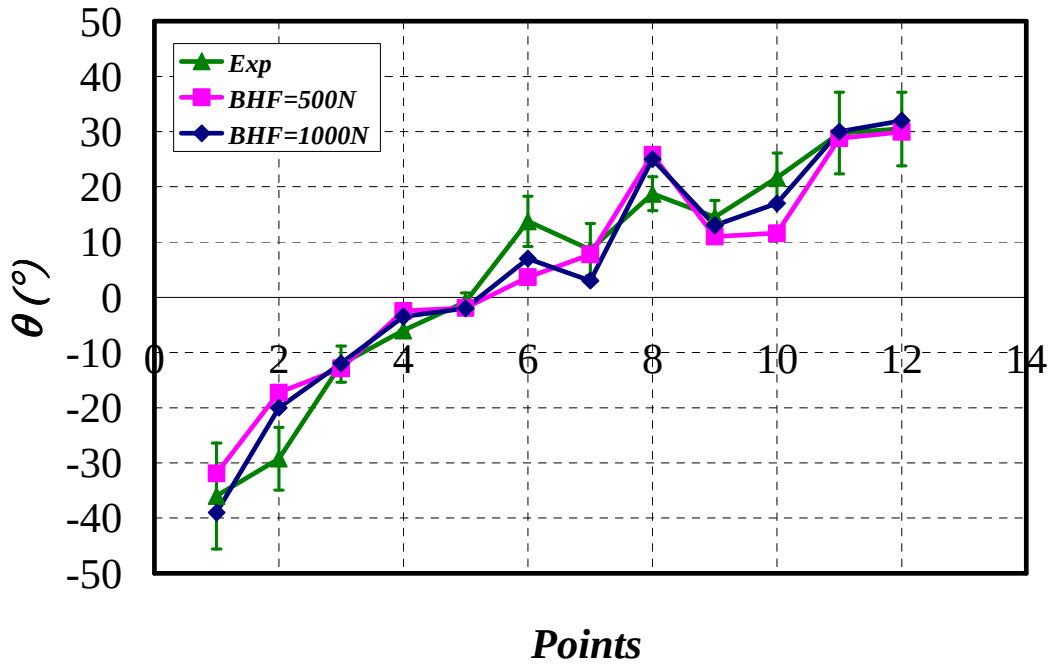


Figure 5.62. Comparison between the predicted shear deformation of cgPP with initial orientation of 0/90° using a non-variable mesh for two different BHFs 500 and 1000N

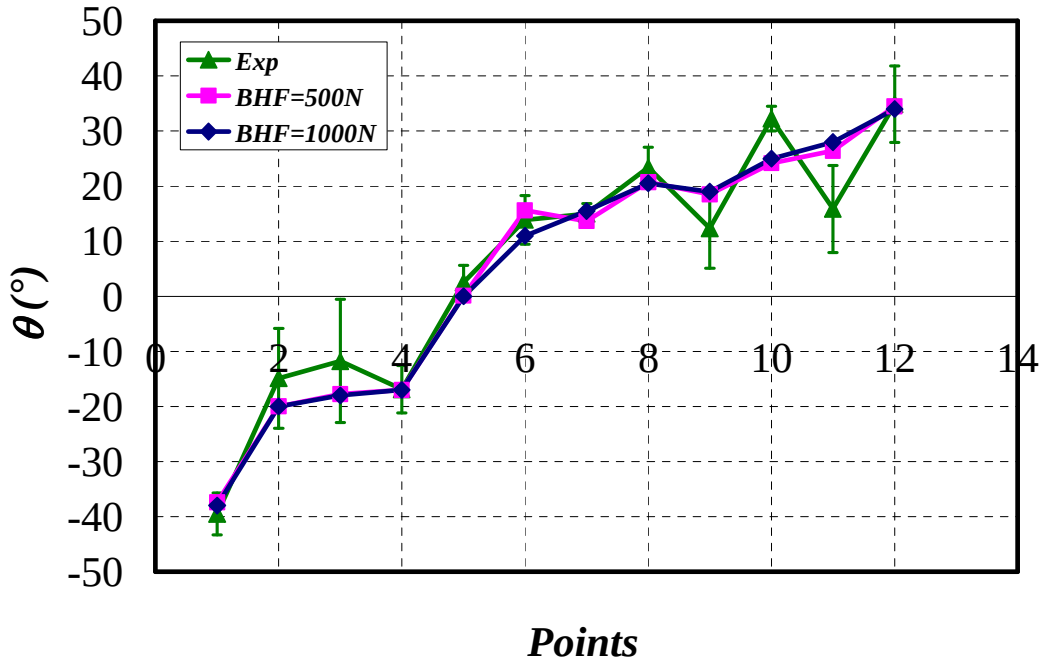


Figure 5.63. Comparison between the predicted shear deformation of cgPP with initial orientation of ±45° using a non-variable mesh for two different BHFs 500 and 1000N

### 5.6.2 Effect of Friction Coefficient

The Coulomb friction model provided in Abaqus for contact analysis was used to model friction between tools and blank during the forming simulations. Two different values of friction coefficient were used in the forming simulations of cgPP with two orientations 0/90° and ±45° respectively. The friction coefficients used in the simulations are 0.3 and 0.5 with 1000N blank-holder force. The contour plot of the local shear deformation of the numerical forming process of cgPP for the two friction coefficients 0.3 and 0.5 are shown in Figures 5.64 and 5.65 for 0/90° and ±45° initial orientations respectively. Figures 5.66 and 5.67 show the local shear deformation of the cgPP with 0/90° and ±45° non-variable meshes using CS-NOCM respectively. Figures 5.66 and 5.67 suggest the results are quite sensitive to changes in friction, which is an unexpected result given that this should be equivalent to a change in the blank-holder pressure, and that the shear angle distribution was found to be insensitive to the latter. This result requires further investigation but has to the deferred to future work due to time constraints.

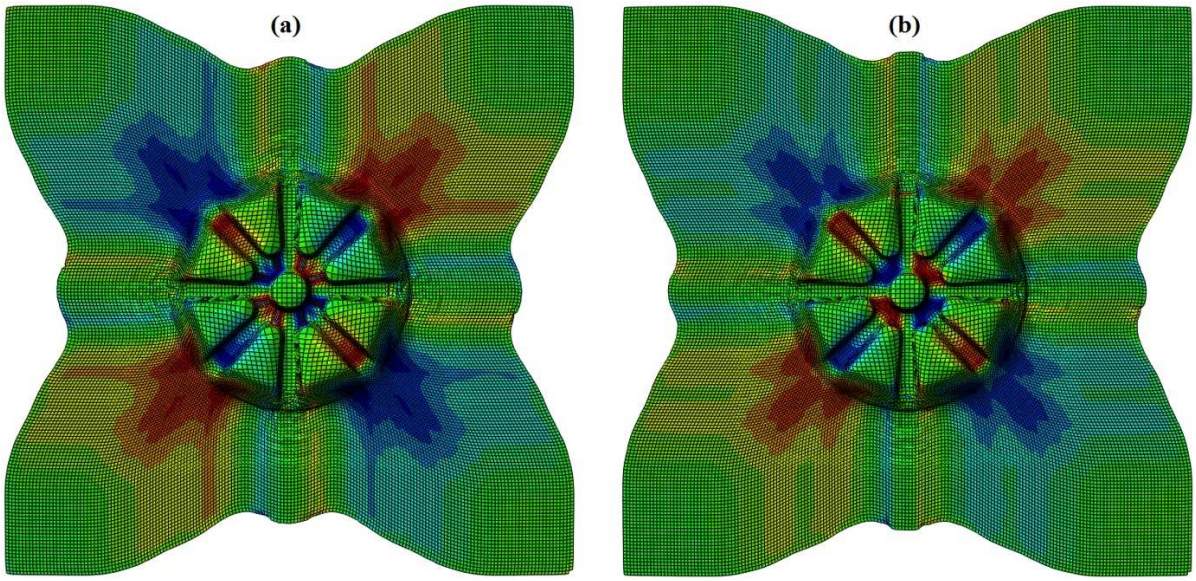


Figure 5.64. The contour plot of the shear deformation of cgPP with 0/90° non-variable mesh using the coupling model (a) friction coefficient = 0.3 (b) friction coefficient = 0.5

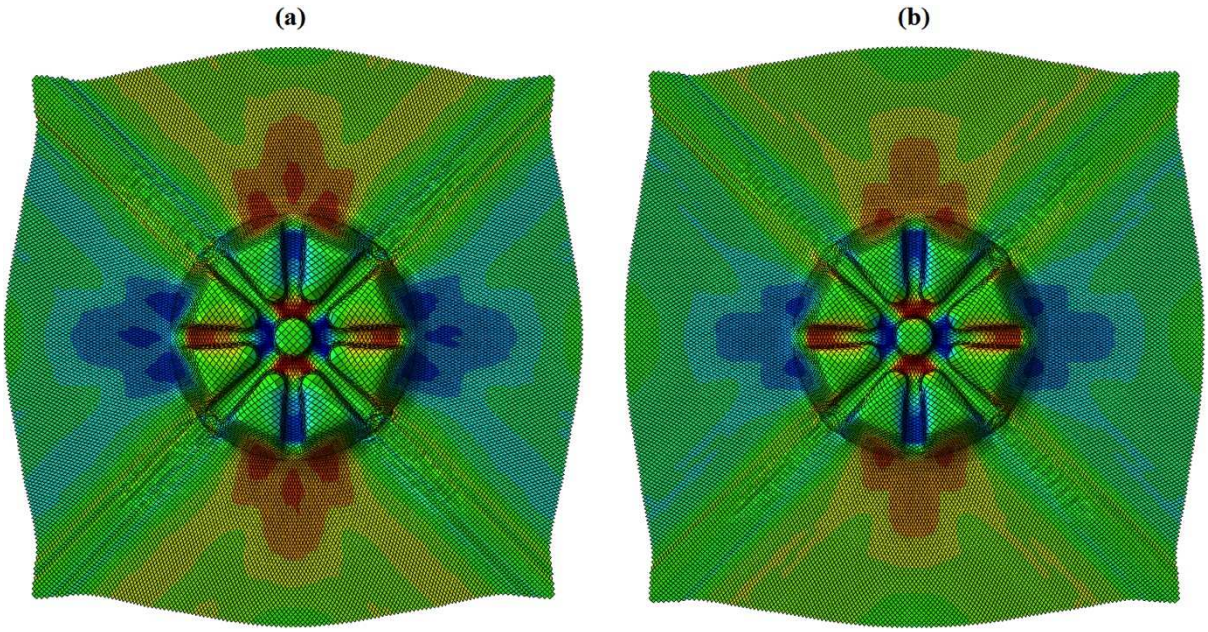


Figure 5.65. The contour plot of the shear deformation of cgPP with ±45° non-variable mesh using the coupling model (a) friction coefficient = 0.3 (b) friction coefficient = 0.5

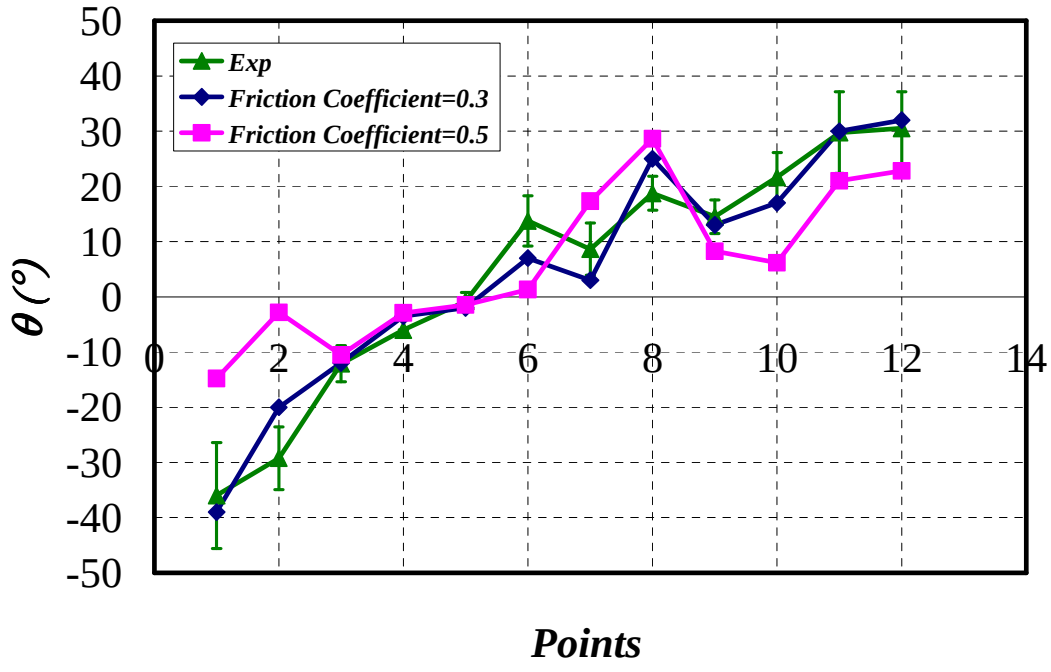


Figure 5.66. Comparison between the predicted shear deformations of cgPP with 0/90° using a non-variable mesh of two different friction coefficients with the experimental results

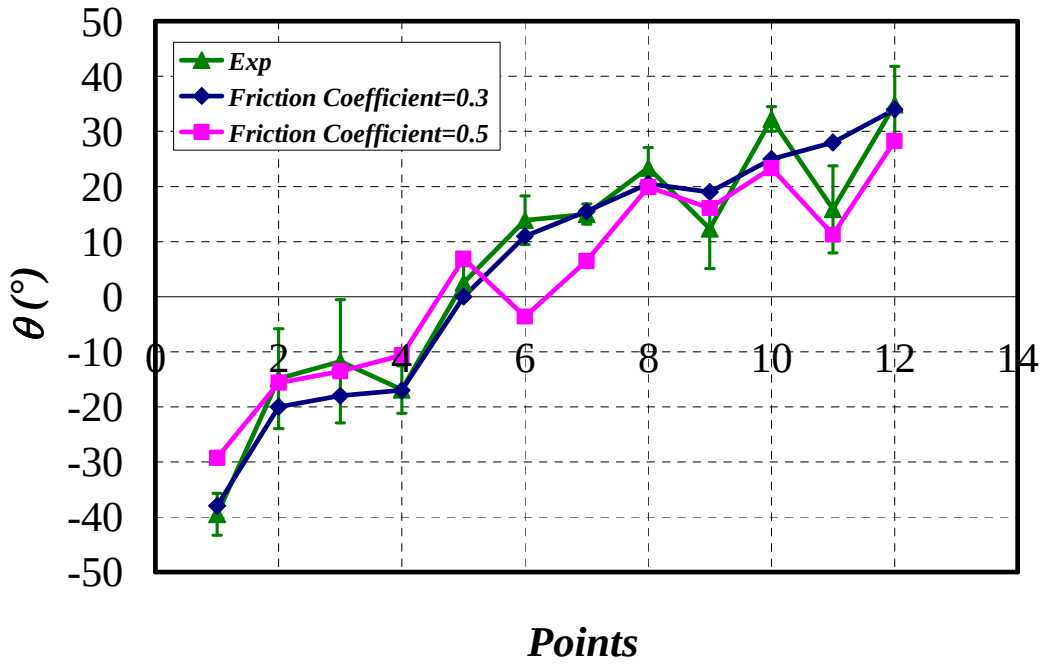


Figure 5.67. Comparison between the predicted shear deformations of cgPP with ±45° using a non-variable mesh of two different friction coefficients with the experimental results

### 5.6.3 Effect of Different Shear Compliances

This section explores the effect of changing the shear compliance of the cgPP material on local shear deformation. Both the CS-NOCM and S-NOCM models were used in the following forming simulations. Two simulations using the S-NOCM, one with a high and another with a low shear compliance, taken from the BBE tests with 100 and 5 N transverse force (see Table 4.10 in Chapter 4), have been conducted and compared against another forming simulation using the CS-NOCM (see Tables 4.10 in Chapter 4). Note that because both these input curves are of higher stiffness than the UBE input shear curves used in the Sections 5.5.1 and 5.5.2, it was found that the simulations could be run without the need for mass scaling (only for a ±45° non-variable mesh) and therefore permit a more valid comparison with the CS-NOCM predictions. Figure 5.68 shows a contour plot of the predicted shear deformation of cgPP with a ±45° non-variable mesh using (a) low shear compliance (BBE with 5 N transverse force) using S-NOCM, (b) high shear compliance (BBE with 100 N transverse force) using S-NOCM and (c) a coupled shear compliance using the CS-NOCM (repeated from Figure 5.44a to ease comparison). The distribution of shear deformation is clearly different for the three cases as can be seen in Figure 5.68. However, the shear angle distribution of the high shear compliance (BBE with 100 N transverse force) Figure 5.68a is quite close to the shear distribution of coupling shear

compliance Figure 5.68c, which is to be expected since the applied blank holder force is high and more likely to use a high shear compliance in the coupling model. Figure 5.69 shows a comparison between locally predicted results using the different shear compliances with the experimental results. The shear compliances that have been used in the comparison are high and low BBE shear compliances BBE with 5 and 100 N transverse force) using S-NOCM and coupling shear compliances (see Table 4.10 Chapter 4)) using CS-NOCM. In Figure 5.69 *'Pre S-NOCM-H-BBE'* is short for predicted results obtained using S-NOCM with high BBE shear compliance BBE with 100 N transverse force) and *'Pre S-NOCM-L-BBE'* is short for predicted results obtained using S-NOCM with low BBE shear compliance BBE with 5 N transverse force).

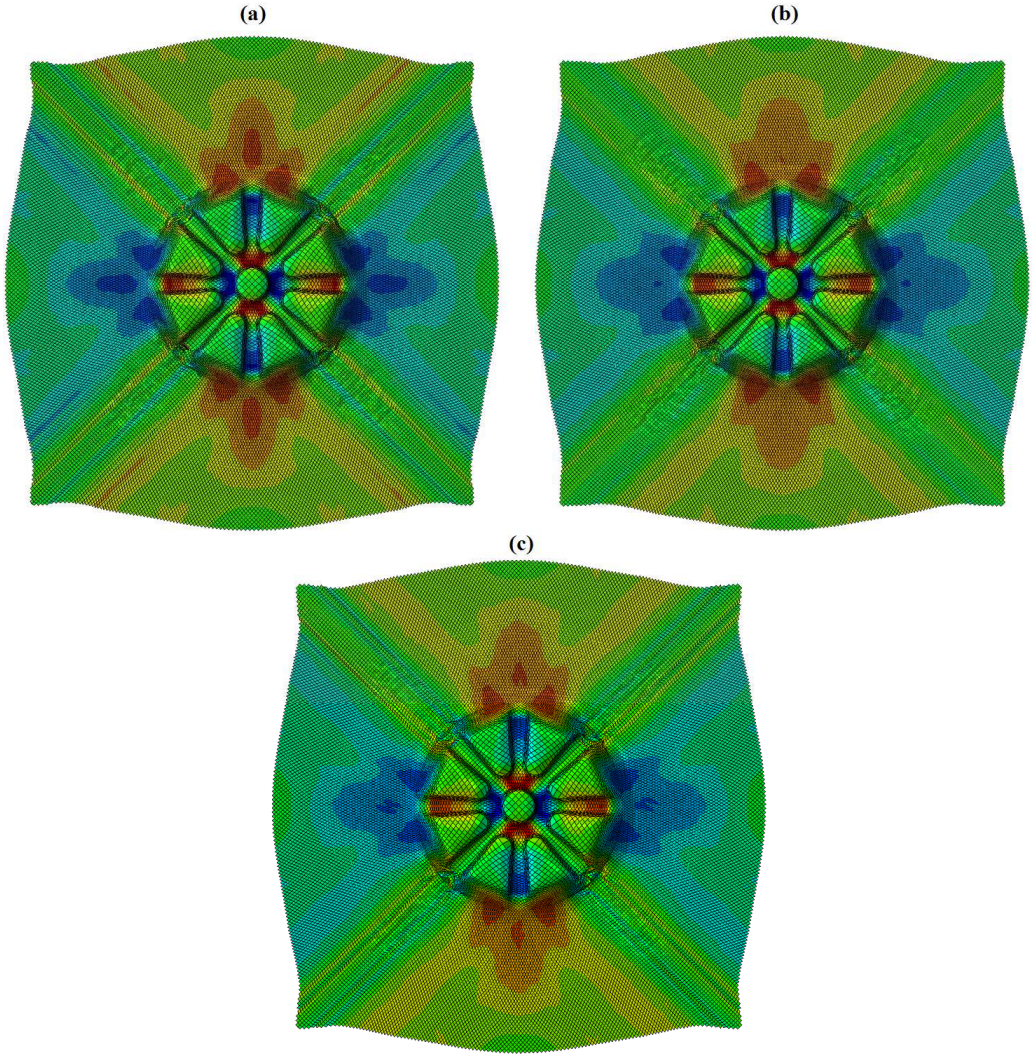


Figure 5.68. The contour plot of the predicted shear angle SDV6 with ±45° non-variable mesh using (a) low shear compliance (BBE with 5 N transverse force), (b) high shear compliance (BBE with 100 N transverse force) and (c) coupling shear compliance.

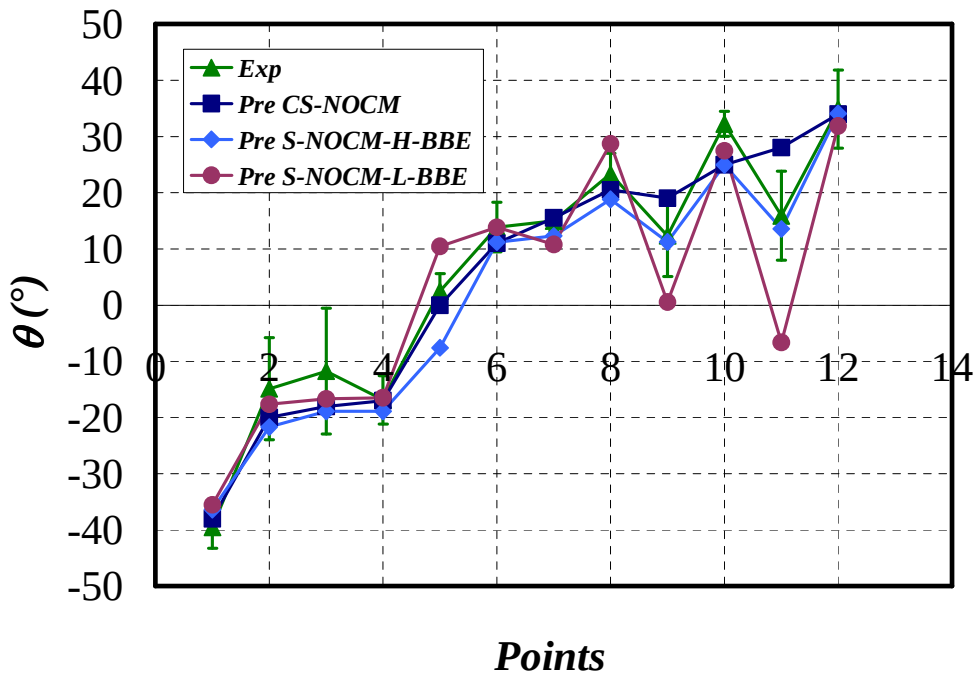


Figure 5.69. Comparison between the predicted shear deformations of cgPP non-variable mesh with ±45° using the two constitutive models (S-NOCM with (high and low BBE shear compliances) and CS-NOCM with coupling shear compliances (see table 4.10 Chapter 4)) with the experimental results

The shear deformation obtained by using high BBE shear compliance in the S-NOCM is close to the shear deformation obtained by using coupling shear compliances (see Table 4.10 Chapter 4) in the CS-NOCM which is to be expected since the applied blank holder force is high (1000 N) and more likely to use high shear compliance in the CS-NOCM.

### 5.6.4 Effect of Mass Scaling on Shear Deformation

This section explores the effect of changing the mass scaling of cgPP material on local shear deformation. The CS-NOCM model was used in the following forming simulations of cgPP with a ±45° non-variable mesh using the shear compliance properties of BBE with 5N transverse force (see Table 4.10 Chapter 4)). Two simulations have been conducted with fixed mass scaling factor (MSF) = 5 and 10. The shear deformation results at certain positions were compared against the predicted results obtained earlier in Section 5.6.3 using low BBE with 5N transverse force with zero MSF. Figure 5.70 shows a contour plot of the predicted shear deformation of the three cases. As can be seen clearly from Figure 5.70, increasing the mass scaling factor decreases the draw-in shape and reduces the values of shear deformation across out the blank.

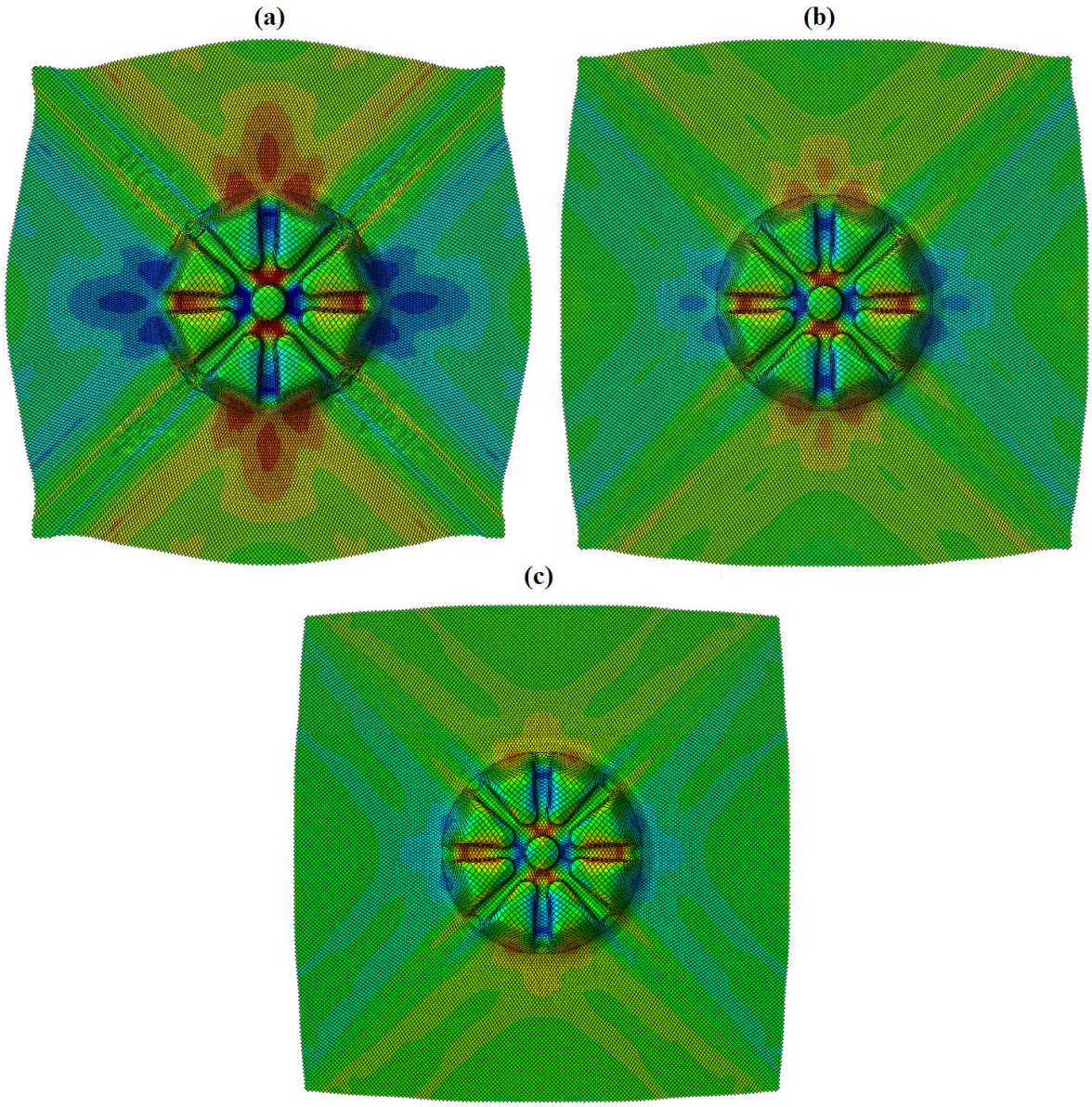


Figure 5.70. The contour plot of the predicted shear angle SDV6 with ±45° non-variable mesh using (a) MSF = 0 (repeated from Figure 5.68a and to ease comparison), (b) MSF = 5 and (c) MSF = 10.

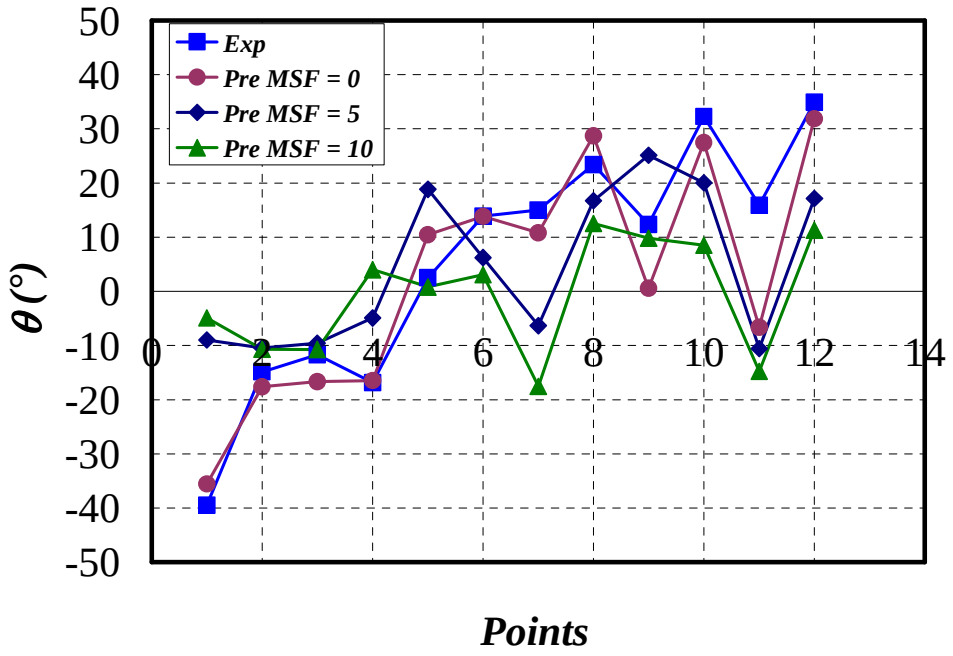


Figure 5.71. Comparison between the predicted shear deformations of cgPP non-variable mesh with ±45° using using (a) MSF = 0 (repeated from Figure 5.68a and to ease comparison), (b) MSF = 5 and (c) MSF = 10

Figure 5.71 shows a comparison between predicted results obtained by using different mass scaling factors. As can be seen clearly from Figure 5.71 including mass scaling has noticeable effect on shear deformation. As the mass scaling increased the discrepancy between the predicted and experimental results were also increased which indicates that mass scaling has a negative effect on shear deformation predictions. The S-NOCM simulations which used the UBE test result as an input required mass-scaling in order to run to completion, see Section 5.5. In contrast, those conducted using the CS-NOCM required no such mass scaling. This sensitivity study shows that the inclusion of mass scaling leads to an adverse influence on the predictions. However, given that this was the only way found to run the simulations using the UBE input curves, use of the mass scaling was considered justified. Nevertheless, the influence of mass scaling on the predictions should be born in mind when comparing the results in Section 5.5.

## 5.7 Conclusion

In this chapter, novel tooling for a kart wheel (die, punch and blank-holder) was designed and manufactured. FE forming simulations of the kart wheel using two materials, cgPP and wrGF, have been conducted. The performance of two different constitutive models for the

shear behaviour of the fabrics (S-NOCM and CS-NOCM) implemented in membrane elements have been evaluated in complex forming simulations. Blank initial orientations of 0/90° and ±45° have been considered. Inherent variability of fibre orientation in the initial blank has been modelled using the output of the Varifab code (see Chapter 3). The numerical results using the coupled model (CS-NOCM) show improved agreement with the experimental results in comparison with predictions of the original S-NOCM using the UBE shear force measurements. However, the experimental and numerical draw-in shape of the wheel with both orientations and for both constitutive models are not in good agreement even when variable meshes, which matched statistically the inherent variability of the virtual fabric samples, are used. This discrepancy is believed to be due to the use of a simple linear elastic model to represent the tensile stiffness of the tows, a method that fails to take into account the complex biaxial coupling behaviour of warps and wefts tows due to their crimp. In terms of time and effort, forming the actual cgPP wheels was much quicker and easier than forming the wrGF wheels. For example, the process of forming and extracting the cgPP wheel from the mould took about one hour, whereas the process of forming and extracting the wrGF wheel took about 2 days due to the tedious and time-consuming resin curing process and difficulty when extracting the part from the mould. Finally, the sensitivity of the CS-NOCM to different friction coefficients, shear compliances and blank holder force on the kart wheel forming simulations when using the cgPP data with a non-variable mesh was investigated. The results show that there is a slight variation between the numerical results and the experimental results when the blank-holder force is reduced and the friction coefficient is increased. On the other hand, a noticeable variation from the experimental result can be seen clearly when low BBE shear compliance was used, however the predicted result was very close to the experimental results when high BBE shear compliance was used, which is expected since the applied blank holder force is high and more likely to use a high shear compliance in the coupling model. Increasing mass scaling factor has negative effect on the simulation such as decreases the amount of draw-in shape and the shear deformation diverse from the experimental shear deformation.

# 6. Achievements, Conclusions and Future Developments

## 6.1 Achievements

Shear tests on three types of fabrics have been performed using three shear test methods, the PF, UBE and BBE tests. A coupling between in-plane tension and shear resistance has been characterised using the BBE test for three woven biaxial engineering fabrics (wrGF, srPP and cgPP). Two novel analysis techniques, namely the transmitted backlighting intensity technique and the analysis of tracer lines technique have been used in determining wrinkling onset and propagation during all three shear test methods.

Characterisation of the variability of the tow orientation in a pre-consolidated glass/PP textile composite (prccgPP) and three engineering fabrics (wrGF, srPP and cgPP) has been performed using a simple manual image processing method. The measured global statistics of the variability of the tow orientation have been used in reproducing representative variability with realistic spatial correlations in finite element meshes consisting of mutually constrained truss elements (representing the high tensile stiffness fibres) and membrane elements (representing the shear properties of the fabric) suitable for use in finite element forming simulations. This has been accomplished using a computer code, Varifab$^{GA}$, which is based on pin-jointed net kinematics. The code is able to reproduce variability in the full-field inter-tow angle based on the measured inherent variability using a simple genetic algorithm programming technique called 'Varifab$^{GA}$'. Finally, a semi-automated image processing technique has been developed, based on an edge detection method that can reduce the amount of labour involved in manual image analysis and can produce a more accurate characterisation.

Investigating the effect of misalignment (tow meander) on shear compliance has been carried out by incorporating realistic tow meander into shear test simulations of PF, UBE and BBE test using a method of assigning the initial fibre directions to each element in the finite element mesh. Further, a method of modelling the coupling between shear compliance and in-plane tension in woven engineering fabrics has been demonstrated. The

method is based on incorporating the observed shear tension coupling in the shear part of the original non-orthogonal constitutive model (S-NOCM). The enhanced model was named the coupled non-orthogonal constitutive model (CS-NOCM). The method is similar to that used previously to create rate-dependent 'viscous' behaviour using a hypo-elastic model [88] though here the average in-plane strain along the two tow directions, rather than the angular shear rate, is used to control the selection of the shear force versus shear angle curve for use in the non-orthogonal constitutive model NOCM (used to relate the shear force and shear stress) [50, 53]. Furthermore, a simple normalisation procedure has been proposed when validating the CS-NOCM against the experimental results by conducing BBE simulations with different transverse on wrGF and cgPP.

A novel 3D geometrically complex forming tool based on a kart wheel design has been manufactured for use in experimental and numerical forming tests. A segmented blank-holder, similar to that first introduced by Adams [213] and used by Lin, et al. [34] has also been re-manufactured to produce symmetric and asymmetric boundary conditions during forming. An internal mould heating and cooling system have been incorporated within the tooling, for quick forming and consolidation. Prior to that, steady state thermal FE simulations of the forming tools were performed to understand the thermal response of the tooling and to visualize the temperature field. The latter should be almost homogenous across the tooling surface during forming and consolidation experiments. Experimental forming of two different materials, wrGF and cgPP, were conducted. FE forming simulations of the same materials in four case studies were conducted in order to understand the influence of the measured shear-tension coupling and variability on forming predictions. The effects of different tensile stiffnesses in the warp and weft directions on the draw-in shape were also investigated for the cgPP for 0/90° and ±45° non-variable mesh predictions using the enhanced CS-NOCM. Finally, a sensitivity study of the blank-holder force, friction coefficient between tools and blank and different shear compliances is verified on the kart wheel-forming simulation of non-variable mesh with the enhanced CS-NOCM.

## 6.2 Conclusions

A strong dependence of shear compliance on in-plane tension has been demonstrated with the measured shear force increasing by a factor of about 30 to 40 times at a shear angle of 20° when comparing data measured using a small (5 N) compared to a high (100 N) transverse load. The transmitted backlighting intensity technique of characterising wrinkling propagation has been found to be less sensitive than the analysis of tracer lines in determining wrinkling onset. The latter technique has the added advantage of being useful for both translucent and opaque fabrics, though both methods can provide reasonable results The BBE test technique was found to be an effective method of measuring a woven fabric's shear-tension coupling and its wrinkling-onset shear angle as a function of in-plane tension.

Comparison of experimental and predicted tow directional variability generated by 'Varifab' shows excellent agreement with the statistical distribution of shear angles observed in actual engineering fabrics and textile composites. Furthermore, not only the same statistical distribution of the shear angles were reproduced but the spatial correlations of the shear angles observed in actual engineering fabrics and textile composites were also reproduced successfully. The inherent variability of cgPP fabric, when exposed to frequent handling, was characterised using a semi-automated and a manual image processing method. The semi-automated method was found to be extremely promising in terms of increasing accuracy and saving manual effort. However, the slow speed of the algorithm meant that long run times of several hours were required for the analysis.

Results of the effect of misalignment on shear compliances suggest that tow meander and sample misalignment are the main causes of variability observed in PF, UBE and BBE tests. Further, because the variability produces both decreases and increases in the measured force, it is apparent that sample misalignment is almost certainly not the cause of the increase in shear resistance observed in the three shear characterization experimental tests (Chapter 2). In other words, these simulations suggest the shear tension coupling observed in [175] is a real effect and not the result of sample misalignment or tow meander. A numerical method of modelling the shear-tension coupling in woven engineering fabrics, the so called enhanced CS-NOCM has been found to give reasonable results when modelling the BBE shear test, clearly showing a coupling between shear

compliance and in-plane strains in the fibre directions. When evaluating complex forming simulation predictions using a very complex forming tool, comparison between experimental and predicted local shear deformation using both a 0/90° and a ±45° non-variable mesh showed that the S-NOCM, with a UBE shear input curve, showed relatively poor agreement at most of the measured points. In contrast, a similar comparison between experimental and predicted local shear deformation when using 0/90° and ±45° variable and non-variable meshes together with the enhanced CS-NOCM showed much better agreement at most of the measured points. Further numerical investigations suggested that the input shear data is the key factor in this improvement of predictions. Simulations incorporating the entire set of BBE test data via the CS-NOCM produced much better predictions than those incorporating just the much lower UBE data via the S-NOCM. No obvious improvement in the comparison of experimental and numerical results was found when variable meshes were used, though the introduction of variability did allow the prediction of error bars on the simulation predictions. The latter were of comparable size to the experimentally measured error bars.

## 6.3 Future Developments

Improvements to the BBE test method could be achieved by consolidating Region C of the test specimen to prevent stretching and intra-ply slip during the tests; it would be interesting to see how this affects the results and how much extra effort would be required. A further interesting test for model evaluation purposes could be the gradual increase of the transverse load versus the shear angle.

The 'Varifab$^{GA}$' code may be further developed to include more fitness functions to reproduce ever more realistic tow orientations, though this would inevitably require powerful computational resources to run the code. Another option is to use a spectral expansion of several arbitrary wavelengths and amplitudes to determine the perturbation and stretch along the centre of the digital mesh, in order to explore further possible modes of in-plane deformation across the fabric.

The CS-NOCM could be improved further by refining the modelling and normalisation process in order to improve the accuracy of the predictions. The model could be then used

to evaluate the importance of shear-tension coupling on the predictions of complex forming simulations involving both high and low in-plane tensions. For example, it would be interesting to compare the behaviour of the model when draped over a hemisphere with no in-plane tension applied.

A disadvantage of using metal tooling is that the consolidation of the horizontal surfaces in the formed part is much better than that of the vertical and highly inclined surfaces within the tooling. To overcome this problem a hydrostatic pressure on all surfaces regardless to their position is needed. A silicon rubber or polyurethane punch could be used in place of metal one to achieve this goal.

# Appendix A

Table A.1. Experimental and predicted shear deformation of a deformed part using non-variable mesh of cgPP with 0/90° initial orientation

| Points | Experimental Shear Angle (º) | Error Bar | Predicted Shear Angle (º) |
|---|---|---|---|
| 1 | -36 | 9.6 | -13.4 |
| 2 | -29.2 | 5.7 | -9.1 |
| 3 | -12.1 | 3.3 | -18.5 |
| 4 | -6 | 0 | -3.9 |
| 5 | -0.8 | 1.6 | -0.4 |
| 6 | 13.7 | 4.6 | 0.1 |
| 7 | 8.6 | 4.7 | 12.6 |
| 8 | 18.7 | 3.1 | 26.2 |
| 9 | 14.5 | 3.0 | 4.4 |
| 10 | 21.6 | 4.5 | 3.2 |
| 11 | 29.7 | 7.4 | 26.0 |
| 12 | 30.5 | 6.6 | 27.0 |

Table A.2. Experimental and predicted shear deformation of a deformed part using a non-variable mesh of wrGF with 0/90° initial orientation

| Points | Experimental Shear Angle (º) | Error Bar | Predicted Shear Angle (º) |
|---|---|---|---|
| 1 | -42.9 | 7.6 | -8.4 |
| 2 | -13.0 | 3.5 | -5.4 |
| 3 | -11.0 | 4.2 | -7.2 |
| 4 | 1.7 | 1.5 | 5.0 |
| 5 | 13.2 | 4.8 | 0.3 |
| 6 | 18.6 | 3.7 | 3.2 |
| 7 | 17.2 | 10.4 | 30.7 |
| 8 | 36.4 | 5.6 | 20.7 |
| 9 | 17.5 | 4.5 | 2.0 |
| 10 | 24.1 | 5.6 | 7.0 |
| 11 | 49.7 | 4.1 | 41.5 |
| 12 | 23.1 | 5.4 | 25.7 |

Table A.3. The co-ordinates of the 12 points in each single quarter of the four quarters used to make the comparisons of wheel with 0/90°

| Points | URQ | | ULQ | | LRQ | | LLQ | |
|---|---|---|---|---|---|---|---|---|
| | X (mm) | Y (mm) | X (mm) | Y (mm) | X (mm) | Y (mm) | X (mm) | Y (mm) |
| 1 | 120.4 | 12.1 | -120.4 | 12.1 | 120.4 | -12.1 | -120.4 | -12.1 |
| 2 | 46.3 | 24.8 | -46.3 | 24.8 | 46.3 | -24.8 | -46.3 | -24.8 |
| 3 | 14.00 | 52.3 | -14.00 | 52.3 | 14.00 | -52.3 | -14.00 | -52.3 |
| 4 | 0.00 | 0.00 | 0.00 | 0.00 | 0.00 | -0.00 | -0.00 | -0.00 |
| 5 | 138.2 | 132.2 | -138.2 | 132.2 | 138.2 | -132.2 | -138.2 | -132.2 |
| 6 | 106.6 | 114.6 | -106.6 | 114.6 | 106.6 | -114.6 | -106.6 | -114.6 |
| 7 | 25.3 | 88.8 | -25.3 | 88.8 | 25.3 | -88.8 | -25.3 | -88.8 |
| 8 | 64.7 | 97.0 | -64.7 | 97.0 | 64.7 | -97.0 | -64.7 | -97.0 |
| 9 | 131.2 | 96.5 | -131.2 | 96.5 | 131.2 | -96.5 | -131.2 | -96.5 |
| 10 | 93.8 | 91.0 | -93.8 | 91.0 | 93.8 | -91.0 | -93.8 | -91.0 |
| 11 | 77.2 | 59.3 | -77.2 | 59.3 | 77.2 | -59.3 | -77.2 | -59.3 |
| 12 | 113.9 | 42.9 | -113.9 | 42.9 | 113.9 | -42.9 | -113.9 | -42.9 |

Table A.4. Experimental and predicted shear deformation of a deformed part using non-variable mesh of cgPP with ±45° initial orientation

| Points | Experimental Shear Angle (º) | Error Bar | Predicted Shear Angle (º) |
|---|---|---|---|
| 1 | -39.5 | 3.785939 | -17.56 |
| 2 | -14.875 | 9.077215 | -11.02 |
| 3 | -11.75 | 11.17661 | -10.92 |
| 4 | -16.875 | 4.289036 | -6.73 |
| 5 | 2.5 | 3.109126 | 24.06 |
| 6 | 13.875 | 4.40407 | 8.40 |
| 7 | 15 | 1.825742 | 1.94 |
| 8 | 23.375 | 3.68273 | 24.09 |
| 9 | 12.33333 | 7.234178 | 27.21 |
| 10 | 32.25 | 2.217356 | 22.22 |
| 11 | 15.875 | 7.920175 | -15.52 |
| 12 | 34.875 | 6.956711 | 20.87 |

Table A.5. Experimental and predicted shear deformation of a deformed part using a non-variable mesh of wrGF with ±45° initial orientation

| Points | Experimental Shear Angle (º) | Error Bar | Predicted Shear Angle (º) |
|---|---|---|---|
| 1 | -45.25 | 4.112988 | -28.29 |
| 2 | -21.125 | 6.433959 | -30.43 |
| 3 | -8.25 | 13.76893 | -32.71 |
| 4 | -6.00 | 0.816497 | -11.16 |
| 5 | 7.25 | 8.098354 | 10.73 |
| 6 | 1.00 | 7.071068 | 30.23 |
| 7 | 8.333333 | 4.725816 | 3.86 |
| 8 | 1.75 | 11.37614 | 29.00 |
| 9 | -4.83333 | -4.83333 | 18.81 |
| 10 | 38 | 4.396969 | 27.51 |
| 11 | -8 | 14.08013 | 1.67 |
| 12 | 40.125 | 6.860211 | 35.81 |

Table A.6. The co-ordinates of the 12 points in each single quarter of the four quarters used to make the comparisons of wheel with ±45°

| Points | URQ | | ULQ | | LRQ | | LLQ | |
|---|---|---|---|---|---|---|---|---|
| | X (mm) | Y (mm) | X (mm) | Y (mm) | X (mm) | Y (mm) | X (mm) | Y (mm) |
| 1 | 107.5 | 16.4 | -107.5 | 16.4 | 107.5 | -16.4 | -107.5 | -16.4 |
| 2 | 89.9 | 48.3 | -89.9 | 48.3 | 89.9 | -48.3 | -89.9 | -48.3 |
| 3 | 123.5 | 70.2 | -123.5 | 70.2 | 123.5 | -70.2 | -123.5 | -70.2 |
| 4 | 15.7 | 45.8 | -15.7 | 45.8 | 15.7 | -45.8 | -15.7 | -45.8 |
| 5 | 70.2 | 118.2 | -70.2 | 118.2 | 70.2 | -118.2 | -70.2 | -118.2 |
| 6 | 55.3 | 55.0 | -55.3 | 55.0 | 55.3 | -55.0 | -55.3 | -55.0 |
| 7 | 38.6 | 18.7 | -38.6 | 18.7 | 38.6 | -18.7 | -38.6 | -18.7 |
| 8 | 35.4 | 70.1 | -35.4 | 70.1 | 35.4 | -70.1 | -35.4 | -70.1 |
| 9 | 12.4 | 12.7 | -12.4 | 12.7 | 12.4 | -12.7 | -12.4 | -12.7 |
| 10 | 16.2 | 66.4 | -16.2 | 66.4 | 16.2 | -66.4 | -16.2 | -66.4 |
| 11 | 78.5 | 62.1 | -78.5 | 62.1 | 78.5 | -62.1 | -78.5 | -62.1 |
| 12 | 12.1 | 78.5 | -12.1 | 78.5 | 12.1 | -78.5 | -12.1 | -78.5 |

Table A.7. Predicted shear deformation of cgPP and wrGF deformed parts of non-variable meshes using the CS-NOCM with 0/90° initial orientation

| Points | Predicted Shear Angle (º) of cgPP | Predicted Shear Angle (º) of wrGF |
|---|---|---|
| 1 | -39.00 | -30.30 |
| 2 | -20.00 | -14.37 |
| 3 | -12.00 | -13.10 |
| 4 | -3.50 | 2.15 |
| 5 | -2.00 | -8.69 |
| 6 | 7.00 | 13.63 |
| 7 | 3.00 | 21.62 |
| 8 | 25.00 | 26.11 |
| 9 | 13.00 | 10.12 |
| 10 | 17.00 | 24.87 |
| 11 | 30.00 | 46.06 |
| 12 | 32.00 | 27.02 |

Table A.8. Predicted shear deformation of cgPP and wrGF deformed parts of non-variable meshes using the CS-NOCM with ±45° initial orientation

| Points | Predicted Shear Angle (º) of cgPP | Predicted Shear Angle (º) of wrGF |
|---|---|---|
| 1 | -38.00 | -38.28 |
| 2 | -20.00 | -19.40 |
| 3 | -18.00 | -16.85 |
| 4 | -17.00 | -5.23 |
| 5 | 0.00 | 19.05 |
| 6 | 11.00 | -2.55 |
| 7 | 15.50 | 10.27 |
| 8 | 20.50 | 16.20 |
| 9 | 19.00 | -8.33 |
| 10 | 25.00 | 36.74 |
| 11 | 28.00 | 8.16 |
| 12 | 34.00 | 42.75 |

Table A.9. Predicted shear deformation of cgPP deformed parts of variable meshes using the CS-NOCM with 0/90° initial orientation

| Points | URQ | ULQ | LRQ | LLQ | Average | Stdv |
|---|---|---|---|---|---|---|
| 1 | -44.70 | -21 | -20 | -25.08 | -27.7 | 11.5 |
| 2 | -16.29 | -17 | -15 | -15.15 | -15.9 | 1.0 |
| 3 | -12.09 | -13.5 | -15 | -14.37 | -13.7 | 1.3 |
| 4 | -2.04 | -1.2 | -1.5 | -1.71 | -1.6 | 0.4 |
| 5 | -1.54 | -2 | -1.2 | 1.33 | -0.9 | 1.5 |
| 6 | 3.02 | 2.5 | 3 | 0.61 | 2.3 | 1.1 |
| 7 | -2.93 | -3.5 | -2 | -1.97 | -2.6 | 0.7 |
| 8 | 26.72 | 27.5 | 25 | 27.45 | 26.7 | 1.2 |
| 9 | 17.07 | 18 | 17 | 15.16 | 16.8 | 1.2 |
| 10 | 17.13 | 15 | 16.5 | 23.90 | 18.1 | 3.9 |
| 11 | 29.40 | 33 | 28.5 | 26.19 | 29.3 | 2.8 |
| 12 | 31.15 | 28 | 20 | 31.21 | 27.6 | 5.3 |

Table A.10. Predicted shear deformation of wrGF deformed parts of variable meshes using the CS-NOCM with 0/90° initial orientation

| Points | URQ | ULQ | LRQ | LLQ | Average | Stdv |
|---|---|---|---|---|---|---|
| 1 | -29.4 | -25.3 | -32 | -40.63 | -31.8 | 6.5 |
| 2 | -9.0 | -9.5 | -8.5 | -9.97 | -9.2 | 0.6 |
| 3 | -5.2 | -8.5 | -10.1 | -9.1 | -8.2 | 2.1 |
| 4 | 2.4 | 1.5 | 2.1 | 1.66 | 1.9 | 0.4 |
| 5 | -2.5 | -2.8 | -3.2 | -2.17 | -2.7 | 0.4 |
| 6 | 21.4 | 14.6 | 10.5 | 16.19 | 15.7 | 4.5 |
| 7 | 21.5 | 18.2 | 20.2 | 6.83 | 16.7 | 6.7 |
| 8 | 28.1 | 25.7 | 28.4 | 35.76 | 29.5 | 4.4 |
| 9 | 20.8 | 15.4 | 10.6 | -13.41 | 8.3 | 15.1 |
| 10 | 31.0 | 25.8 | 25.5 | 32.05 | 28.6 | 3.4 |
| 11 | 46.3 | 42.7 | 48.5 | 49.22 | 46.7 | 2.9 |
| 12 | 26.6 | 22.1 | 23.5 | 14.97 | 21.8 | 4.9 |

Table A.11. Predicted shear deformation of cgPP deformed parts of variable meshes using the CS-NOCM with ±45° initial orientation

| Points | URQ | ULQ | LRQ | LLQ | Average | Stdv |
|---|---|---|---|---|---|---|
| 1 | -42.3 | -40 | -27 | -40.0 | -37.3 | 7.0 |
| 2 | -21.2 | -22 | -24 | -24.3 | -22.9 | 1.5 |
| 3 | -17.2 | -23 | -21 | -18.2 | -19.9 | 2.6 |
| 4 | -16.6 | -13 | -11.5 | -15.3 | -14.1 | 2.3 |
| 5 | 16.7 | 18 | 22 | 14.9 | 17.9 | 3.0 |
| 6 | 10.8 | 15 | 12 | 14.4 | 13.1 | 2.0 |
| 7 | 16.2 | 15 | 16.5 | 14.1 | 15.5 | 1.1 |
| 8 | 22.9 | 23 | 25.5 | 25.2 | 24.2 | 1.4 |
| 9 | 16.3 | 18 | 20 | 17.3 | 17.9 | 1.6 |
| 10 | 34.1 | 38 | 37.5 | 35.6 | 36.3 | 1.8 |
| 11 | 27.2 | 24 | 28 | 25.6 | 26.2 | 1.8 |
| 12 | 41.1 | 38 | 40 | 37.7 | 39.2 | 1.6 |

Table A.12. Predicted shear deformation of wrGF deformed parts of variable meshes using the CS-NOCM with ±45° initial orientation

| Points | URQ | ULQ | LRQ | LLQ | Average | Stdv |
|---|---|---|---|---|---|---|
| 1 | -41.54 | -23 | -32.5 | -41.40 | -34.6 | 8.8 |
| 2 | -19.44 | -23 | -20 | -23.91 | -21.6 | 2.2 |
| 3 | -18.30 | -22 | -21 | -17.19 | -19.6 | 2.3 |
| 4 | -10.00 | -8 | -6 | -5.23 | -7.3 | 2.1 |
| 5 | 19.03 | 22 | 21 | 19.20 | 20.3 | 1.4 |
| 6 | -2.55 | -5 | 7 | 7.15 | 1.7 | 6.3 |
| 7 | 10.85 | 5 | 9 | 3.50 | 7.1 | 3.4 |
| 8 | 17.11 | 20 | 22 | -1.03 | 14.5 | 10.6 |
| 9 | -8.46 | -6 | -7 | -3.55 | -6.3 | 2.1 |
| 10 | 36.62 | 43 | 42.5 | 33.13 | 38.8 | 4.8 |
| 11 | 7.45 | 10 | 15.5 | -20.74 | 3.1 | 16.2 |
| 12 | 43.56 | 45 | 40 | 42.09 | 42.7 | 2.1 |

# References


[1] (11/02/2013). *http://www.boeing.com/commercial/aeromagazine/articles/qtr_4_06/article_04_2.html*.

[2] (11/02/2013). *http://www.bis.gov.uk/assets/BISCore/corporate/docs/C/Composites-Strategy.pdf*.

[3] (11/02/2013). *http://www.renewableenergyfocus.com/view/22657/wind-turbine-blade-production-new-products-keep-pace-as-scale-increases/*.

[4] E. J. Barbero, *Introduction to composite materials design*: CRC, 2010.

[5] (19 Sep 2012). *http://www.csuchico.edu/~jpgreene/m247/m247_ch02/sld023.htm*.

[6] P. Morgan, *Carbon fibers and their composites* vol. 27: CRC, 2005.

[7] (19 Sep 2012). *http://www.shopmaninc.com/epoxy.html*

[8] (29 May 2012). *http://bateau2.com/howto/cure_times.php*

[9] S. Sandler, W. Karo, J. Bonesteel, and E. Pearce, "Polymer synthesis and characterization: a laboratory manual. 1998," ed: San Diego: Academic Press.

[10] F. C. Campbell Jr, *Manufacturing processes for advanced composites*: Elsevier Science, 2003.

[11] (20 Sep 2012). *http://scholar.lib.vt.edu/theses/available/etd-42198-113329/unrestricted/ch1.pdf*

[12] D. Mann, *Automotive Plastics & Composites-Worldwide Markets & Trends to 2007*: Elsevier Science & Technology, 1999.

[13] C. Maier and T. Calafut, *Polypropylene: the definitive user's guide and databook*: William Andrew, 1998.

[14] TORAYCA®. (2010, 22 Sep 2012). *EXPLANATION OF PRODUCT CODE*. Available: http://www.toraycfa.com/pdfs/ExplanationofProductCode.pdf

[15] K. Friedrich, S. Fakirov, and Z. Zhang, *Polymer composites: from nano-to macro-scale*: Springer, 2005.

[16] X. Li, Y. Shimizu, A. Pyatenko, H. Wang, and N. Koshizaki, "Tetragonal zirconia spheres fabricated by carbon-assisted selective laser heating in a liquid medium," *Nanotechnology*, vol. 23, p. 115602, 2012.

[17] (29 May 2012). *www.bolton.ac.uk/codate/spguidetocomposites.pdf*.

[18] (29 May 2012). *http://www.advancedcomposites.co.uk/data_catalogue/catalogue%20files/sm/SM1010-INTRO%20TO%20ADV%20COMPS-Rev06.pdf*.

[19] P. Boisse, *Composite reinforcements for optimum performance*: Woodhead Publishing, 2011.

[20] T.-W. Chou, *Microstructural design of fiber composites*: Cambridge University Press, 2005.

[21] J. Wang, "Predictive modelling and experimental measurement of composite forming behaviour," University of Nottingham, 2008.

[22] J. R. Thagard, "Investigation and development of the resin infusion between double flexible tooling (RIDFT) process for composite fabrication," 2003.

[23] A. Willems, "Forming simulation of textile reinforced composite shell structures," PhD, Faculteit Ingenieurswetenshapen Arenbergkasteel, Katholieke Universiteit Leuven, Leuven Leuven, 2008.

[24] J. Thagard, O. Okoli, Z. Liang, H.-P. Wang, and C. Zhang, "Resin infusion between double flexible tooling: prototype development," *Composites Part A: Applied Science and Manufacturing*, vol. 34, pp. 803-811, 2003.

[25] (18 March 2013). *http://www.composites.ugent.be/home_made_composites/documentation/FibreGlast_Vacuum_infusion_process.pdf*.

[26] A. C. Long, *Composites Forming Technologies*. University of Nottingham, UK: Woodhead Publishing Series in Textiles No. 61, 2007.
[27] A. Ragondet, "Experimental Characterization of the Vacuum Infusion Process," PhD thesis, University of Nottingham, 2005.
[28] R. Garcia-Gil, "Forming and consolidation of textile composites," University of Nottingham, 2003.
[29] S. Das, *The cost of automotive polymer composites: a review and assessment of DOE's lightweight materials composites research*: Oak Ridge National Laboratory Oak Ridge, TN, 2001.
[30] D. Trudel-Boucher, B. Fisa, J. Denault, and P. Gagnon, "Experimental investigation of stamp forming of unconsolidated commingled E-glass/polypropylene fabrics," *Composites Science and Technology*, vol. 66, pp. 555-570, 2006.
[31] C. D. Rudd, A. C. Long, K. N. Kendall, and C. Mangin, *Liquid moulding technologies: Resin transfer moulding, structural reaction injection moulding and related processing techniques*: Woodhead Publishing, 1997.
[32] P. Boisse, N. Hamila, E. Vidal-Sallé, and F. Dumont, "Simulation of wrinkling during textile composite reinforcement forming. Influence of tensile, in-plane shear and bending stiffnesses," *Composites Science and Technology*, vol. 71, pp. 683-692, 2011.
[33] H. Lin, P. Evans, P. Harrison, J. Wang, A. Long, and M. Clifford, "An experimental investigation into the factors affecting the forming performance of thermoset prepreg," in *9 th International ESAFORM Conference on Materials Forming*, 2006.
[34] H. Lin, J. Wang, A. Long, M. Clifford, and P. Harrison, "Predictive modelling for optimization of textile composite forming," *Composites Science and Technology*, vol. 67, pp. 3242-3252, 2007.
[35] A. Cherouat and J. L. Billoët, "Mechanical and numerical modelling of composite manufacturing processes deep-drawing and laying-up of thin pre-impregnated woven fabrics," *Journal of materials processing technology*, vol. 118, pp. 460-471, 2001.
[36] Q. Fu, W. Zhu, Z. Zhang, and H. Gong, "Effect of variable blank holder force on rectangular box drawing process of hot-galvanized sheet steel," *Cailiao Kexue Yu Jishu(Journal of Materials Science & Technology)*, vol. 21, pp. 909-913, 2005.
[37] M. Hou, "Stamp forming of continuous glass fibre reinforced polypropylene," *Composites Part A: Applied Science and Manufacturing*, vol. 28, pp. 695-702, 1997.
[38] P. Harrison, J. Wiggers, A. Long, and C. Rudd, "A constitutive model based on meso and micro kinematics for woven and stitched dry fabrics," 2003.
[39] A. Prodromou and J. Chen, "On the relationship between shear angle and wrinkling of textile composite preforms," *Composites Part A: Applied Science and Manufacturing*, vol. 28, pp. 491-503, 1997.
[40] O. Rozant, P. E. Bourban, and J. A. E. Månson, "Drapability of dry textile fabrics for stampable thermoplastic preforms," *Composites Part A: Applied Science and Manufacturing*, vol. 31, pp. 1167-1177, 2000.
[41] J. Cao, R. Akkerman, P. Boisse, J. Chen, H. Cheng, E. De Graaf, J. Gorczyca, P. Harrison, G. Hivet, and J. Launay, "Characterization of mechanical behavior of woven fabrics: Experimental methods and benchmark results," *Composites Part A: Applied Science and Manufacturing*, vol. 39, pp. 1037-1053, 2008.
[42] P. Harrison, M. Clifford, and A. Long, "Shear characterisation of woven textile composites," in *10th European Conference on Composite Materials*, 2002, pp. 3-7.
[43] G. Hivet and A. V. Duong, "A contribution to the analysis of the intrinsic shear behavior of fabrics," *Journal of Composite Materials*, vol. 45, pp. 695-716, 2011.
[44] J. Launay, G. Hivet, A. V. Duong, and P. Boisse, "Experimental analysis of the influence of tensions on in plane shear behaviour of woven composite reinforcements," *Composites Science and Technology*, vol. 68, pp. 506-515, 2008.
[45] J. Launay, G. Hivet, A. Vu Duong, and P. Boisse, "Experimental analysis of in plane shear behaviour of woven composite reinforcements. Influence of tensions," in *10th ESAFORM Conference on Material Forming*, 2007, pp. 1033-1038.
[46] S. Sharma, M. Sutcliffe, and S. Chang, "Characterisation of material properties for draping of dry woven composite material," *Composites Part A: Applied Science and Manufacturing*, vol. 34, pp. 1167-1175, 2003.

[47] C. Galliot and R. Luchsinger, "The shear ramp: A new test method for the investigation of coated fabric shear behaviour–Part I: Theory," *Composites Part A: Applied Science and Manufacturing*, vol. 41, pp. 1743-1749, 2010.
[48] C. Galliot and R. Luchsinger, "The shear ramp: A new test method for the investigation of coated fabric shear behaviour–Part II: Experimental validation," *Composites Part A: Applied Science and Manufacturing*, vol. 41, pp. 1750-1759, 2010.
[49] W. Lee and J. Cao, "Numerical simulations on double-dome forming of woven composites using the coupled non-orthogonal constitutive model," *International Journal of Material Forming*, vol. 2, pp. 145-148, 2009/08/01 2009.
[50] W. Lee, J. Cao, P. Badel, and P. Boisse, "Non-orthogonal constitutive model for woven composites incorporating tensile effect on shear behavior," *International Journal of Material Forming*, vol. 1, pp. 891-894, 2008.
[51] X. Q. Peng and J. Cao, "A continuum mechanics-based non-orthogonal constitutive model for woven composite fabrics," *Composites Part A: Applied Science and Manufacturing*, vol. 36, pp. 859-874, 2005.
[52] P. Xue, X. Peng, and J. Cao, "A non-orthogonal constitutive model for characterizing woven composites," *Composites Part A: Applied Science and Manufacturing*, vol. 34, pp. 183-193, 2003.
[53] W. Lee, M. K. Um, J. H. Byun, P. Boisse, and J. Cao, "Numerical study on thermo-stamping of woven fabric composites based on double-dome stretch forming," *International Journal of Material Forming*, vol. 3, pp. 1217-1227, 2010.
[54] A. Willems, S. V. Lomov, I. Verpoest, and D. Vandepitte, "Picture frame shear tests on woven textile composite reinforcements with controlled pretension," in *AIP Conference Proceedings*, 2007, p. 999.
[55] P. Harrison and P. Potluri, "Shear tension coupling in biaxial bias extension tests," in *17th International Conference on Composite Materials, 27th-31st July, Edinburgh, Scotland*, 2009.
[56] P. Harrison, P. Potluri, K. Bandara, and A. Long, "A normalisation procedure for biaxial bias extension tests," *International Journal of Material Forming*, vol. 1, pp. 863-866, 2008.
[57] P. Potluri, D. A. P. Ciurezu, and R. J. Young, "Biaxial Shear Testing of Textile Preforms for Formability Analysis," in *16th International Conference on Composite Materials*, 2007.
[58] J. Wang, J. Page, and R. Paton, "Experimental investigation of the draping properties of reinforcement fabrics," *Composites Science and Technology*, vol. 58, pp. 229-237, 1998.
[59] W. R. Yu, M. Zampaloni, F. Pourboghrat, K. Chung, and T. J. Kang, "Analysis of flexible bending behavior of woven preform using non-orthogonal constitutive equation," *Composites Part A: Applied Science and Manufacturing*, vol. 36, pp. 839-850, 2005.
[60] R. WS., "ImageJ, U. S. National Institutes of Health," ed. U. S. National Institutes of Health, Bethesda, Maryland, USA: Rasband WS. , 1997-2005.
[61] P. Xue, J. Cao, and J. Chen, "Integrated micro/macro-mechanical model of woven fabric composites under large deformation," *Composite structures*, vol. 70, pp. 69-80, 2005.
[62] B. Zhu, T. Yu, and X. Tao, "Large deformation and slippage mechanism of plain woven composite in bias extension," *Composites Part A: Applied Science and Manufacturing*, vol. 38, pp. 1821-1828, 2007.
[63] P. Harrison, M. Tan, and A. Long, "Kinematics of Intra-ply slip in textile composites during bias extension tests," in *8th International ESAFORM Conference on Materials Forming, 27th-29th April, Cluj-Napoca, Romania*, 2005, pp. 987-990.
[64] G. Lebrun, M. N. Bureau, and J. Denault, "Evaluation of bias-extension and picture-frame test methods for the measurement of intraply shear properties of PP/glass commingled fabrics," *Composite structures*, vol. 61, pp. 341-352, 2003.
[65] C. M. Harrison P, *In Design and manufacture of textile composites, Chapter 4, Rheological behaviour of pre-impregnated textiles.* Cambridge, UK: Woodhead Publishing Ltd, 2005.
[66] X. Peng and Z. U. Rehman, "Textile composite double dome stamping simulation using a non-orthogonal constitutive model," *Composites Science and Technology*, vol. 71, pp. 1075-1081, 2011.
[67] P. Harrison, J. Wiggers, and A. C. Long, "Normalization of shear test data for rate-independent compressible fabrics," *Journal of Composite Materials*, vol. 42, pp. 2315-2344, 2008.

[68] I. Koyama, "Development of a mesh generator including directional variability," IAESTE Summer Trainee, Department of Mechanical Engineering (from Dept of Mech Sci & Eng, Nagoya Uni, Japan) University of Glasgow, Glasgow, Uk, 2006.
[69] A. Beaumont, "Development of a mesh generator for finite element simulations," BEng, Department of Mechanical Engineering University of Glasgow, Glasgow, UK, 2006.
[70] A. Endruweit and A. C. Long, "Influence of stochastic variations in the fibre spacing on the permeability of bi-directional textile fabrics," *Composites Part A: Applied Science and Manufacturing,* vol. 37, pp. 679-694, 2006.
[71] A. Endruweit, A. C. Long, F. Robitaille, and C. D. Rudd, "Influence of stochastic fibre angle variations on the permeability of bi-directional textile fabrics," *Composites Part A: Applied Science and Manufacturing,* vol. 37, pp. 122-132, 2006.
[72] C. Wong, A. Long, M. Sherburn, F. Robitaille, P. Harrison, and C. Rudd, "Comparisons of novel and efficient approaches for permeability prediction based on the fabric architecture," *Composites Part A: Applied Science and Manufacturing,* vol. 37, pp. 847-857, 2006.
[73] B. Markicevic, D. Heider, S. Advani, and S. Walsh, "Stochastic modeling of preform heterogeneity to address dry spots formation in the VARTM Process," *Composites Part A: Applied Science and Manufacturing,* vol. 36, pp. 851-858, 2005.
[74] A. C. Long, J. Wiggers, and P. Harrison, "Modelling the Effects of Blank-Holder Pressure and Material Variability on Forming of Textile Preforms," ed, 2004.
[75] A. A. Skordos and M. P. F. Sutcliffe, "Stochastic simulation of woven composites forming," *Composites Science and Technology,* vol. 68, pp. 283-296, 2008.
[76] W. Yu, P. Harrison, and A. Long, "Finite element forming simulation of NCF considering natural fibre variability," 2005.
[77] F. Desplentere, S. V. Lomov, D. Woerdeman, I. Verpoest, M. Wevers, and A. Bogdanovich, "Micro-CT characterization of variability in 3D textile architecture," *Composites Science and Technology,* vol. 65, pp. 1920-1930, 2005.
[78] K. Woo and J. D. Whitcomb, "Effects of fiber tow misalignment on the engineering properties of plain weave textile composites," *Composite structures,* vol. 37, pp. 343-355, 1997.
[79] D. Liu, N. Fleck, and M. Sutcliffe, "Compressive strength of fibre composites with random fibre waviness," *Journal of the Mechanics and Physics of Solids,* vol. 52, pp. 1481-1505, 2004.
[80] S. K. Ha, S. W. Tsai, S. J. Kim, K. Hayat, and K. K. Jin, "Life Prediction of Composite Pressure Vessels Using Multi-Scale Approach," 2010.
[81] S. Hind and F. Robitaille, "Measurement, modeling, and variability of thermal conductivity for structural polymer composites," *Polymer Composites,* vol. 31, pp. 847-857, 2009.
[82] A. Endruweit, Long, A., Robitaille, F., and Rudd, C., "Dependence of permeability variations on the textile structure," presented at the Proc. 11th ECCM, Euro. Conf. Comp. Mat, Rhodes, Greece, 2004.
[83] M. Ralló, J. Escofet, and M. S. Millán, "Weave-repeat identification by structural analysis of fabric images," *Applied optics,* vol. 42, pp. 3361-3372, 2003.
[84] A. Clarke, G. Archenhold, N. Davidson, W. Slaughter, and N. Fleck, "Determining the power spectral density of the waviness of unidirectional glass fibres in polymer composites," *Applied Composite Materials,* vol. 2, pp. 233-243, 1995.
[85] C. Creighton, M. Sutcliffe, and T. Clyne, "A multiple field image analysis procedure for characterisation of fibre alignment in composites," *Composites Part A: Applied Science and Manufacturing,* vol. 32, pp. 221-229, 2001.
[86] J. Gan, S. Bickerton, and M. Battley, "Quantifying Variability within Glass Fiber Reinforcements using an Automated Optical Method," *Composites Part A: Applied Science and Manufacturing,* 2012.
[87] H. Bale, M. Blacklock, M. R. Begley, D. B. Marshall, B. N. Cox, and R. O. Ritchie, "Characterizing Three-Dimensional Textile Ceramic Composites Using Synchrotron X-Ray Micro-Computed-Tomography," *Journal of the American Ceramic Society,* vol. 95, pp. 392-402, 2011.
[88] P. Harrison, W. R. Yu, and A. C. Long, "Rate dependent modelling of the forming behaviour of viscous textile composites," *Composites Part A: Applied Science and Manufacturing,* vol. 42, pp. 1719-1726, 2011.

[89] D. Jauffrès, J. A. Sherwood, C. D. Morris, and J. Chen, "Discrete mesoscopic modeling for the simulation of woven-fabric reinforcement forming," *International journal of material forming*, vol. 3, pp. 1205-1216, 2010.
[90] R. L. Haupt and S. E. Haupt, *Practical genetic algorithms*: Wiley-Interscience, 2004.
[91] (9-04-2011). *http://www.obitko.com/tutorials/genetic-algorithms/ga-basic-description.php*.
[92] D. E. Goldberg, "Genetic algorithms in search, optimization, and machine learning," 1989.
[93] S. L. Jackson, *Research methods and statistics: A critical thinking approach*: Wadsworth Publishing Company, 2011.
[94] L. Ott and M. Longnecker, *An introduction to statistical methods and data analysis*: Duxbury press, 2010.
[95] R. Poli, "Recursive Conditional Schema Theorem, Convergence and Population Sizing in Genetic Algorithms," in *Foundations of Genetic Algorithms 6*, N. M. Worthy and M. S. William, Eds., ed San Francisco: Morgan Kaufmann, 2001, pp. 143-163.
[96] J. M. Utts and R. F. Heckard, *Statistical ideas and methods*: Duxbury Press, 2005.
[97] M. P. M. P. software), "MS Paint (Microsoft Paint software)," Windows xp ed, 2003.
[98] R. Schmitt, A. Orth, and C. Niggemann, "A method for edge detection of textile preforms using a light-section sensor for the automated manufacturing of fibre-reinforced plastics."
[99] R. Schmitt, T. Pfeifer, C. Mersmann, and A. Orth, "A method for the automated positioning and alignment of fibre-reinforced plastic structures based on machine vision," *CIRP Annals-Manufacturing Technology*, vol. 57, pp. 501-504, 2008.
[100] K. Searles, J. McCarthy, and M. Kumosa, "An image analysis technique for evaluating internal damage in graphite-fabric/polyimide composites," *Composites Science and Technology*, vol. 58, pp. 1607-1619, 1998.
[101] T. Acharya and A. K. Ray, *Image processing: principles and applications*: Wiley-Interscience, 2005.
[102] J. Canny, "A computational approach to edge detection," *Pattern Analysis and Machine Intelligence, IEEE Transactions on*, pp. 679-698, 1986.
[103] R. Kaur, M. Verma, and H. K. Kalpna, "Classification of various edge detectors," *Department of Computer Science, RIEIT*.
[104] J. S. Lim, "Two-dimensional signal and image processing," *Englewood Cliffs, NJ, Prentice Hall, 1990, 710 p.*, vol. 1, 1990.
[105] J. R. Parker, *Algorithms for image processing and computer vision*: Wiley Publishing, 2010.
[106] R. Gonzales and R. Woods, "Digital Image Processing. 2002," *New Jersey: Prentice Hall*, vol. 6, p. 681.
[107] A. C. Bovik, *The essential guide to Image Processing*: Academic Press, 2009.
[108] W. R. Yu, F. Pourboghrat, K. Chung, M. Zampaloni, and T. J. Kang, "Non-orthogonal constitutive equation for woven fabric reinforced thermoplastic composites," *Composites Part A: Applied Science and Manufacturing*, vol. 33, pp. 1095-1105, 2002.
[109] W. R. Yu, M. Zampaloni, F. Pourboghrat, K. Chung, and T. J. Kang, "Sheet hydroforming of woven FRT composites: non-orthogonal constitutive equation considering shear stiffness and undulation of woven structure," *Composite structures*, vol. 61, pp. 353-362, 2003.
[110] W.-R. Yu, P. Harrison, and A. Long, "Finite element forming simulation for non-crimp fabrics using a non-orthogonal constitutive equation," *Composites Part A: Applied Science and Manufacturing*, vol. 36, pp. 1079-1093, 2005.
[111] P. Boisse, A. Gasser, B. Hagege, and J. L. Billoet, "Analysis of the mechanical behavior of woven fibrous material using virtual tests at the unit cell level," *Journal of materials science*, vol. 40, pp. 5955-5962, 2005.
[112] D. Laroche, T. Vu-Khanh, I. Industrial Materials, and i. Institut des matériaux, *Modelling of the forming of complex parts from fabric composites*. Boucherville, Québec: Industrial Materials Institute, National Research Council of Canada, 1991.
[113] K. Vanclooster, S. V. Lomov, and I. Verpoest, "Experimental validation of forming simulations of fabric reinforced polymers using an unsymmetrical mould configuration," *Composites Part A: Applied Science and Manufacturing*, vol. 40, pp. 530-539, 2009.
[114] P. Boisse, Y. Aimène, A. Dogui, S. Dridi, S. Gatouillat, N. Hamila, M. Aurangzeb Khan, T. Mabrouki, F. Morestin, and E. Vidal-Sallé, "Hypoelastic, hyperelastic, discrete and

semi-discrete approaches for textile composite reinforcement forming," *International journal of material forming*, vol. 3, pp. 1229-1240, 2010.
[115] P. Boisse, N. Hamila, F. Helenon, Y. Aimene, and T. Mabrouki, "Draping of textile composite reinforcements: continuous and discrete approaches," *Advanced Composites Letters*, vol. 16, pp. 125-131, 2007.
[116] P. Boisse, N. Hamila, F. Helenon, B. Hagege, and J. Cao, "Different approaches for woven composite reinforcement forming simulation," *International journal of material forming*, vol. 1, pp. 21-29, 2008.
[117] I. Verpoest and S. V. Lomov, "Virtual textile composites software WiseTex: Integration with micro-mechanical, permeability and structural analysis," *Composites Science and Technology*, vol. 65, pp. 2563-2574, 2005.
[118] M. Sherburn, "TexGen v2," v2 ed, 2007.
[119] M. Sherburn, "TexGen v3," v3 ed, 2007.
[120] G. Hivet, J. Launay, A. Gasser, J. L. Daniel, and P. Boisse, "Mechanical behavior of woven composite reinforcements while forming," *Journal of Thermoplastic Composite Materials*, vol. 15, pp. 545-555, 2002.
[121] M. Komeili and A. Milani, "The effect of meso-level uncertainties on the mechanical response of woven fabric composites under axial loading," *Computers & Structures*, 2011.
[122] P. Boisse, N. Hamila, P. Wang, S. Gatouillat, S. Bel, and A. Charmetant, "COMPOSITE REINFORCEMENT FORMING SIMULATION: CONTINUOUS AND MESOSCOPIC APPROACHES."
[123] H. Lin, M. J. Clifford, A. C. Long, and M. Sherburn, "Finite element modelling of fabric shear," *Modelling and Simulation in Materials Science and Engineering*, vol. 17, p. 015008, 2008.
[124] G. Creech and A. Pickett, "Meso-modelling of Non-Crimp Fabric composites for coupled drape and failure analysis," *Journal of materials science*, vol. 41, pp. 6725-6736, 2006.
[125] R. Tavana, S. S. Najar, M. T. Abadi, and M. Sedighi, "Meso/macro-scale finite element model for forming process of woven fabric reinforcements," *Journal of Composite Materials*, July 20, 2012 2012.
[126] D. Ballhause, M. König, and B. Kröplin, "Modelling fabric-reinforced membranes with the Discrete Element Method," *Textile Composites and Inflatable Structures II*, pp. 51-67, 2008.
[127] M. Duhovic and D. Bhattacharyya, "Simulating the deformation mechanisms of knitted fabric composites," *Composites Part A: Applied Science and Manufacturing*, vol. 37, pp. 1897-1915, 2006.
[128] D. Durville, "Numerical simulation of entangled materials mechanical properties," *Journal of materials science*, vol. 40, pp. 5941-5948, 2005.
[129] D. Durville, "Finite element simulation of textile materials at the fiber scale," *arXiv preprint arXiv:0912.1268*, 2009.
[130] D. Durville, "Simulation of the mechanical behaviour of woven fabrics at the scale of fibers," *International journal of material forming*, vol. 3, pp. 1241-1251, 2010.
[131] D. Durville, "Finite Element Modelling of Textile and Fibrous Materials at Microscopic Scale," presented at the ESMC-2012: 8th European Solid Mechanics International Conference, Austria, Graz, 2012.
[132] A. Pickett, "Review of finite element simulation methods applied to manufacturing and failure prediction in composites structures," *Applied Composite Materials*, vol. 9, pp. 43-58, 2002.
[133] T. Vu, Durville, D. and Davies, P, "Simulation of the Bend-Over-Sheave Behaviour of Braided Synthetic Ropes," presented at the ESMC-2012: 8th European Solid Mechanics International Conference, Austria, Graz, 2012.
[134] P. Harrison, M. Clifford, A. Long, and C. Rudd, "A constituent-based predictive approach to modelling the rheology of viscous textile composites," *Composites Part A: Applied Science and Manufacturing*, vol. 35, pp. 915-931, 2004.
[135] G. McGuinness and C. ÓBrádaigh, "Development of rheological models for forming flows and picture-frame shear testing of fabric reinforced thermoplastic sheets," *Journal of non-newtonian fluid mechanics*, vol. 73, pp. 1-28, 1997.
[136] A. Spencer, "Theory of fabric-reinforced viscous fluids," *Composites Part A: Applied Science and Manufacturing*, vol. 31, pp. 1311-1321, 2000.

[137] S. Bickerton, M. J. Buntain, and A. A. Somashekar, "The viscoelastic compression behavior of liquid composite molding preforms," *Composites Part A: Applied Science and Manufacturing*, vol. 34, pp. 431-444, 2003.
[138] P. A. Kelly, R. Umer, and S. Bickerton, "Viscoelastic response of dry and wet fibrous materials during infusion processes," *Composites Part A: Applied Science and Manufacturing*, vol. 37, pp. 868-873, 2006.
[139] Y. Luo and I. Verpoest, "Compressibility and relaxation of a new sandwich textile preform for liquid composite molding," *Polymer Composites*, vol. 20, pp. 179-191, 1999.
[140] F. Robitaille and R. Gauvin, "Compaction of textile reinforcements for composites manufacturing. III: Reorganization of the fiber network," *Polymer Composites*, vol. 20, pp. 48-61, 1999.
[141] P. Simacek and V. M. Karbhari, "Notes on the Modeling of Preform Compaction: I - Micromechanics at the Fiber Bundle Level," *Journal of Reinforced Plastics and Composites*, vol. 15, pp. 86-122, January 1, 1996 1996.
[142] G. E. Mase, *Schaum's outline of theory and problems of continuum mechanics / by George E. Mase.* : New York : McGraw-Hill, c1970, 1970.
[143] Y. Aimene, E. Vidal-Salle, B. Hagège, F. Sidoroff, and P. Boisse, "A hyperelastic approach for composite reinforcement large deformation analysis," *Journal of Composite materials*, vol. 44, pp. 5-26, 2010.
[144] G. A. Holzapfel, "Nonlinear solid mechanics: a continuum approach for engineering," 2000.
[145] X. Peng, Z. Guo, and P. Harrison, "A simple anisotropic fiber reinforced hyperelastic constitutive model for woven composite fabrics," *International journal of material forming*, vol. 3, pp. 723-726, 2010.
[146] E. Vidal-Salle, Y. Aimene, and P. Boisse, "Use of a hyperelastic constitutive law for dry woven forming simulations," *AIP Conference Proceedings*, vol. 1353, pp. 883-888, 2011.
[147] X. Peng and J. Cao, "A continuum mechanics-based non-orthogonal constitutive model for woven composite fabrics," *Composites Part A: Applied Science and Manufacturing*, vol. 36, pp. 859-874, 2005.
[148] P. Harrison, A. Long, W. Yu, and M. Clifford, "Investigating the Performance of Two Different Constitutive Models for Viscous Textile Composites," in *8th international conference on textile composites (TEXCOMP), 16th–18th October, Nottingham, UK*, 2006.
[149] A. Cherouat and J. Billoët, "Finite element model for the simulation of preimpregnated woven fabric by deep-drawing and laying-up processes," *Journal of advanced materials*, vol. 32, pp. 42-53, 2000.
[150] K. A. Fetfatsidis, D. Soteropoulos, A. Petrov, C. J. Mitchell, and J. A. Sherwood, "Using Abaqus/Explicit to Link the Manufacturing Process to the Final Part Quality for Continuous Fiber-Reinforced Composite Fabrics."
[151] S. Sharma and M. Sutcliffe, "A simplified finite element model for draping of woven material," *Composites Part A: Applied Science and Manufacturing*, vol. 35, pp. 637-643, 2004.
[152] M. Duhovic, P. Mitschang, and D. Bhattacharyya, "Modelling approach for the prediction of stitch influence during woven fabric draping," *Composites Part A: Applied Science and Manufacturing*, vol. 42, pp. 968-978, 2011.
[153] H. Lin, A. Long, M. Clifford, J. Wang, and P. Harrison, "Predictive FE modelling of prepreg forming to determine optimum processing conditions," in *AIP Conference Proceedings*, 2007, p. 1092.
[154] B. Hagège, P. Boisse, and J. L. Billoët, "Finite element analyses of knitted composite reinforcement at large strain," *Revue Européenne des Eléments*, vol. 14, pp. 767-776, 2005.
[155] M. Khan, T. Mabrouki, and P. Boisse, "Numerical and experimental forming analysis of woven composites with double dome benchmark," *International journal of material forming*, vol. 2, pp. 201-204, 2009.
[156] P. Harrison, W.-R. Yu, and A. C. Long, "Rate dependent modelling of the forming behaviour of viscous textile composites," *Composites Part A: Applied Science and Manufacturing*, vol. 42, pp. 1719-1726, 2011.
[157] K. J. Bathe, *Finite Element Procedures*: Cambridge, MA: Klaus-Jürgen Bathe, 2007. (Formerly published by Prentice Hall, 1996.).

[158] D. Chapelle, and K. J. Bathe, *The Finite Element Analysis of Shells*. New York: NY: Springer, 2011.
[159] Abaqus, "Abaqus Analysis User's Manual, 26.1.5 Connection-type library," ed.
[160] D. Jung, "Study of dynamic explicit analysis in sheet metal forming processes using faster punch velocity and mass scaling scheme," *Journal of materials engineering and performance*, vol. 7, pp. 479-490, 1998.
[161] A. Prior, "Applications of implicit and explicit finite element techniques to metal forming," *Journal of materials processing technology*, vol. 45, pp. 649-656, 1994.
[162] Z. J. Zhang and G. H. Paulino, "Wave propagation and dynamic analysis of smoothly graded heterogeneous continua using graded finite elements," *International journal of solids and structures*, vol. 44, pp. 3601-3626, 2007.
[163] F. Abdiwi, P. Harrison, I. Koyama, W. Yu, A. Long, N. Corriea, and Z. Guo, "Characterising and modelling variability of tow orientation in engineering fabrics and textile composites," *Composites Science and Technology*, 2012.
[164] D. Lussier and J. Chen, "Material characterization of woven fabrics for thermoforming of composites," *Journal of Thermoplastic Composite Materials*, vol. 15, pp. 497-509, 2002.
[165] A. Milani, J. Nemes, G. Lebrun, and M. Bureau, "A comparative analysis of a modified picture frame test for characterization of woven fabrics," *Polymer Composites*, vol. 31, pp. 561-568, 2009.
[166] M. Komeili and A. S. Milani, "Shear response of woven fabric composites under meso-level uncertainties," *Journal of Composite Materials*, 2012.
[167] M. Whyte, "Design and manufacture of a picture frame testing rig," BEng, Deptartment of Mechnical Engineering, University of Glasgow, Glasgow, UK, 2006.
[168] P. Badel, S. Gauthier, E. Vidal-Sallé, and P. Boisse, "Rate constitutive equations for computational analyses of textile composite reinforcement mechanical behaviour during forming," *Composites Part A: Applied Science and Manufacturing*, vol. 40, pp. 997-1007, 2009.
[169] P. Badel, E. Vidal-Sallé, and P. Boisse, "Computational determination of in-plane shear mechanical behaviour of textile composite reinforcements," *Computational Materials Science*, vol. 40, pp. 439-448, 2007.
[170] M. A. Khan, T. Mabrouki, E. Vidal-Salle, and P. Boisse, "Numerical and experimental analyses of woven composite reinforcement forming using a hypoelastic behaviour. Application to the double dome benchmark," *Journal of materials processing technology*, vol. 210, pp. 378-388, 2010.
[171] X. Peng and J. Cao, "A dual homogenization and finite element approach for material characterization of textile composites," *Composites Part B: Engineering*, vol. 33, pp. 45-56, 2002.
[172] P. Boisse, M. Borr, K. Buet, and A. Cherouat, "Finite element simulations of textile composite forming including the biaxial fabric behaviour," *Composites Part B: Engineering*, vol. 28, pp. 453-464, 1997.
[173] P. Boisse, B. Zouari, and A. Gasser, "A mesoscopic approach for the simulation of woven fibre composite forming," *Composites Science and Technology*, vol. 65, pp. 429-436, 2005.
[174] P. Harrison, P. Gomes, R. Correia, F. Abdiwi, and W. Yu, "Press forming the double-dome benchmark geometry using a 0/90 uniaxial cross-ply advanced thermoplastic composite," 2012.
[175] P. Harrison, F. Abdiwi, Z. Guo, P. Potluri, and W. Yu, "Characterising the shear-tension coupling and wrinkling behaviour of woven engineering fabrics," *Composites. Part A, Applied science and manufacturing*, vol. 43, pp. 903-914, 2012.
[176] F. Abdiwi, P. Harrison, W. R. Yu, and Z. and Guo, "Modelling the Shear-Tension Coupling of Engineering Fabrics," presented at the 8th European Solid Mechanics Conference (ESCM2012), Graz, Austria, 2012.
[177] P. Harrison, "Normalisation of biaxial bias extension test results considering shear tension coupling," *Composites Part A: Applied Science and Manufacturing*, 2012.
[178] R. Sidhu, R. Averill, M. Riaz, and F. Pourboghrat, "Finite element analysis of textile composite preform stamping," *Composite structures*, vol. 52, pp. 483-497, 2001.
[179] E. B. Belov, S. V. Lomov, I. Verpoest, T. Peters, D. Roose, R. S. Parnas, K. Hoes, and H. Sol, "Modelling of permeability of textile reinforcements: lattice Boltzmann method," *Composites Science and Technology*, vol. 64, pp. 1069-1080, 2004.

[180] R. Gauvin, F. Trochu, Y. Lemenn, and L. Diallo, "Permeability measurement and flow simulation through fiber reinforcement," *Polymer Composites*, vol. 17, pp. 34-42, 1996.
[181] N. Hamila and P. Boisse, "Simulations of textile composite reinforcement draping using a new semi-discrete three node finite element," *Composites Part B: Engineering*, vol. 39, pp. 999-1010, 2008.
[182] N. Hamila, P. Boisse, and S. Chatel, "Semi-discrete shell finite elements for textile composite forming simulation," *International journal of material forming*, vol. 2, pp. 169-172, 2009.
[183] F. Abbassi, I. Elfaleh, S. Mistou, A. Zghal, M. Fazzini, and T. Djilali, "Experimental and numerical investigations of a thermoplastic composite (carbon/PPS) thermoforming," *Structural Control and Health Monitoring*, vol. 18, pp. 769-780, 2011.
[184] L. Dong, C. Lekakou, and M. Bader, "Processing of composites: simulations of the draping of fabrics with updated material behaviour law," *Journal of Composite Materials*, vol. 35, pp. 138-163, 2001.
[185] J. S. Lee, S. J. Hong, W.-R. Yu, and T. J. Kang, "The effect of blank holder force on the stamp forming behavior of non-crimp fabric with a chain stitch," *Composites Science and Technology*, vol. 67, pp. 357-366, 2007.
[186] X. Peng and F. Ding, "Validation of a non-orthogonal constitutive model for woven composite fabrics via hemispherical stamping simulation," *Composites Part A: Applied Science and Manufacturing*, vol. 42, pp. 400-407, 2011.
[187] S. Sadough, F. Biglari, M. Shirani, and A. Agahi, "Reinforced thermoplastic sheet composite deep drawing investigation."
[188] A. A. Skordos, C. Monroy Aceves, and M. P. Sutcliffe, "A simplified rate dependent model of forming and wrinkling of pre-impregnated woven composites," *Composites Part A: Applied Science and Manufacturing*, vol. 38, pp. 1318-1330, 2007.
[189] K. Vanclooster, S. V. Lomov, and I. Verpoest, "Simulation of multi-layered composites forming," *International Journal of Material Forming*, vol. 3, pp. 695-698, 2010.
[190] M. A. Khan, T. Mabrouki, S. Gauthier, E. Vidal-Salle, and P. Boisse, "Preforming simulation of the reinforcements of woven composites: continuous approach within a commercial code," *International Journal of Material Forming*, vol. 1, pp. 879-882, 2008.
[191] X. Peng and Z. U. Rehman, "Numerical Simulation of Textile Composite Stamping On Double Dome," in *AIP Conference Proceedings*, 2011.
[192] K. Vanclooster, S. V. Lomov, and I. Verpoest, "Simulating and validating the draping of woven fiber reinforced polymers," *International Journal of Material Forming*, vol. 1, pp. 961-964, 2008/04/01 2008.
[193] A. Willems, S. Lomov, D. Vandepitte, and I. Verpoest, "Double dome forming simulation of woven textile composites," in *Proceedings of the 9th ESAFORM conference on material forming. Publishing House Akapit, Poland*, 2006, pp. 747-750.
[194] A. Willems, S. Lomov, I. Verpoest, D. Vandepitte, P. Harrison, and W. Yu, "Forming simulation of a thermoplastic commingled woven textile on a double dome," *International Journal of Material Forming*, vol. 1, pp. 965-968, 2008.
[195] A. Long, A. A. Skordos, P. Harrison, M. Clifford, and M. P. Sutcliffe, "Optimisation of Sheet Forming for Textile Composites using variable Peripheral Pressure," presented at the 27th International Conference SAMPE EUROPE Paris, France, 2006.
[196] S. Sharma and M. Sutcliffe, "Draping of woven fabrics: Progressive drape model," *Plastics, rubber and composites*, vol. 32, pp. 57-64, 2003.
[197] N. Hamila, P. Wang, E. Vidal-Sallé, and P. Boisse, "Simulation of Forming and Wrinkling of Textile Composite Reinforcements," in *AIP Conference Proceedings*, 2011, p. 942.
[198] P. Wang, N. Hamila, and P. Boisse, "Numerical simulation of multi-layered textile composite reinforcement forming," in *AIP Conference Proceedings*, 2011, p. 918.
[199] A. Cherouat and H. Borouchaki, "Present State of the Art of Composite Fabric Forming: Geometrical and Mechanical Approaches," *Materials*, vol. 2, pp. 1835-1857, 2009.
[200] J. Wiggers, "Analysis of textile deformation during preforming for liquid composite moulding," University of Nottingham, 2007.
[201] N. Burnford, "Development of Drape Simulation Software and the Optimisation of Variable-Length Textiles," 2011.

[202] N. Hamila, P. Boisse, F. Sabourin, and M. Brunet, "A semi-discrete shell finite element for textile composite reinforcement forming simulation," *International Journal for Numerical Methods in Engineering*, vol. 79, pp. 1443-1466, 2009.
[203] Q. Chen, P. Boisse, N. Hamila, A. Saouab, C. Park, and J. Bréard, "A finite element method for the forming simulation of the reinforcements of thermoplastic composite," *International Journal of Material Forming*, vol. 2, pp. 213-216, 2009.
[204] F. Dumont, C. Weimer, D. Soulat, J. Launay, S. Chatel, and S. Maison-Le-Poec, "Composites preforms simulations for helicopters parts," *International Journal of Material Forming*, vol. 1, pp. 847-850, 2008.
[205] M. R. Garnich and N. A. Klymyshyn, "Multiscale analysis of stamp forming of a woven composite," *Journal of Thermoplastic Composite Materials*, 2011.
[206] P. Harrison, W. R. Yu, J. Wang, T. Baillie, A. C. Long, and M. J. Clifford, "Numerical evaluation of a rate dependent model for viscous textile composites," in *15th International Conference on Composite Materials*, Durban, South Africa, 2005.
[207] R. a. H. Thije ten, Sebastiaan "Multi-layer thermoplastic composites manufacturing processes: simulations and experiments," presented at the In: SAMPE Europe International Conference & Forum, SEICO 2011, Paris, France., 2011.
[208] N. Hamila, Y. Aimène, S. Gatouillat, S. Bel, E. Vidal-Sallé, and P. Boisse, "Textile Composite Reinforcement Forming Simulation: Continuous, Discrete and Semi Discrete Approaches," in *Recent Advances in Textile Composites: Proceedings of the 10th International Conference on Textile Composites*, 2010, p. 437.
[209] P. Potluri, S. Sharma, and R. Ramgulam, "Comprehensive drape modelling for moulding 3D textile preforms," *Composites Part A: Applied Science and Manufacturing*, vol. 32, pp. 1415-1424, 2001.
[210] *Carbon Revolution*. Available: http://carbonrevolution.weareanyone.com/index.php
[211] (21 November ). *WEDS SPORT FULL CARBON FIBER WHEEL*.
[212] A. Easdale, "Design and manufacture of a carbon composite bicycle frame, BEng, Dept Mech Eng, Uni of Glasgow, April 2010 [pdf]," BEng, School of Engineering, , University of Glasgow, James Watt South Building, Glasgow G12 8QQ, Scotland, 2010.
[213] S. Adams, "Introduction of a segmented blankholder to press forming of carbon fibre composites," MEng, school of mechanical materials and manufacturing engineering, university of nottingham 2005.
[214] Abaqus. *Abaqus Theory Manual, Section 2.11.1 Uncoupled heat transfer analysis.* Available: ref-far:2080/v6.9/books/stm/default.htm
[215] S. V. Lomov, D. S. Ivanov, I. Verpoest, M. Zako, T. Kurashiki, H. Nakai, J. Molimard, and A. Vautrin, "Full-field strain measurements for validation of meso-FE analysis of textile composites," *Composites Part A: Applied Science and Manufacturing*, vol. 39, pp. 1218-1231, 2008.
[216] R. E. Robertson, E. S. Hsiue, E. N. Sickafus, and G. S. Y. Yeh, "Fiber rearrangements during the molding of continuous fiber composites. I. Flat cloth to a hemisphere," *Polymer Composites*, vol. 2, pp. 126-131, 1981.
[217] A. Willems, S. V. Lomov, I. Verpoest, and D. Vandepitte, "Optical strain fields in shear and tensile testing of textile reinforcements," *Composites Science and Technology*, vol. 68, pp. 807-819, 2008.
[218] A. Willems, S. V. Lomov, I. Verpoest, and D. Vandepitte, "Drape-ability characterization of textile composite reinforcements using digital image correlation," *Optics and Lasers in Engineering*, vol. 47, pp. 343-351, 2009.
[219] A. C. Long, "Preform Design for Liquid Moulding Processes," PhD, The University of Nottingham, 1994.
[220] F. Van Der Weeen, "Algorithms for draping fabrics on doubly-curved surfaces," *International Journal for Numerical Methods in Engineering*, vol. 31, pp. 1415-1426, 1991.
[221] B. Souter, "Effects of fibre architecture on formability of textile preforms," PhD, The University of Nottingham, 2001.
[222] K. A. M., "Numerical and experimental forming analysis of textile composite reinforcements based on a hypoelastic behavior," PhD, Institut National Des Science Appliquees De Lyon Lyon, 2009.

[223] Abaqus, "Abaqus Analysis Users' Manual, 6.3.3 Explicit dynamic analysis ", 6.9-1, Ed., ed.
[224] V. Carvelli, J. Pazmino, S. V. Lomov, and I. Verpoest, "Deformability of a non-crimp 3D orthogonal weave E-glass composite reinforcement," *Composites Science and Technology*, vol. 73, pp. 9-18, 2012.

# Publications


1. Abdiwi, F., Harrison, P. , Guo, Z., Potluri, P., and Yu, W.R. (2011) Measuring the shear-tension coupling of engineering fabrics. AIP Conference Proceedings, ESAFORM, Belfast, 2011. pp. 889-894.

2. Abdiwi, F., Harrison, P. , Koyama, I., Yu, W.R., Long, A.C., and Guo, Z. (2011) Modelling Variability of Tow Orientation for Woven Textile Composites. In: 18th International Conference of Composite Materials, 21-26 August 2011, Jeju Island, Korea.

3. P. Harrison, R. Gomes, N. Correia, F. Abdiwi, W.R. Yu, Press Forming the Double Dome Benchmark Geometry using a 0/90 Uni-axial Cross Ply Advanced Thermoplastic Composite, ECCM15 - 15TH EUROPEAN CONFERENCE ON COMPOSITE MATERIALS, Venice, Italy, 24-28 June 2012

4. Harrison, P., Abdiwi, F., Guo, Z., Potluri, P., and Yu, W.R. (2012) Characterising the shear–tension coupling and wrinkling behaviour of woven engineering fabrics. Composites Part A: Applied Science and Manufacturing, 43 (6). pp. 903-914.

5. Abdiwi, F., Harrison, P. , Koyama, I., Yu, W.R., Long, A.C., Corriea, N., and Guo, Z. (2012) Characterising and modelling variability of tow orientation in engineering fabrics and textile composites. Composites Science and Technology , Volume 72, Issue 9, 1034–1041

6. Abdiwi, F., Harrison, P. , Yu, W.R. and Guo, Z., Modelling the Shear-Tension Coupling of Engineering Fabrics, 8th ESMC July 2012, Graz, Austria Available upon request.

7. Abdiwi, F., Harrison, P. , Guo, Z., Potluri, P., and Yu, W.R. (2011) Effect of Tow Meander on the Shear Compliance of Woven Engineering Fabrics Measured using the Biaxial Bias Extension Test. Submitted to the 16th annual ESAFORM Conference on Material Forming, ESAFORM, 22-24 April 2013, in Aveiro, Portugal, 2013.

8. Abdiwi, F., Harrison, P., and Yu, W.R. (2013) Modelling the Shear-Tension Coupling of Woven Engineering Fabrics. Submitted to Advances in Materials Science and Engineering Journal.